Universität Potsdam

Catastrophic Sediment Pulses in the Pokhara Valley, Nepal

Amelie Stolle

Kumulative Dissertation

Zur Erlangung des akademischen Grades

Doktor der Naturwissenschaften (Dr.rer.nat)

In der Wissenschaftsdisziplin Geomorphologie

eingereicht an der

Mathematisch- Naturwissenschaftlichen Fakultät

Institut für Erd- und Umweltwissenschaften

der Universität Potsdam

Disputation: 03.Juli 2018

Published online at the
Institutional Repository of the University of Potsdam:
URN urn:nbn:de:kobv:517-opus4-413341
http://nbn-resolving.de/urn:nbn:de:kobv:517-opus4-413341

Supervisor:

Oliver Korup

Monique Fort

Anne Bernhardt

Independent Reviewer:

Ramón Arrowsmith

Water is the driver of Nature

(Leonardo da Vinci)

Prologue

High mountain regions around the world were fascinating for me throughout my life. Rough landscapes and mountain peaks with lush meadows between and in front are the beauty of these regions. However, this environment is a tough place for people who call these unpredictable regions their home. Nevertheless, valley fills, fan surfaces and river sides are preferred locations where people profit from the abundance of water and often from productive land. The Himalayas are drained by some major rivers along which, people have been settling for several thousand years. The adjustment of rivers after disturbances, in a country like Nepal with high magnitude earthquakes and many landslides, is still poorly understood. I am happy to be part of a research team studying the origin of the Pokhara Valley infill. During field work, I got to know Nepal as a fascinating and unique place because of its landscape: mountains, large rivers, culture and people. The locals and their way of life are of great interest to me in many ways as many of them live with almost nothing. However, they are pleased with what they have, sharing the little they possess with friends, neighbors, and foreigners. They are friendly, helpful, curious and always happy to talk to you. For tourists, Pokhara is the place to go before starting the next trekking tour or to admire the stunning view to the Annapurna peaks during sunrise. Many locals run hotels and restaurants at Phewa lake side or run shops to sell Nepalese clothes, scarfs, hats or Himalayan tea. Those in the tourism business may earn sufficient money for living, but many others need to earn their money by farming, road construction, or in gravel mining on the Seti River. The river cuts through Pokhara city and during monsoon season it is very fast flowing, while during the dry season it becomes a calm meandering stream. This is the time when gravel miners work at river banks. Some families even move for this time of the year to Ramghat, a place in Pokhara city (see Fig. 3.1 for location) along the river. Ramghat forms a topographic depression surrounded by up to 60 m high terraces on which the city is built on. Some children are not able to go to school during low river flow because they need to work in gravel mining. Ramghat appears as a gaping hole in the alluvial landscape (see images on the previous and the next page) where hundreds of people are working in gravel pits, shoveling, sifting sand, and sorting gravels to finally carry the sands to the top of the terrace. It is a surreal

view to witness the sheer size and scale of river mining in a popular tourist city; hundreds of people are dotted along Seti's river bed with yellow or white plastic bags, some of them carry baskets on their back. I remember seeing children, women, and men working in these gravel pits, picking up bags of sand, silt, and gravel of estimated 70 kg, and carrying them up to the top of the terrace on little trails hoping to get 20 rupees (about 15-20 euro cent) per bag. River mining has become automated in most parts of the world, while in Nepal human labor is cheaper than digging equipment. Moreover, the Ramghat river mine is technically illegal like so many in the Pokhara and Kathmandu Valley. Nonetheless, huge amounts of material are taken from the river gravel beds each day.

With this thesis, I got the chance to learn not only the geological history of the Pokhara Valley, but also the culture and Nepalese people; I learned to combine different topics from sedimentology and their archives to radiocarbon dating, the earthquake history of the country and fluvial adjustment after strong perturbation. In Nepal, it seems the clock is ticking slower than in Europe. For me, the people and their future is the motivation studying the geological history of the valley. Knowing about the modern hazards and learning from the past may provide some of them with a better life in future.



Abstract

Fluvial terraces, floodplains, and alluvial fans are the main landforms to store sediments and to decouple hillslopes from eroding mountain rivers. Such low-relief landforms are also preferred locations for humans to settle in otherwise steep and poorly accessible terrain. Abundant water and sediment as essential sources for buildings and infrastructure make these areas amenable places to live at. Yet valley floors are also prone to rare and catastrophic sedimentation that can overload river systems by abruptly increasing the volume of sediment supply, thus causing massive floodplain aggradation, lateral channel instability, and increased flooding. Some valley-fill sediments should thus record these catastrophic sediment pulses, allowing insights into their timing, magnitude, and consequences.

This thesis pursues this theme and focuses on a prominent ∼150 km^2 valley fill in the Pokhara Valley just south of the Annapurna Massif in central Nepal. The Pokhara Valley is conspicuously broad and gentle compared to the surrounding dissected mountain terrain, and is filled with locally more than 70 m of clastic debris. The area's main river, Seti Khola, descends from the Annapurna Sabche Cirque at 3500-4500 m asl down to 900 m asl where it incises into this valley fill. Humans began to settle on this extensive fan surface in the 1750's when the Trans-Himalayan trade route connected the Higher Himalayas, passing Pokhara city, with the subtropical lowlands of the Terai. High and unstable river terraces and steep gorges undermined by fast flowing rivers with highly seasonal (monsoon-driven) discharge, a high earthquake risk, and a growing population make the Pokhara Valley an ideal place to study the recent geological and geomorphic history of its sediments and the implication for natural hazard appraisals.

The objective of this thesis is to quantify the timing, the sedimentologic and geomorphic processes as well as the fluvial response to a series of strong sediment pulses. I report diagnostic sedimentary archives, lithofacies of the fan terraces, their geochemical provenance, radiocarbon-age dating and the stratigraphic relationship between them. All these various and independent lines of evidence show consistently that multiple sediment pulses filled the Pokhara Valley in medieval times, most likely in connection with, if not triggered by, strong seismic ground shaking. The geomorphic and sedimentary evidence is consistent with catastrophic fluvial aggradation tied to the timing of three medieval Himalayan earthquakes in ∼1100, 1255, and 1344 AD. Sediment provenance and calibrated radiocarbon-age data are the key to distinguish three individual sediment pulses, as these are not evident from their sedimentology alone. I explore various measures of adjustment

and fluvial response of the river system following these massive aggradation pulses. By using proxies such as net volumetric erosion, incision and erosion rates, clast provenance on active river banks, geomorphic markers such as re-exhumed tree trunks in growth position, and knickpoint locations in tributary valleys, I estimate the response of the river network in the Pokhara Valley to earthquake disturbance over several centuries. Estimates of the removed volumes since catastrophic valley filling began, require average net sediment yields of up to 4200 t km^{-2} yr^{-1} since, rates that are consistent with those reported for Himalayan rivers. The lithological composition of active channel-bed load differs from that of local bedrock material, confirming that rivers have adjusted 30-50% depending on data of different tributary catchments, locally incising with rates of 160-220 mm yr^{-1}. In many tributaries to the Seti Khola, most of the contemporary river loads come from a Higher Himalayan source, thus excluding local hillslopes as sources. This imbalance in sediment provenance emphasizes how the medieval sediment pulses must have rapidly traversed up to 70 km downstream to invade the downstream reaches of the tributaries up to 8 km upstream, thereby blocking the local drainage and thus reinforcing, or locally creating new, floodplain lakes still visible in the landscape today.

Understanding the formation, origin, mechanism and geomorphic processes of this valley fill is crucial to understand the landscape evolution and response to catastrophic sediment pulses. Several earthquake-triggered long-runout rock-ice avalanches or catastrophic dam burst in the Higher Himalayas are the only plausible mechanisms to explain both the geomorphic and sedimentary legacy that I document here. In any case, the Pokhara Valley was most likely hit by a cascade of extremely rare processes over some two centuries starting in the early 11^{th} century. Nowhere in the Himalayas do we find valley fills of comparable size and equally well documented depositional history, making the Pokhara Valley one of the most extensively dated valley fill in the Himalayas to date. Judging from the growing record of historic Himalayan earthquakes in Nepal that were traced and dated in fault trenches, this thesis shows that sedimentary archives can be used to directly aid reconstructions and predictions of both earthquake triggers and impacts from a sedimentary-response perspective. The knowledge about the timing, evolution, and response of the Pokhara Valley and its river system to earthquake triggered sediment pulses is important to address the seismic and geomorphic risk for the city of Pokhara. This thesis demonstrates how geomorphic evidence on catastrophic valley infill can help to independently verify paleoseismological fault-trench records and may initiate re-thinking on post-seismic hazard assessments in active mountain regions.

Kurzfassung

Der Transport von Sedimenten in Flüssen ist wichtig, um Landschaftsformen in Gebirgsregionen entstehen zu lassen. Eine erhöhte, plötzliche Sedimentzufuhr, beispielsweise durch Massenbewegungen ausgelöst, kann ein Flusssystem schnell aus dem Gleichgewicht bringen. Innerhalb kurzer Zeit transportiertes Sediment wird häufig an Überschwemmungsflächen abgelagert, was zu instabilen Flussverläufen, erhöhtem Sedimentabtrag und vermehrten Überschwemmungen führen kann. Talverfüllungen, Schwemmmfächer, Flussterrassen und Überschwemmungsebenen sind in diesem Zusammenhang die am häufigsten vorkommenden Landschaftsformen, um große Materialvolumen zu speichern. Weil Wasser und Sediment als Baustoff in ausreichenden Mengen zur Verfügung stehen, sind sie bevorzugte Siedlungsflächen.

Diese Dissertation untersucht in drei Studien die Entstehung, geomorphologische und sedimentologische Prozesse, sowie die Anpassung des Flusssystems auf einen erhöhten Sedimenteintrag des heute mit Sedimenten verfüllten Pokhara Tals im zentralen Himalaya. Die Stadt Pokhara liegt am Fuße des bis zu 8000 m hohen Annapurna Massivs auf einem $\sim$150 km^2 großen, aus klastischen Sedimentablagerungen bestehender Fächer. Das Tal ist von bis zu 70 m hohen Terrassen gekennzeichnen und auffallend flach im Vergleich zur umliegenden Topographie. Der Seti Khola entwässert das Annapurna Massiv in einer Höhe von 3500-5000 m ü.N.N. und erreicht nach kurzer Distanz den Pokhara Fächer. Erste Bewohner siedelten sich in den 1750er Jahren an als die frühere Handelsroute den Hohen Himalaya mit dem subtropischen Tiefland (Terai) verbunden hat. Seither wächst die Stadt stetig und ist heute, nach Kathmandu, die zweitgrößte Stadt Nepals.

Durch die Nähe der geologischen Hauptstörung zwischen dem Hohen Himalaya und dem tiefer liegenden Vorderen Himalaya herrscht ein hohes Erdbebenrisiko im Pokhara Tal. Die Kombination aus hohen Terrassen und tiefen, von schnell fließenden Flüssen ausgespülten Schluchten, machen das Tal zu einem geeigneten Ort, um die kaum untersuchte geologische und geomorphologische Geschichte der in diesem Tal abgelagernten Sedimente zu erforschen. Um Landschaftsveränderungen und -entwicklungen zu verstehen sowie die Reaktion des Flussnetzes auf erhöhte Sedimentzufuhr zu überblicken, ist es unabdingbar, den Ursprung des Materials, die sedimentologischen Prozesse und mögliche Auslöser der Talverfüllung zu analysieren.

Daten und Proben aus dem Gelände, die später im Labor datiert, ausgewertet, mit sedimentologischen Aufzeichnungen kombiniert und durch fernerkundliche Methoden ergänzt

und analysiert wurden, bilden die Basis der Ergebnisse dieser Dissertation. Da solche massiven, in sehr kurzer Zeit abgelagerten Sedimente auf eine katastrophale Entstehung hindeuten, spielt auch der zeitliche Aspekt eine wichtige Rolle.

Verschiedene Beweise zeigen, dass mindestens drei Sedimentereignisse das Pokhara Tal verfüllt haben. Ich dokumentiere ein aufschlussreiches Sedimentarchiv, Sedimentabfolgen geochemische Provenienz, Radiokarbonalter und die stratigraphische Beziehung zwischen diesen Ergebnissen. Diese unabhängig voneinander gewonnenen Ergebnisse zeigen, dass geomorphologische und sedimentologische Beweise mit den Altersdatierungen konsistent sind und wir mit diesen Untersuchungen die abgelagerten Geröllmassen mit historischen Starkbeben in Verbindung bringen können (∼1100, 1255, 1344 AD). Provenienz in Kombination mit den Altersdatierungen lassen uns wiederum die drei Ereignisse in ihren Mächtigkeit unterscheiden und individuell das Volumen bestimmen. Messungen zur Anpassung des Flusssystems ergeben, dass das System noch stark von seinem Gleichgewicht abweicht, da erst 30-70% des über kurze Zeit abgelagerten Materials aus dem Flussbett ausgeräumt wurden. Hierfür benutzte Marker sind unter Anderem volumetrische Berechnungen, Erosions- und Einschneideraten der Flüsse, Bäume in ihrer Wachstumsposition zur Altersdatierung und Stufen im Längsgerinneprofil der Seitenflüsse. Das bis heute abgetragene Volumen ergibt Sedimentaustragsraten von bis zu 4200 t km^{-2} yr^{-1} am Fuße des Fächers. Die lithologische Zusammensetzung aktiver Flussbänke in Seitentälern zeigt, dass Material der Formation gegenüber lokalem Grundgestein immer noch dominiert. Dieses lithologische Ungleichgewicht verdeutlicht, wie schnell Sedimentmassen in drei Ereignissen über 70 km talabwärts und bis zu 8 km flussaufwärts (in die Seitentäler) abgelagert wurden. Lokale Einschneideraten in die Pokhara Formation liegen zwischen 0.16-0.22 m yr^{-1} und weisen auf einen sich schnell verändernden Flussverlauf hin.

Um die Landschaftsentwicklung nach solch massiven Sedimentablagerungen analysieren zu können, müssen die Sedimentologie, die geomorphologischen Prozesse, der Ursprung und die Mechanismen der Talverfüllung verstanden und als Basiswissen vorausgesetzt werden. Aus den gewonnen Resultaten schließen wir, dass das Pokhara Tal von mehreren katastrophal aufeinanderfolgenden Naturereignissen in einem Zeitraum von ∼200 Jahren seit dem 12. Jahrhundert heimgesucht wurde. Nirgendwo im Himalaya finden wir vergleichbare Talverfüllungen, weder in ihrer Größe, noch in dieser detailliert aufgenommenen geomorphologischen Geschichte und sedimentologischen Aufzeichnungen. Das Pokhara Tals ist damit eine der am besten datierten Talverfüllungen des gesamten Himalaya. Diese Arbeit zeigt, dass in sedimentären Archiven - unabhängig von der Paläoseismologie - historische

Starkbeben datiert und erkannt werden können. So hilft das Wissen über den zeitlichen Verlauf der Talverfüllung, die Entwicklung des Fächers und die Anpassung des Flusssystems in Zukunft Entscheidungen zu treffen, die das geomorphologische Risiko für die Stadt Pokhara vermindern und gleichzeitig bauliche Maßnahmen besser an die lokalen Risikofaktoren angepasst werden können.

Acknowledgements

I would like to begin by expressing my deep gratitude to my supervisors, Oliver Korup, Monique Fort, and Anne Bernhardt for their support and grateful guidance through these last years. My experience at the Institute and with my precious Geohazards Research Group was always friendly and with great support from all sides. I will keep this time in warm and good memory. I'd like to thank Oliver for his indispensable support and valuable inputs whenever I needed help. His scientific guidance, immense knowledge full of ideas, his time and motivation always helped to look ahead, never loosing the goal. My gratitude goes to Monique, who spent lots of weeks with me in the field. Her stories and pictures about the Pokhara Valley some 30 years ago, and her knowledge in the field made them to great experiences. Monique, I am very thankful you shared this time with me. I'd like to thank Anne for her great support and help when ever I needed it. Having you as a personal sedimentology teacher in the field was my resort, the Pokhara gravels were (and still are) overwhelming when I first started with sedimentological logs and descriptions at these huge terraces and massive slackwater deposits.

My time in Potsdam would not have been the same without these amazing colleques and office mates: I'd like to thank Wolfgang Schwanghart for his time and support in the field, and his ideas whenever I did not know how to solve one or the other topographic problem; and I thank, Swenja Rosenwinkel, Georg Veh, Henry Munack, Agostiny Lontsi for their helpful discussions, inspiration and ideas, and for sharing laughs and coffee breaks - thanks for making my PhD time to such great years.

I will never forget Basanta Ray Adhikari's support in Nepal; thanks for your help by the organization of all field trips, for being our translator when English did not help anymore to communicate with locals, and for your assistance at the DMG to get samples back home to Potsdam. I'd like to thank Bhairab Sitaula for his great support getting research permits for me in Nepal.

I'd like to thank all my co-authors of the three studies that are part of this thesis, for sharing their knowledge, for proof reading the manuscripts, providing data, and for giving the opportunity to work together. Researchers, colleagues and students helped me with field work, data processing, and managing the project. Thank you: Cornelia Becker, Tim Cohen, John Jansen, Tanja Klaka-Tauscher, Marina Meiners, Ines Münch, Pramod Pokharel, Miriam Roschlaub, Elisabeth Schönfeldt, Jan Seidemann, Bastian Steinke, and Jana Tesch.

I also like to thank the German Bakery at the lakeside in Pokhara, for coffee, Apfelstrudels, pancakes, and porridge - without your breakfast, fieldwork would not have been started successfully every morning.

I'd like to acknowledge the German Research Foundation (Ko 3937/9-1), the Graduate School "Natural Hazards and Risks in a Changing World" (NatRiskChange), and the Potsdam University Graduate School (PoGS) for funding this research project.

Last but certainly not least, I'd like to thank friends and my family, for sharing beautiful times and vacations. A special thank goes to my dear friend Carly for proof reading and correcting my English grammar. Thanks to my Mom for lovely words and her motivation before starting and during my PhD, even I was far away from home; thanks for your support even you cannot be with me anymore. Thanks to my Dad for great discussions about Nepal and geo-informatics, and for proof reading this thesis. A special thank goes to Moriz for his support, for lots of discussions, his time, cooking, for drinks and chocolate; thanks to my siblings, nephew, and niece for being there, and the times between to start again motivated after a weekend I spent with them.

Declaration of Authorship

I, Amelie Stolle, hereby confirm that I have authored this thesis entitled **"Catastrophic Sediment Pulses in the Pokhara Valley, Nepal"** independently and without use of others than the indicated sources. This thesis was carried out at the Institute of Earth- and Environmental Sciences, University of Potsdam. All passages which are literally or in general matter taken out of publications or other sources are marked as such.

I confirm that:

- This work was done wholly or mainly while in candidature for a research degree at this University.
- Where any part of this thesis has previously been submitted for a degree or any other qualification at this University or any other institution, this has been clearly stated.
- Where I have consulted the published work of others, this is always clearly attributed.
- Where I have quoted from the work of others, the source is always given. With the exception of such quotations, this thesis is entirely my own work.
- I have acknowledged all main sources of help.
- Where the thesis is based on work done by myself jointly with others, I have made clear exactly what was done by others and what I have contributed myself.

Amelie Stolle

Potsdam, February, 2018

Contents

List of Figures

All photographs by the Author unless otherwise noted

List of Tables

Abbreviation and Symbols

AD Anno Domini

AMS Accelerator Mass Spectrometry

BP Before Present

asl above sea level

C.E. Common Era

CRM Certified Reference Material

DEM Digital Elevation Model

dGPS differential Global Positioning System

Fm Formation

GIS Geographic Information Systems

GPS Global Positioning System

HDI Highest Density Interval

HH Higher Himalayan; involves HHC and TSS material

HHC Higher Himalayan Crystalline

ka Thousand years

LHS Lesser Himalayan Series

$\mathbf{M}_w$ Earthquake Magnitude

MCT Main Central Thrust

MFT Main Frontal Thrust

MHT Main Himalayan Thrust

PDF Probability Distribution Function

TSS Tethyan Sedimentary Series

XRD X-Ray Diffraction

XRF X-Ray Fluorescence Spectrometry

1 Introduction

1.1. Motivation

Fluvial processes reflected in river morphology are transportation, sedimentation, and erosion; together with mass wasting, these processes develop drainage basins. Rivers transport fine-grained sediments to large boulders depending on their capacity and flow regime. The amount of sediment supply to rivers varies from natural geomorphic processes such as fluvial scour, landslides, debris flows or flash floods, to anthropogenic disturbances in the watershed like landcover changes (Wolman, 1979; Venditti et al., 2010; Gran and Czuba, 2017). Sediment supply from hillslope to rivers is an ongoing process, while extremely large and rare sediment transport events deliver sediments in very short time that usually deposit in a whole or many year(s) (Korup, 2012). Brundsen and Thornes (1979) made the basic proposition: "For any given set of environmental conditions, through the operation of a constant set of processes, there will be a tendency over time to produce a set of characteristic landforms". These landforms are formed over longer or shorter times. For example, catastrophic floods are capable of changing the surrounding landscape, and to transport and deposit huge sediment volumes to a river network (Russell, 2005), aggrading sediment on floodplains over short time. Sudden catastrophic sediment supply imbalances the system making the river dynamics dependent to the type of perturbation, the magnitude, extent and duration (Gran and Czuba, 2017). Catastrophic sedimentation in mountain rivers remains a frequently observed, though still, under-researched problem for people, built infrastructure, and land use. The sudden or rapid raising of channel beds and floodplains by aggrading sediment may compromise channel stability, change flood frequencies, impact on bridges, and deliver contaminants. Triggers of catastrophic aggradation events range from earthquakes to volcanic eruptions, but those are not required to explain large sediment transports, as extreme precipitation events can also trigger debris and rock avalanches that lead to massive aggradation of low-gradient flood-

plains and valley fills (Hewitt et al., 2008; Gran and Czuba, 2017). Keefer (1994) argues that earthquake triggered massive sedimentation in active orogens increase the supply of sediment to rivers; background rates stay high, but usually return to pre-earthquake levels within a few years to decades (Dadson et al., 2004; Hovius et al., 2011; Marc et al., 2015). Other, and potentially more rare, causes include the failure of large glacier lakes or otherwise naturally dammed lakes (O'Connor and Baker, 1992; Rudoy and Baker, 1993; Coxon et al., 1996; Clague, 2000; Clarke et al., 2003; Montgomery et al., 2004; Westoby et al., 2014). However, these are important events whose legacy may dominate Holocene valley-floor evolution in some mountain regions (Montgomery et al., 2004). Examples include rivers impacted by volcanic eruptions that show the highest recorded specific sediment yields (e.g. the volcanic eruption of Mount Pinatubo in 1991 with $>10^6$ Mg km^{-2} yr^{-1}), accompanied with channel changes (Hayes et al., 2002); aggradation on a nearby alluvial fan at Mount Pinatubo took place some 6-8 years after the volcanic eruption with 2.2 m of sedimentation within 5 weeks. Other examples are the Lake Missoula outburst floods (O'Connor and Baker, 1992), the Altai floods in Siberia (Carling et al., 2010), or the megafloods at Tsangpo River in Tibet (Montgomery et al., 2004). Rivers often cut through these developed landforms while ever responding to external disturbances and adapting to new conditions of form and flow roughness (Knighton, 1989). Many of the conditions, i.e. mostly giant meltwater lakes, for generating similar landscape-transforming flood impacts are not given today. Nonetheless, the (pre-)historic record of catastrophic sedimentation remains scarce and in need of better study to inform hazard and risk appraisals concerned with mountain rivers, let alone with the long-lasting geomorphic consequences of rainstorms and earthquakes.

Gradual vs. catastrophic sedimentation

Catastrophic sedimentation is a process that mobilizes sediments in very short time that usually deposit in a whole or many year(s). Channel changes in response to high sedimentation rates are very common (Hayes et al., 2002), and sediments that move rapidly, could be considered as a catastrophic event (Strom, 2009). Reading (1996) defines *gradual* or background sedimentary processes as such that persist most of the time. However, gradual processes also include ice, wind or fluvial currents, "which, in some cases, have very high levels of physical energy" (Reading, 1996). Some of these processes transport and deposit sediments very slowly, while wind, tidal or fluvial currents, are also able to deposit quickly. But, erosion is almost as fast as their depo-

sition. *Catastrophic* processes occur instantaneously, with frequently involved energy levels that are several orders of magnitude greater than those of a normal sedimentation. Storms, heavy rain, earthquakes or volcanic eruptions are typical triggers for such mass flows, such as storm surges or flood currents (Reading, 1996). Such sediment layers are characterized as sharp-based, graded, or deposits with a large proportion of the total rock record from the surrounding area. Reading (1996) defines a third form of sedimentation processes; *exceptional* events that have an intensity at least an order of magnitude greater than a catastrophic event; such processes are rare for a certain environment and mainly caused by earthquakes that mobilizes thousands of cubic kilometers in volume. "The deposits that are produced by exceptional events are recognized by their uniqueness in the sedimentary record" (Reading, 1996).

The Himalayas are one such example for high sediment supply and large rivers, featuring the highest mountain peaks, active tectonic shortening, one of the world's most extreme reliefs, highly monsoonal precipitation, high magnitude earthquakes, appropriate erosion and incision rates (Lavé and Avouac, 2001; Montgomery et al., 2004), and sedimentation processes from normal to catastrophic or even exceptional events. Moreover, the Himalayas are drained by rivers that deliver huge amounts of sediment to the ocean (Blöthe and Korup, 2013). In mountain regions, sediments are stored in valley fills, fluvial terraces, floodplains and alluvial fans, one of the main landforms to decouple hillslopes from river-channel processes (Fryirs et al., 2007; Straumann and Korup, 2009). Eventually, a complex sedimentary assemblage develops and may "provide a record of individual depositional events and seasonal and longer-term sedimentation episodes. Some valley fills resulting from aggradation episodes are vast" (Hewitt et al., 2008), representing abandoned river courses, sedimentological features and low-gradient surfaces which are important to understand the geomorphic evolution of mountainous regions (Chaudhary et al., 2015). Valley fills in the Himalayas are thought to form as a result of high precipitation events, triggering of landslides or enhanced sediment supply to river networks (Pratt et al., 2002; Chaudhary et al., 2015). Epigenetic gorges result from the superimposition of a river after large aggradation. They may play an important role in delaying: 1) the process of long-profile adjustment and 2) the export of catastrophic deposition (Ouimet et al., 2009). The understanding of such valley fill features in the Himalayan fluvial systems is very limited still; a few referenced examples in Nepal (e.g. in the Marsyandi River) imply local landsliding and catastrophic events (lake breaching) help to reconstruct their

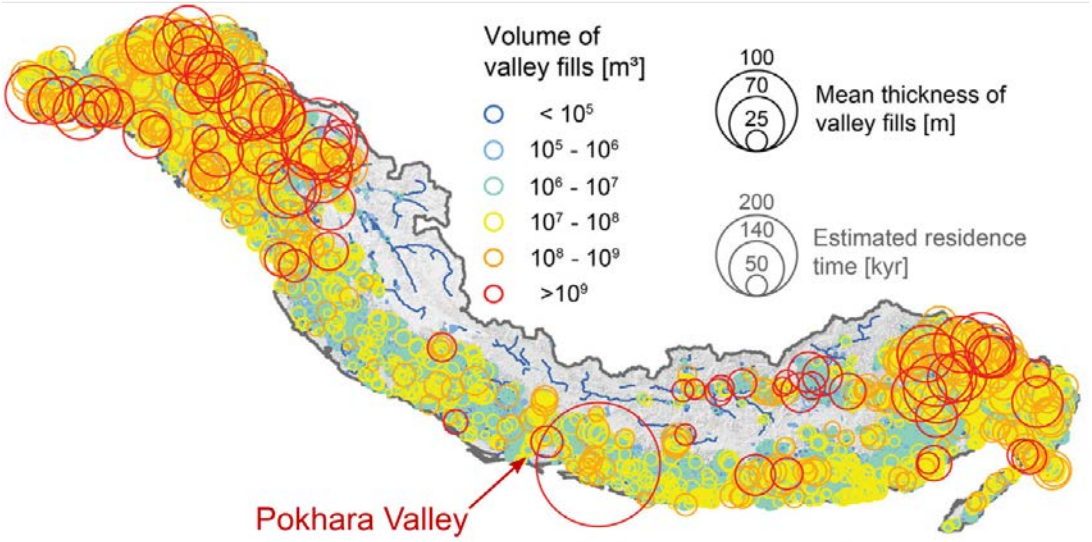

Figure 1.1.: Distribution of Himalayan valley fills with estimated volumes of each fill (n = 38197, the volumes are shown in colored open circles). The "inferred mean valley-fill thickness and minimum residence times assuming mean aggradation and removal rates of 1 mm yr^{-1}" (Blöthe and Korup, 2013). The Pokhara Valley is one of a few large valley fills in the central Himalayas, Nepal. Modified after Blöthe and Korup (2013).

formation and development (Pratt et al., 2002; Pratt-Sitaula et al., 2007; Chaudhary et al., 2015). However, valleys are a great locations to store sediment over thousands of years. Sediment budgets have a significant variability to decadal measurements of sediment flux that might increase as stored sediments are being reworked relentlessly (Simpson and Castelltort, 2012; Blöthe and Korup, 2013). Quantifying sediment storage is fundamental for the calculation of sediment budgets, but is often documented with high sediment yield uncertainties for large drainage basins (Blöthe and Korup, 2013). Stored sediments may also hold the key to answering questions about the timing and magnitude of past catastrophic sedimentation.

Open research questions concern the long-term variability of sediment yields, sediment transport and deposition processes, and resulting residence times. The quantification of sediment storage helps to resolve these questions (Hinderer, 2012). Himalayan sediment storage is likely in large parts contained in intermontane valley fills (Blöthe and Korup, 2013). Valleys filled with sediments are present along the Indus basin and in the Karakorum region, in the eastern part of the Himalayas, but these valleys are rare in the Central Himalayas of Nepal (Fig. 1.1). Such sedimentary landforms are the most preferred human habitats and settlements worldwide (Korup, 2012) because they offer water supply and sediment as construction material. People may have been settling the Himalayas thousands of years ago, though Himalayan archaeology is still developing. The

west Himalayas, for example, were populated some 2500 years ago (English, 1985; Ives and Messerli, 1989), in the central and eastern part people migrated from southeast Asia in the first millennium BC, and the third wave of people settled in the High Himalayan valleys in the early century AD (Ives and Messerli, 1989). In Nepal, the first people arrived to the Kathmandu valley, which was once a big lake (Adhikari and Seddon, 2002) known as the Paleo-Kathmandu lake that drained at least twice (around 48 and 38 ka). After a refill phase the lake basin got tapped and drained into Bagmati River following an earthquake around 12 ka (Sakai et al., 2016). Remnants of the lake are Plio-Pleistocene age lacustrine and fluvial sediments up to 550 m thick (Paudel and Sakai, 2008) on which Kathmandu city is located today. The Kathmandu basin is by far the largest sediment fill in the Central Himalayas, and one of the better studied. Similarly, Nepal's second largest city Pokhara also rests on a large and conspicuous valley fill that stands out from the otherwise dissected mountain terrain.

1.2. The geomorphic evolution of the Pokhara Valley

The Pokhara Valley (Fig. 1.2) is an intermontane basin, located in the Lesser Himalaya, just south of the Annapurna Massif (Fig. 1.2). The Main Central Thrust (MCT) runs through the northern part of the study area making it to a tectonically and geomorphically very active and dissected area. From the MCT, the Pokhara fan spreads over ∼150 km^2 from an elevation of 1200 to about 350 m asl. The valley is filled with Quaternary deposits of layered clastics that originated in the Annapurna Cirque. Distinctive geomorphic features characterize the Pokhara Valley: 1) a flat, low-gradient morphology, 2) unpaired sets of alluvial terraces, 3) steep bedrock and older indurated deposit gorges along the main river Seti and its tributaries, and 4) a braided channel pattern. Steep mountain slopes, highly variable sediment transports, and a tectonic active and geological diverse settings characterize the shape and hazards of this region of the Nepal Himalayas. The Pokhara area has the most intensive monsoonal precipitation of Nepal (4,500-5,000 mm) (Pokhrel et al., 2015a; Leibundgut et al., 2016), but also a documented history of strong earthquakes and postglacial debutressing (Hasegawa et al., 2009). High rock uplift rates in the north (Hodges et al., 2004) interplay with rapid erosion, thus maintaining a high-mountain landscape with diverse natural hazards such as earthquakes, and landslides. The flat morphology of the Pokhara plain is striking. The surface gently slopes

from north to south with 3.2 to 0.9% (Fort et al., in press). This longitudinal gradient is accompanied by a laterally gradient from the central axis into tributary valleys forming a fan-shaped surface in the Pokhara Valley. This surface is cut by the meandering Seti Khola shaping terraces of >70 m high relative to their river bed. Steep gorges are intriguing features (Fort, 2010) mostly found in the city center of Pokhara, interrupting the longitudinal profile of the Seti river and its wide flood plain bounded by flights of terraces. These gorges are up to 1,000 m long, 10-25 m wide and deeply entrenched in indurated gravels and boulders forming an older valley infill and conglomeratic bedrock (Ghachok Formation, Fort (1987)). This older valley infill is related to the Pokhara Valley as both formations share the same source of deposits (Yamanaka, 1982; Fort, 1987). The city of Pokhara is build on this fan surface and spread on both sides of the Seti river and its terraces. A "pool of water" - *pokhari* - is the Nepali meaning for Pokhara city, perhaps derived from legends about the city. Legends tell about a big glacial lake that burst through its ice-moraine dam, flooding the old town and the present Pokhara region some 600 years ago. The soils and lack of forests may be due to this event (Tuladhar and Shrestha, 2010).

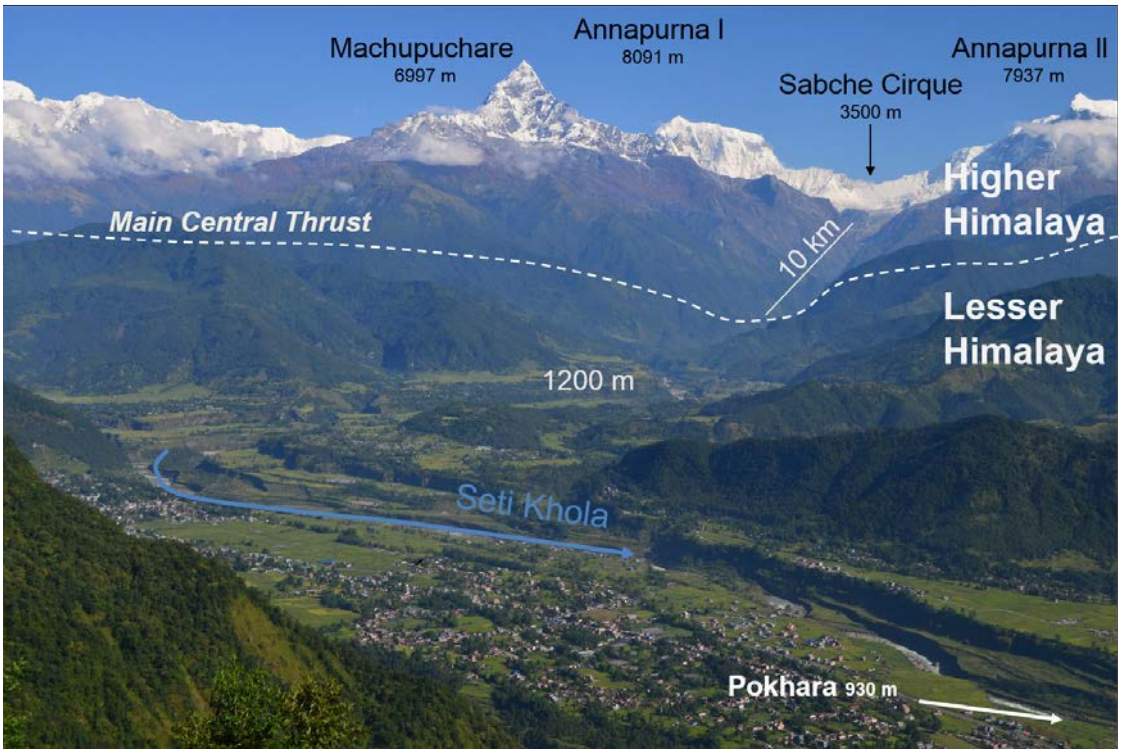

Figure 1.2.: Overview of the northern part of the Valley with a view to the Annapurna Range in the back with the Machupuchare peak in the middle and west of the Annapurna Cirque, the source of the debris deposited in the Pokhara Valley (see Chapter 2 and 3).

In this context, the interpretation of Pokhara's geological foundations is essential, though it has been long debated. Early studies interpreted the Pokhara Valley as remnants of one big lake (Hagen, 1969), while later the well-developed terraces along the entire valley were described as glacio-fluvial (Hormann, 1974). Yamanaka (1982) ascribed these sediments to two debris flows involving between 3-7 km^3. They claimed that both debris flows filled the entire Pokhara Valley, blocking all tributary valleys, and forming lakes, most of which have silted up today. The earlier event has been dated to approximately 13,000-15,000 yrs BP (Koirala et al., 1998) - at the end of the last glaciation. The second debris flow was dated between 1,000 and 3,000 yrs BP (Yamanaka, 1982; Fort, 1987; Koirala et al., 1998). These open interpretations and hypotheses build the motivation for this thesis to explore the origin of this very young valley fill at this exceptional and beautiful location.

1.3. A rapidly growing city on a geomorphic surface

The Pokhara city has been settled as late as the 1750s (Adhikari and Seddon, 2002). The surrounding hills "were most probably inhabited by prehistoric people, as attested by some Neolithic tools" (Fort et al., in press) that have been found northwest of Pokhara city (Kaskikot) (Pandey, 1987; Adhikari and Seddon, 2002). Pokhara became very important early on because of its location between the high mountains and the Terai, which was the perfect location for the Trans-Himalayan trade route. After the unification of Nepal in 1768, traders discovered the beauty of the city, attracting touristy activities, and focusing social and cultural heritage which are responsible for the city's and region's sustained popularity (Adhikari and Seddon, 2002). Pokhara's population has been growing rapidly (United Nations Develop Program et al., 2009) to ~250,000 people; the whole valley already is home to more than 400,000 inhabitants in 2010 (Central Bureau of Statistics, 2011). Accordingly, the history of Pokhara city is very short, while the rate of urban development is increasing and high (Adhikari and Seddon, 2002). This rapid population growth is emblematic for many mountain regions worldwide, and often concomitant with poverty and an increase of land use where people have to expand into more hazardous areas (Lennartz, 2015). The combination of natural hazards and an increasing exposition of vulnerable population raises natural risk and compromises the sustainable development in the long-term (Björnsen Gurung et al., 2012), and emphasizes the need to study valley fills

or signs of past catastrophic sedimentation that might compromise the safety of people living on those deposits.

Table 1.1.: Land use change of Pokhara area 1977-2010.

Year	1977		1990		1999		2010		2021		Change 2010-2021	
Land use	km^2	%	km^2	%	km^2	%	km^2	%	km^2	%	km^2	%
Urban area	3.5	6.33	11.11	20.08	18.62	33.66	28.44	51.42	32.45	58.67	4.01	7.45
Water body	7.73	13.97	6.85	12.38	7.1	12.84	7.02	12.69	6.92	12.51	-0.1	-0.18
Open field	6.46	11.68	4.44	8.03	3.53	6.38	4.26	7.7	4.55	8.23	0.29	0.53
Forest cover	0.84	1.52	0.75	1.36	0.87	1.57	1.22	2.21	1.44	2.6	0.22	0.39
Cultivated land	33.59	60.73	29.18	52.76	21.4	38.7	11.21	20.27	7.35	13.29	-3.86	-6.98
Sandy area	3.19	5.77	2.98	5.39	3.79	6.85	3.16	5.71	2.6	4.7	-0.56	-1.01

Rimal (2013)

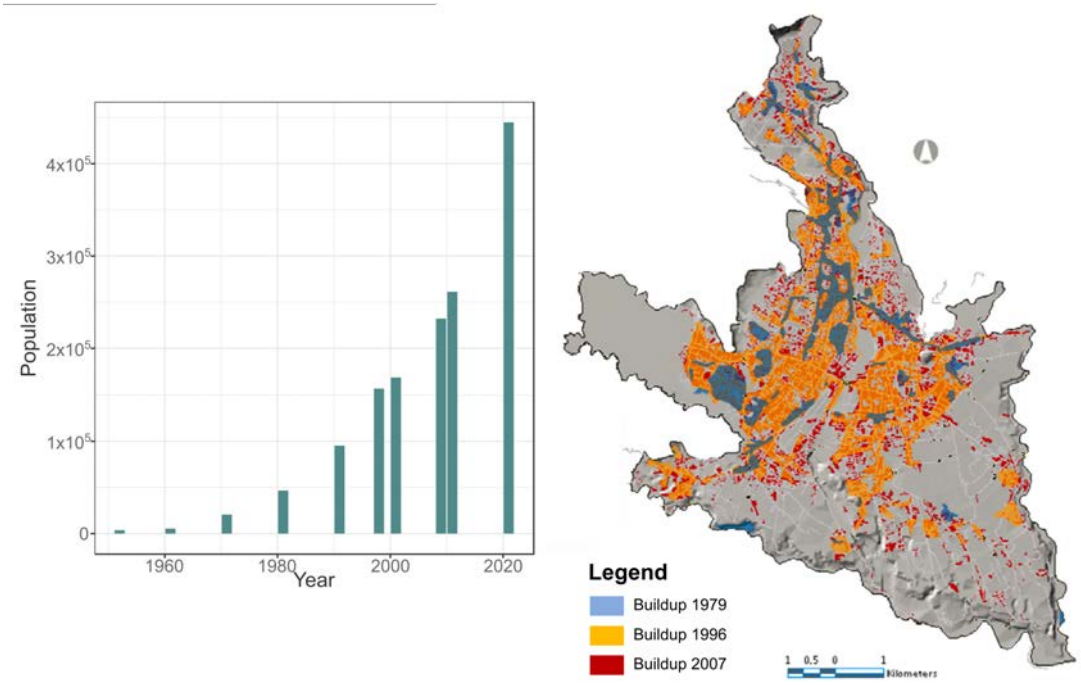

Figure 1.3.: Population growth in Pokhara city, 1979-2021. The map shows land use changes from 1979 to 1996 and 2007 (Table 1.1), while in the graph the estimates for the year 2021 are also given. The values for this figure are shown in Table 1.2 (from United Nations Develop Program et al., 2009).

Cultural heritage in Pokhara

One of the most famous cultural heritage sites in Pokhara is the "Tal Barahi" Temple which is situated on an island in Phewa Lake; it is part of the legend with the big flood ~600 years ago. During this time villagers were supposedly wicked people when a divine messenger was sent by god to test their compassion; only one woman believed her prophecy and left the place before it started to rain instantly; the present day Pokhara region got flooded and left an island in Phewa Lake, the lone woman's place,

was left by the god for her kindness (Tuladhar and Shrestha, 2010). Other important cultural heritage is the "World Peace Pagoda (Bishwo Shanti Stupa)", a large stupa on top of Anadu hill close to Phewa Lake. Tourists have a panoramic view to the Annapurna mountain range that are reflected in the water. The same view they have from Sarangkot, a small village on top of another hill (Image view of Fig. 1.2). Several caves in the city are washed out and made by subsurface flows. One example is Devi's fall, a subsurface waterfall in a cave, where visitors can walk through a natural tunnel during winter times, when the water level is low. Many other temples can be found in the old part of Pokhara city such as "Bhimkali Temple", "Dharmashila Buddha Bihar", and the "Bhadrakali Temple".

Table 1.2.: Population growth in the Pokhara area from 1952 to 2021.

year	population	population growth rate (yearly in %)
1952	3755	-
1961	5413	5.3
1971	20611	14.3
1981	46642	8.5
1991	95286	7.4
1998	157055	7.4
2001	169160	2.5
2009	232254	4
2011	261264	6
2021	444830	5.5

data collected from Adhikari and Seddon (2002); Rimal (2013)

To establish an efficient tourism infrastructure, an international airport was already planned some 40 years ago; the construction began in 2016 and will be completed within the next five years (Pokhrel, 2016). Up to 800,000 foreign tourists come to Nepal, of which more than 500,000 come to Pokhara each year (MCTCA and Ministry of Culture, Tourism & Civil Aviation, 2014). The popularity of Pokhara grow while more and more people settled the area. Pokhara's population increased 42-fold in the past 46 years (Adhikari and Seddon, 2002); today, Pokhara is the fastest growing of Nepal's cities (Rimal et al., 2015), and moderately vulnerable to earthquake hazards (United Nations Develop Program et al., 2009). Risk turns higher where the city settlement is very dense (central part of the city) because urban growth is limited by Phewa Lake in the western part and by mountains in the north. Most dramatic shifts have occurred in land use and land cover changes such as cultivated land (Rimal, 2013). The construction of the Prithivi Rajmarga highway (finished in 1971) connected Pokhara with the Terai in the south and with the

capital of Kathmandu in the east. As a result, the growth of Pokhara town expanded with a rate as high as 14-18% per year (Adhikari and Seddon, 2002; Rimal, 2013). The road was and still is very important not only as a supply route for food, fuel and cooking gas but also made it significantly cheaper to bring construction materials such as cement, pipes and iron rods for buildings into the Pokhara area, encouraging for locals to build shops and new houses along the highway. Villagers from the countryside were settling along the roads, new villages appeared and expanded from tens to hundreds of shops and from a few to some 600 houses within 5 years (Adhikari and Seddon, 2002). This road changed not only the number of local residents, but by the extent of transport and infrastructure, it also improved the economy of the town and its quality of life. By the construction of a bridge over the Seti River in 1965, this place converted into a major trading center (Adhikari and Seddon, 2002), touristy place and attractive place to live.

Several open questions follow from this short review. For one, the recent geological history of Nepal's second largest and currently fastest growing city is still unclear. At the same time, modern geological hazards such as landslides, river-bank collapses, and sinkholes seem to have been on the rise in the past few years (Rijal, 2017). It is unclear how those hazards link up with the recent geological past.

Besides these hazard and risk implications, the geological foundations of Pokhara have also another very practical relevance as readily available natural resources. Many road and house constructions are ongoing that need new material, and these gravels come from the river channels (Fig. 1.4). Sand that mostly is excavated from the channel of the main river Seti. Excavating river gravels from the channels and active river banks for infrastructural purposes seems like a great opportunity to use local material and to secure jobs. Figure 1.4 shows different snapshots from the field of how people influence the Seti Khola's gradient, way and channel stability by river mining on active banks.

Examples from different river mining locations

The rapid urbanization has increased excessive demands of sands and gravel for construction purposes. River mining became a cheap and readily accessible option, and amounts of sands and gravel were supplied from river beds. In the Kathmandu valley, river bed mining was prohibited in 1991 (Kharel et al., 1992) because of bridge collapses due to undermining of river banks and bridge constructions, while terrace mining began. However, in many regions in Nepal illegal river mining is common.

Figure 1.4.: Field images of excavation work along the main river. A) Panoramic view in the Ramghat area (see Fig. 3.1 for the location) in the center of Pokhara city. Seti Khola runs along the outcrop in the back while hundred of people screen, sort, and carry gravels (**C)**) from sand to boulder sizes. **B)** Same location as A) and C), at the outlet where the Seti disappears in a bedrock gorge. **D)** Place for river mining north of Pokhara city. Groins are set to trap sand particles carried by the river during the monsoon season. **E)** Groups of locals collect river clasts in the Seti Khola. Note the boulders outsizing the tractor. **F)** Downstream at the confluence to Pudi Khola (Fig. 3.1), one of the biggest construction areas, where machines sort gravels from the channel beds.

Unsystematic mining has caused many problems such as erosion, river bank instability and river pollution (Tamrakar, 2004; Adhikari and Tamrakar, 2005). For Kathmandu, the growth of infrastructure and population has demanded about 3100 m^3 of sand per day in 2001, while only 35% of the terrace mining is registered (Sayami and Tamrakar, 2007), and that number excludes the illegal river mining supply. Excavating the gravel from the river bed, may accelerate erosion rates. An example from Greece shows severe riverbed lowering due to an estimated 9.6 million m^3 of gravel over 32 years (Manariotis and Yannopoulos, 2014) (equal to approximate 825 m^3 per day the volumes given by excavations in Nepal). There are no official numbers for the Pokhara Valley; Ramghat is one of several focus locations of river mining in the center of the city (see Fig. 1.4 for some field photos and 3.1 for the location). People carry up sediment bags of 70 kg to a ∼70 m higher terrace level, hoping to get 20 rupees for each bag.

The past, present and likely future situation in the Pokhara Valley revolves around better understanding the valley fill on which the city is built. This valley fill may contain indications about catastrophic sedimentation and other sedimentary processes in the recent geological past, while also offering opportunities as the storage of natural resources in the form of easily accessible river gravel. Hence, the objective of this thesis is to systematically investigate the recent geological history of the Pokhara basin before the backdrop of past and possibly recurring hazards. Estimates hold that hazards and risk are increasing because of unsustainable land use practices, the town "is under intense pressure from rapid urbanization [...]" (Rimal et al., 2015). To be able to better quantify this potential increase, we need to learn first the sources, causes, and triggers of such hazards. Again, the sediment fill of the Pokhara basin is a natural archive in this respect. The structure of this thesis revolves around a seemingly simple question: where did all the gravel come from? The Pokhara valley is one of the larger bits of low-gradient land in the central Himalayas (besides Kathmandu, see Fig. 1.1, Blöthe and Korup (2013)). It is not only the expansion of urban areas on the Pokhara fan, but rather modern hazards (see Section 5.5) resulting from historic deposits (Yamanaka et al., 1982; Fort, 1987) which makes Pokhara city a hazardous and vulnerable place to live.

1.4. Aims and Structure

The aim of this thesis is to explore and investigate the timing, origin, sedimentologic and geomorphic processes to consequently research fluvial response and river adjustment to several catastrophic episodes of valley-floor sedimentation in the Pokhara Valley. In essence, the main aim is to learn more from the Pokhara Formation as to reconstruct past and predict future processes linked to its emplacement and erosion. The strategy behind this approach is to start with various pieces of a geologic puzzle from previous studies and add field observations, sediment descriptions, radiocarbon age dating, provenance analysis, and different possibilities of triggering mechanisms that are able to release huge amounts of sediments, to the fate of this catastrophically deposited valley fill.

Following this introduction, this thesis focuses on the understanding of the heavily disputed Pokhara Formation; the origin, mechanism, and development on a timescale starting at ∼1100 AD until the present. Finally, I address the issue of the future situation with increasing modern hazards the local population has to deal with today. Therefore, this thesis approaches:

- the current knowledge about the Pokhara Formation that underlies most of the valley,
- the timing of the valley fill,
- a new catalog of the sedimentologic features of the Pokhara Formation with respect to different lithofacies allocated from the center of the fan to tributary mouths until the upstream margin of the fan,
- to independently consider and augment paleoseismological fault-trench records of great historic earthquakes by sedimentary archives in catastrophically infilled valleys,
- to quantify river recovery times of earthquake triggered sediment pulses,
- to discuss possible triggers that release this amount of material in very short time,
- and to test whether the geologic past is responsible, in a certain way, for modern hazards around the city of Pokhara.

To address these topics, this thesis is segmented in three core chapters (Chapter 2 - 4) that broadly deal with, *Earthquake Concurrency*, *Sedimentary Fingerprints*, and *Fluvial*

Response to these catastrophic events (Fig. 1.5). The following paragraphs will address these three topics as the Pokhara Valley is the perfect place to investigate catastrophic sediment deposits and archives, as well as fluvial adjustment.

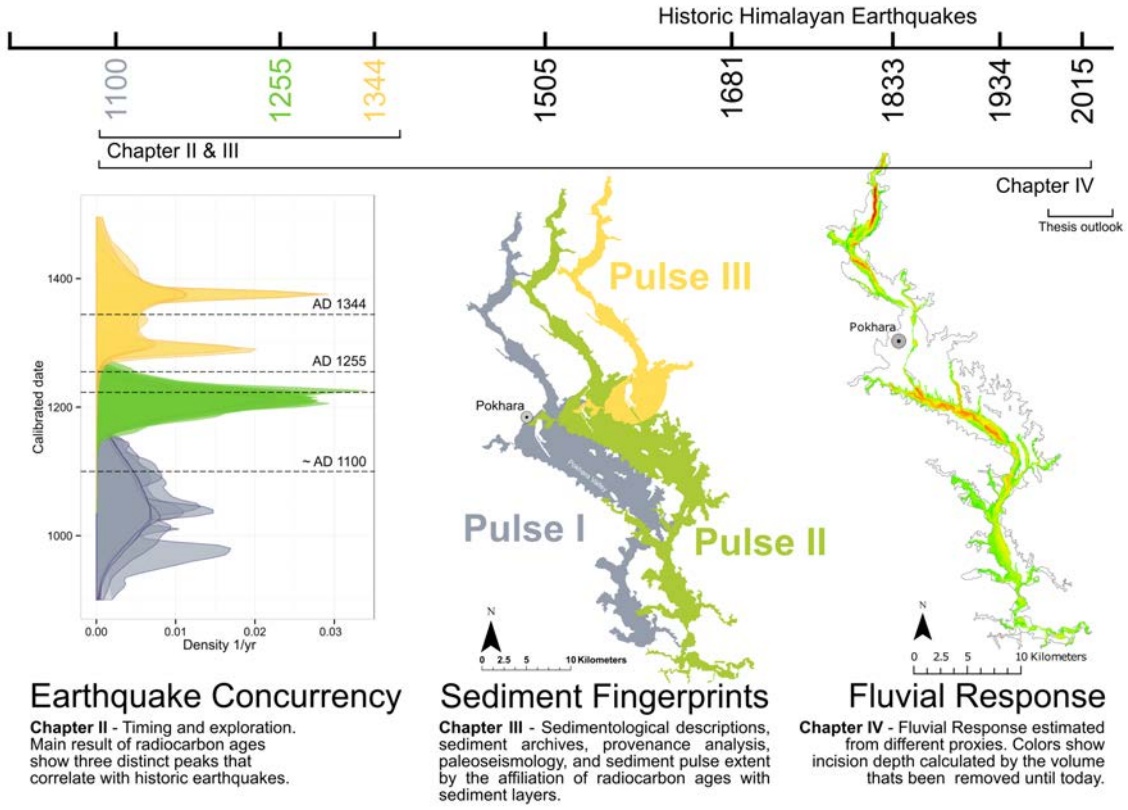

Figure 1.5.: Content of this thesis along a tentative timescale starting at ~1100 AD (Chapter 2) to the present (Chapter 4).

Earthquake Concurrency - The first core chapter aims to resolve age relationships of the Pokhara Valley infill. Radiocarbon age dating has already been successful in the Pokhara Valley (Yamanaka et al., 1982; Fort, 1987) that we used this method for the timing of deposition. Chapter 2 further concentrates on the origin of deposited material as well as possible trigger mechanisms that are able to release the amount of material to fill the Pokhara Valley.

Sedimentary Fingerprints - This chapter concentrates on the sedimentology of the Pokhara Formation. The geomorphic impact of the fan surface and the relationship of radiocarbon ages to sediment layers. Carling (2013) and Baker (1987) studied the sedimentology of mega floods around the world, while in the Himalayas such catastrophic sedimentation awaits more detailed research. Chapter 3 aims at the paleoseismic history of

great Himalayan earthquakes and the importance of how sediment archives independently help to augment earthquake records.

Fluvial Response - Chapter 4 opens the topics of the previous two chapters to the question of how much material has been removed since the deposition of the Pokhara gravels. It has been known for thousands of years that large earthquakes are able to release large volumes of sediments (Matthes, 1930; Keefer, 1994; Hovius et al., 2011; Marc et al., 2016; Ren et al., 2017) mostly proportional with earthquake magnitude or distance from the rupturing fault in a large area. However, little is known about the long-term hazard and fluvial response of such sediment volumes deposited and their influence and importance on slope and background erosion. The Pokhara area provides a rare opportunity to quantitatively study the geomorphic impact of historic earthquakes that triggered sediment pulses, inducing erosion and thus, distinguishing the timescale of when the material was deposited until today, rather than predicting long-term erosion by the recurrence interval of the earthquake (Ren et al., 2017). With various proxies, I present results that appraise the recovery times for the Pokhara Valley.

The key findings and conclusions of the three studies are presented in Chapter 2 - 4, while the final discussion (Chapter 5) comprises the entirety of this thesis objectives. We used the geologic past to investigate the timing and sedimentology, to further find out more about river adjusting mechanisms (Fig. 1.5). A condensed outlook on research possibilities and the closing Chapter 6 providing a synthesis regarding the significance of Himalayan valley fills, complete this thesis.

1.4.1. Research Questions

To reconstruct the earthquake concurrency of material deposition, the sediment record and the impact of fluvial adjustment to modern hazards, we need to approach the following research questions:

1. *Dates and origins: When, how rapidly, and why was the Pokhara Formation deposited?*
2. *Sedimentary diagnostics: Which insights about transport processes and episodes does the sedimentology of the Pokhara Formation reveal?*
3. *River signs: What effects did the emplacement of the Pokhara Formation have on the drainage network?*

Referring to Research Question 1 - **Dates and origins** - Chapter 2 investigates sediment section of very fine grained material that provide insights into the depositional process. These sections contain organic matter for radiocarbon dating elucidating the timing of valley fills. This study aims to broaden our knowledge about the history of the Pokhara Formation, the frequency of sediment deposition, and possible triggering mechanisms. We review previous research (Hagen, 1969; Hormann, 1974; Yamanaka, 1982; Fort, 1987) on the timing and geomorphology of the valley fill, and summarize our findings in a research letter. We use different statistical models to calibrate the radiocarbon ages to exclude all artifacts that may affect our results. The trigger of the events is still debatable, we suggest a working hypothesis from heavy monsoonal rainfall, glacial lake outburst flood, glacier surge or an earthquake induced rock/ice fall (Fort, 1987) and test several possibilities. Chapter 2 contains the publication on - "Repeated catastrophic valley infill following medieval earthquakes in the Nepal Himalaya" - and deals with the earthquake concurrency of the valley infill. We test these hypothesis by combining data from the field, laboratory and remote sensing to quantify processes, sediment structures and radiocarbon ages to one coherent storyline.

Chapter 3 - **Sedimentary diagnostics** - aims at answering Research Question 2 and can be considered as a complement of Chapter 2. We compile, review and augment the body of the existing research on the Pokhara Formation with new sediment logs, define lithofacies for the whole valley, add radiocarbon ages to our chronology, and study the paleoseismic history of the Nepal Himalayas. We analyze geomorphic sediment markers and investigate outcrops along the main river Seti and its tributary valleys. This study provides a first sedimentary catalog with detailed characterization of the lithofacies presented by their lateral distribution from the fan center into tributary valleys towards the fan margins. We further analyze the spatial and temporal relation of ^{14}C ages and combine those with sediment logs to estimate the extent of each individual sediment pulse. Chapter 3 includes the publication on - "Catastrophic valley fills record large Himalayan earthquakes, Pokhara, Nepal" - where we improve the understanding of the relationship between past earthquakes, geomorphologic surfaces and their sedimentary legacy in an active mountain belt. We show data that have the potential to discuss the consequences about large earthquakes in Nepal and may help to localize the affected area of these past events.

Addressing the last Research Question 3 - **Fluvial signs** - Chapter 4 provides insights to the consequences of massive valley aggradation. This study aim is to investigate the fluvial

response and adjustment of the river network over hundreds of years. The imbalance of a river system after perturbation and the recovery time to pre-earthquake conditions is the focus in this Chapter containing the submitted manuscript - "Protracted fluvial recovery from medieval earthquakes". We employ different proxies, including exhumed tree trunks, clast counts, knickpoints, erosion, and incision rates to quantify fluvial adjustment to strong sediment aggradation. For this purpose, we estimated volumetric erosion rates and calculate the proportion of the river reaching an optimum concave longitudinal profile. Other proxies such as radiocarbon ages of tree trunks, clast counts and their provenance, and knickpoints help to embed our results into an ongoing debate about how river recovery is defined and measured. Moreover, we discuss the human influence on to erosion rates and modern hazards by river mining and land cover changes.

1.5. Author Contribution

Most of the work presented in this thesis has been performed by the author. Though, all co-authors on the papers and manuscript (see Chapter 2 to 4) have helped to develop and accomplish this research. Inspiring discussions, help with lab work, statistical methods and invaluable comments and ideas. Moreover, great support during field work of undergraduate students of Potsdam University and Tribhuvan University, Kathmandu, is very much appreciated. The three studies represented within this PhD thesis have been, or are submitted and are intended to be published in international peer-reviewed journals. The paper/manuscript layout has been adjusted to the formatting of this thesis, text and figures remain as published. Therefore, abbreviations in Chapter 2 to 4 might be repeated and figure colors, are different for the same formation. Author contributions of the three studies are as follows:

Chapter 2: O.K. designed and drafted the project; W.S., A.B., A.S., B.R.A., C.A., M.F., and O.K. carried out the fieldwork; W.S., A.B., and A.S. analyzed the digital topographic and sedimentary data; P.H. assisted with the XRF and XRD analyses; S.T. prepared samples for ^{10}Be exposure dating; S.M., G.R., and C.A. ran the ^{10}Be AMS analysis; and W.S., A.B., A.S., and O.K. wrote the manuscript with inputs from all co-authors. Supporting data are available in the supplementary materials.

Chapter 3: A.S. and O.K. designed the study. A.S led the manuscript writing process; A.S., A.B., W.S., B.R.A., M.F. and O.K. participated in field work and field data acqui-

sition; A.S. and A.B. described and analyzed the sedimentary data; A.S., W.S. and O.K. analyzed the digital topographic and calibrated the radiocarbon data; P.H. assisted with the XRF analyses; A.S., A.B., W.S. and O.K. wrote the manuscript with inputs from all co-authors.

Chapter 4: A.S and O.K. designed the study and led the manuscript writing process; A.S., W.S., C.A., A.B., M.F., J.D.J., B.R.A., and O.K. carried out the fieldwork and field data acquisition; A.S. and W.S. processed the digital elevation models and volume calculations; C.A., H.W., S.M. and G.R. were responsible for the ^{10}Be lab work and AMS analyses, respectively; A.S. and O.K. wrote the manuscript with inputs from all co-authors.

2

Repeated catastrophic valley infill following medieval earthquakes in the Nepal Himalaya

Published as: Schwanghart, W., Bernhardt, A., Stolle, A., Hoelzmann, P., Adhikari, B.R., Andermann, C., Tofelde, S., Merchel, S., Rugel, G., Fort, M., Korup, O., Repeated catastrophic valley infill following medieval earthquakes in the Nepal Himalaya. Science (New York, N.Y.), v. 351, no. 6269, p. 147-150, doi: 10.1126/science.aac9865.

2.1. Abstract

Geomorphic footprints of past large Himalayan earthquakes are elusive, although they are urgently needed for gauging and predicting recovery times of seismically perturbed mountain landscapes.We present evidence of catastrophic valley infill following at least three medieval earthquakes in the Nepal Himalaya. Radiocarbon dates from peat beds, plant macrofossils, and humic silts in fine-grained tributary sediments near Pokhara, Nepal's second-largest city, match the timing of nearby M >8 earthquakes in ∼1100, 1255, and 1344 C.E. The upstream dip of tributary valley fills and x-ray fluorescence spectrometry of their provenance rule out local sources. Instead, geomorphic and sedimentary evidence is consistent with catastrophic fluvial aggradation and debris flows that had plugged several tributaries with tens of meters of calcareous sediment from a Higher Himalayan source >60 kilometers away.

2.2. Main Article

The M_w 7.8 Gorkha earthquake that struck Nepal in April 2015 confirmed high seismic risk projections for the Himalayas (Bilham et al., 2001; Galetzka et al., 2015), inferred mostly from paleoseismological proxies of past events (Mugnier et al., 2013; Bollinger et al., 2014; Sapkota et al., 2013). Strong ground shaking caused the collapse of more than half a million homes, killing more than 8,500 people and injuring more than 20,000. Landslides buried villages, roads, and river channels, consistent with coseismic impacts reported from other active mountain belts (Kargel et al., 2016). Detailed sediment budgets show that landslides triggered by strong seismic ground shaking may rapidly detach millions to billions of cubic meters of rock, soil, and biomass, providing this material for subsequent entrainment by surface runoff and river flows (Keefer, 2002). The resulting sediment pulses may fill even rapidly incising bedrock rivers by up to several tens of meters (Yanites et al., 2010), thereby causing protracted channel instability, impeding access to emergency areas, destroying hydropower facilities, and compromising post-disaster rehabilitation efforts. Detailed mass balances of recent large earthquakes in China (Li et al., 2014), Taiwan (Hovius et al., 2011), Japan (Koi et al., 2008), and New Zealand (Pearce and Watson, 1986) offer blueprints of how river networks recover from sudden input of excess sediment over several years to centuries. The high sediment transport rates in many mountain rivers, however, rarely sustain evidence of prehistoric earthquake-induced sedimentation pulses. In these cases, depositional records of catastrophic aggradation in forelands are more instructive (Berryman et al., 2012). Both of these lines of evidence for understanding river network recovery have remained elusive in the Himalayas. We present exceptionally well-preserved sedimentary archives that connect landscape-scale disturbance around Pokhara, Nepal, to at least three documented medieval megathrust earthquakes (Mugnier et al., 2013).

The city of Pokhara (28°13'N, 83°59'E, 870 m above sea level) is located at the foot of the >8000-m peaks of the Annapurna Massif in the Seti Khola valley (Fig. 2.1). This steep orographic gradient receives monsoonal rainfall of ∼4,000 mm yr^{-1} (Gabet et al., 2004). Pokhara's geology features primarily Precambrian metamorphic sandstones, shales, and dolomites. Other rocks include Paleozoic phyllites and schists of the Lesser Himalayan Series (LHS). Higher Himalayan Crystalline (HHC) rocks north of the Main Central Thrust (MCT) are Precambrian high-grade metamorphic quartzites, schists, and gneisses

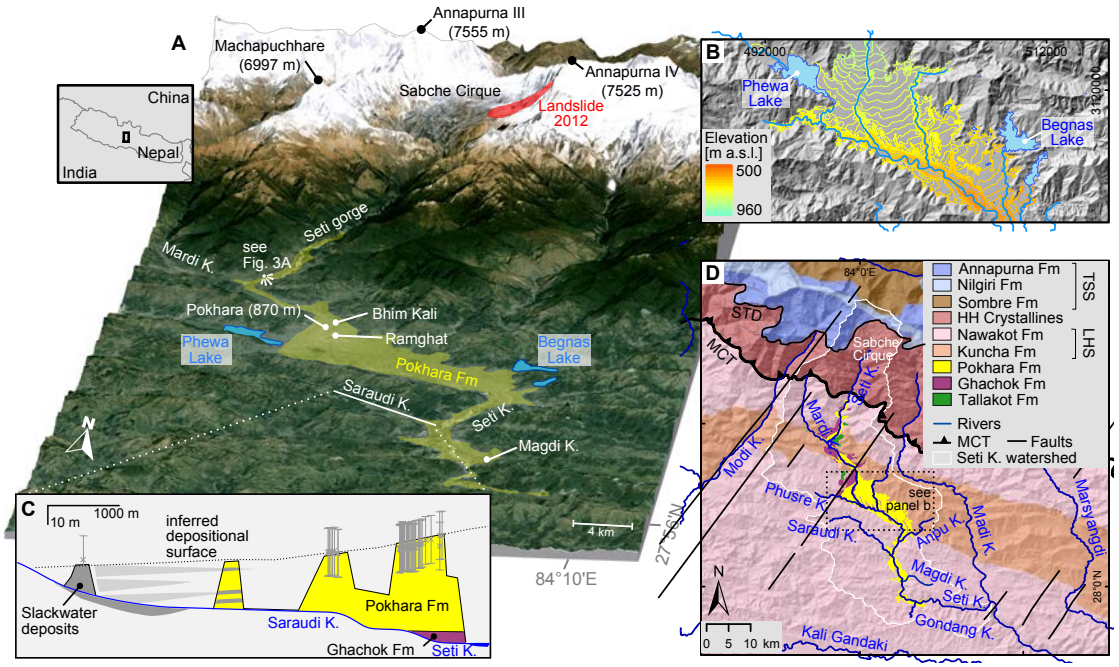

Figure 2.1.: Topographic and geological setting of the Pokhara Valley. The valley is covered by 4-5 km^3 fan deposits that attest to massive aggradation from the Annapurna Massif. **(A)** Oblique view of the Pokhara region, Nepal Himalaya, with the fan-shaped Pokhara Formation (yellow) ponding several lakes (light blue) and tributaries (K. = Khola = "River"), and 2012 rock-ice avalanche. **(B)** Shaded relief map from 15-m digital elevation model. Concentric color-coded contours define the large sediment fan formed by the Seti Khola issuing from the Higher Himalayan Annapurna Massif. **(C)** Example of a longitudinal profile of small tributary backfilled by slackwater deposits (gray) of the Pokhara Formation (yellow). Error bars ($\pm 2\sigma$) refer to GPS-derived elevation measurements of former aggradation surface. **(D)** Simplified geological map (Robinson and Martin, 2014) highlights the extent of the catastrophically emplaced Formation; see text for abbreviations.

(Robinson and Martin, 2014; Parsons et al., 2015). Marine calcareous metasediments of the Tethyan Sedimentary Series (TSS) prevail north of the South Tibetan Detachment Zone (Bollinger et al., 2004; Waltham, 1972). Pokhara sits on a large sediment fan built by the upper Seti Khola that drains the partly glaciated and debris-filled Sabche Cirque in the Annapurna Massif. The fanhead near the MCT grades into a ~60-km-long flight of prominent terraces downstream that rise up to 140 m above the river bed and envelop several LHS bedrock hills (Fort, 1987). The fan has three stratigraphic units called the Tallakot, Ghachok, and Pokhara Formations. We focus on the youngest Pokhara Formation composed of extensive coarse gravel sheets, numerous boulders >10 m in diameter, and thick debris flow deposits. Digital topographic data (Department of Survey, 1996) confirm damming of the more than a dozen tributaries along Seti Khola's course of >60 km by Pokhara Formation sediments (Fort, 1987). These deposits dip upstream into tributary valleys for >1 km and up to 7 km along the Magdi and Saraudi Khola featuring several

meters of intercalated gravel, sand, and silt beds. We sampled enclosed peat beds, charcoal lenses, and plant macrofossils (Figs. A.1 and A.2) for radiocarbon (^{14}C) dating and for any earthquake-related sedimentation in eight different tributaries (Table A.1).

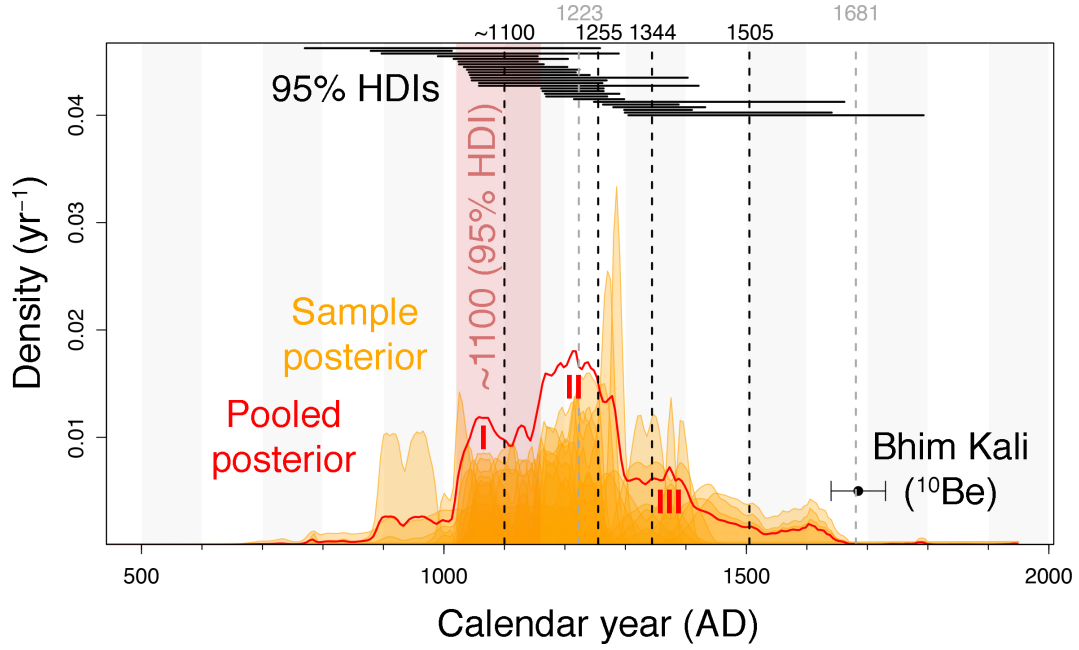

Figure 2.2.: Bayesian calibration of ^{14}C ages of the Pokhara Formation. Posterior probability densites (orange) of 26 ^{14}C dates from the Pokhara Formation, and cosmogenic ^{10}Be exposure age of Bhim Kali boulder (whiskers are $\pm 1\sigma$ error). Horizontal lines are 95% highest density intervals (HDIs). Pooled posterior (red) has three distinct sedimentation peaks (I-III) tied to dates of M > 8 medieval earthquakes in ~1100, 1255, 1344 C.E. (black dashed lines; gray dashed lines are other large earthquakes with little information on rupture extent; the 1505 C.E. earthquake is not reflected in our ^{14}C dates). Red box is 95% HDI for the ~1100 C.E. earthquake based on recalibrated ^{14}C ages (Lavé et al., 2005).

Bayesian calibration of 26 ^{14}C ages with a prior informed by stratigraphic relationships between the samples (see Appendix A) returned a pooled posterior distribution with three distinct peaks that match, within error, the timing of three large medieval earthquakes in ~1100, 1255, and 1344 C.E. (Mugnier et al., 2013; Bollinger et al., 2014; Lavé et al., 2005) (Fig. 2.2, Figs. A.3 to A.4, and Table A.2). Our oldest ^{14}C dates offer support for the timing of the ~1100 C.E. earthquake, which has so far been inferred from fault trenches (Lavé et al., 2005). Each of the three medieval earthquake dates lies within the 95% highest density intervals of at least five ^{14}C dates. Our dates form a highly credible cluster that may match with another historically documented large event in 1223. The size and impact of this earthquake are unclear (Bollinger et al., 2014), however, when compared to studies on the 1255 C.E. earthquake. Four statistically indistinguishable ^{14}C dates spanning an 8-m-thick section of the trimmed fan toe in the Phusre Khola mark

rapid aggradation tied to these earthquakes (Fig. A.6). A prominent and partly rounded 3000-ton HHC boulder (Fig. A.2), located on top of the Pokhara Formation and stranded ∼50 m above the channel bed of the Seti Khola, has a cosmogenic ^{10}Be exposure age coeval with another major earthquake in 1681 C.E. (Mugnier et al., 2013). Regardless of whether this boulder was moved by sediment-laden flows, etched from the underlying deposits, or simply toppled, it provides a minimum age for the Pokhara Formation and attests to a sudden disturbance of its surface about 330 years ago.

Figure 2.3.: Sediments of the Pokhara Formation. Fluvial processes and debris flows deposited extensive horizontal layers of poorly sorted conglomerate. **(A)** Panorama of the Pokhara sediment fan surface dissected by the Seti Khola and its tributaries (see Fig. 2.1A for location). **(B** and **C)** Poorly sorted, gravel-to-boulder, clast-supported conglomerate lacking erosional features and current structures. **(D)** Slackwater deposits in Saraudi Khola with cohesive debris flow deposits (light gray) topped by intercalated massive mud (dark gray), sands, and silts (light brown); white ellipses show persons for scale. **(E)** Mud matrix-supported, fining-upward conglomerate interpreted as long-runout debris flow deposits >40 km from their source. **(F)** Rip-up clasts in basal debris flow unit. **(G)** Massive dark gray, clast-supported, fining-upward pebble-to-granule layers with interbedded sands (light brown) indicate rapid settling from sediment-laden flow.

We found numerous outcrops of the Pokhara Formation that illustrate its catastrophic origin. Two main facies of conglomeratic sediments are exposed within the trunk valley of the Seti Khola and form continuous layers for tens to hundreds of meters that dip at shallow angles (∼0.5°to 1.2°measured by a tachymeter) in the direction of paleoflow. The first facies comprises >10-m-thick beds of a massive, matrix-supported, very poorly sorted,

and locally fining-upward conglomerate of HHC gravels, boulders, and rip-up clasts that indicate emplacement by cohesive debris flows (Fig. 2.3 and Fig. A.7). At least three fining-upward cycles point to large debris flows, but they may equally well represent surges within one large event. The second conglomerate facies forms clast-supported units up to 40 m thick. The lack of current structures and erosive contacts, together with fining upward massive pebble- to granule-bearing sheets, indicates rapid fallout from high concentrations of solids (Fig. 2.3). We interpret these clast-supported conglomerates to reflect rapid aggradation during turbulent, sediment-laden flows. The massive, structureless clay and silt layers in tributary valleys indicate rapid suspension fallout that we attribute to a waning flow velocity and possibly ponding. The dominance of dark limestone together with occasional HHC kyanite-sillimanite gneiss, pyroxenic marble, and augen gneiss excludes local LHS sediment sources.

Using x-ray fluorescence spectrometry of the fine-grained fraction of the Pokhara Formation, we confirmed an elemental composition different from the phyllitic bedrock in these LHS tributaries (Fig. 2.4). We found instead with x-ray diffraction a mineral composition rich in calcium carbonates, dolomite, muscovite, and traces of pyrite (Table A.3) characteristic of TSS rocks, particularly Nilgiri Limestone (Waltham, 1972), from Sabche Cirque. We infer a catastrophic sediment transport over >60 km that culminated in deposits invading for several kilometers the lower reaches of several tributaries.

Catastrophic outbursts from natural dams and large rock-ice avalanches are two possible mechanisms for producing the long-runout debris flows. The clustered ^{14}C dates, the confined sediment provenance, and the dammed tributary mouths are consistent with one or several dam-break flows (Carling, 2013). We interpret the thick stacks of fine-grained sediments as slackwater deposits trapped in tributary valleys during backwater flooding (Baker et al., 1983). The Seti bedrock gorge upstream of the MCT had previously accommodated temporary lakes, judging from at least three dissected landslide dams up to 300 m in height (Fig. A.8). Dam-break modeling (see Appendix A) shows that sudden failure of a 300-m-high dam could release up to 1 km^3 of water at a peak discharge of 45,000 to 600,000 $m^3\ s^{-1}$ in the lower Seti gorge. Although exceeding the largest historic lake outbursts in the Himalaya (Korup and Tweed, 2007), several such major events would be needed to deliver the 4 to 5 km^3 of sediments in the Pokhara Formation downstream (Fort, 1987), assuming a solids concentration of 80% by volume that is characteristic of cohesive debris flows. Some 10 to 15 km^3 of debris and lake sediments lining the Sabche

Cirque floor (Fort, 1987) could feed lake outbursts and provide the necessary geochemical fingerprint for repeated catastrophic aggradation in the Pokhara basin.

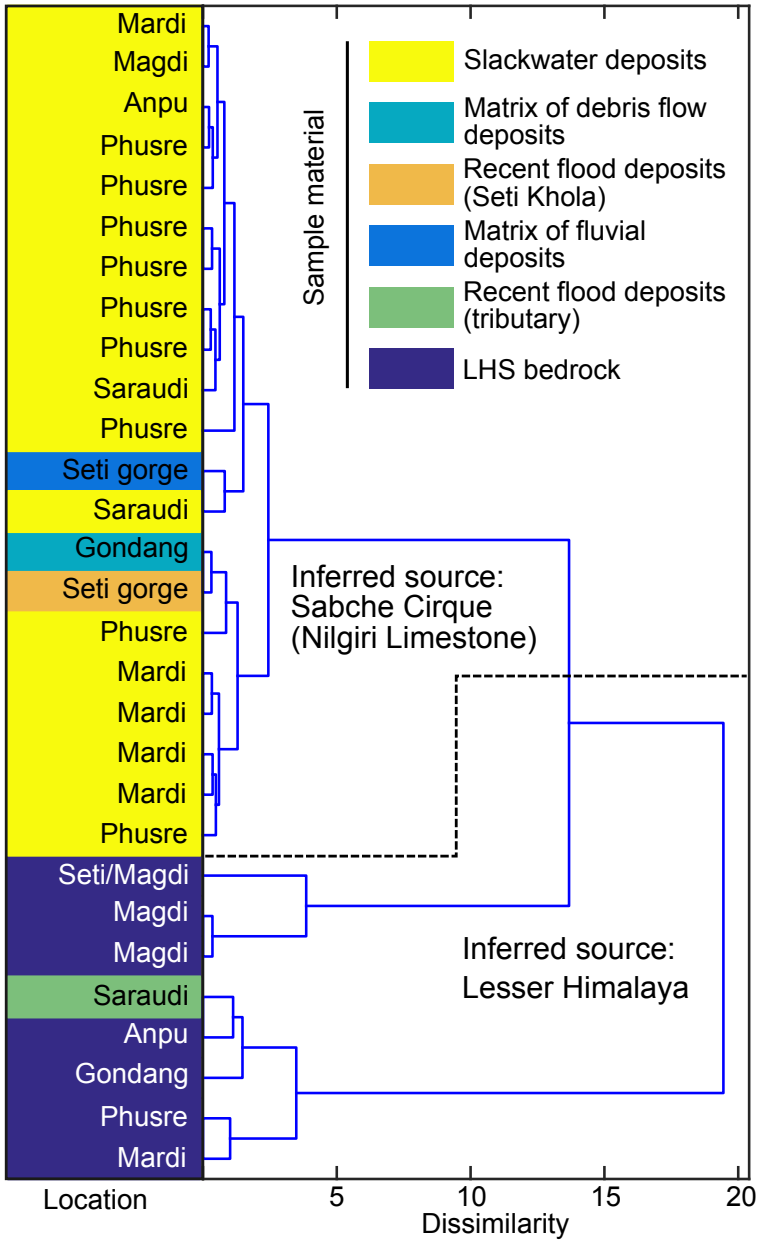

Figure 2.4.: Provenance of slackwater deposits from x-ray fluorescence spectrometry indicating highly localized High Himalayan source of the Pokhara Formation. Hierarchical cluster analysis yields three major classes of elemental compositions of LHS bedrock, slackwater deposits, fine-grained flood and debris flow deposits of the Pokhara Formation, and recent flood sediments of the Seti Khola and its tributaries. The three classes indicate sediment sources. Elemental compositions of the sedimentary fills in tributary mouths are highly similar, indistinguishable from load transported by the Seti Khola, and attest to a common source in the Sabche Cirque. Compositional variation of LHS bedrock reflects locally occurring limestone at the Seti and Magdi Khola confluence.

Catastrophic rock-ice avalanches from the Annapurna Massif (Fort, 1987) represent an alternative initiation process for long-runout debris flows. Historic case studies from Peru (Evans et al., 2009a), Tibet (Shang et al., 2003), and the Caucasus (Evans et al., 2009b) showed how rock avalanches detaching >107 m^3 from >4000-m-high mountains entrained glacier ice and transformed into debris flows and sediment-laden flows, which traveled as far as 130 km at average velocities of >30 km $hour^{-1}$ (Evans et al., 2009a). The case of the earthquake-triggered rock-ice avalanche from the Andean peak of Nevados Huascarán (6654 m) that buried the town of Yungay beneath a large debris flow fan (Evans et al., 2009a) in 1970 is strikingly similar to that of Pokhara in terms of topographic relief contrasts and far-reaching geomorphic impact, although much smaller in size. Some of the debris mounds in Sabche Cirque may partly derive from catastrophic rock slope failures, possibly larger than the recent one that detached ∼59 Mt of rock and ice from the flanks of Annapurna IV and evolved into a flash flood that killed more than 70 people in the lower Seti gorge in May 2012 (Ekström and Stark, 2013).

Our findings substantiate previous hypotheses of a catastrophic origin of the Pokhara Formation (Fort et al., 2009), merging several lines of evidence that point consistently to highly mobile mass movements from the upper Seti catchment triggered by medieval earthquakes. This geomorphic legacy of multiple earthquake-driven sedimentation pulses is unique in the Himalayas, recording episodic plugging of tributaries by rapid fluvial aggradation and long-runout debris flows from a single HHC source rather than aggradation in response to local coseismic landsliding. The large medieval sediment pulse(s) from the confined source area of the upper Seti Khola would have been accompanied by thousands of smaller landslide point sources, judging from the patterns of historic earthquakes including the 2015 Gorkha events (Kargel et al., 2016). Yet evidence of repeated catastrophic valley infill following the cluster of medieval earthquakes so far remains limited to the Pokhara region. We cannot discount the remote probability that our ^{14}C dates might have no causal connection with the timing of large medieval earthquakes; at least, our ^{14}C dates show no conclusive correlation with temperature and monsoon proxies for the region (Fig. A.9). Contemporary rates of river incision into the Pokhara Formation remain high, triggering widespread bank erosion, terrace slumps, local ground subsidence, and high sediment yields. Thus, geomorphic adjustment to several medieval catastrophic aggradation pulses has been ongoing for at least three centuries and clearly outweighs previously documented periods of postseismic river recovery in the Himalayas or elsewhere (Keefer,

2002; Yanites et al., 2010; Li et al., 2014; Hovius et al., 2011; Koi et al., 2008; Pearce and Watson, 1986). We conclude that Pokhara's current earthquake vulnerability profile (United Nations Develop Program et al., 2010) should consider in more detail the potential impacts and consequences of postseismic sediment pulses.

2.3. Acknowledgements

Funded by the German Research Foundation (KO 3937/9) and the Potsdam Research Cluster for Georisk Analysis (PROGRESS). We thank B. Sitaula for arranging logistical support; Alpine Consultancy Pvt. Ltd. Nepal and the Department of Survey, Nepal, for digital topographic data; J. Jansen, M. Roschlaub, E. Schönfeldt, J. Seidemann, and J. T. Weidinger for help with fieldwork; and H. Wittmann-Oelze for processing the Bhim Kali sample at GFZ-HELGES, Potsdam. C.A. acknowledges support from the Helmholtz Postdoc Program (PD-039) of the German Helmholtz Association. Supporting data are available in the supplementary materials.

3

Catastrophic valley fills record large Himalayan earthquakes, Pokhara, Nepal

Published as: Stolle, A., Bernhardt, A., Schwanghart, W., Hoelzmann, P., Adhikari, B., Fort, M., Korup, O., 2017. Catastrophic valley fills record large Himalayan earthquakes, Pokhara, Nepal. Quaternary Science Reviews, 177, p. 88-103,
doi: 10.1016/j.quascirev.2017.10.015.

3.1. Abstract

Uncertain timing and magnitudes of past mega-earthquakes continue to confound seismic risk appraisals in the Himalayas. Telltale traces of surface ruptures are rare, while fault trenches document several events at best, so that additional proxies of strong ground motion are needed to complement the paleoseismological record. We study Nepal's Pokhara basin, which has the largest and most extensively dated archive of earthquake triggered valley fills in the Himalayas. These sediments form a 148-km^2 fan that issues from the steep Seti Khola gorge in the Annapurna Massif, invading and plugging 15 tributary valleys with tens of meters of debris, and impounding several lakes. Nearly a dozen new radiocarbon ages corroborate at least three episodes of catastrophic sedimentation on the fan between ~700 and ~1700 AD, coinciding with great earthquakes in ~1100, 1255, and 1344 AD, and emplacing roughly >5 km^3 of debris that forms the Pokhara Formation. We offer a first systematic sedimentological study of this formation, revealing four lithofacies characterized by thick sequences of mid fan fluvial conglomerates, debris-flow beds, and fan-marginal slackwater deposits. New geochemical provenance analyses reveal that these upstream dipping deposits of Higher Himalayan origin contain lenses of locally derived river clasts that mark time gaps between at least three major sediment pulses that buried different parts of the fan. The spatial pattern of ^{14}C dates across the fan and the prove-

nance data are key to distinguishing these individual sediment pulses, as these are not evident from their sedimentology alone. Our study demonstrates how geomorphic and sedimentary evidence of catastrophic valley infill can help to independently verify and augment paleoseismological fault-trench records of great Himalayan earthquakes, while offering unparalleled insights into their long-term geomorphic impacts on major drainage basins.

Keywords: Catastrophic valley infill; Great Himalayan earthquakes; Radiocarbon age dating; Provenance analysis; Paleoseismology; Nepal

3.2. Introduction

Destructive earthquakes such as the ones that killed nearly 9000 people in Nepal in 2015 are a direct consequence of the rapid convergence of the Indian and Eurasian continental plates, and call for reliable seismic risk assessments to mitigate future losses in the Himalayan region. The record of instrumental records of strong seismic ground shaking is limited to few decades, so that researchers rely on methods of paleoseismology. Historic documents mention several large earthquakes in the past millennium, but the return periods of major fault ruptures and possible connections to geological evidence remain partly elusive (Bollinger et al., 2014). The search for a consistency between historical reports and fault-trench studies has fueled a lively debate about the magnitudes and rupture lengths of potential Himalayan megathrust earthquakes (Mugnier et al., 2013; Sapkota et al., 2013; Rajendran et al., 2015; Bollinger et al., 2016; Mishra et al., 2016). Most paleoseismological data come from fault trenches, historical records, offset river terraces, seismically deformed or liquefied sediments, and have so far been tied to five major earthquakes since about 1100 AD (Bollinger et al., 2016). Blind fault ruptures, such as during the 2015 Gorkha earthquakes, however, limit a comprehensive coverage by fault trenching alone. Few trenches reveal data on more than one large fault rupture, and a viable chance of missing out on past large earthquakes remains (Sapkota et al., 2013; Mishra et al., 2016). Other earthquake proxies such as giant rockslide deposits (Blöthe and Korup, 2013) or precariously balanced boulders (Balco et al., 2011) have seen little application in the Himalayas, though demand for alternative sources of information about past earthquakes is high.

To meet this demand, we investigate the Pokhara Formation, a suite of catastrophic valley fills in the Lesser Himalayas of Nepal (Fort, 1987; Fort and Peulvast, 1995; Fort et al.,

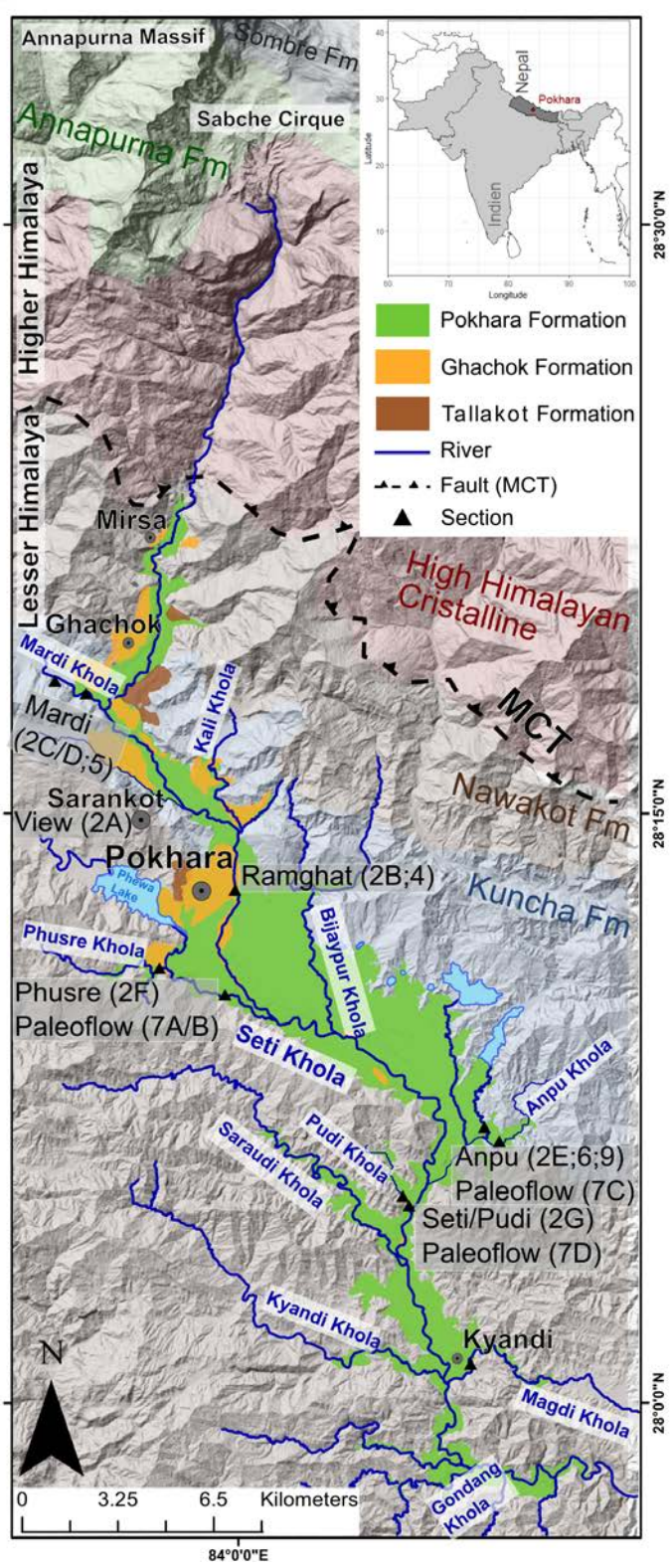

Figure 3.1.: Overview map of the Pokhara Valley. Topography and simplified stratigraphy of the Pokhara basin, Nepal Himalaya, with the known extent of the three major stratigraphic formations. Numbers and letters in brackets following place names keyed to subsequent figures. Shaded relief data from 15-m digital elevation model. The geological setting is dominated by the Higher Himalayan rocks (Sobre Fm, Annapurna Fm, HHC) featuring mainly gneisses and Nilgiri Limestone, and the Lesser Himalayan rocks known as the Nawakot unit. The Kuncha Formation forms the lower part of this unit and contains mostly phyllites and quartzites (geological map simplified after Martin et al. (2005)).

2009); these valley fills appear to have formed in the wake of several medieval earthquakes (Schwanghart et al., 2016). Our objective is to derive from these valley fills a catalogue of diagnostic sedimentary and geomorphic features of past earthquake-triggered sedimentation. We do so by reviewing, partly building on, and refining previous work (Hagen, 1969; Gurung, 1970; Hormann, 1974; Yamanaka, 1982; Fort et al., 2009; Schwanghart et al., 2016). We add new radiocarbon, sedimentological and geomorphic, provenance, dGPS, and laser scanning data that highlight how the Pokhara basin aggraded dramatically in at least three major pulses. We consolidate an existing chronology (Schwanghart et al., 2016) of the Pokhara Formation with 11 new ^{14}C ages, demonstrate that the formation took less than a millennium to form, and test further its relation to medieval earthquakes, based on new data on sediment characteristics, lithofacies, and provenance.

3.3. Study Area

The Nepal Himalayas straddle the active collision zone of the Indian and Eurasian tectonic plates, where rock uplift rates are high, monsoonal precipitation is intensive, and erosion is rapid (Lavé and Avouac, 2000, 2001). Nepal's second largest and fastest growing city Pokhara (28°15'N, 83°58'E, 870 m) lies in the "Pahar" (midland) region, pinched between the Lesser Himalaya in the south and the Higher Himalayan Annapurna Massif in the north (Fort, 2010) (Figs. 3.1 and 3.2A). More than 300,000 people have settled in and around Pokhara since about 1700 AD, and its population tripled in the past 25 years (Rimal et al., 2015). Elevation rises from 1000 m north of the city to 8000 m over only ∼20 km of horizontal distance, forming one of the steepest topographic gradients on Earth. This physiographic transition (Wobus et al., 2003) or High Himalayan Front (Godard et al., 2012) largely coincides with the location of the Main Central Thrust (MCT), a structurally complex, north dipping shear zone (Hodges et al., 1996). The Higher Himalayan Crystalline Series (HHC) (Le Fort et al., 1987; Martin et al., 2005) consists mainly of Precambrian high-grade metamorphic quartzite, schist and gneisses north of the MCT. The South Tibetan Detachment Zone separates High Himalayan metamorphic rocks from Paleozoic and Mesozoic marine calcareous metasediments and limestones of the northern Tethyan Sediment Series (TSS) forming the peaks of the Annapurna Massif (Mascle et al., 2012; Dhital, 2015). South of the MCT, the Pokhara basin features

Precambrian metamorphic sandstones, shales, and dolomites, though mostly Paleozoic phyllites and schists of the Lesser Himalayan Series (LHS) (Dhital, 2015).

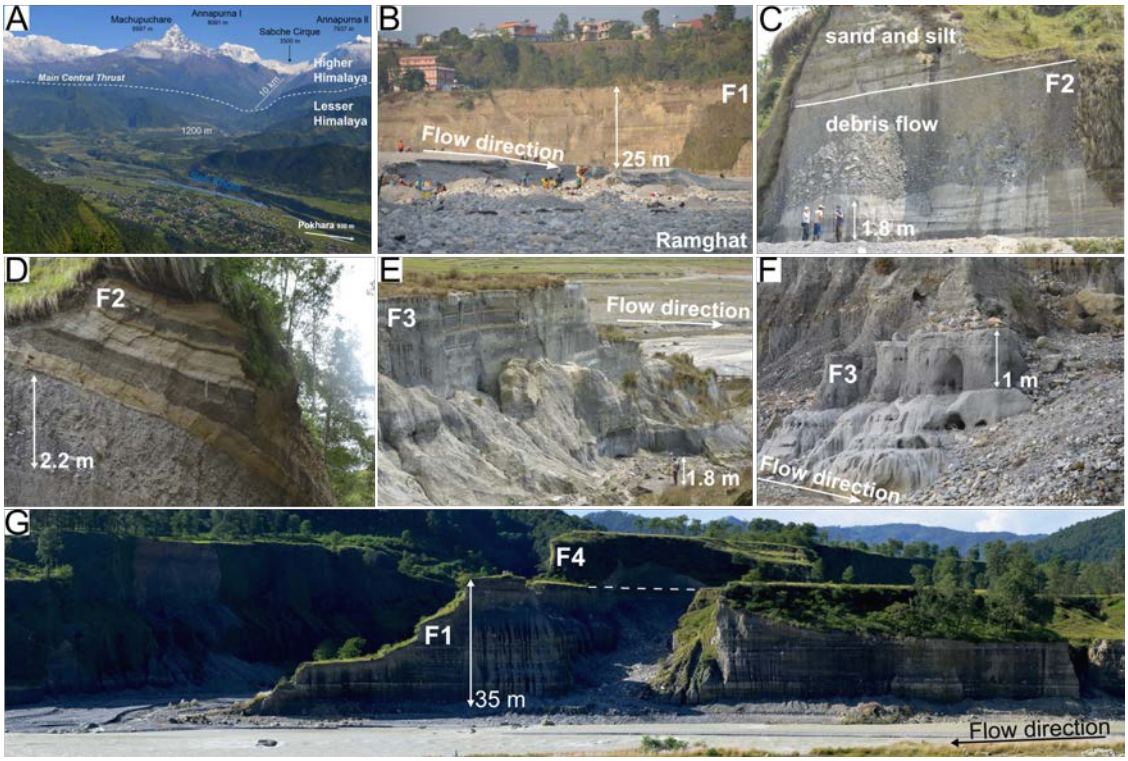

Figure 3.2.: Field images from various outcrops along the Seti Khola. Photographs of the Pokhara basin and Pokhara Formation. **A)** Northward view from Sarangkot (1530 m asl) to the Annapurna Massif and Sabche cirque. **B)** Terraces of the Pokhara Formation (lithofacies F1) with laterally extensive conglomerate and coarse sand layers, Ramghat, central Pokhara city. **C)** Massive debris-flow deposits between sands and silts (F2), Mardi Khola. **D)** Massive, matrix-supported conglomerate (2.2 m) overlain by pebble to -granule layers with interbedded sands (light brown) indicating rapid settling from suspension, lithofacies F2, Magdi Khola. **E)** Thick layers of slackwater sands and silts of lithofacies F3, Anpu Khola. **F)** Slackwater deposits (F3), massive homogeneous mud overlain by matrix-supported conglomerate (1 m thick) with small limestone pebbles, Phusre Khola. **G)** Panorama of an outcrop along the Seti Khola at the confluence to Pudi Khola; note extensive sand and conglomerate layers, and gray capping debris flow (lithofacies F4). See Fig. 3.2 for all locations. (For interpretation of the references to colour in this figure legend, the reader is referred to the web version of this article.)

We focus on the youngest fill of the Pokhara basin, the Pokhara Formation (Yamanaka et al., 1982; Fort, 1987), which forms an alluvial fan that covers ∼148 km^2 from 1350 m to 400 m asl, and sustains most of Pokhara's urban area. The fan is incised by the Seti Khola (= 'river'), which drains the Annapurna massif, originating in Sabche cirque and plunging through a steep and narrow bedrock gorge. The catchment area upstream of the fan head is ∼270 km^2, and includes the peaks of Machapuchhare (6997 m), Annapurna III (7557 m), and Annapurna IV (7525 m) (Fig. 3.2A). The fan head is located near the MCT, where the Seti gorge opens into the gently sloping Pokhara basin. Cut-and-fill terraces

interrupted by short, narrow, and steep gorges flank the Seti Khola over a distance of 70 km (Fig. 3.1), and the Pokhara Formation partly covers several LHS bedrock hills (Fort, 1987). Two other major stratigraphic units, the Tallakot and Ghachok Formations, predate and intersect with the Pokhara Formation (Fig. 3.1). The Tallakot Formation in the northern part of the basin is mostly calcareous, cemented, granule to boulder-size conglomerates with a silty matrix (Yamanaka et al., 1982). The undated Ghachok Formation is stratigraphically higher than the Tallakot Formation and occurs throughout much of the Pokhara basin, containing mainly calcareous conglomerates that are indurated by a light brown silty matrix (Fort, 1987; Dhital, 2015), and that support steep slot gorges and some caves.

Hagen (1969) interpreted the Pokhara valley as a former lake basin, and (Hormann, 1974) linked several outcrops of lacustrine deposits to episodes of former damming. He speculated that the well-developed flights of fan terraces fringing the Seti Khola were glaciofluvial gravels from two major glaciations, though having obtained a radiocarbon (^{14}C) age with a recalibrated 95% highest density interval (HDI) of 993-1157 AD for a tree trunk encased in these terraces (Fort, 1984). Follow-up studies brought to light more young ^{14}C ages between 905 and 1437 AD (95% HDI) (Yamanaka, 1982), casting doubt on a Pleistocene origin of the fan terraces, and instead raising the possibility of medieval debris flows from catastrophically failed moraine dams, filling the valley, blocking tributaries of the Seti Khola, and forming the lakes that still dot Pokhara's landscape today.

Obtaining more and slightly younger ^{14}C ages, Fort (1987) proposed that some 4 km^3 of the Pokhara Formation formed following an earthquake in 1505 AD (Table 3.1). The few samples, their large scatter, high measurement errors ($\pm$ 100 years; 2σ), and cursory documentation made it difficult, however, to identify a basal age of the Pokhara Formation, leaving both the 1255 and 1505 AD earthquakes as potential candidates for triggering catastrophic sedimentation, if accepting a seismic trigger (Fort, 2010; Hanisch and Koirala, 2010). Schwanghart et al. (2016) re-calibrated all available ^{14}C ages and added 18 new AMS ^{14}C ages using several Bayesian priors (Bronk Ramsey, 2009b), and found that three distinct peaks in the pooled age distributions coincided with the timing of nearby M $>$ 8 earthquakes in ~1100, 1255, and 1344 AD. They speculated that catastrophic failure of one or several natural dams, likely tied to large runout rock-slope failures, in the Annapurna Massif could have produced megaflood and debris-flows deposits that make up the Pokhara Formation.

Table 3.1.: Large historic earthquakes of Nepal

Year	Month	Day	Date (AD	^{14}C Age* (calAD)		Location			Magnitude	Length	Measure	Reference
				From	To		N (°)	E (°)		(km)		
1100			~1100	1160	1020	Eastern nepal			~8.6-8.8	280-400	Fault strands exposed in trenches	Lavé et al. (2005)
1255	6	7	1255	1442	1224	Central nepal	27.7	85.3	~8.1	300-400	Fault strands exposed in trenches	Mugnier et al. (2011)
1344	9	14	1344	1422	1222	Kumaon (India)			~8.4-9.2	300-500	Fault strands exposed in trenches	Kumar et al. (2006)
1505	6	6	1505	1610	1410	Western Nepal	29.5	83	8.1	250-400	Defined by surface damage	Yule et al. (2006)
1934	1	15	1934	1630		Eastern Nepal; Bihar plain	27.55	87.09	8.1	160-250	Instrumental data	Mugnier et al. (2013); Sapkota et al. (2013)
2015	4	25	2015			Gorkha	28.15	84.71	7.8	120	Instrumental data	(Avouac, 2015)

* For the ^{14}C age listed in the two columns we used the radiocarbon dates from the References listed. The numbers are the 95% HDIŠs

3.4. Methods

3.4.1. Geomorphic and sedimentological fieldwork

To learn more about the sedimentary characteristics and chronology of the Pokhara Formation, we inspected several dozens of cut banks distributed over more than 30 km along the Seti Khola and its tributaries. We logged in detail 26 sedimentary sections, identifying major lithofacies, and searching in particular for evidence of megafloods (Richard and Waitt, 1985; Baker, 1987; Carling, 2013). We laser-scanned six of these outcrops with a Leica Multistation MS50 to measure the thickness and dip of beds in the Pokhara Formation over horizontal distances of 50-150 m, referenced to separately measured differential GPS (dGPS) points captured by Leica GNSS GS10 high-precision receivers. Repeat measurements indicate that individual points are accurate to 0.02 m and 0.1 m in the vertical and horizontal, respectively. We cross-checked the LiDAR data of outcrops with tape measures, and logged sections at centimeter-scale resolution, focusing on sedimentary structure, texture, grain size, and paleo-current directions.

3.4.2. Radiocarbon dating

We sampled charcoal, wood, plant macrofossils, humic silt, and buried soils for ^{14}C dating to constrain the age of the Pokhara Formation in eight tributaries of the Seti Khola. Previously reported ^{14}C dates are from fine-grained sediments or conglomerates (Fig. 3.3A, Table 3.3) exposed in these and other tributaries (Schwanghart et al., 2016). To the 26 published ^{14}C dates (Yamanaka et al., 1982; Fort, 1987; Schwanghart et al., 2016)

we add ten new ones that we collected in November 2014 and March 2015, and one recalibrated, previously unpublished, age by K. Hormann (Fort, 1986). We computed a posterior probability density function of all ^{14}C ages from Bayesian calibration using OxCal 4.2 with the IntCal13 (Reimer et al., 2013) curve, using as priors the field-based stratigraphic relationship of the samples. The calibration model assumes a uniform-three-phase model with ages spread evenly around the historic dates of three major earthquakes in ∼1100, 1255, and 1344 AD (Schwanghart et al., 2016). We also tested several variants of the OxCal charcoal model (Bronk Ramsey, 2009b), including one that assumes all dates are outliers, as wood takes some time to grow so that charcoal ages often predate the timing of charcoal deposition (Schiffer, 1986). We also explored a model variant with all samples in stratigraphic order, assuming that deposition took place in one single phase only. Consistent with the findings of Schwanghart et al. (2016), the exact choice of this and other priors hardly changed the posterior distribution featuring three distinct peaks in calendar years. We also conducted simulations with synthetic radiocarbon dates at evenly spaced time intervals to verify that peaks in our calendric age distributions did not result from kinks and plateaus in the calibration curve.

3.4.3. Provenance analyses

We used X-Ray fluorescence (XRF) spectrometry to analyze the chemical composition of 60 samples taken from LHS bedrock, recent flood sediments, and the Pokhara Formation (Fig. 3.3B). We homogenized and powdered our samples after drying at 50°C. Each sample was measured twice with a portable energy dispersive XRF spectrometry (P-EDXRF) for 120 s with different filters to detect different specific elements. Only elements with means larger than four times the mean 2σ error of the measurements were taken into account, i.e. Al, Ca, Cl, Fe, K, Mg, P, Pb, Rb, S, Si, Sr, Ti, V, and Zn. The P-EDXRF was calibrated using the certified reference material (CRM) GBW07312; recovery values for the main oxides were between 99.4% and 112.1%. We then classified the samples based on their similarities of geochemical signature with a hierarchical cluster analysis using squared Euclidian distances and Ward's minimum variance criterion (Willet, 1987). A dendrogram of this unsupervised learning method depicting the dissimilarity, which measures the distance between individual samples in parameter space, helped us decide whether samples belonged more likely to the HHC or the local LHS bedrock.

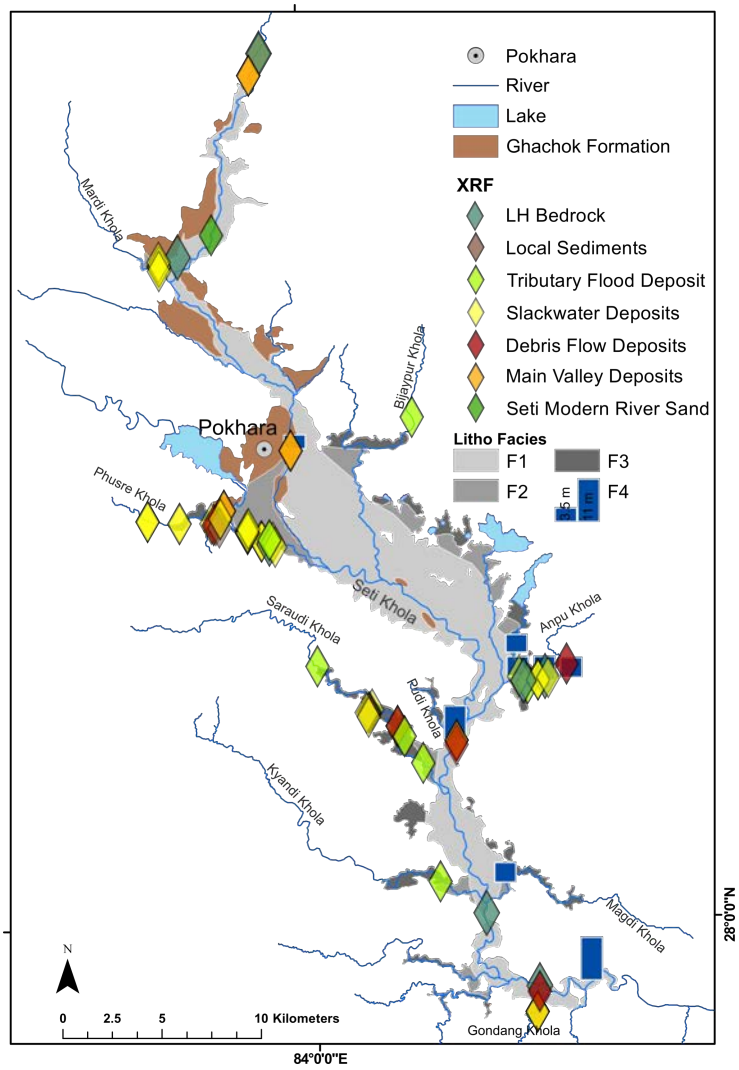

Figure 3.3.: Overview map of the sampling sites and types of deposits studied. Gray shades delineate the Pokhara fan. See Fig. 3.1 for more details on the study area.

3.5. Results

3.5.1. Sedimentological analyses

The most striking geomorphic feature of the Pokhara fan is that it migrated into several tributaries for between 0.7 and 7.5 km upstream (Fig. 3.1). Detailed laser scans and dGPS measurements reveal that the fan sediments dip upstream into these tributaries at inclinations of 0.5-0.8°near Saraudi Khola, blocking, deflecting or narrowing the smaller channels. In the detailed sediment logs of 26 outcrops we distinguish four sedimentary lithofacies (F1-F4, Fig. 3.3, Table 3.2) of the Pokhara Formation, reflecting individual depositional environments that change perpendicular to the fan axis (Fig. 3.2B); the central fan portion along the active channel of the Seti Khola (F1); a transitional zone where the tributaries

confluence with the Seti Khola (F2); a distal zone in the lower reaches of these tributaries (F3); and an extensive debris-flow deposit (F4) capping F1, F2, and F3 in upstream parts of the fan.

Lithofacies F1 - fan center

Lithofacies F1 is best exposed at the head (e.g. north of the Mardi Khola confluence, Fig. 3.1) and in central parts of the Pokhara fan (Figs. 3.3 and 3.4A), featuring up to 10-m thick units of sub-horizontally bedded, poorly sorted, and clast-supported conglomerates alternating with <3-m coarse layers of sands, granules, and outsize boulders with an average diameter of about 2 m (Table 3.2).

In outcrops along the trunk channel, the lowermost conglomerate units are 5-10 m thick, and change upwards from a clast-supported to matrix-supported texture. Grading is crude and normal from cobbles to coarse pebbles; these units extend along the fan axis for more than 100 m (Fig. 3.2G). An overlying unit of ~40-m thick sediments consists of stratified and clast-supported cobble conglomerates that fine downstream over a distance of ~45 km into pebble-sized conglomerates alternating with sand layers that are 0.5-3.0 m thick (Fig. 3.2B). Tributary mouths feature nests of sub-rounded, boulder-sized, and indurated conglomerates encased in medium-sandy beds (e.g. Pudi Khola, Fig. 3.1).

We interpret the poorly sorted and laterally extensive matrix-supported conglomerate in F1 as deposits of cohesive debris flows (Hungr et al., 2001). In contrast, the overlying stratified, clast-supported coarse conglomerates likely indicate deposition in highly energetic, non-cohesive, bedload-rich, turbulent water flows characteristic of river floods.

Lithofacies F2 - tributary mouths

Lithofacies F2 is limited to tributary mouths (Figs. 3.3 and 3.4B). Its basal units are 1-6 m thick, disorganized, very poorly sorted, fining upward and clast-supported conglomerates with a sandy matrix. The conglomerates are cobble-to granule-sized and lack current structures.

Distinct interspersed, well-sorted finer layers grade upwards from pebbles to granules, and have many undulating contacts and deformation features (Fig. 3.2C). The conglomerates

Table 3.2.: Sediment lithofacies of the Pokhara formation.

Litho-Facies	Lithology	Texture	Thickness	Bedding geometry and Structure	Transport and Inferred processes	Depositional Environment
F1	Clast-supported conglomerate	Grain Size: Pebble to boulder. Matrix: Poorly sorted, coarse, sub-rounded sand.		Sub-horizontal dip (0.8°), laterally extensive and parallel bedded for at least 100 m. Lack of current structures.	Transport by Newtonian-like fluids with high sediment concentration – turbulent flow. High sedimentation rates suppress current reworking	Central fan
	Sand layers	Grain Size: Coarse sands to granules with some outsized boulders	0.5-3 m for single beds; the unit is up to 25 m thick			
	Matrix-supported conglomerate	Grain Size: Pebbles to boulders. Matrix: Poorly sorted, fine, angular sands to muds.	5-10 m	Sub-horizontally and laterally extensive layer	Cohesive debris flow	
F2	Mud, silt to sand alternation	Silts to coarse sands	0.3-3 m	Extensive, shallow dipping (1.2°) and laminated beds. Rare cross bedding and soft sediment structures.	Rapid settling from suspension/sediment-laden flow.	Tributary mouths
	Clast-supported conglomerate interbedded with sand	Conglomerate: Grain Size: Granules to cobbles, with some boulders. Matrix: Normally-graded sand. Sand layers: Grain Size: Silts to sands	1-6 m	No current structures Shallow dipping and extensive beds	Rapid suspension fallout and partly bedload	
	Matrix-supported conglomerate	Grain Size: Granules to cobbles. Matrix: mud featuring oblate limestone clasts	3-5 m Limestone clasts are 1-5 cm	Undulating at the base	Cohesive debris flow	
F3	Alternation of mud and silt layers	Grain Size: Clays to medium, normally graded sand with some medium to coarse pebbles, and massive mud and silt layers	0.5-4 m	Bedding geometry: Laterally extensive and continuous for at least 50 m. Low upstream dip of 1.4-1.5°. Soft sediment deformation: flames, loading and dewatering. Current structures: ripple cross-lamination are rare	Fall-out from high concentration suspensions in peak flow stage. Rapid aggradation suppresses the development of current structures.	Fan margins
	Matrix-supported conglomerate	Grain Size: Normally graded medium to coarse, sub-angular to sub-rounded, pebbles. Matrix: Mud	0.5-2 m, max. 5 m	Bedding geometry: Laterally continuous for at least 50 m	Cohesive debris flow	
F4	Matrix-supported conglomerate	Grain Size: medium cobbles to boulders. Up to 3 normally graded units; Poorly sorted, angular clasts. Matrix: mud and sand	4-11 m	Bedding geometry: Laterally continuous from the main fan into tributary valleys and downstream increasing thickness (Fig. 3.2A)	Cohesive debris flow	Capping unit

alternate with tabular, up to 3-m thick, silty to coarse sandy layers that are laminated, though the sands are cross-bedded in places. F2 also contains interbedded layers of mud matrix-supported conglomerates with cobble-to granule-sized limestone clasts, and some undulating basal contacts (Fig. 3.2D).

We interpret the clast-supported conglomerates with sand and silt beds as fallout from rapid suspension in water flows. The soft-sediment deformation structures at the contacts suggest rapid sedimentation without much dewatering of uppermost layers (Carling, 2013).

We interpret the overlying matrix-supported conglomerates as cohesive debris flows (Hungr et al., 2001) that eroded or at least deformed water-saturated units at their base, with little time passing between successive pulses.

Lithofacies F3 - fan distal zone

The tributary valleys of the Seti Khola store the finest sediments of the Pokhara Formation (Fig. 3.4C). F3 makes up the distal parts of the formation (Fig. 3.3), where it invaded the tributaries, featuring homogeneous sand, silt, and massive mud layers organized into 0.5-4.0 m thick units (Table 3.2) that alternate with mud to medium-grained sand with some pebbles (Fig. 3.2E). The beds are planar, and extend along tributaries for more than 50 m, grading normally from medium sand to clay. The contacts are tabular or show flames, loading and dewatering structures with few erosional contacts, and some current ripples (Fig. 3.5). Poorly-sorted, mud matrix-supported conglomerate layers between these alternating mud, silt, and sand beds (in average 0.5-2 m thick) contain sub-angular to sub-rounded clasts fining upwards from coarse pebbles to fine granules.
We interpret the finest units as slackwater deposits that rapidly dropped out of suspension in decelerating flows of catastrophic floods (Baker, 1987) and high-concentration sediment flows (Fig. 3.2F) (Carling, 2013). These silty to fine sandy slackwater sequences are exclusively of HHC provenance, more than 14 m thick in Saraudi Khola, 3 km upstream of the Seti Khola (Fig. 3.1), and devoid of any organic material. Their rapid deposition explains the lack of current structures. In contrast, the mud-matrix supported, pebbly conglomerates, are indicative of hyperconcentrated flows and cohesive flows (Jakob and Hungr, 2005).

Lithofacies F4 - capping conglomerate

An extensive, poorly sorted, mud- and silt-matrix supported, conglomerate forms lithofacies F4. It is the most poorly sorted lithofacies with a sharp and locally undulating basal contact and up to three fining-upward units. Angular clasts include medium cobbles to coarse boulders (<0.4 m). In the northern parts this conglomerate is 3-5 m thick, whereas in the southern parts of the Pokhara Formation it can be up to 11 m thick; confined bedrock reaches of the Seti Khola have even thicker stacks (Figs. 3.3, 3.4A and 3.4C).
We interpret F4 as cohesive debris-flow deposits based on their poorly sorted and massive

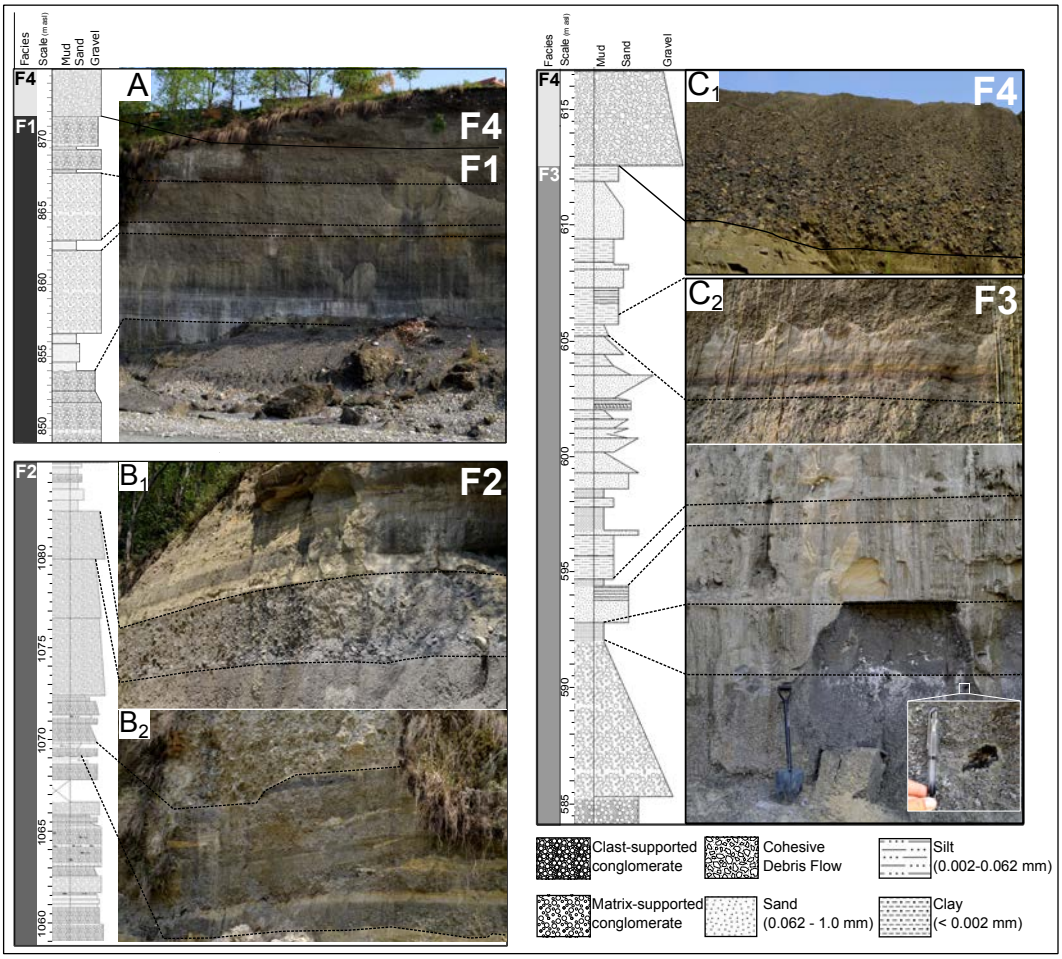

Figure 3.4.: Examples of lithofacies classification. A) Lithofacies F1-Fan center. Sediment log and field images of lithofacies F1 at Ramghat, Seti Khola, central Pokhara city (Fig. 3.1). Conglomerates (cgl) alternating with thin beds of sands. **B)** Lithofacies F2 - Tributary mouths. B1) Massive beds of debris-flow deposits in the Mardi Khola (mud-matrix supported conglomerate) on top of B2) sands and silts that alternate between clast-supported conglomerates (cgl). F2 occurs mostly at the tributary mouths of the Seti Khola. **C)** Lithofacies F3-Fan distal zone. Lithofacies F3 and F4, Anpu Khola (Fig. 3.1). C1) F3: massive silt and mud layers dominate this lithofacies; the lower conglomerate (cgl) is a hyperconcentrated flow with Nilgiri limestone pebbles (HHC) in a muddy matrix. Insert show a radiocarbon sample (Poz-69260, Table 3.3) taken from this silty layer. C2) F4: the capping debris-flow deposit mainly occurs in the Seti Khola valley though reaches some of its eastern tributaries.

texture and its muddy matrix (Hungr et al., 2001; Carling, 2013). The enclosed fining-upward units represent either one debris-flow event consisting of multiple pulses or several debris flows without clearly visible erosional contacts.

3.5.2. Geochemical analyses

Our geochemical analyses show that the Nilgiri Limestone, a prominent lithology in the Annapurna Massif rich in calcium carbonate, dolomite and muscovite (Waltham, 1972;

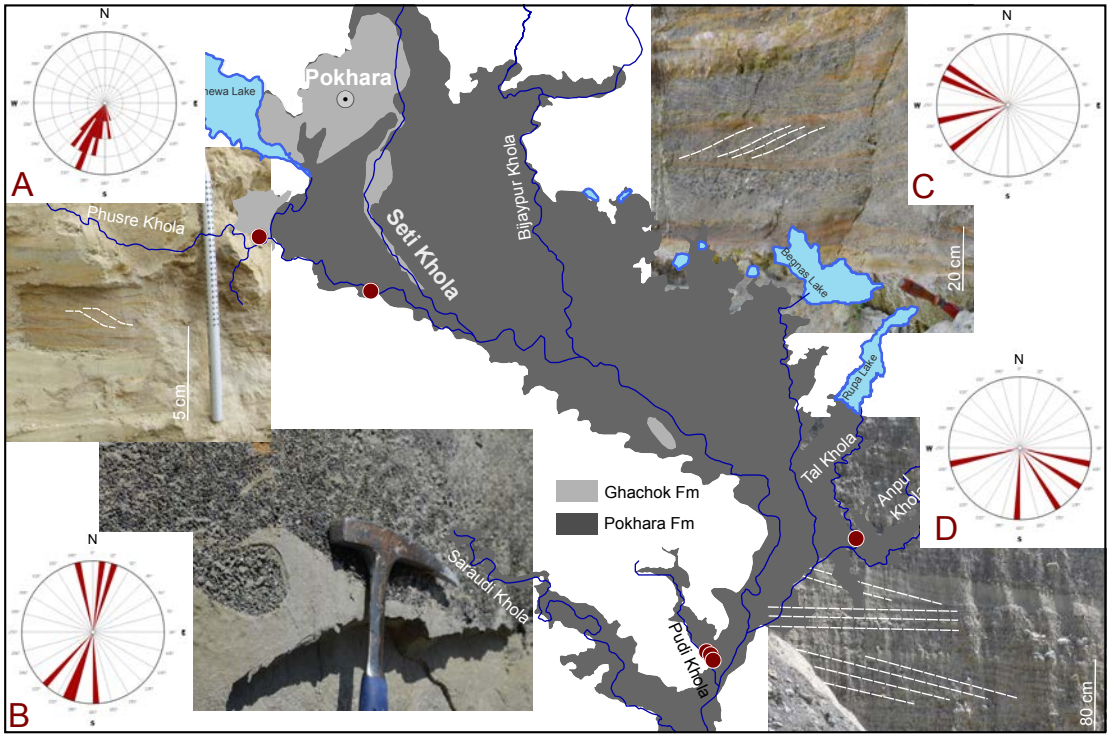

Figure 3.5.: Paleo-Currents along the Seti Khola. Measured paleo-current directions of the Pokhara Formation. **A)** Ripples (n = 25) in slackwater deposits, Phusre Khola. **B)** Flames (n = 7), Phusre Khola, adjacent to a bedrock flow obstacle, explaining the two differing paleo-flow directions; **C)** Cross-beds (n = 4), Anpu Khola, dipping downstream along the Seti Khola, and away from the bedrock flow obstacles. **D)** Cross-beds (n = 5), Pudi Khola, about 0.2-0.5 km upstream of the Seti Khola; flow was entering the tributary but also returned back into the trunk valley. Rose diagrams were compiled with the free software Georose (www.yongtechnology.com).

Colchen et al., 1981), dominates the clast composition of the Pokhara Formation, together with scattered HHC gneisses, granites, and marbles. The main differences in element content of the LHS and HHC samples concern Ca (0.03-16% and 19-40% in the LHS and HHC, respectively), Al (1-32% and 10-21%), and Si (17-45% and 13-26%) concentrations. We measured Ca values of up to 40%, indicating that pure calcite ($CaCO_3$) occurs in the HHC Series. X-Ray fluorescence spectrometry of fine slackwater deposits, conglomerates, debris-flow layers and LHS bedrock confirms that the elemental composition of the Pokhara Formation differs strongly from that of the local LHS bedrock (Fig. 3.6). A few layers of local LHS sediments enclosed in thick beds of HHC-derived slackwater deposits attest to local input that separates multiple phases of rapid aggradation. The clearly separable LHS and HHC samples independently support our sedimentological interpretation of lithofacies F3 as HHC-derived slackwater deposits rather than LHS-derived lake sediments in the lower tributary reaches, so that we reject previous hypotheses (Hagen, 1969; Hormann, 1974; Yamanaka et al., 1982; Fort, 1987) that the fine sediments resulted

from local ponding. Our sediment logs independently confirm that HHC sediments extend upstream into tributaries in laterally graded facies instead of interfingering with local LHS material (Figs. 3.7 and 3.10).

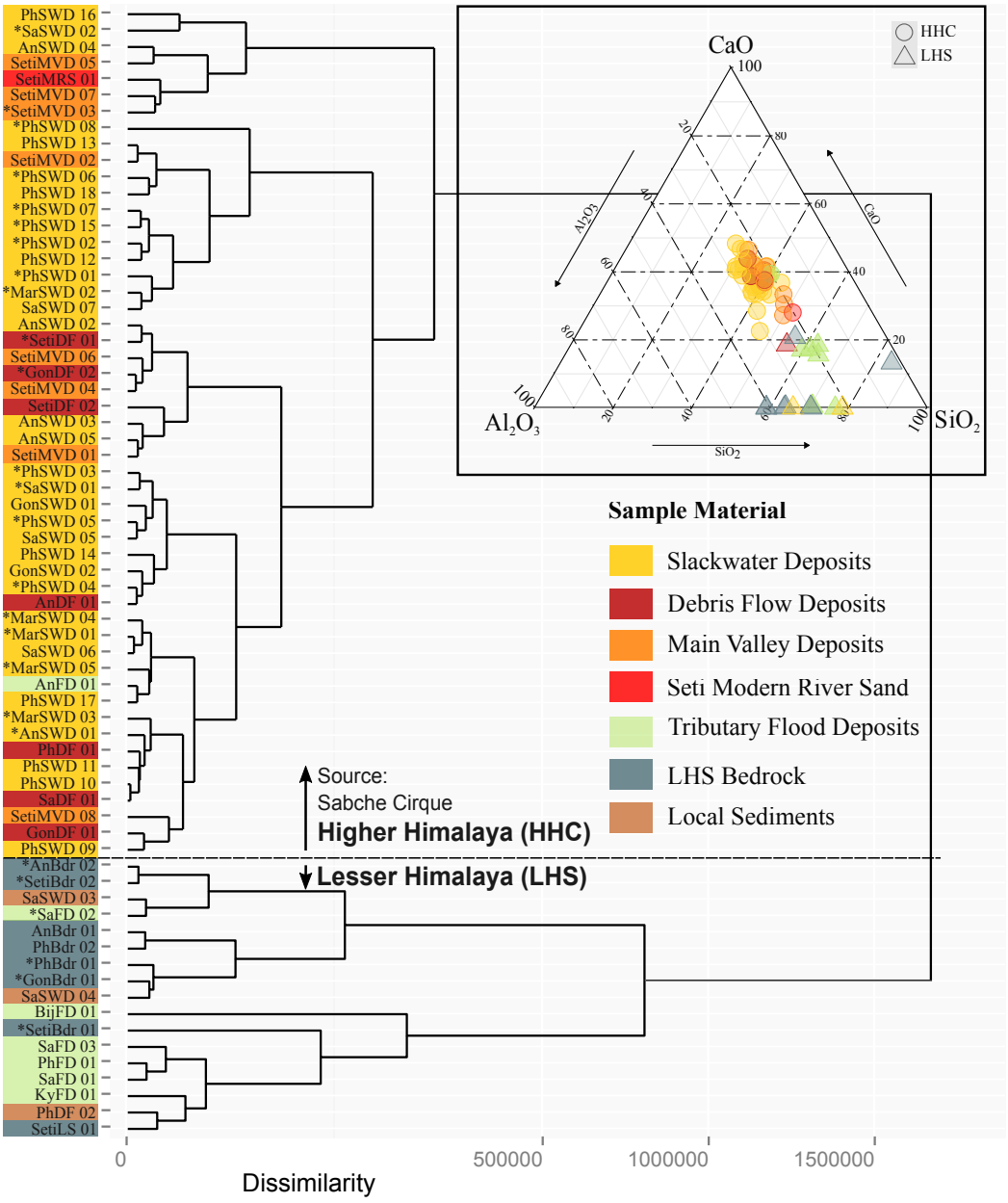

Figure 3.6.: Geochemical Analysis of lithofacies. Geochemical (P-EDXRF) analysis of 60 samples from the lithofacies of the Pokhara Formation, Lesser Himalayan Series (LHS) bedrock, and modern flood deposits. "Main Valley Deposits" = lithofacies F1; "Slackwater Deposits" = lithofacies F3; "Debris-Flow Deposits" = lithofacies F1-F4; "Local Material" is LHS sediment between and on top of HHC sediments of the Pokhara Formation. Inset shows the three most separable chemical compositions of the samples. Bubbles and triangles are HHC and LHS sediments, respectively. The samples indicated with an asterisk are from Schwanghart et al. (2016) and clustered by their lithological dissimilarity, a measure of distance in the parameter space.

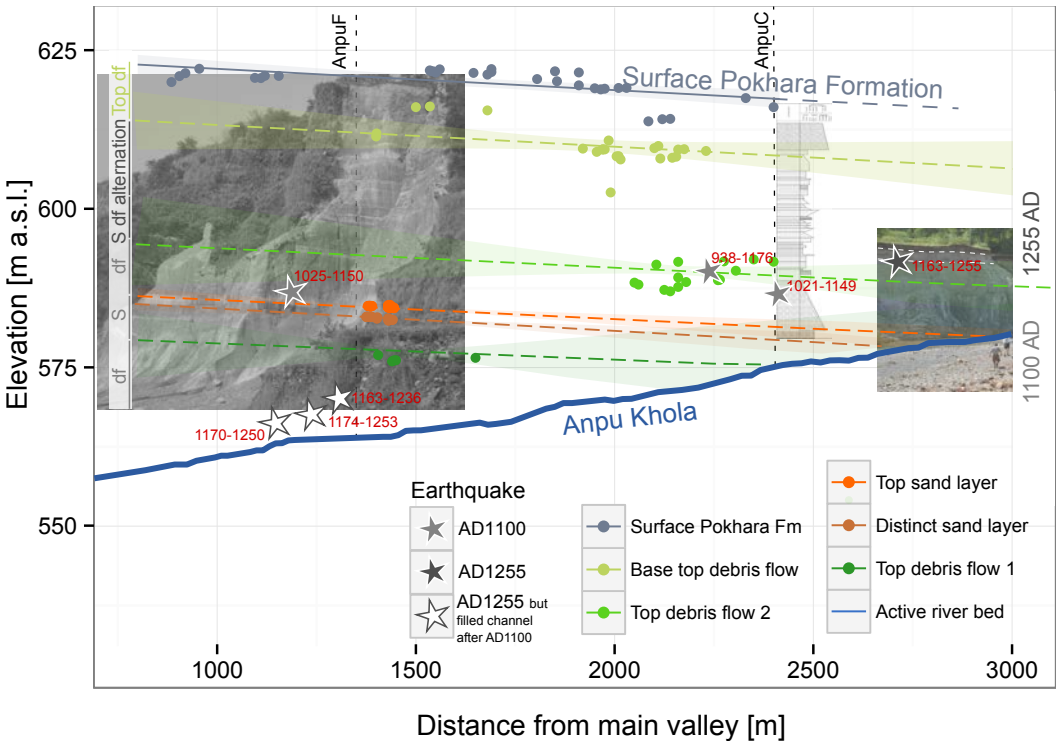

Figure 3.7.: Relation between sediment units and ^{14}C ages. Terrestrial laser scanning points of selected beds in the Pokhara Formation lithofacies F3, Anpu Khola. Distance is measured from the main valley upstream into the tributary valley. The dashed lines are based on tracing of individual sediment layers (cohesive debris flow layers and sand layers) in the field, which are continuous along the lateral extent of the outcrop/figure. Note that three ^{14}C ages (white stars) are stratigraphically inverted with respect to younger ages (gray stars). We interpret this as river incision following the first sediment pulse at around 1100 AD, and refilling with slackwater deposits during the second pulse at around 1255 AD; df - debris flow; S - sand layer; Fm - Formation; all ages (stars) indicated as AD; Anpu F is a scanned outcrop; AnpuC is a sediment log shown in Fig. 3.4C.

3.5.3. Radiocarbon dating

Our ten new ^{14}C dates are highly consistent with the chronology of 26 dates of the Pokhara Formation compiled by (Schwanghart et al., 2016) (Figs. 3.8 and 3.9, Table 3.3). The dates consolidate the scenario of catastrophic sedimentation connected to three large earthquakes in ~1100, 1255, and 1344 AD, within measurement and calibration errors. None of our samples produced outlier ages. Even the recalibrated, unpublished date by K. Hormann (Fort, 1986) has a 95% HDI ranging from 933 to 1157 AD. A new charcoal sample (Poz-75103) from a paleosol between the Pokhara Formation and LHS bedrock in Anpu Khola has a 95% HDI from 655 to 769 AD. This gives a tentative maximum age for the Formation,

Table 3.3.: (Re-)Calibrated ^{14}C dates from the Pokhara Valley.

Lab.No	Sample ID	River	N (°)	E (°)	Elevation (m asl)	Material	Radiocarbon age (BP) ± 1σ	95% HDI (AD) From	To
Fort (1987)									
BS-464	83-PQ523	Bijaypur	28.21	84.029	-	Charcoal	390 ± 110	1264	1507
BS-465	83-PQ525	Bijaypur	28.21	84.023	-	Wood	510 ± 140	1270	1473
Gif-6220	83-PQ641	Phusre	28.18	83.971	-	Wood	450 ± 100	1280	1486
Fort (1986)									
Hormann unpublished		Magdi				Wood	950 ± 54	993	1157
Yamanaka (1982)									
-	TH-719	Phusre	28.18	83.971	-	Wood	750 + 100/- 90	1166	1258
-	TH-720	Phusre	28.18	83.971	-	Wood	970 + 100/- 110	936	1177
-	TH-721	Phusre	28.186	83.956	-	Humic Silt	1070 ± 100	905	1150
-	TH-722	Bijaypur	28.215	84.03	-	Peat	590 ± 110	1274	1437
-	TH-723	Bijaypur	28.218	84.031	-	Peat	770 + 100/- 110	1166	1257
Schwanghart et al. (2016)									
COL1915.1.1[a]	BIJ02	Bijaypur	28.219	84.029	820	Humic Silt	772 ± 46	1177	1262
COL1916.1.1[a]	PH02C	Phusre	28.18	83.968	730	Leaves	846 ± 42	1166	1248
COL1917.1.1[a]	PHUSRE03	Phusre	28.183	83.951	740	Charcoal	944 ± 46	935	1177
COL2150.1.1[a]	SARA1-1	Saraudi	28.096	84.029	541	Wood	746 ± 37	1187	1268
COL2151.1.2[a]	MADHI2	Magdi	28.015	84.117	495	Charcoal	985 ± 36	926	1170
COL2151.1.1[a]	PH6	Phusre	28..175	83.976	703	Wood	880 ± 36	1159	1233
Poz-69082[b]	Phusre010	Phusre	28.175	83.982	705.59	Wood	875 ± 30	1160	1225
Poz-69083[b]	Phusre012	Phusre	28.175	83.982	697.81	Leaves	810 ± 30	1180	1256
Poz-69084[b]	Phusre013	Phusre	28.175	83.982	696.06	Wood	845 ± 30	1166	1244
Poz-69085[b]	Phusre14	Phusre	28.175	83.982	700.5	Charcoal	825 ± 30	1164	1255
Poz-69086[b]	PhusreFa	Phusre	28.185	83.958	728	Charcoal	910 ± 30	1160	1250
Poz-69088[b]	PRE 14C 1	Phusre	28.184	83.934	747.9	Charcoal	595 ± 30	1255	1463
Poz-69089[b]	GD03	Gondang	27.958	84.112	479.02	Charcoal	890 ± 30	1161	1252
Poz-69090[b]	GD06	Gondang	27.958	84.112	481.12	Soil	1110 ± 30	906	1020
Poz-69092[b]	KBP03	Bijaypur	28.218	84.027	824.99	Wood	695 ± 30	1269	1390
Poz-69093[b]	TAL02	Tal	28.117	84.105	583.42	Wood	830 ± 30	1170	1250
Poz-69094[b]	TAL05	Tal	28.117	84.105	614	Wood	930 ± 30	1025	1150
Poz-69260[b]	Anpu02	Anpu	28.109	84.116	590.56	Humic Silt	950 ± 30	1021	1149
This Study									
Poz-75093[b]	GD01	Gondang	27.958	84.112	479.03	Soil	800 ± 30	1181	1260
Poz-75094[b]	KBP02	Bijaypur	28.218	84.027	824.99	Humic Silt	870 ± 30	1160	1230
Poz-75095[b]	Phusre11	Phusre	28.175	83.982	697.84	Wood	860 ± 30	1163	1236
Poz-75098[b]	Tal01	Tal	28.117	84.105	584.84	Humic Silt	820 ± 30	1174	1253
Poz-75100[b]	14C Anpu11	Anpu	28.108	84.114	590.3	Charcoal	930 ± 30	938	1176
Poz-75101[b]	14C Anpu01	Anpu	28.111	84.105	556	Leaves	860 ± 30	1163	1236
Poz-75102[b]	14C Anpu16	Anpu	28.11	84.12	591.8	Charcoal	830 ± 30	1163	1255
Poz-75104[b]	BIJ 03	Bijaypur	28.219	84.029	820	Humic Silt	680 ± 30	1275	1390
Poz-75171[b]	Ph6u_14C	Phusre				Wood	905 ± 30	1157	1221
Poz-75103[b]	EBGcc01	Anpu	28.111	84.12	608.5	Charcoal	1310 ± 30	491	912

[a] Radiocarbon ages processed in the CologneAMS, University of Cologne - Center for Accelerator Mass Spectronometry, Germany
[b] Radiocarbon ages processed in the Radiocarbon Laboratory Poznan, Poland.

whereas a rounded 3000-ton HHC boulder, called Bhim Kali, on top of the Pokhara fan sets a minimum age at 1686 ± 45 AD (±2σ), estimated from cosmogenic ^{10}Be surface-exposure dating (Schwanghart et al., 2016), Fig. 3.3A). The ^{14}C dates allow discerning two sediment pulses at around 1100 and 1255 AD with a time gap of >100 years at one outcrop in Anpu Khola (Fig. 3.7). The sharp contact between these two pulses is a conglomerate (belonging to the older pulse) capped by fluvial silts and sands that we attribute to the 1255 AD earthquake (green contact between debris-flow and sand layers, Fig. 3.7); we identified this sequence of sediment layers in various outcrops. Plotting all recalibrated ^{14}C ages and their sampling locations (Fig.3.8), we obtain a spatial stratification of dates along the Seti Khola, consistent with three major pulses coincident with the times of known large medieval earthquakes (Fig. 3.9). The relative stratigraphy of these dates, our

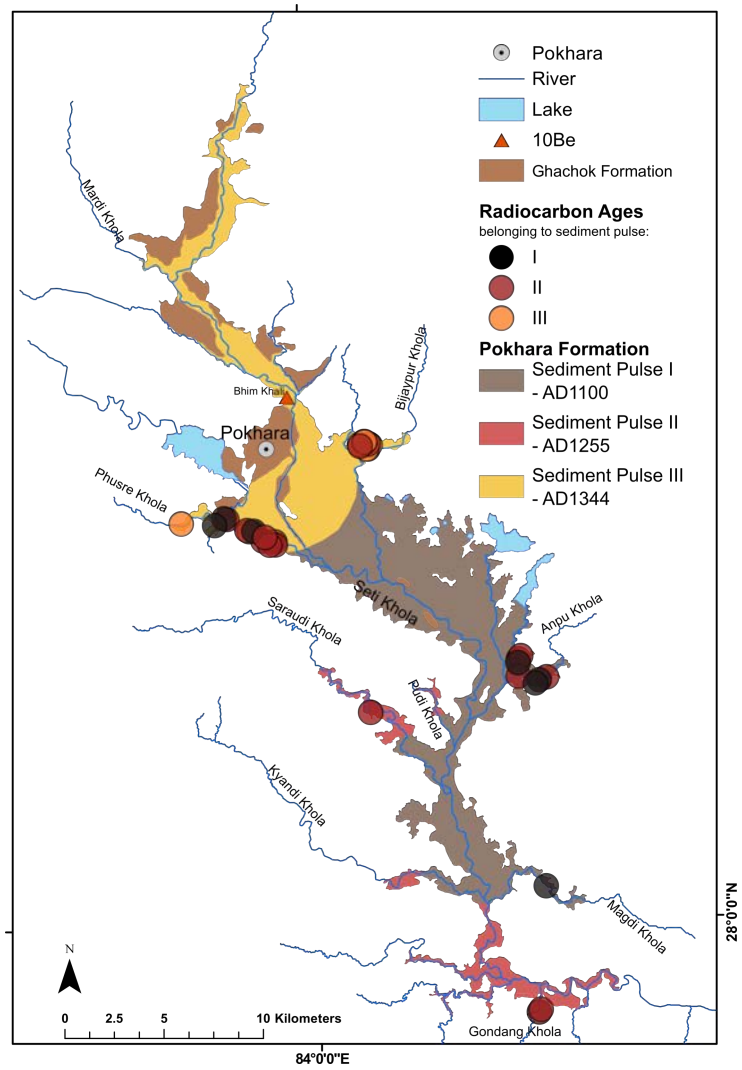

Figure 3.8.: Approximate extent of sediment pulses. Estimated extent of catastrophic aggradation inferred from lithofacies and calibrated ^{14}C data (Fig. 3.9, Tab 3.3) coincident with the timing of major nearby earthquakes. Note how younger earthquake-related sediment pulses reach less far down the Seti Khola valley.

sedimentary logs, and geochemical provenance allow estimating to first order the volume of each pulse, simplistically using an average deposit thickness. The sediments that we attribute to the ~1100 AD earthquake are 15-25 m thick, and cover an area of ~130 km^2 (Figs. 3.8-3.10A); this aggradation phase dumped between 1.9 and 3.3 km^3 of sediment. The second pulse around the time of the 1255 AD earthquake was the most extensive, depositing HHC materials >60 km downstream from their source, burying an area of ~148 km^2 with 2.9-3.7 km^3 of sediment (Figs. 3.8 and 3.9). Another sediment pulse at around 1344 AD laid down 0.3-0.5 km^3 of debris-flow and fluvial gravels on the northern fan over ~50 km^2. Lithofacies F4 is 6 m thick on average, has an estimated volume of ~1 km^3, and represents the youngest, though undated, debris flow of the Pokhara Formation. We

surmise that F4 is either part of the last sediment pulse or that it forms an individual younger unit with a minimum age set by the Bhim Kali boulder at ~1686 AD (Schwanghart et al., 2016).

3.6. Discussion

3.6.1. A new depositional model of the Pokhara Formation

Combining our results from lithofacies analysis, the spatial pattern of ^{14}C dates, sediment provenance, dGPS and laser-scanning surveys, we propose a new depositional model for the Pokhara Formation, and revise earlier models of the most recent geological history of this densely inhabited stretch along the MCT (Figs. 3.7 and 3.10). In summary, the key diagnostic of lithofacies F1 to F3 is their consistent lateral fining across the fan axis toward its margins and into the lower reaches of tributaries except for several clusters of large boulders at tributary mouths (Fig. 3.4). Lithofacies F1 has thick sequences of fining-upward conglomerates, while sandy to muddy units appear in F2, where they alternate with conglomerates.

F3 is mostly massive layers of fine sands, silts, and muds, and the only lithofacies in which we found ripples and flame structures indicating flow upstream into the trunk valley (Fig. 3.5), local backflow against bedrock obstacles, and eddying at tributary mouths. Lithofacies F4 features thick cohesive debris-flow deposits capping all other lithofacies (Fig. 3.3). Our dGPS measurements confirm that sand and conglomerate layers (lithofacies F2, F3) extend continuously from the Seti Khola valley upstream into tributaries for nearly 8 km (Fig. 3.7). The upstream dip, lateral continuity, and provenance of these sediments do not support the long-lived hypothesis that HHC sediments impound and interfinger with lake sediments derived locally from LHS bedrock (Hagen, 1969; Hormann, 1974; Yamanaka et al., 1982; Fort, 1987; Koirala et al., 1998) or sustained input from the dammed tributaries (Fort, 1987) (Fig. 3.10). Instead, our results jointly point at rapidly settled slackwater deposits that plugged the mouths and lower reaches of tributaries with HHC debris. These slackwater deposits superficially resemble lake sediments, but lack the high organic carbon content of lacustrine deposits in existing lakes in the Pokhara Valley (Ross and Gilbert, 1999), while being dominantly, if not exclusively, of HHC provenance (Fig. 3.6). Several lakes that appear ponded by the Pokhara Formation could have existed

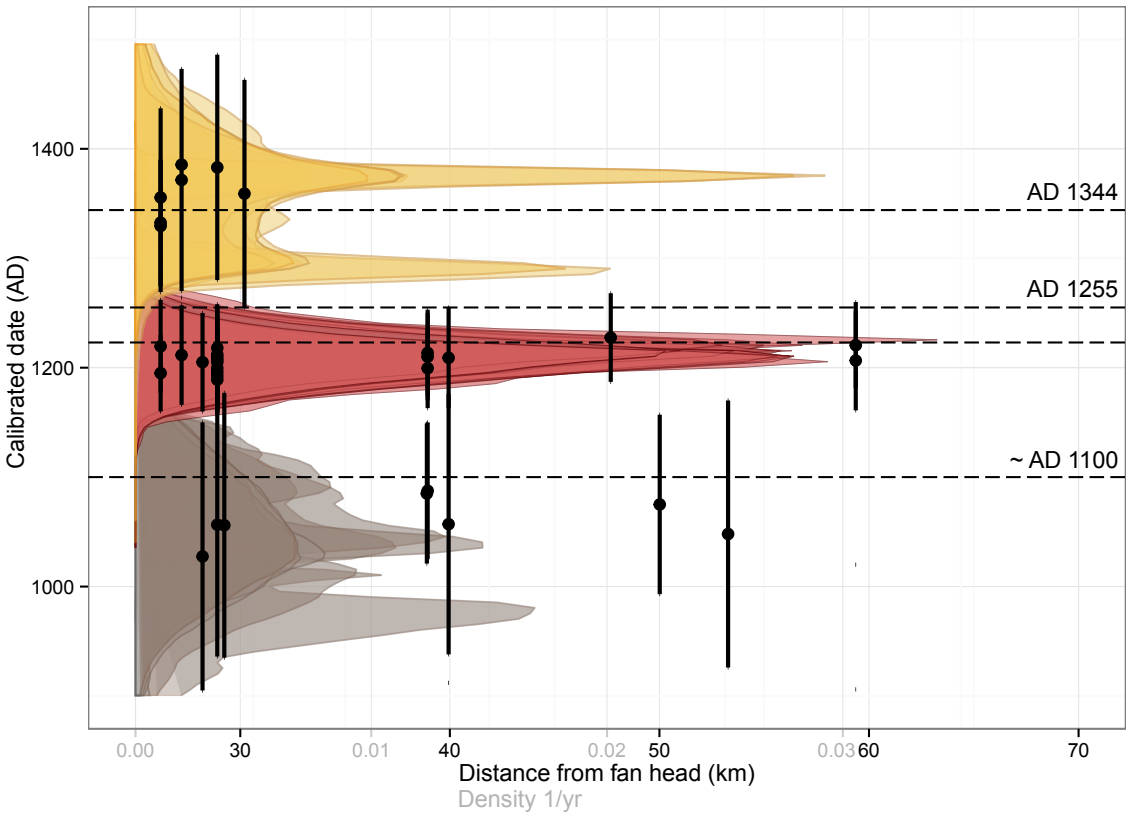

Figure 3.9.: Densities of calibrated radiocarbon ages. Calendar dates of calibrated ^{14}C ages support the notion of several catastrophic sediment pulses with differing extent from the head of the Pokhara fan. Gray shades are posterior probability density functions of calibrated ^{14}C ages. The sediment pulse at around 1344 AD merely covered the upper part of the fan and its tributaries just including today's Pokhara city, whereas the pulse around 1255 AD reached farthest downstream.

before. A >20-m deep, subaqueous channel at the bottom of Phewa Lake, for example, has incised into the Ghachok Formation and requires that the lake must have been dammed by these older sediments before. An increased carbonate content at ~0.7 m below the floor of Phewa Lake documents a phase of massive allochthonous input into an existing lake. This sedimentary layer has previously been attributed to construction works in Pokhara (Ross and Gilbert, 1999), but is geochemically strikingly similar to HHC material. Overall, the lithofacies of the Pokhara Formation share many diagnostics of megaflood deposits described by Carling (2013) and Baker (1987): the capping debris-flow facies (F4) thickens downstream (Fig. 3.3), whereas lithofacies F2 and F3 have characteristics consistent with back-flooding flows upon entering tributary mouths, ramping slackwater deposits up to 8 km against the valley gradient. Other conspicuous features such as large cross-beds dipping into tributaries or rhythmically bedded gravels (Carling, 2013) remain elusive in the Pokhara Formation, though rare cross beds and current structures (Fig. 3.5) and locally indistinguishable ^{14}C dates point to rapid valley filling with sediment up to tens

of meters thick (Figs. 3.8 and 3.9). In some sections (e.g. Anpu or Saraudi Khola), the uppermost bed of the ~1100 AD sediment pulse consists of a debris-flow deposit, whereas the lowermost bed that we connect to the 1255 AD pulse has mostly medium sands and silts.

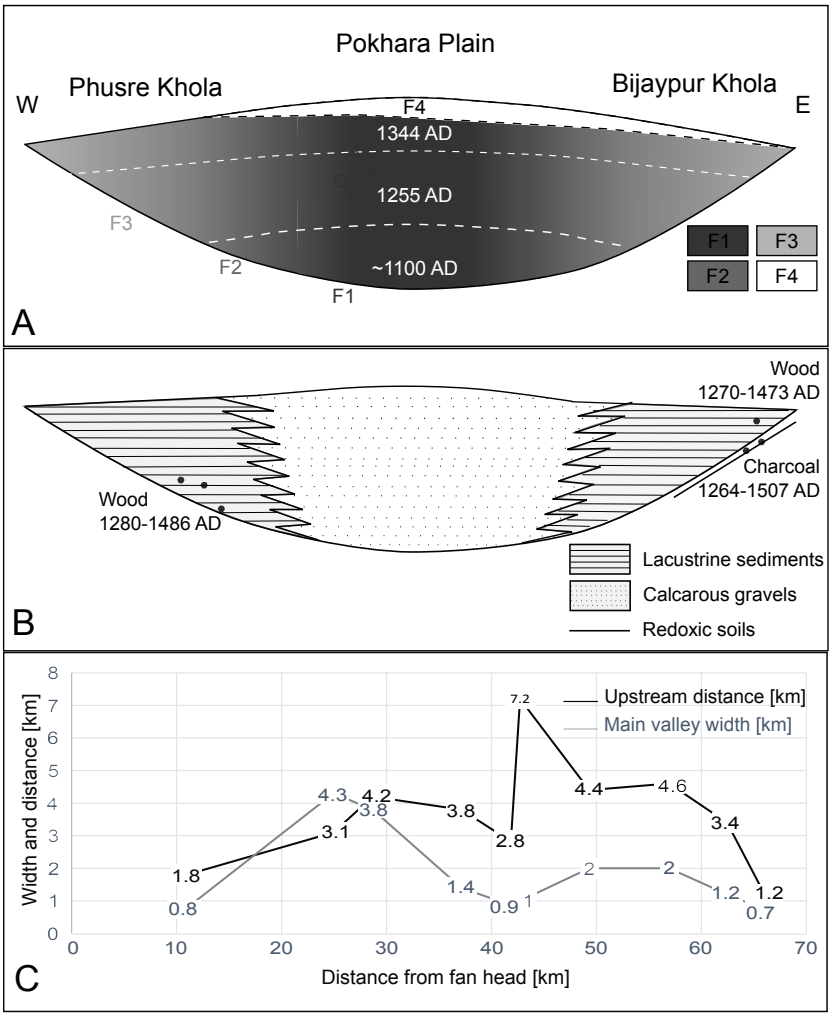

Figure 3.10.: Comparison of two hypotheses of how the Pokhara Fan formed. Revised (A) versus previous (B) depositional model for the Pokhara Formation. **A)** This study model is based on relative stratigraphy, dGPS surveys (Fig. 3.7), and provenance analyses (Fig. 3.6). In our new model, the sediments of the Pokhara Formation entered the lower reaches of tributaries, leaving thick and extensive beds of HHC-derived slackwater sediments that were previously interpreted as lake sediments. All lithofacies that we identified in the Pokhara Formation have their source in the Annapurna massif (HHC). **B)** The former model suggested that the Pokhara Formation interfingered with lacustrine sediments (Fort, 1987). **C)** Downstream trends of the length of tributary channels invaded by the Pokhara Formation, and the width of the Pokhara fan along the Seti Khola. The wider the fan, the less HHC sediments invaded tributaries, except at bedrock constrictions near Anpu, Pudi and Saraudi Khola (Fig. 3.1).

Our XRF data also reveal previously unreported breaks in the deposition of the Pokhara Formation, supporting the idea of individual sediment pulses, and possibly explaining why sand layers and local debris-flow deposits of LHS provenance alternate with slackwater

deposits of HHC provenance (Fig. 3.6). The spatial and temporal clustering of our ^{14}C dates in Anpu Khola highlights at least two major phases of sedimentation at around 1100 and 1255 AD (Figs. 3.1 and 3.7). Elsewhere, however, our extended ^{14}C chronology shows that younger silts and muds that had infilled former channels are below stratigraphically older ones (Fig. 3.7). This re-filling of channels could have occurred between individual sediment pulses: at Anpu and Phusre Khola channels migrated and backfilled between the first and second pulse, whereas at Bijaypur Khola it happened between the second and third pulses. Our ^{14}C dates of slackwater deposits (F3) onlap onto the conglomerates (F2 and F3) and likewise record rapid infilling of a former channel network. Hence, tributaries must have incised between the sediment pulses to form canyons with cut-and-fill terraces into F2 deposits, which slackwater deposits (F3) then backfilled during the next sedimentation pulse. Erosional contacts and channel fills are common on the upper fan, confirming that channels avulsed frequently. The spatial pattern of ^{14}C dates across the fan and the XRF data are key to distinguishing the individual sediment pulses, as these are not evident from their sedimentology alone. We did not find any buried soils that could have formed during the depositional gaps. Intervals of 100-150 years between major earthquake-triggered sediment pulses may have been too short to allow recognizably thick soils to form, especially on fresh, coarse-grained alluvial-fan surfaces prone to continuous reworking by shifting channels and heavy seasonal rainfall. Detached organic material from nearby hillslopes would also be hardly sufficient to cover the whole fan surface to aid soil formation (Fig. 3.1).

3.6.2. Catastrophic valley fills and medieval Himalayan earthquakes

The geomorphic legacy of multiple earthquake-driven sedimentation pulses at Pokhara appears rare, if not unique, in the Himalayas in that long-runout debris flows from a High Himalayan source coevally invaded and plugged several tributaries in the Lesser Himalayas several tens of kilometers downstream. Valley fills of similar size and history are yet to be found in the Himalayas, let alone potential landslide deposits that could deliver sufficient volumes of sediment. Studies of earthquake-triggered slope failures (Keefer, 2002; Kargel et al., 2016) report several spatial patterns of landslides, local seismic ground motion and distance from the fault rupture. Such detailed characteristics remain obscure for large medieval earthquakes and complicate the search for suitable paleoseismological proxies. Neighboring valleys from Pokhara such as the Kali Gandaki, Madi Khola, Modi Khola

or Marsyandi Khola do feature debris terraces several tens of meters thick (Yamanaka et al., 1982; Fort, 2000; Pratt-Sitaula et al., 2004), but nowhere do these form any major intermontane fan comparable to that around Pokhara. Yet ^{14}C dates from debris-flow deposits in the Modi Khola west of Pokhara are similarly young (recalibrated to 777-1242 AD) and might be coeval with the first sediment pulse of the Pokhara Formation (Yamanaka et al., 1982). Similar deposits in Madi Khola, east of Pokhara, formed between 3176 and 2513 cal yr BP (Yamanaka et al., 1982). However, most dated valley fills around the Annapurna Massif are much older, such as debris terraces of a massive landslide deposit from the HHC dated to 5300-4420 cal yr BP (recalibrated 95% HDI) in the Marsyandi River (Yamanaka et al., 1982); the higher fill terraces are of HHC-derived angular matrix-supported conglomerates, and subrounded, partially clast-supported conglomerates are Pleistocene in age (Pratt-Sitaula et al., 2004). Whether these valley fills are connected to large earthquakes remains to be tested, although the massive beds and fine grained material indicating rapid sedimentation followed by fluvial reworking (Pratt-Sitaula et al., 2004) suggest sediment phases similar to those in the Pokhara basin.

In any case, our ^{14}C chronology of the Pokhara Formation allows us to independently test and augment paleoseismologic data from trenches and offset landforms. Historic documents mention a cluster of damaging earthquakes between 1255 and 1344 AD (Rajendran et al., 2015), but the epicenters, rupture lengths, and affected shaking areas of these large medieval earthquakes remain disputed (Fig. 3.11) (Mugnier et al., 2013; Bollinger et al., 2016). Our radiocarbon dates of the Pokhara Formation might help to refine areas of significant ground motion, if not rupture lengths, for great Himalayan earthquakes in ∼1100, 1255, and 1344 AD, assuming that strong ground shaking was necessary to trigger either massive rock-slope failure or natural dam bursts in Sabche Cirque to release long-runout debris flows into the Pokhara basin (Schwanghart et al., 2016). The timing of fault ruptures inferred from offset fluvial beds and colluvial wedges in trenches and outcrops (Sir Khola, Fig. 3.11) (Rajendran et al., 2015)closely correlates with the timing of the first two sediment pulses that we dated in the Pokhara Valley. The notion of a great earthquake in ~1100 AD has so far only been grounded on data from several trenches east of Kathmandu (Lavé et al., 2005), so that this postulated rupture could be have been mistaken instead with the 1255 AD earthquake (Rajendran et al., 2015); the broad range of recalibrated radiocarbon dates of 700-1270 AD complicates this issue (Lavé et al., 2005; Sapkota et al., 2013; Bollinger et al., 2014; Rajendran et al., 2015). The 1255 AD earthquake is historic

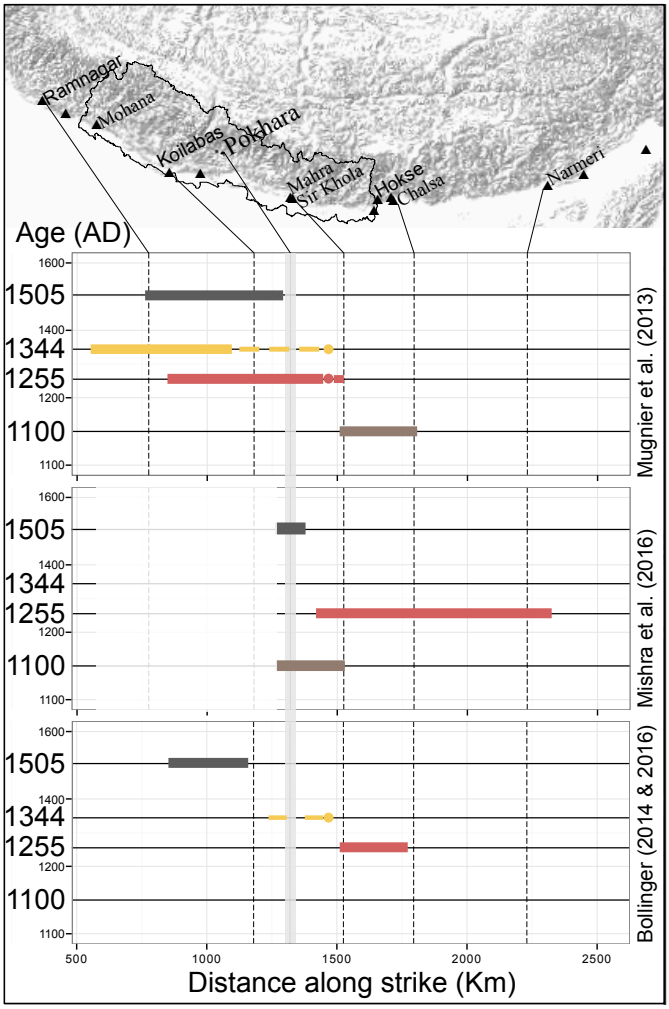

Figure 3.11.: Summary and review of surface displacements along the Himalayan front. Surface displacements of four historic earthquakes (1100, 1255, 1344, and 1505 AD) inferred from fault trenches along the Himalayan front, Nepal. Horizontal scale is the distance along the Himalayan arc. Horizontal bars are estimated rupture lengths; vertical gray bar delimits Pokhara basin. Dated earthquakes in more nearby trenches would have affected the Pokhara Valley more strongly. Adapted from (Mugnier et al., 2013; Bollinger et al., 2014; Mishra et al., 2016).

and may have ruptured the surface in central and western Nepal, possibly forming seismites in Kumaon, India (Fig. 3.11) (Mugnier et al., 2013). Apart from local dewatering structures and load casts we did not find any traces of seismites in the Pokhara Formation. Finally, the 1344 AD earthquake is recorded in trenches in Kathmandu and may have ruptured the surface as far away as Kumaon as well (∼500 km), with an estimated magnitude of ≥8.6 (Mugnier et al., 2013). According to our results, this earthquake deposited the smallest volume of sediment in the Pokhara basin. We caution against correlating the inferred volumes of the medieval sediment pulses with local shaking intensities, and recommend more detailed slope stability and dam-break studies to pin down the mechanistic

plausibility of large rockslides or outburst floods as the sources of the Pokhara Formation.

3.7. Conclusion

Detailed sedimentary logs, new ^{14}C ages, and X-ray fluorescence spectrometry support the hypothesis of at least three earthquake related sediment pulses originating in the Higher Himalayan Annapurna massif, leading to massive and widespread sedimentation up to 70 km downstream (Schwanghart et al., 2016). Our sedimentological work is the first systematic enquiry of its kind into the Pokhara Formation, and highlights four different lithofacies that connect to massive aggradation pulses affecting large parts of the Pokhara fan. Radiocarbon dates from widely scattered locations cluster conspicuously to a short medieval period and establish that these pulses are largely coincident with the documented dates of three great Himalayan earthquakes. The Pokhara region has seen several catastrophic disturbances in its recent geological past, resulting in the largest, youngest, and most extensively dated sedimentary record of earthquake-triggered valley infill found in the Himalayas so far. We add new insights into the Pokhara Formation and its relation to former large earthquakes by constraining the spatial and temporal relationship of 37 ^{14}C ages (Table 3.3) that corroborate previous hypotheses of rapid sedimentation and their connection to three historic strong earthquakes. Our ^{14}C dates demonstrate the use of valley fills to constrain and complement the catalogue of past Himalayan earthquakes. The four distinct lithofacies offer key diagnostics of this catastrophic sedimentation, fining from the fan axis toward the Seti Khola's tributary mouths and sandy to silty slackwater deposits in their lower reaches. New XRF and geochemical data highlight layers of local LHS-derived material indicating that HHC sediment invaded the tributaries in several turns. The radiocarbon dates of the first sediment pulse offer independently support paleoseismological data for a great earthquake in 1100 AD, which has so far been inferred exclusively from fault trenches. The 1255 AD earthquake likely triggered the largest sediment pulse reaching the southern tip of the Pokhara Formation. Deposits of comparable size and history are yet to be found in the Himalayan region, or active mountain belts elsewhere.

3.8. Acknowledgments

This work was supported by the German Research Foundation (KO 3937/9-1); and the Potsdam Research Cluster for Georisk Analysis (PROGRESS). Alpine Consultancy Pvt. Ltd. Nepal, and the Department of Survey, Nepal, provided digital topographic data. T. Cohen, J. Jansen, M. Roschlaub, E. Schönfeldt, J. Seidemann, G. Veh, and J.T. Weidinger helped with fieldwork and contributed to many fruitful discussions. We used the free R programming environment for computing most of the statistics, and in particular the ggdendro library (de Vries and Ripley, 2016).

4

Protracted fluvial recovery from medieval earthquakes

Submitted as: Stolle, A., Schwanghart, W., Andermann, C., Bernhardt, A., Fort, M., Jansen, D.J., Wittmann, H., Merchel, S., Rugel, S., Adhikari, B., Korup, O., Protracted fluvial recovery from medieval earthquakes. Earth Surface Landforms and Processes, February 2018.

4.1. Abstract

Mountain rivers respond to strong earthquakes by rapidly aggrading to accommodate excess sediment delivered by co-seismic landslides. Detailed sediment budgets indicate that rivers need several years to decades to recover from seismic disturbances, depending on how recovery is defined. We examine three principal criteria or proxies of river recovery around Pokhara, Nepal's second largest city. We use a freshly exhumed cohort of floodplain trees in growth position as a marker of rapid sedimentation that formed a fan covering 150 km^2 in a Lesser Himalayan basin with tens of metres of debris. Radiocarbon dates of buried trees are consistent with those of nearby valley deposits linked to major medieval earthquakes, such that we can estimate average rates of sedimentation and re-incision since. We combine high-resolution digital elevation data, geodetic field surveys, aerial photos, and dated tree trunks to reconstruct geomorphic marker surfaces. The volumes of sediment relative to these surfaces require average net sediment yields of up to 4200 t km^2 yr^1 for the 650 years since the last inferred earthquake. The lithological composition of channel-bed load differs from that of local bedrock, confirming that rivers are still mostly evacuating medieval valley fills, locally incising at rates of up to 0.2 m yr^1. Pronounced knickpoints and epigenetic gorges at tributary junctions further illustrate the protracted fluvial response; only the distal portions of the earthquake-derived sediment wedges have been cut to near

their base. Our results challenge the notion that mountain rivers recover speedily from earthquakes within years to decades. The valley fills around Pokhara show that even highly erosive and dynamic Himalayan rivers may need more than several centuries to adjust to catastrophic perturbations. Our results motivate some rethinking of post-seismic hazard appraisals and infrastructural planning in active mountain regions.

Keywords: Fluvial recovery, sediment yield, earthquakes, Nepal, Himalaya

4.2. Introduction

Understanding how mountain rivers and landscapes respond to earthquakes is indispensable for managing water and sediment fluxes, planning mitigation and remediation measures, and safeguarding the livelihoods of people. Earthquakes can mobilize large volumes of landslide debris that enters and disturbs mountain rivers (Keefer, 1994). How long this excess sediment lingers in the landscape remains debated (Blöthe and Korup, 2013). A growing number of detailed sediment budgets suggest variable residence times of earthquake-produced debris in rivers, ranging from a few years (Pain and Bowler, 1973; Lin et al., 2008b; Hovius et al., 2011) to several decades (Koi et al., 2008; Howarth et al., 2012; Bolla Pittaluga et al., 2014; Uchida et al., 2014). Sediment yields can be as high $>10^5$ t km^{-2} yr^{-1} in the first years following seismic disturbance (Pain and Bowler, 1973; Korup, 2012; Marc et al., 2016), forcing channels to aggrade by tens of metres in places (Chen, 2009). Suspended sediment yields after the 1999 Chi-Chi earthquake, Taiwan, were roughly four times higher than before the earthquake, but fell back to this former level after about six years (Yanites et al., 2010). Similarly, rivers impacted by landslides from the 1970 M_w 7.0 Madang earthquake, Papua New Guinea, flushed out most of the excess debris within a few years (Pain and Bowler, 1973). In contrast, 80% of coseismic landslide debris from the 2004 M_w 6.8 Mid-Niigata earthquake, Japan, still remained in a catchment after several years despite high yields of $\sim$4 x 10^4 t km^{-2} yr^{-1} (Matsuoka et al., 2008). And similarly, contemporary sediment yields remain elevated in many small mountain rivers as a consequence of the 1923 Kanto earthquake (Koi et al., 2008).

Clearly, mitigating such river dynamics requires that we objectively detect and measure fluvial response and recovery. Common metrics include changes and adjustments, in channel geometry, such as planform and bed-elevation (Simon, 1992; Chen, 2009), and changes in suspended sediment loads (Lin et al., 2008b,a). Several studies have charac-

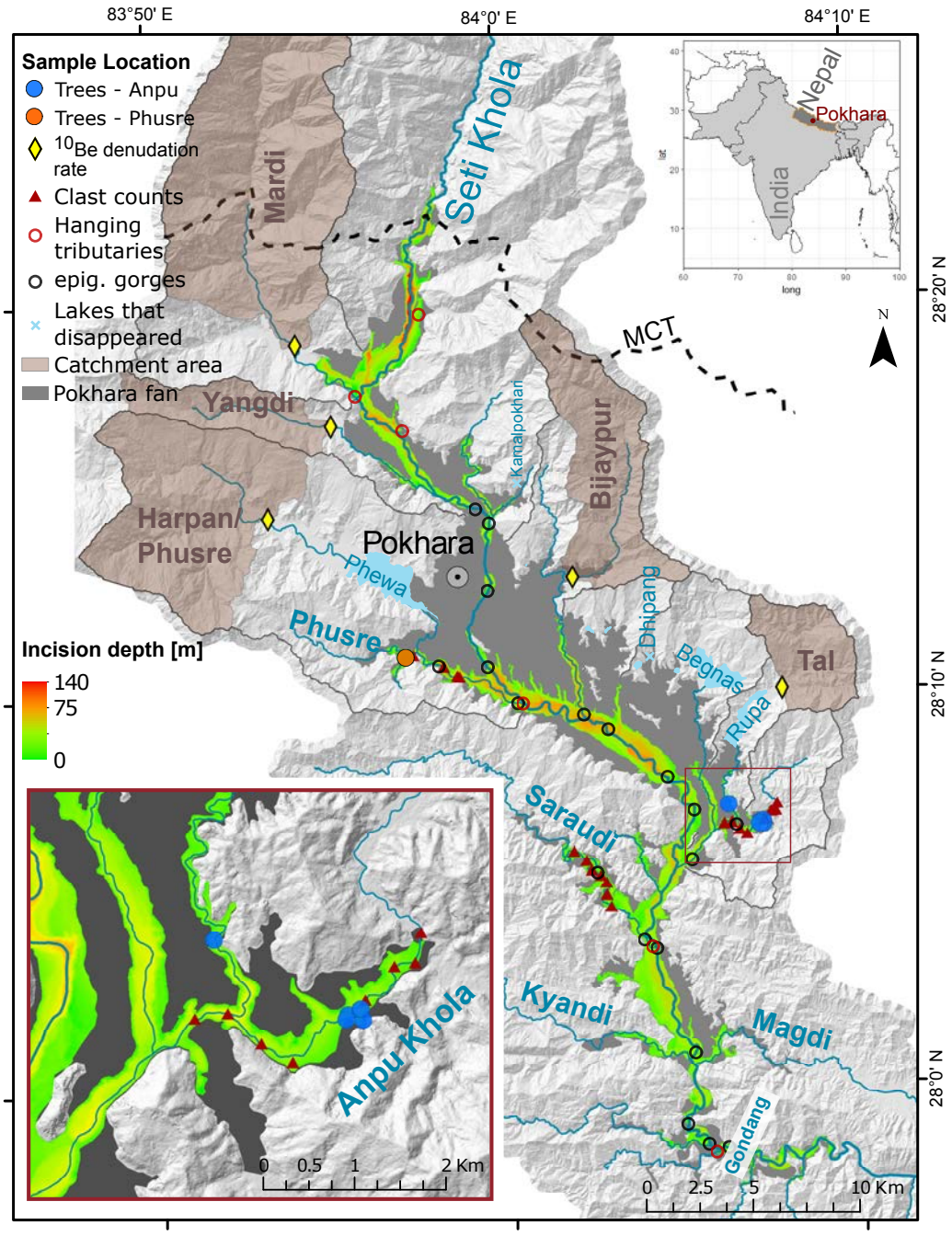

Figure 4.1.: Overview map of the Pokhara Valley and the Lesser Himalaya of central Nepal drained by the Seti Khola. Inset shows geomorphic setting and the sample sites in the Anpu Khola tributary.

terised fluvial response in terms of changing bed load (sediment slugs; e.g. Dunne and Aalto (2013)), changing sediment budgets (Huang and Montgomery, 2012), migrating and disappearing knickpoints (Liu and Yang, 2015; Olen et al., 2015), cosmogenic nuclide abundance in river sediments (West et al., 2014; Wang et al., 2017), and with numerical models (Croissant et al., 2017). Compound measures such as river sensitivity use the ratio

of recurrence interval to relaxation or recovery time (Brundsen and Thornes, 1979; Downs and Gregory, 2004; Fryirs, 2017). All these metrics require a known reference state before the earthquake, say channel geometry or sediment load. Recovery then expresses the time needed to regain, at least within an arbitrarily specified range, this presumably undisturbed reference state. Whether a given choice of multiple metrics of river response or recovery is consistent remains debatable; for example, sediment loads may have recovered, whereas channel geometry may have not.

Here, we wish to shed more light on this issue. Our aim is to investigate several criteria or proxies of river recovery from catastrophic sediment pulses triggered by large medieval earthquakes in the Nepal Himalaya. Specifically, we use the age, elevation, and locations of a cohort of dead trees encased in valley-fill deposits, offering dateable markers of fluvial aggradation. We also estimate fluvial recovery using sediment provenance, sediment yields from volumetric calculations, and river longitudinal profiles derived from high resolution digital elevation models (DEMs) (Figs. 4.1, 4.2). Finally, we reflect upon whether and how consistently these different criteria represent fluvial recovery.

4.3. Study Area

The Nepal Himalayas formed by active collision of the Indian and Eurasian tectonic plates from about 50 Ma (Hodges et al., 1996), and maintains high rock uplift rates (Grandin et al., 2012) combined with strong earthquakes (Hasegawa et al., 2009) and rapid erosion (Burbank et al., 2003; Parsons et al., 2015), particularly in our study area of the Pokhara Valley, south of the Annapurna Massif (Fig.4.1). These high peaks comprise the Tethyan Sedimentary Series (TSS) dominated by marine calcareous meta-sediments and limestones (Pêcher, 1991) and the High Himalayan Crystalline Sequence (HHC) (Colchen et al., 1981; Pêcher, 1991; Martin et al., 2005) - here we refer to these two groups as High Himalayan (HH). The Annapurna Massif is drained by the Seti Khola ("Khola" = river in Nepali) with a catchment area of $\sim$1400 km^2. The river descends from Sabche Cirque in the High Himalayas and traverses the Main Central Thrust (MCT) to the Pokhara Valley in the Lesser Himalaya (Martin et al., 2005; Fort, 2010). Estimated denudation rates in the High Himalayan zone are between 2.0 and 2.7 mm yr^{-1}, and 0.1 to 0.8 mm yr^{-1} in the Lesser Himalaya (Robert et al., 2009; Godard et al., 2014). Cosmogenic nuclide abundance and

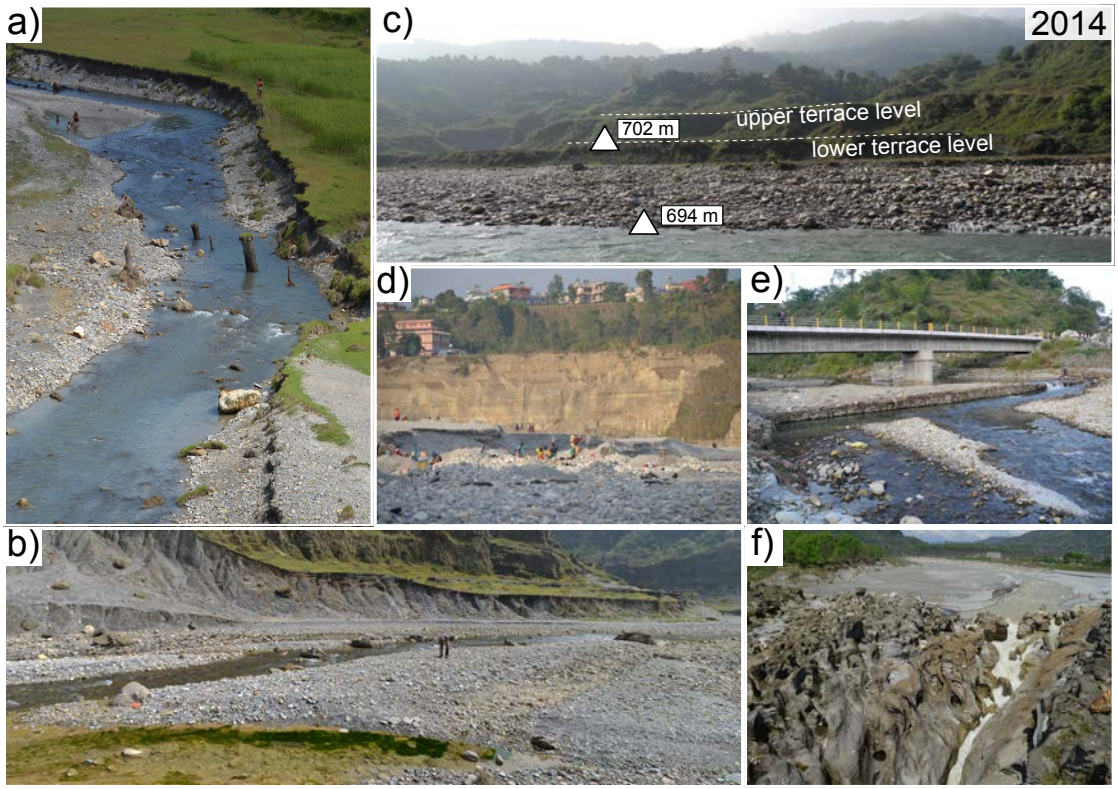

Figure 4.2.: Field photographs illustrating the proxies of river recovery used in this study. a) Exhumed tree trunks in growth position. Calibrated ^{14}C dates from 1188 to 1265 cal AD (95% highest density intervals, HDI), indicate that this tree cohort was killed by rapid aggradation within a few years to decades. **b)** Clast counts on active channel bars, Anpu Khola. **c)** Historic channel changes along Phusre Khola. We used newly the formed terrace level between 1967 and 2014 to calculate incision rates (∼0.16 m yr^1) over the past 50 years. **d)** Terraces along the Seti Khola at Ramghat, Pokhara city; note active river mining. **e)** Rip-rap for erosion control and undercutting prevention, Phusre Khola. **f)** Gorge incising older, indurated valley fill (Ghachok Formation) along the Seti Khola downstream of the tributary confluence forming pronounced knickpoints, Saraudi Khola.

suspended sediment yields in major rivers leaving the mountain range indicate basin-wide erosion rates of 1-2 mm yr^{-1} (Lupker et al., 2012; Andermann et al., 2012).

Pokhara Valley features some of the steepest topographic relief in the Himalayas (Fig. 4.1). The headwaters of the Seti Khola rise ∼7 km over ∼20 km of horizontal distance to the Annapurna peaks, though much of the tributary network drains the Lesser Himalaya, bound to the south by the Main Boundary Thrust (Parsons et al., 2015). South of the MCT, the Pokhara Valley hosts extensive fan sediments of the Pokhara Formation (Yamanaka, 1982; Fort, 1987), estimated at a volume of 5-7 km^3 and covering ∼150 km^2 over a distance of 70 km at elevations from 400 to 1350 m asl. This fan sustains much of Pokhara, Nepal's second largest city (Fig. 4.1). North of the valley, the Pokhara Formation lies inset within the Ghachok Formation, an older indurated valley fill, whereas from

Pokhara city southward, the Pokhara Formation onlaps the Ghachok Formation. The dissected fan surface comprises gravelly cut-and-fill terraces interrupted by short, narrow and steep bedrock gorges. A radiocarbon chronology of 47 samples documents rapid sedimentation following three medieval earthquakes dated to ∼1100, 1255 and 1344 AD (Schwanghart et al., 2016; Stolle et al., 2017). Lakes stand at several tributary margins along the Pokhara fan (Fig. 4.1) damming by these sediment pulses and possibly older events (Yamanaka et al., 1982).

4.4. Methods

We sampled eight tree trunks from cohorts exposed by active channel erosion along the Phusre and Anpu Khola (Fig. 4.1 and 4.2a), small tributaries of the Seti Khola at the fringes of the Pokhara fan. All trees were encased in gravelly valley-fill sediments in growth position at different elevations. We sampled the outermost layer of the trees to ensure that we obtained the youngest material for ^{14}C dating. In total, we identified at least a dozen trees sticking out of floodplain deposits and channel banks. We calibrated the radiocarbon ages of the tree trunks using a Bayesian approach in the OxCal 4.2 software with the IntCal13 (Reimer, 2013) calibration curve. We encoded the stratigraphic relationship of the trees in a prior distribution, thus eliminating from the posterior age distributions the effects of plateaus in the radiocarbon calibration curve. We also tested other prior distributions assuming different phases of aggradation, but found only slight differences in the resulting posterior age distributions (Schwanghart et al., 2016). Without detailed data on the local sedimentation rates, we used a uniform-one-phase model as the simplest approach (Stolle et al., 2017).

To establish independent denudation rates from the Lesser Himalayan terrain draining the Seti Khola, we collected samples of quartz-rich channel bed-load from five tributary catchments for in situ-cosmogenic nuclide analysis. We sampled upstream of the Pokhara fan margins to exclude actively eroding valley fill, and to minimize the effects of human disturbance (Fig. 4.1). We detail the processing and measurement of these samples in the supplemental information. Our set of basin-wide denudation rates is augmented by those from previous work (Godard et al., 2014; Kim et al., 2017).

Our first criterion of fluvial response is the modern bedload fraction derived from reworked valley fill versus local, Lesser Himalayan sources. To this end, we surveyed bed material

in the active channels cut into the Pokhara Formation (Fig. 4.2b) following Brierley and Hickin (1985), a modified version of Wolman (1954) method. Along each of the Anpu, Phusre, and Saraudi Khola we identified mid-channel bars and recorded the intermediate axis and lithology of 100 clasts ≥8 mm at 0.5 m intervals. We ascribed the lithologies to either Higher Himalayan (HH) or LHS provenance according to the geological map of the Pokhara Valley (Koirala et al., 1998) and our own provenance analyses based on X-ray fluorescence spectrometry, which distinguishes the HH signature in the Pokhara Formation from the local LHS sources (Schwanghart et al., 2016; Stolle et al., 2017). The proportions of upstream catchment area underlain by these major lithologies should roughly indicate their commensurate mixture in channel-bed sediments under transport-limited and equilibrated conditions. We cannot exclude the influence of different transport distances on clast comminution, though the short tributary lengths and similar grain size distributions imply a negligible effect. A two-sample Kolmogorov-Smirnov test rejects the hypothesis that the two lithologies have significantly ($\rho = 0.05$) different distributions at each site. We propose that the mixing ratio M_r expresses the mean relative deviation from a well-mixed sediment distribution:

$$M_r = \left(\int_{r_A=0}^{1} c_A(r_A) dr_A - 0.5 \right) / 0.5 x 100\%$$

where c_A is the proportion of non-local clasts, and r_A is the fraction of upstream area underlain by these non-local deposits. Here, M_r is 100% for a channel filled with non-local clasts immediately following their emplacement, and lower as locally derived bedload contributes. Negative values of M_r indicate that the fraction of non-local bed load clasts is smaller than their source area divided by the catchment area upstream (Fig. 4.3a).

We mapped channel changes in the Phusre Khola over the past decades, using 4-m resolution Corona aerial imagery from 1967, 15-m resolution LANDSAT imagery from 2013, and 2.5-m ALOS images from 2010. We identified historic cut-and-fill terraces (Fig. 4.2c) that we surveyed with dGPS in the field to constrain channel incision rates averaged over the past years to decades. We used three different DEMs to reconstruct former aggradation surfaces in the Pokhara Valley and to estimate the volume of material excavated by rivers as a function of DEM resolution. We chose the 5-m ALOS 3D enhanced DEM (AW3D), the 12.5-m Tandem-X DEM, and a 15-m DEM derived from topographic map contours. The fan surface is locally cut by gorges >45 m deep and 5-15 m wide that are poorly captured by the DEMs. We thus hydrologically corrected the data with TopoToolbox software

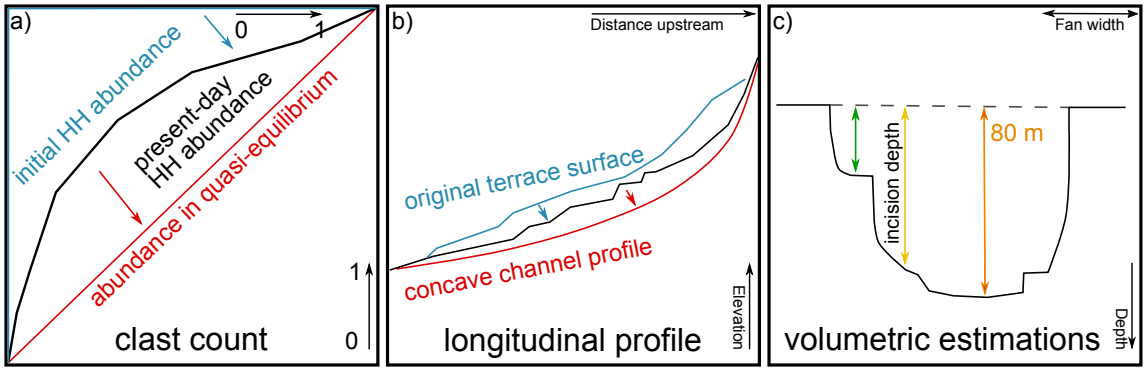

Figure 4.3.: Three approaches to quantify fluvial response and recovery according to **a)** clast surveys of modern bed load composition, **b)** longitudinal profiles, and **c)** volumetric estimates of sediment export since the catastrophic emplacement of Pokhara Formation (HH = Higher Himalayan) gravels in medieval times.

(Schwanghart and Scherler, 2014) and carved one-pixel wide channels. Most gorges are ≥5 m, judging from field and dGPS data, so that we defined the minimal carved stream widths to 15 m in the AW3D DEM.

The second criterion of river recovery from catastrophic disturbance concerns the volumes of sediment exported. We mapped the highest terrace levels and fan-surface elevations manually (1:10.000 scale) from a 2.5-m ALOS panchromatic image combined with maps of local slope and hillshade derived from the AW3D DEM (estimated standard error of 15 m). We then masked the contemporary network of gorges in the DEM with an edge detection algorithm to identify maximum variations in pixel intensities at the edges of the mask (Press, 2010; Hoeltgen et al., 2013). We assumed that all gorges post-dated the deposition of the Pokhara Formation. We used a Laplace interpolator to smoothly reconstruct the former aggradation surfaces for each dataset (DEM) using MATLAB's function `regionfill` (Mathworks, 2017). By subtracting the present topography from the reconstructed former, we estimated the amount of local incision and sediment volumes eroded by the river network (Fig. 4.3c). We computed sediment yields assuming bulk densities of 1.6-2.0 t m^{-3} (Phusre Khola, Fig. 4.1), and three age scenarios based on the published radiocarbon chronology (Stolle et al., 2017).

Our third criterion of river recovery is the adjustment of channel longitudinal profiles in the river network to their lower concave envelope. Rivers slicing through the Pokhara Formation contain several knickpoints and low-gradient sections (Fig. 4.3b), and we calculated their lower concave envelopes similar to a convex hull (Jarvis, 1973). The resulting geometry is similar to the lowermost shape enclosed by rubber bands stretched from the

basin outlet to each channel head of the river network. Based on this lower concave envelope of channel-bed elevations z_c, we estimated recovery as the ratio Z_r between the average vertical offsets between the actual river bed z and z_c and the average vertical offset between the aggraded surface z_a and z_c:

$$Z_r = \frac{(z - z_c)}{(z_a - z_c)} x100\%$$

We also mapped river knickpoints by fitting strictly concave upward profiles to the raw data. We then incrementally relaxed the concavity constraint where offsets between the raw and the concave profile were highest, thus dividing the profile into strictly concave sections punctuated by convex knickpoints. Recording the locations of the knickpoints, we recursively repeated this procedure until offsets were <20 m. We chose this arbitrary value to extract only major convexities in the longitudinal profile and to account for uncertainties of elevation errors in the data. This procedure is implemented in the function `knickpointfinder` in TopoToolbox (Schwanghart and Scherler, 2014). We used the knickpoints to calculate their χ-values m/n ratios ranging from 0.2 to 0.9 (Perron and Royden, 2013; Willet et al., 2014). This allows us to test whether the knickpoints have propagated upstream along the river network from a common origin. If so, knickpoints would cluster at one horizontal position in χ-space (Perron and Royden, 2013).

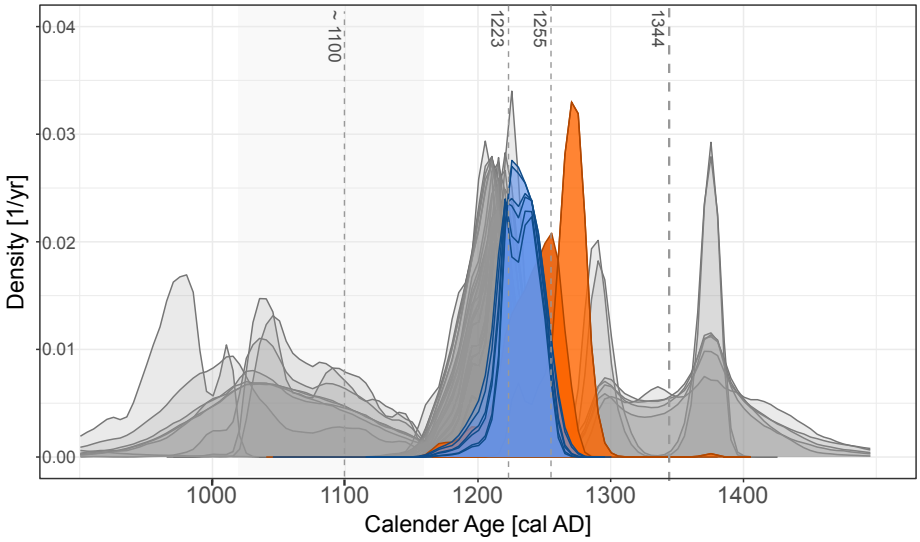

Figure 4.4.: Chronology of ^{14}C tree ages (posterior probability distributions) along the Anpu Khola, with all calibrated radiocarbon dates in the Pokhara Valley; blue and orange density curves refer to new tree samples in Anpu and Phusre Khola, respectively. Gray shaded densities are from Stolle et al. (2017). Our ^{14}C age is consistent with previous interpretations of multiple sediment pulses that filled the Pokhara Valley in the early 13^{th} century. Dashed lines indicate the timing of known medieval strong earthquakes.

4.5. Results

The radiocarbon results from eight dead trees in growth position in Phusre and Anpu Khola show that the trees died synchronously in the early 13^{th} century, but no later than ~1260 AD (Fig. 4.4, Table 4.1). The trees in our dataset located at lower elevations may have been killed slightly earlier than higher ones, but the error margins are close to the resolution of the method. The trees stand up to 18 km apart at the margin of the Pokhara fan and were all buried by up to 20-m in Pokhara Formation gravels. Clast-provenance work shows that this gravel comes mainly from the meta-limestones of the High Himalayan, with negligible local contributions (Fig. 4.5). Like all other tributaries of the Seti Khola around Pokhara, both the Phusre and Anpu Khola have incised up to 70 m into the Pokhara Formation, forming pronounced flights of terraces, and locally exposing trees in growth position (Fig. 4.2a). Many of the terraces episodically collapse in response to river undercutting (Fig. 4.2d). Extensive channel bars and local braiding channel planforms indicate that the river system is transport-limited with respect to the valley fill. This fill buffers most of the local hillslope debris (Fig. 4.2b) from the channels so that Higher Himalayan material makes up >80% of the contemporary bed load (Fig. 4.5).

Table 4.1.: Radiocarbon ages of formerly buried and re-exhumed tree trunks in Phusre and Anpu Khola

Lab.No	Sample ID	Location	Lat	Long	Elevation	Radiocarbon age	95% HDI [AD]	
			[ÂřN]	[ÂřE]	asl [m]	[BP]	From	To
Poz-87756	PhTree1	Phusre	28.183	83.953	725	810 ± 30	1190	1275
Poz-87757	PhTree2	Phusre	28.183	83.953	725	735 ± 30	1275	1290
Poz-87758	AnpuTrib	Anpu	28.118	84.105	587	835 ± 30	1190	1260
Poz-87759	AnpuTree1	Anpu	28.111	84.120	601	790 ± 30	1208	1265
Poz-87760	AnpuTree2	Anpu	28.110	84.122	608	795 ± 30	1206	1265
Poz-87761	AnpuTree3	Anpu	28.111	84.121	591	815 ± 30	1200	1262
Poz-87763	AnpuTree4	Anpu	28.111	84.121	591	845 ± 30	1188	1259
Poz-87764	AnpuTree5	Anpu	28.110	84.120	592	820 ± 30	1198	1261

Only the upper 12% of active river banks in the Anpu Khola incised into the Pokhara Formation show dominance of LHS over HH sources (Fig. 4.5). Several tributary catchments are still transporting mainly HH material in their lower, aggraded reaches (Fig.4.6), with high mixing ratios in the Anpu (72%) and Saraudi Khola (50%). One exception is the Phusre Khola, which trims the fan toe of the Pokhara Formation, and receives HH and LHS sediments from its left and right banks, respectively; local sources dominate the bedload in this tributary.

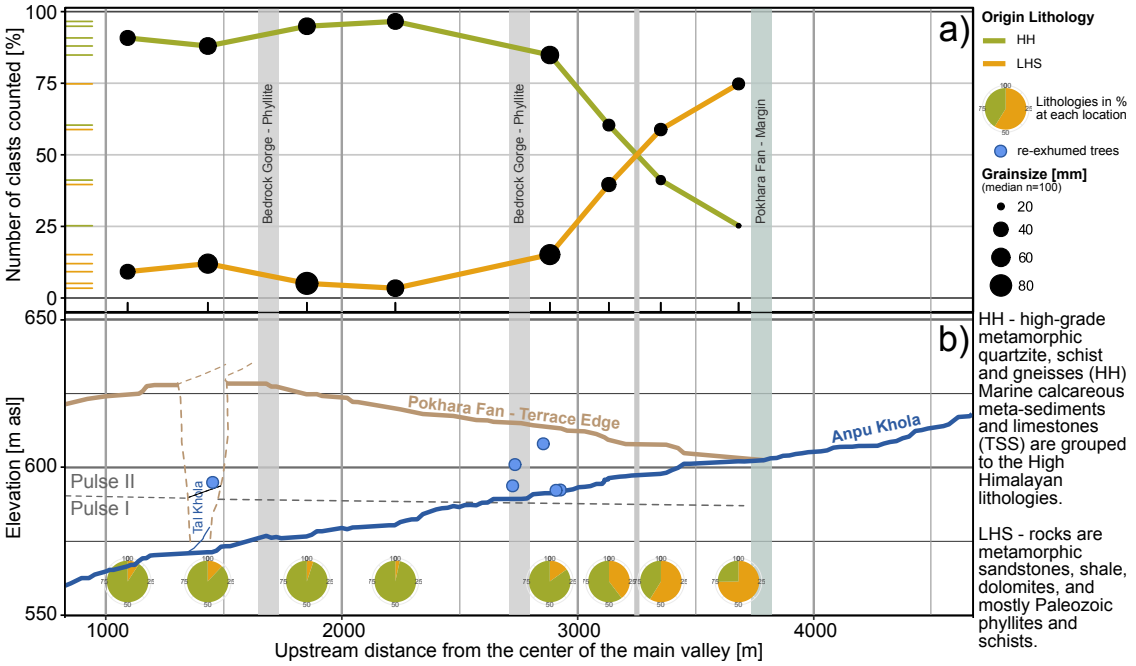

Figure 4.5.: Clast survey data along Anpu Khola. **a)** Black dots show median grain size for each site and lithology (n = 100 clast counts per site); lithologies are split into HH or LHS groups; green and orange colours refer to the number of HH and LHS clasts, respectively. **b)** Longitudinal profile of Anpu Khola with tree trunk positions (blue dots); fan surface and terrace level along the active channel is shown in brown; positions of the clast-count sites with estimated % of lithologies are given as in a).

We estimate from historical air photos and dGPS field surveys that average incision was 0.16-0.22 m yr^1 in the past 50 years (Fig. 4.2c, Phusre Khola), and up to ~0.12 m yr^1 since catastrophic aggradation commenced in the early 13^{th} century. Our morphometric analysis of terraces cut into the Pokhara Formation valley fill indicates that depending on the DEM, some 1.7 ± 0.2 km^3 of sediment was eroded by rivers, fuelling yields of up to 4200 t km^2 yr^1 at the fan toe (Table B.1). Based on previous estimates (Stolle et al., 2017) of a total emplaced volume of 5-7 km^3, we infer that 34 ± 5% of the sediment volume has been exported since deposition. The corresponding mean volumetric erosion rate over the entire catchment is 0.1 to 2.2 mm yr^1 (Fig. 4.2d); when measured at individual tributary mouths along the Seti Khola, this rate increases downstream from 1.1 to 2.3 mm yr^1 (Table B.1). Similarly, the rates for tributary catchment areas also decrease downstream, though slightly more pronounced (Fig.4.7).

Longitudinal profiles of the Seti Khola and its northern tributaries highlight contrasting channel-bed elevations consistent with ongoing adjustment to catastrophic trunk-stream aggradation (Figs. 4.7, 4.8). Knickpoints are prolific close to the Seti confluence and are tied to steep and narrow bedrock and gorges cut into the older Ghachok Formation

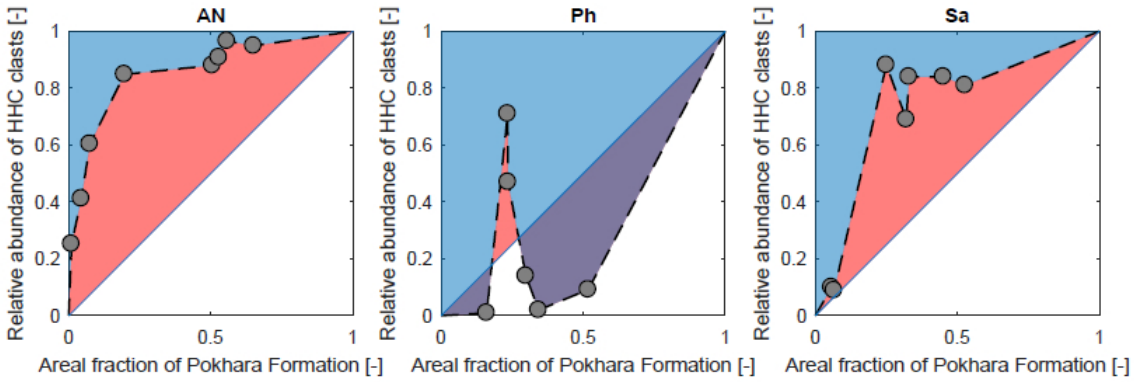

Figure 4.6.: Clast survey data used to estimate the proportion of lithologies exposed in river banks. tBlue colour shows initial HH abundance; red colour shows the present day HH abundance to reach perfect mixture; purple colour shows abundance of LHS material. AN – Anpu Khola, Ph – Phusre Khola, Sa – Saraudi Khola.

(Fig. 4.2f). We identified 16 major (Fig. 4.9) and 11 minor knickpoints, mostly clustered 30-50 m above the Seti channel bed (Fig. 4.8b). Knickpoints abound where the Pokhara fan is widest, and where the volumetric erosion rates increase most sharply downstream. The fan surface has a characteristic convex cross section (Fig. 4.8a) at this location, and it narrows further downstream where the Pokhara Formation was more actively ramped into tributary catchments. The longitudinal profile together with the original fan surface and a fitted theoretical concave channel profile indicates that the rivers have adjusted by 70% from the catastrophic sediment input (Fig. 4.9). Knickpoints are widely scattered in χ-space so that the river profiles do not adjust to a single base-level change that propagates upstream. Field observations show that many knickpoints are lithologically controlled where rivers cut through bedrock or the indurated Ghachok Formation.

4.6. Discussion

What do our data on channel geometry, sediment yields, and clast provenance reveal about the state of the response of Seti Khola and its tributaries to catastrophic aggradation in medieval times? The geomorphology of the fan, and especially the many lakes or dried lake basins at its fringe, allows some further insights into the overall fluvial response. The origin of the tributary-mouth lakes remains undated, hence firm connection with the medieval sediment pulses awaits future work. In any case, the existence of these lakes attests to the protracted fluvial response to extreme depositional events in the recent geological past. Phewa Lake might have been dammed by HH gravel during the Pleistocene (Fort and

Freytet, 1982; Yamanaka et al., 1982), while two superimposed dams formed between 1100 and 600 BP (Yamanaka et al., 1982). Sediment influx to the lake during the monsoon season is estimated at up to 21-547 t d^{-1} (Ross and Gilbert, 1999), and cores in the proximal delta area indicate sedimentation rates of up to 23.5 mm yr^{-1}. The delta front advances by up to 1 m annually (Ross and Gilbert, 1999). Sedimentation rates of the smaller and shallower Begnas and Rupa lakes are even higher (Rai, 2000).

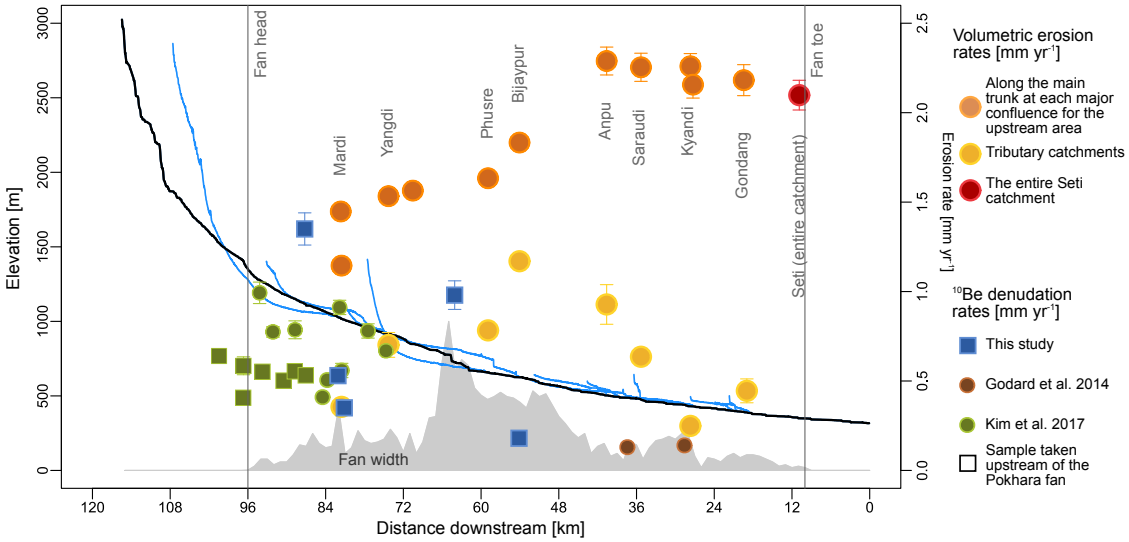

Figure 4.7.: Erosion rates derived by different methods in the Seti Khola catchment. Erosion rates largely fed by reworking of medieval valley fills (orange); error bars are in some cases smaller than circles; transparent ^{10}Be symbols are samples along the trunk stream and squares are samples upstream of Pokhara fan; all other samples (circle) are from within the fan. Longitudinal profile of the Seti Khola (black) and its tributaries (light blue) with volumetric erosion rates calculated for the upstream area at each confluence (orange) of Seti Khola and for each tributary catchment (yellow). Cosmogenic ^{10}Be derived denudation rates in tributary catchments upstream of the fan margin (square) and within the fan system (circle); ^{10}Be denudation rates from this study are in blue, published values from Godard et al. (2014) and Kim et al. (2017) are in green and brown, respectively.

Our volumetric rate estimates depend on robust dating of the geomorphic surfaces that we reconstructed. We do not account for active river mining at many locations in the Seti Khola; hence, from this perspective, our sediment yield estimates are upper bounds. These yields rest on calibrated radiocarbon dates and integrate over seven to eight centuries. We point out that our new radiocarbon ages and their geomorphic setting are consistent with the recently proposed chronology of medieval catastrophic aggradation in the Pokhara Valley (Yamanaka, 1982; Fort, 1987; Schwanghart et al., 2016; Stolle et al., 2017) and pave the way for quantifying the aftermath. The volumetric erosion rates increase downstream along the Seti Khola, and reflect the growing contributing catchment area and possibly water discharge (Fig. 4.7, Table B.1). For this period, the net sediment yields

are extremely high and comparable to those estimated from single point sources such as breached rockslide dams (Fig. 4.10). Our results show that the contemporary sediment yield from the Pokhara area is dominated by reworking of the medieval valley at rates that nominally outweigh estimates of millennial-scale denudation rates (Vance et al., 2003; Herman et al., 2010) in surrounding Lesser Himalayan catchments (Godard et al., 2014). Abundance of cosmogenic ^{10}Be in river sands at some 30 locations (Table 4.2); 5 new measurements plus published data of (Godard et al., 2014) and Kim et al. (2017) in the Seti Khola drainage have integration timescales of 500 to 1750 years. Some of the scatter in these timescales (Fig. 4.7) might come from river mixing of low ^{10}Be abundances from the rapidly eroding High Himalayan and greater ^{10}Be abundances from local sources. In any case, the ^{10}Be concentrations reveal that rivers also carry material nominally older than the Pokhara Formation even in reaches that still cut through it.

Table 4.2.: Catchment-wide denudation rates derived from concentrations of cosmogenic ^{10}Be in river sands.

Sample ID	Location	Lat	Long	Mean Cat.	Shield	[Be^{-10}]	P Spallogenica	P fMuonsa	P sMuonsa	erosion rate	Integration
		[°N]	[°E]	Elev. (m)	%	at g^{-1}	at g^{-1} yr^{-1}	at g^{-1} yr^{-1}	at g^{-1} yr^{-1}	[mm yr^{-1}]	time scale [yr]
CNP12_6	Mardi	28.316	83.904	2296	0.870	9710±667.03	16.311	0.034	0.077	1.12±0.08	541
CNP12_7	Yangdi	28.282	83.920	1416	0.902	12550±748.43	8.268	0.023	0.053	0.45±0.03	1336
CNP12_8	Bijaypur	28.216	84.034	1368	0.909	6730±566.80	8.309	0.023	0.053	0.85±0.07	714
CNP12_9	Tal	28.167	84.132	929	0.914	26300±1182.46	5.858	0.019	0.043	0.16±0.01	3876
CNP12_10	Harpan	28.243	83.889	1400	0.925	18770±938.23	8.476	0.024	0.054	0.31±0.02	1949

a P are already corrected for topographic shielding.

The downstream trend in volumetric erosion rates of the Pokhara fan is partly mirrored in the longitudinal profile of the Seti Khola and its tributaries. The drainage network has several large knickpoints (Fig. 4.8), although the DEMs fail to resolve several deeply cut gorges. Channel-bed elevations differ widely along upstream reaches, consistent with the notion of ongoing adjustment to trunk-stream aggradation (Fig. 4.1, around Pokhara city). Further downstream, several tributary mouths have knickpoints where they are blocked by Pokhara gravels (Fig. 4.7). These knickpoints may reflect the faster pace of downcutting of the Seti Khola compared to its tributaries (Crosby et al., 2007; Goode and Burbank, 2009). In some cases, the knickpoints are epigenetic gorges (Fig. 4.1) cut through older, indurated valley fills (Fig. 4.2f) or Lesser Himalayan bedrock. Rapid aggradation of the valley occasionally pushed rivers laterally away from their former courses, making them to incise into lower bedrock hillslopes (Ouimet et al., 2009). Incision rates at a 42-m high epigenetic gorge in Saraudi Khola might be >60 mm yr^{-1} since emplacement of the Pokhara gravels. Yet the knickpoints that we identified are randomly distributed with

no clear signs of a common base-level trigger (Fig. 4.9). Either tributaries were unable to keep pace with the more rapidly incising Seti Khola (Goode and Burbank, 2009), or knickpoints stall at epigenetic gorges cut in more resistant substrate (Phillips and Lutz, 2008). We infer that knickpoint distributions should be viewed with caution when it comes to gauging fluvial recovery times.

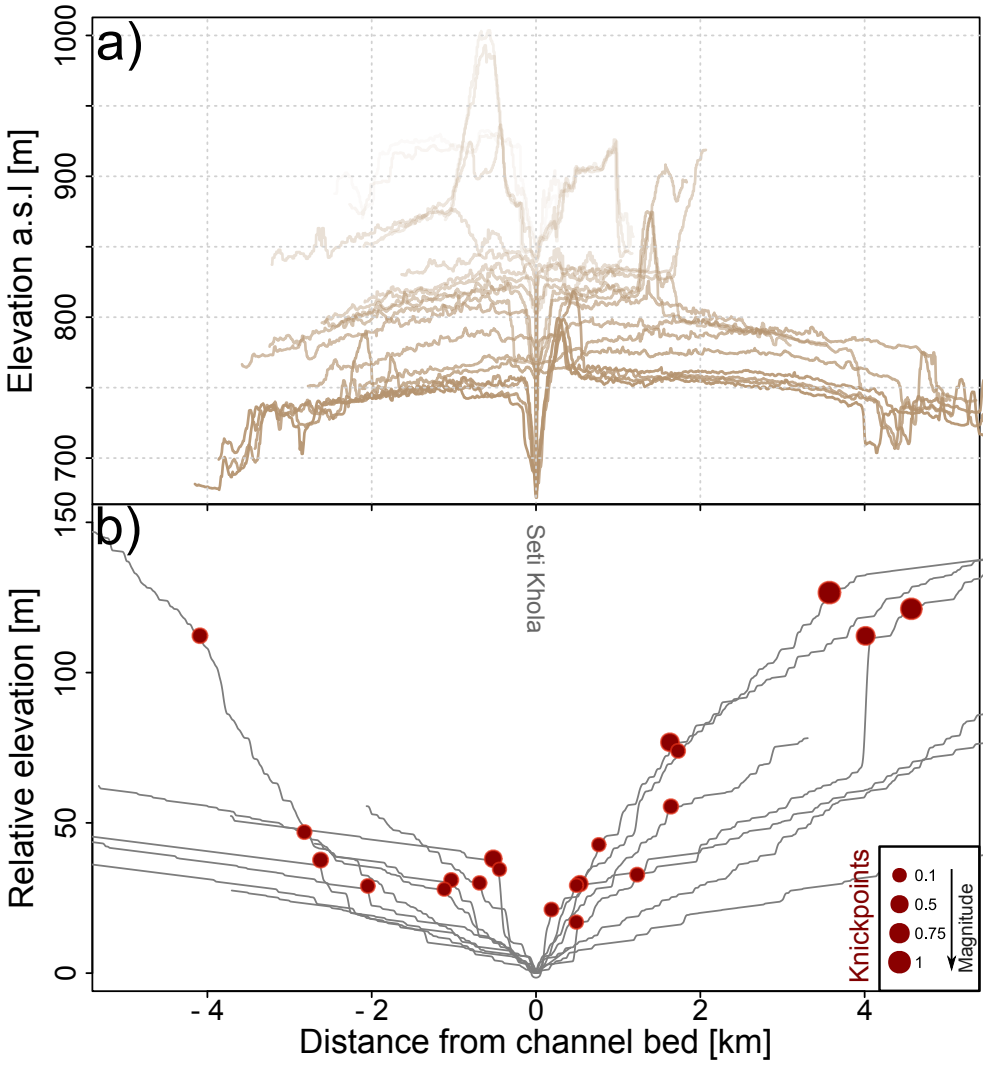

Figure 4.8.: Topographic sections showing a) the convex Pokhara fan surface at 10-m contour equidistance, and **b)** projected longitudinal profiles of tributaries centred about the confluence with Seti Khola (view upstream); knickpoints are normalized by their magnitude, so that larger circles represent more pronounced knickpoints.

Historical air photos and GNSS measurements of selected terrace treads of the Pokhara Formation in the Phusre Khola, however, emphasise contemporary channel dynamics. Average incision rates have been up to 0.2 m yr^{-1} in the past decades (Fig. 4.2c), accompanied by active bank erosion so that rivers also shift sideways; gully-head cuts at the toe

of the Pokhara fan have remained largely stable over the same period, however. During our fieldwork between 2013 and 2016, we witnessed how flood terraces formed by channels that locally incised at 0.4 m yr^1. Such high erosion rates may have caused the main Seti Khola bridge to collapse in 1991 (Shrestha et al., 1992). Erosion by groundwater sapping along the interface between the Pokhara Formation and underlying bedrock or the less permeable Ghachok Formation may be a key mechanism for triggering such collapses; the calcareous Pokhara gravels promote karst in the Kali Khola with subsurface channels, cavities, sinkholes, and chimneys (Waltham, 1996; Gautam et al., 2000), whereas near Pokhara city caves and the adjacent Seti gorges are cut into the Ghachok Formation. Indeed, some degree of river recovery may have occurred underground by shifting groundwater flows.

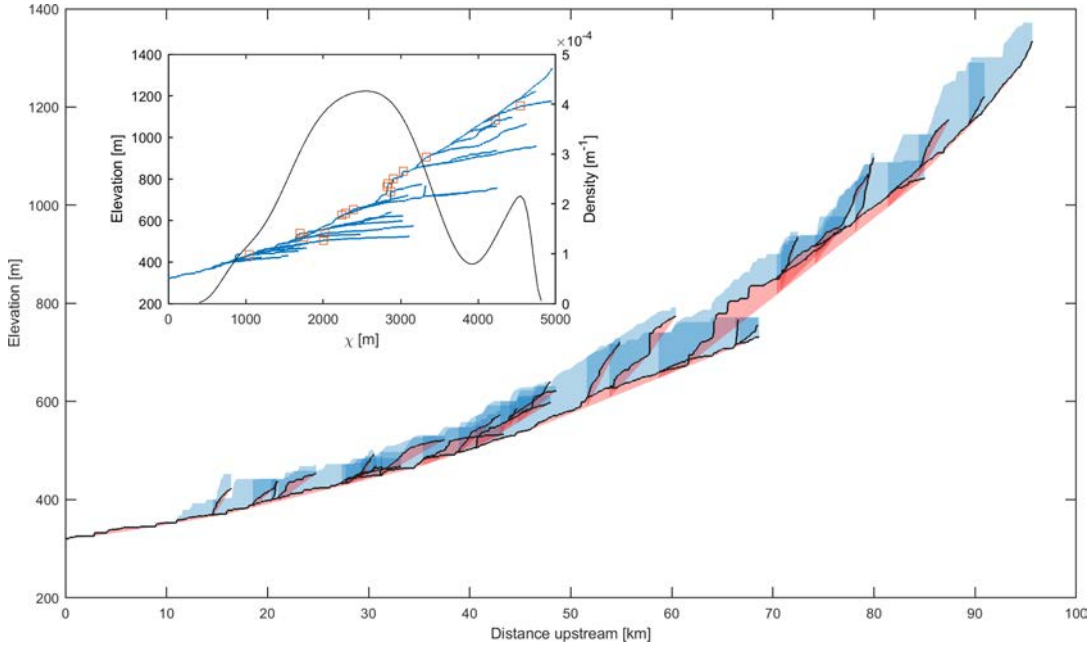

Figure 4.9.: Longitudinal profile evolution of the Seti Khola catchment channel network. Black lines indicate the present day channel profiles; blue shading shows the thickness of Pokhara Formation gravels, the base of the red shading represents idealised concave channel profiles. The inset shows the river network (blue) with knickpoints (red squares) scattered in χ-space (density curve).

Another strong evidence for ongoing river recovery comes from the sediment provenance. Our clast counts consistently tie sedimentological and geochemical provenance data together with our radiocarbon chronology including the new dated tree trunks (Fig. 4.4). Most of the modern bed load in the lower tributaries derives from the Annapurna Massif rather than the surrounding Lesser Himalayan sources despite frequent floods and landsliding in this monsoon-drenched area. Yet the modern channel bed-load composition indicates that response to medieval catastrophic aggradation is ongoing (Fig. 4.5). On the other hand, if fluvial recovery is signified by the degree to which the channel bed has

returned to its pre-disturbance elevation, we would argue that the Phusre and Anpu Khola are close to full recovery (Figs. 4.1, 4.2), that is, assuming that our dated trees were part of a continuous floodplain level and did not grow on hillslopes buried by the aggradation.

Summarizing all evidence from the three principal proxies, we infer that the rivers in the Pokhara Valley are still responding to several medieval earthquake sediment pulses. We report a wide range (30-70%) of recovery states depending on the proxy used and assuming that recovery can be approximated by an exponential decay function. Extrapolating these functions until they reach a level of 10% of remnant recovery yield, recovery times could lies between 1400-5600 years (Fig. 4.11). Despite the wide range of estimates, our study is the first to show from multiple proxies that fluvial response to earthquakes can exceed many centuries and potentially much longer.

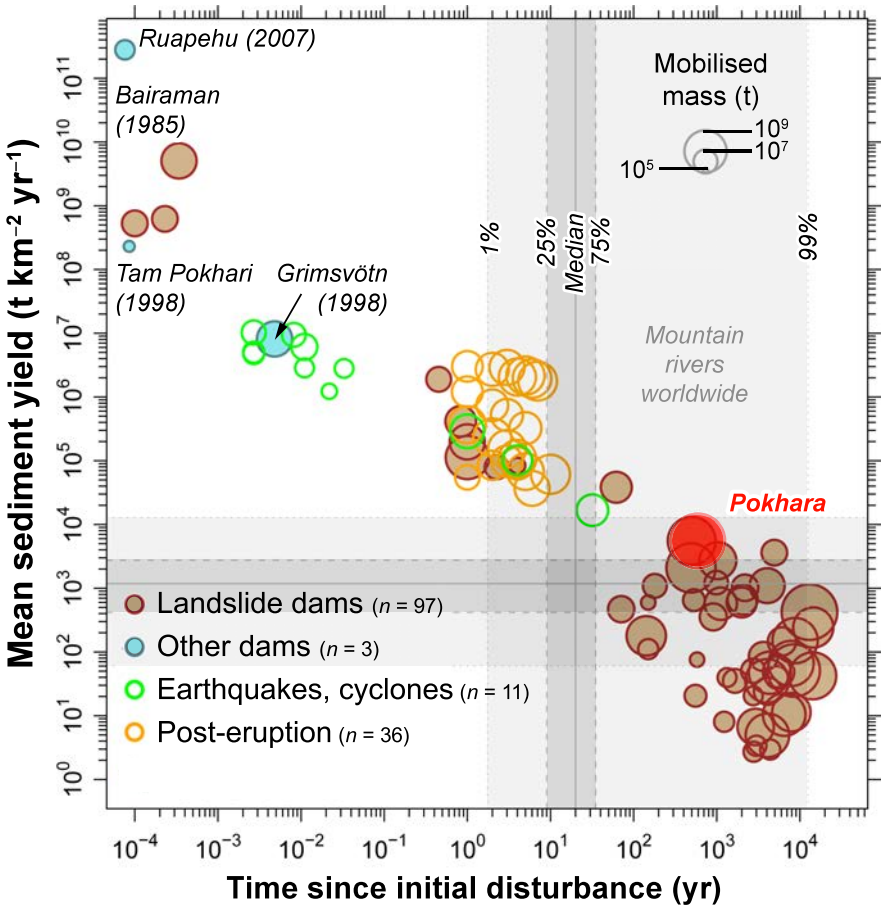

Figure 4.10.: Global comparison of average sediment yields following local to landscape-scale disturbances as a function of the time since disturbance; modified after Korup (2012). Bubble size is scaled to the volume of sediment catastrophically produced by landslide- and other natural dam failures, earthquake- and tropical cyclone-triggered landslides, and reworking of pyroclastic fallout. Shaded rectangles are percentiles of sediment yields reported in several hundred mountain rivers throughout the world; see Korup (2012) for data sources.

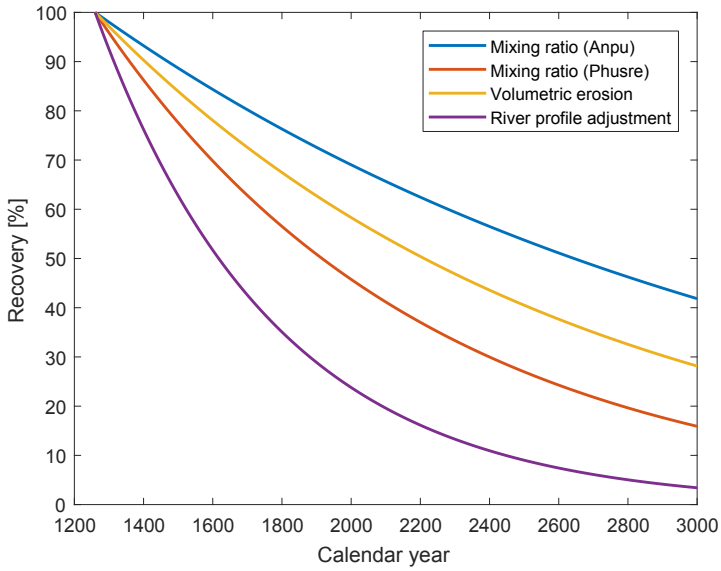

Figure 4.11.: Recovery for three different proxies measured for the Pokhara Valley infill. The mixing ratio is based on clast counts in two tributaries, while volumetric erosion and the river profile adjustment refer to the entire Seti Khola and its tributaries. Fluvial recovery ranges from 30 to ∼70% with respect to a fully equilibrated river.

4.7. Conclusion

We provide some of the first evidence that earthquake-induced sedimentation in mountain rivers may protract fluvial, and hence also, landscape response much more than previously documented. The rivers around Pokhara have been adjusting to catastrophic sediment pulses for nearly eight centuries. A number of independent proxies attest to this adjustment and recovery: dated exhumed tree trunks record sudden aggradation in the early 13^{th} century. Their location and exposure reveal that the river bed has almost reached its pre-disturbance elevation by incising into the valley fill deposits, whereas only the upper 12% of the active channel stores local LHS deposits as opposed to the dominant HH lag material that derives mainly from several strong medieval earthquakes. We document an increase in volumetric erosion further downstream along the main trunk.

Our findings raise the question of whether massive valley fills and terrace staircases widely observed in the central Himalayas (and elsewhere) exclusively and faithfully record climatic or seismic disturbances that may drive sediment availability and river transport capacity (Blöthe and Korup, 2013). The Pokhara Valley has clearly taken many centuries to partially recover from medieval earthquakes: ∼70% of the catastrophic deposits still remain untouched today, whereas the longitudinal profile of the Seti Khola may need another 30% to adjust to reach equilibrated conditions. We argue that longer-lived, in this case

centennial, geomorphic impacts of earthquakes on channel stability and sediment yields should be acknowledged in post-seismic hazard appraisals and infrastructural planning in the Pokhara Valley and mountain regions elsewhere.

4.8. Acknowledgment

This work was supported by the German Research Foundation (DFG) (KO 3937/9-1), and the DFG Graduate School, Natural Hazards and Risks in a Changing World (NatRiskChange). Radiocarbon samples were processed and dated by the team of Tomaz Goslar in the Radiocarbon AMS Laboratory Poznan, Poland. ^{10}Be AMS measurements were supported by DREAMS (Ion Beam Center (IBC) Dresden-Rossendorf) and the IBC team. We thank the German Aerospace Center (DLR) for granting access to TanDEM-X data as part of the project DEM_GEOL1053. J.D.J. was supported by a BRAIN-Marie Sklodowska-Curie fellowship at the University of Potsdam. We thank T. Cohen and G. Veh for discussions and help during fieldwork, B. Sitaula for logistical support, and E. Schönfeldt for her work in Phusre Khola and comparison of historical imagery.

5 Discussion

In the following discussion, I revisit the three research questions about the Pokhara Formation that the three core Chapters (2 - 4) addressed. Instead of reiterating the major findings individually, I first summarize the main results to answer each question, and then discuss several items that arise when integrating those findings. Chapter 2 relied heavily on the radiocarbon chronology of the valley fill and its relation to earthquake coincidence. Therefore, part of this discussion (Section 5.1) focuses on the underlying methodological aspects of the calibration of radiocarbon ages that determine the robustness of the age constraints of the Pokhara valley infill. Chapter 3 focuses on the role of the Pokhara Formation as a sediment archive: I ask whether sedimentary evidence alone is sufficient for inferring three great Himalayan earthquakes in the sediment layers of the Pokhara Formation. Section 5.2 also tries to provide a context for this by briefly reviewing a broad range of existing paleo-seismological records of Nepal. In this regard, I add (Section 5.3) the discussion about triggering mechanisms of the Pokhara Valley infill, and compare it with similar events found in the Himalayas and elsewhere. The discussion of Chapter 4 is focused on various proxies to measure fluvial response, while Section 5.4 highlights fluvial adjustment to massive aggradation in the area of Pokhara and how human influence may affect the fluvial system during its recovery. The perspective and outlook (Section 5.5) of this thesis expands on the urbanization of Pokhara city and its surrounding villages with respect to land use changes and population growth, while hazards such as sinkholes and terrace collapses, risk and vulnerability appear to be increasing (Sakai et al., 2015).

1. *Dates and origins: When, how rapidly, and why was the Pokhara Formation deposited?*

Our ^{14}C ages show evidence for past earthquakes and contribute to the long debated question whether the valley got filled by one or multiple events. We infer and answer this question with our robust ^{14}C age chronology that at least three medieval earthquakes

prompted massive valley-floor sedimentation in the Pokhara Valley within some ∼250 years. Geomorphic footprints and sedimentary evidence agree with massive fluvial aggradation, while the geomorphic legacy of multiple earthquake-driven sediment pulses appears to be unique in the Himalayas; to our knowledge no other study has reported catastrophic sedimentation at comparable size, age or temporal resolution. Deposits from long-runout debris flows and rapid aggradation from a distinct HH headwater source dominate the valley sedimentology rather than aggradation in response to local co-seismic landsliding. We cannot fully discount the possibility that our ^{14}C dates might have no causal connection with the timing of large medieval earthquakes; at least, our ^{14}C dates show no conclusive correlation with temperature and monsoon proxies for the region (Fig. A.9).

2. *Sedimentary diagnostics: Which insights about transport processes and episodes does the sedimentology of the Pokhara Formation reveal?*

A first detailed sedimentological study of the Pokhara Formation (see Table 3.3) gives evidence of catastrophic debris flows, fluvial conglomerates and fan-marginal slackwater deposits. Provenance analysis reveals that these upstream dipping deposits in tributary valleys originate from the upper meta-sedimentary part of the Higher Himalayas tens of kilometers away. Our sedimentological work is the first systematic inquiry of its kind into the Pokhara Formation, and highlights four different lithofacies that connect to massive aggradation pulses affecting large parts of the Pokhara fan. New radiocarbon dates from widely scattered locations cluster conspicuously to a short medieval period, extend the ^{14}C age chronology, and establish that these pulses are largely coincident with the documented dates of three great Himalayan earthquakes. The Pokhara Valley has the hitherto largest and most thoroughly dated archive of (most likely earthquake triggered) valley fills in the Himalayas. Yet only the combination of radiocarbon ages, sediment lithofacies, and provenance analysis is consistent and allows to distinguish the individual sediment pulses. This catastrophic valley infill offers new proxies to independently verify paleoseismological fault-trench records, while affording insights into the centennial geomorphic impacts on major drainage basins, adding to many studies that propose that mountain rivers recover from earthquakes within years to decades.

3. *River signs: What effects did the emplacement of the Pokhara Formation have on the drainage network?*

With the last research question, we show various signs from a river about its fluvial adjustment and recovery after massive aggradation pulses. The rivers around Pokhara have been

adjusting to catastrophic sediment pulses of nearly eight centuries, and are still in the process of doing so. We provide some of the first evidence that earthquake-induced sedimentation in mountain rivers may protract fluvial, and hence also, landscape response much more than previously documented. A number of independent proxies attest to this adjustment and recovery, re-exhumed tree trunks record a fast and continuous aggradation in the early 13^{th} century, while only the upper 12% of a active channel stores local LHS deposits as opposed to the dominant HH lag material. We measure recovery proportions of 35-72% of HH material that still dominates in different tributary catchments, while the total river system needs to adjust around 30% to reach a concave channel profile. Pronounced knickpoints at tributary junctions show a protracted response and still ongoing adjustment process in the fluvial system. We show that humans influence the fluvial adjustment of the Seti river by extensively mining river material for construction purposes. We conclude that some mountain rivers may need a few years to adjust and recover from strong perturbation, while the Pokhara Valley clearly needs centuries to recover from medieval earthquakes, as ∼70% of the catastrophic deposits have remained in place untouched until today.

5.1. Assumptions underlying the radiocarbon chronology

Bayesian calibration of in total 46 ^{14}C ages returned a robust chronology of pooled posterior distributions with three distinct peaks that match, within error, the timing of three large Himalayan earthquakes in ∼1100, 1255 and 1344 AD (Fig. 2.2, 3.9, and 4.4). How certain are these earthquakes as triggering mechanism for the three dated sediment pulses? How do we exclude that these peaks are artefacts of the calibration curve or potential sampling errors? These questions are central to identifying or at least interpreting possible trigger mechanisms, but do not change our findings of a catastrophic valley infill. Moreover, we could similarly ask those questions about samples that were taken in fault trenches to date historic earthquakes ∼1100 AD, Lavé et al. (2005). The calibration procedure has in principle the same uncertainties; the main difference is that samples from trenches date the rupture itself without any delay by sediment transportation that we have to account for in fluvial or debris-flow deposits. Other possible problems can be intermittent storage, the entrainment of residual material (older) or intrusive material (younger) (Bronk Ramsey, 2008). To systematically and objectively investigate these problems, we tested various randomization methods during the calibration of ^{14}C ages.

Radiocarbon calibration using OxCal

The OxCal program (Version 4.2) provides radiocarbon calibration and analysis of environmental chronological information. Such information can be used in various models; the calculation of probable age ranges for dated samples, or the analysis of grouped events which are related through stratigraphic relationships or generic grouping. While any organism is alive it continues to incorporate radiocarbon from the atmosphere, while once it dies, the amount gradually declines because of radioactive decay (Bronk Ramsey, 2008). The IntCal13 calibration curve is made on material of known age (e.g. tree rings). However, the calibration is performed by comparing the radiocarbon concentration of the sample with that of the IntCal13 curve to determine the possible calender age. The OxCal program provides radiocarbon calibration and analysis of environmental chronological information. Such information can be used in various models; the calculation of probable age ranges, or the analysis of grouped events which are related through stratigraphic relationships. Most dating approaches, have a large number of ^{14}C measurements that we wish to relate to past events (Bronk Ramsey, 2009b). The OxCal program uses Bayesian statistic that "provides a coherent framework in which such analysis can be performed and is becoming a core element in many ^{14}C dating projects" (Bronk Ramsey, 2009b). By using the Bayesian approach for calibration the program aims to find a representative set of possible ages in the sedimentary sequence (Buck et al., 1991; Bronk Ramsey et al., 2001). For this calibration model, we used a *prior* knowledge (stratigraphic relationship, components of sedimentary sequences) to incorporate information to the model, while the *likelihood* presents the information of the particular age for each sample (Bronk Ramsey, 2008). The Bayes theorem then uses these information to get all possible solutions with a probability which is the product of the *prior* and *likelihood*. The resulting distributions are the *posterior* probability densities that take account of all information, the deposition model and age measurement (Bronk Ramsey, 2008).

We sampled our radiocarbon material in the lithofacies F2 and F3 mostly in very fine clay and silt layers, some of which included limestone pebbles. Others were sampled in fluvial conglomerates or in cohesive debris flow deposits in fan-distal zones in tributary valleys (see Chapter 3). Altogether, and to our best knowledge, this is one of the largest collection of radiocarbon samples found in valley fills in the Himalayas. Although, this

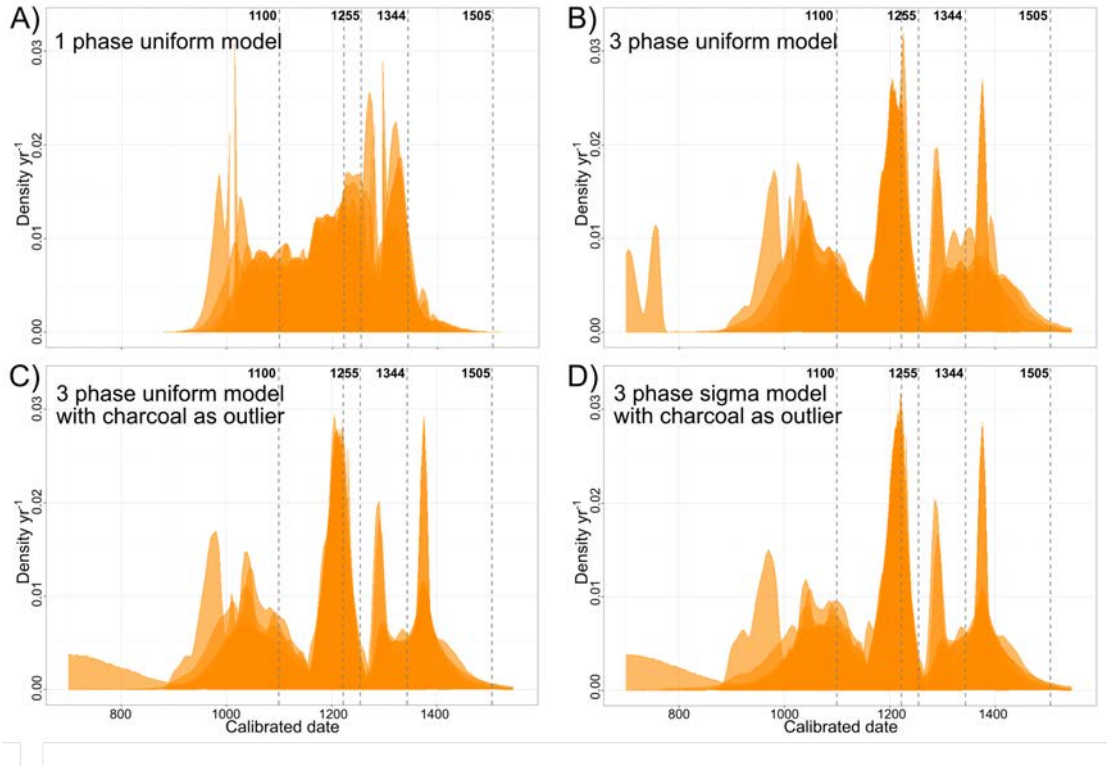

Figure 5.1.: Testing different models for calibration. We used different priors for the Bayesian calibration model using OxCal 4.2 with the IntCal13 (Reimer et al., 2013) curve. **A)** Shows the simplest approach for calibration with a uniform prior for a one phase model. The input radiocarbon ages are assumed to possibly occur equally likely anytime during the phase and within the given minimum and maximum ages. **B)** This calibration model is based on a prior knowledge of sample field stratigraphy and the assumption that our samples were deposited within three sediment pulses (three phase model) that we tied to historic earthquakes. **C)** As charcoal often predates the timing of its deposition (Schiffer, 1986), we used the OxCal charcoal model (Reimer et al., 2013) assuming that all charcoal dates are outliers and fed this assumption to the three phase model in B). **D)** We also tested different models besides the uniform model, but found that either sigma (shown here) nor the exponential model show substantially different results.

study area and valley fill is some 150 km^2 large, we were able to collect samples from almost every tributary valley (Fig. 3.8). We developed and refined our model by testing various possibilities of how the Pokhara Formation was deposited. By starting a model assuming that all radiocarbon ages belong to one event, we later used three and four phases of sediment deposition (Fig. A.4). However, the ^{14}C age chronology remain consistent over the three studies (Chapters 2 - 4). While testing various calibration models with different numbers of events, we also used different priors for the Bayesian approach (Table 5.1). Figure A.4 highlights that the three peaks are hardly dependent on the *prior* distribution used for calibration. Nevertheless, it underlines that if using informed knowledge (*priors*) for the age calibration, the better the Bayesian approach works, and the more radiocarbon

Table 5.1.: Used priors for the Bayesian model approach of all radiocarbon ages calibrated to calendar years.

	prior	Sample Number	OxCal model			
			individual age calibration	1 phase*	3 phases*	4 phases*
Chapter 2		26	x	x	x	x
Chapter 3	Stratigraphic information	37	x	x	x	
Chapter 3	Stratigraphic information; Charcoal as outlier	37	x	x	x	
Chapter 4	Stratigraphic information; Charcoal as outlier	46			x	

*These OxCal models use the, so called, sequence{}. A uniform model that constrains the dated events to be in the order that they are in the sediment. Applicable, if we can not make any direct use of depth information, but about the stratigraphic order (Bronk Ramsey, 2008).

ages we used as input, the more stable the *likelihood*. This resulted in pronounced peaks of calibrated ^{14}C age densities, while some of the model specifics itself did not matter and the chronology stayed consistent. The model returned a pooled posterior distribution with three distinct peaks that match the timing of large historic earthquakes in Nepal. This new knowledge was than used in Chapter 3 and 4 with the refined assumption of having three sediment pulses in a three-phase model (see Fig. 5.1). The dependence of depositional models on 1) random elements in the process and 2) abrupt changes (boundaries) in sedimentological sequences can be use as prior to refine the model (Bronk Ramsey, 2008). However, despite the complexity and randomness of sedimentation process, the deposition rate varies in sufficiently fine scale (as long as one mode of deposition persists) that depositional models appear continuous and uniform (Bronk Ramsey, 2008). Based on this condition, we used a uniform model with the knowledge of having three aggradation phases. By adding a *prior* probability of sample stratigraphic relationships into the model, we obtained more credible results. We added to the previous model (Table 5.1) new data points but also used a posterior probability density function of all samples together with a prior of their field-based stratigraphic relationship and the knowledge that wood takes some time to grow so that charcoal ages may predate the timing of sample deposition (Bronk Ramsey, 2009a).

The oldest ^{14}C age peak and therefore first sediment puls in our chronology (Fig. 5.1) fits to the time range of the ∼1100 AD earthquake, which has so far been inferred by trenches (Lavé et al., 2005). We raise the question about the reliability of these records as well as the historic scripts for the earthquakes around 1255 and 1344 AD. Ages taken for the timing of those earthquakes are mostly from fault trenches, using the IntCal calibration

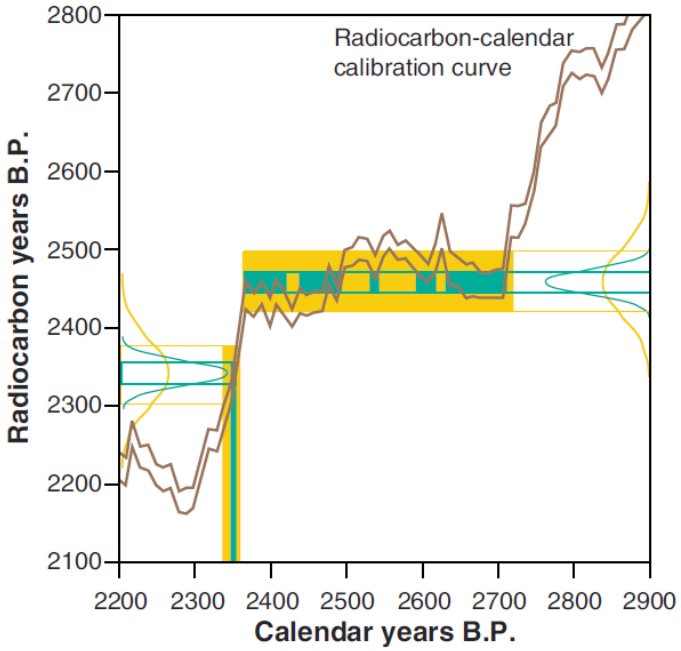

Figure 5.2.: Kinks and plateaus on radiocarbon calibration. An example of the influence of plateaus on radiocarbon curves. The curves are 1σ Gaussian probabilities of hypothetical radiocarbon ages with ± 40 (yellow) and ± 15 (blue) year error bars. The bars show possibilities of the calibration curve that are intercepted by radiocarbon ages and their uncertainties. The intercept region is projected onto the calender year age range. The variation from kinks and plateaus dictate that for the years of a 2340 radiocarbon date, a decadal-scale calender year age range is possible, while for a 2460 date, the derived age range would encompass several centuries. Figure taken from Guilderson et al. (2005)

curve, although from earlier versions. Nonetheless we re-calibrated all relevant radiocarbon ages for better comparison. During calibration, we mostly concerned the consistency and accuracy of our radiocarbon ages, but also took the challenge to artefacts in our chronology, especially those potentially arising from kinks or plateaus in the radiocarbon calibration curve (Fig. 5.3A and 5.2). Guilderson et al. (2005) underline the issue and limitations of calibration curves in more detail. However, in many circumstances, radiocarbon dates allow considerable refinements "through constraints imposed by a priori information (such as stratigraphy) or by the pattern of the radiocarbon dates relative to calibration curve variations (an approach that is sometimes referred to as 'wiggle-matching')" (Guilderson et al., 2005). This 'wiggle-matching' or long-term variations in ^{14}C production approach is documented in detail by Bronk Ramsey et al. (2001) and Walker (2005). It includes different methods of matching radiocarbon dates to "wiggles" of the calibration curve. Besides a Monte-Carlo simulation or the classical Chi-squared fit of the ^{14}C data to the ^{14}C curve, Bayesian statistics calculate for each sample the relative *likelihood* of each possible calendar year fit. This probabilistic approach calculates a range of most likely

dates (Bronk Ramsey et al., 2001). In this case, by using the OxCal program with the Bayesian approach, we already exclude high uncertainties from plateaus and kinks (Bronk Ramsey et al., 2001; Guilderson et al., 2005; Walker, 2005). Nevertheless, medieval times are especially problematic in this context; yet the exact dates of changing concentration of atmospheric ^{14}C do not fully match those of the historically documented Himalayan earthquakes that we have tested our chronology for such artifacts by generating artificial dates (Fig. 5.3B). We have done this for Chapter 2 (see Appendix A) by testing for a Poisson process in our *posterior* age estimates, generating 10,000 simulated data sets and finally excluded with 95% bootstrap confidence that our dates are randomly distributed in time (see Fig. A.3). For Chapter 3 we generated a synthetic data set spaced in 10-year intervals from 1000 to 1500 AD (Fig. 5.3B and C). We processed synthetically generated, randomly distributed ages with the same measurement errors of ±30 years and within the same calibration models we used for our radiocarbon ages. In all cases, the calibrated synthetic dates do return peaks (Fig. 5.3B), but none of them match those that we would expect from plateaus and kinks tied to the calibration curve.

In summary, all variants of calibrating the ^{14}C data return three distinct age peaks regardless of the exact choice of prior or depositional model. Among others, we tried a uniform one-phase model, and a uniform three-phase model including charcoals samples as outliers. In this respect, the three peaks that we obtained turned out to be robust. We could not find any distinct changes resulting from different models and exclude the calibration curve as source for potential artifacts or errors. Other seismic events such as the M_w 7.9 Wenchuan earthquake in 2008 show that mass wasting often delayed by a few years (Li et al., 2014). Hence, radiocarbon ages are not accurately measurable to one definite year; regardless, many case studies of recent events have shown that massive river sedimentation is not limited to a single year, but may more often occur over few years to decades after the earthquake (Hayes et al., 2002; Li et al., 2014; Ulloa et al., 2016).

Our robust chronology in terms of linking sediment pulses to great medieval earthquakes, still addresses the issue that arises in the case of the 1505 AD earthquake; our radiocarbon ages do not peak up around that time. This event is one of the few large earthquakes known for western Nepal (Malik et al., 2017), with an estimated magnitude of ∼8.4 (Kumar et al., 2006) (Table 3.1), and an epicenter that is only ∼170 km away from Pokhara. This earthquake would have likely triggered landslides or released massive sediment transport near the epicenter, though likely not as much in the Pokhara area, given the distance

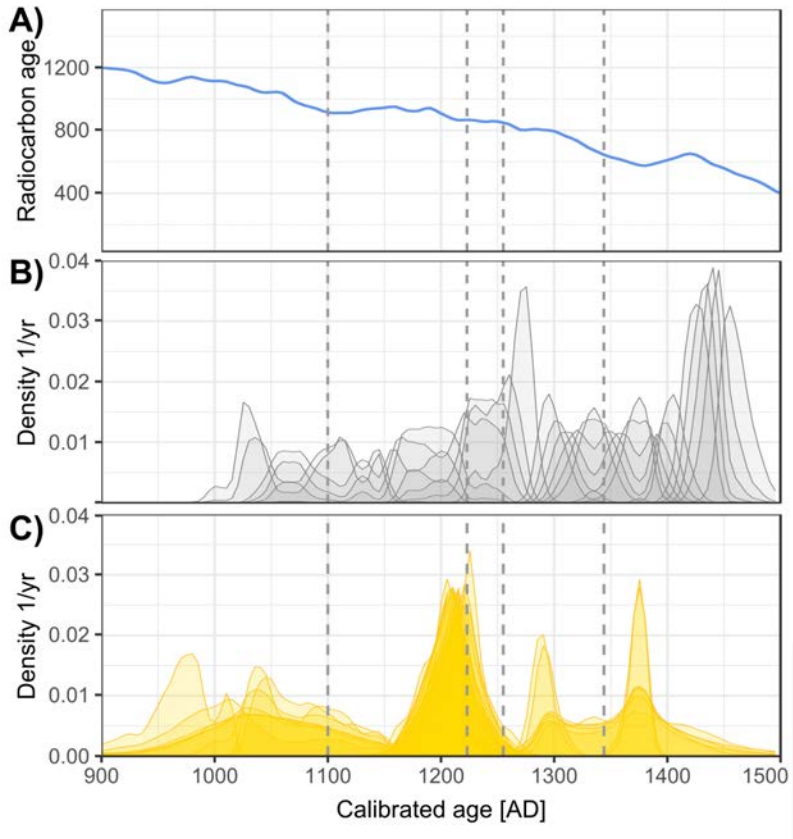

Figure 5.3.: Test for artifacts in the radiocarbon chronology tied to wiggles in the calibration curve. We used a synthetic data set of radiocarbon ages from 1000 - 1500 AD and calibrated the samples using the OxCal calibration software. We further randomly picked the same amount of 36 samples for better comparison to our radiocarbon samples. We did not use any additional Bayesian priors for calibration as we did in the manuscript. **A)** Shows the IntCal13 curve. **B)** 36 randomly generated samples; note that peaks in the synthetic chronology do not coincide with the dates linked to "wiggles" in the calibration curve. **C)** Our samples calibrated without any informed priors.

(Keefer, 1994) from the Sabche Cirque to the epicenter (see Table 5.2). In any case, such coseismic landsliding in the Pokhara area would have mobilized much more local (LHS) sediment than from the HH, at least compared to what we see in the composition of modern river sands; landslide scars and deposits clearly attributable to the 1505 AD earthquake still await detection, let alone documentation. Other possibilities of why the 1505 AD does not show up in our posterior densities might include: 1) The earthquake in 1505 AD may not have been as strong in the Pokhara area as previously thought (Kumar et al., 2006; Malik et al., 2017). The Gorkha earthquake in 2015, was very strong, destructive, but considering the very short distance to Pokhara (only ∼80 km) weak with almost no damage to account in the valley (Rimal et al., 2015; Pokhrel et al., 2015a). 2) The undated lithofacies F4 covering the Pokhara fan might be evidence for the 1505 AD earthquake. This very thick layer of catastrophic deposited cohesive debris flow (HH material) might

belong to the 1344 earthquake; it also could have been triggered by the 1505 or a more recent large earthquake (e.g. the one in 1681 AD, coeval with our ^{10}Be exposure age, Chapter 2, Fig. 2.2). 3) The Seti channel could have already been wide and deep around 1505 AD, so that the sediment pulse would have been largely flushed through without covering much of the fan surface; such was the case for the flash flood in May 2012 in the Seti gorge (Bhandary et al., 2012). This last point is not as realistic as there were only 150 years between which is not much time to create wide and deep channels for a river network with protracted fluvial recovery (Chapter 4). The 2012 event moved an estimated 20×10^6m^3 of sediment, which is a tiny fraction compared to the currently estimated total accommodation volume ($\sim1.5\times10^9$m^3) carved by the Seti channel through the Pokhara Formation until today.

Table 5.2.: Historic earthquakes of Nepal their earthquake magnitude and epicenter location. This table is the base of Fig. 5.5

EQ	Lat [°N]	Long [°E]	Magnitude	Reference	Distance from epicenter to the Sabche Cirque [km]
1100	27	88	8.6 - 8.8	Lavé et al. (2005)	360
			>8.6	Mugnier et al. (2011)	
1255	27.7	85.3	<= 8.1	Mugnier et al. (2013)	155
			8.6 - 9.0	Jayangondaperumal et al. (2013)	
1344	30	80	8.4 - 9.2	Kumar et al. (2006)	420
			>8.6	Mugnier et al. (2013)	
1505	29.6	83.2	8.1	Yule et al. (2006)	135
			8.16	Ambraseys and Douglas (2004)	
			8.2	Kumahara and Jayangondaperumal (2013)	
			>8.6	Bilham (2015)	

Our radiocarbon ages are very promising in that we revealed three medieval earthquakes as highly likely triggering mechanism of catastrophic sedimentation in the Pokhara area. In the following Section 5.2, I discuss the paleo-seismology of Nepal and the fan sedimentology itself. Figure 5.4 nicely combines our ^{14}C ages with slackwater deposits in the Phusre tributary catchment. Fast aggradation inferred from radiocarbon ages are up to 200 mm yr^{-1} on average in places, and directly combine and support the notion of catastrophic deposition, mostly leaving behind homogeneous and thick slackwater deposits (lithofacies F3). The Pokhara Valley is certainly not the only Himalayan location with massive sedimentation (see section 5.3), but very extensive (150 km^2) and unique as it is

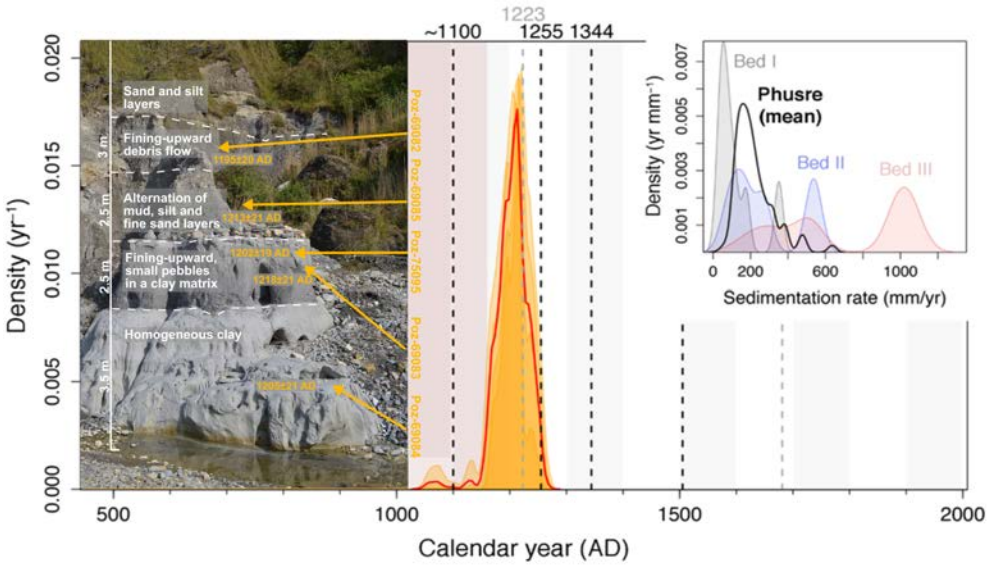

Figure 5.4.: Concurrency of ^{14}C ages in the Phusre Khola catchment. Posterior probability density function (orange) of four radiocarbon ages. The inset shows the field settings and inferred sedimentation rate.

a great sediment archive to reconstruct its mechanism, sedimentological fingerprints, and because the second largest city of Nepal is built on this big fan.

5.2. Sediment archives to detect historic earthquakes

In general, some valley fills might be connected to very strong earthquakes (see examples in section 5.3). But do we expect that earthquakes are regularly and faithfully recorded in those sediment deposits? Do we expect to find remnants of each earthquake in catastrophically filled valleys and incised terraces? We cannot depend on sediment archives if we do not find them or if they were not created in the first place. Despite the ubiquity of triggers (Fort, 1987), slope stability as a supply mechanism for such sediments is also governed by rock mechanics, thus mostly pattern, strength, and orientation of discontinuities, but also topographic relief, earthquake magnitude, peak ground acceleration are some of the important parameters to release landslides or debris flows (McCalpin, 2009). We have no reason to believe or even suggest that each major earthquake routinely triggers debris flows in the Annapurna area. Kargel et al. (2016) conclude in their study about landslides triggered by the Gorkha earthquakes 2015 in Nepal that the "earthquake caused fewer landslides than comparable earthquakes elsewhere"; in other studies large scatter of landslide volumes (Marc et al., 2016) show likewise that a given earthquake with high

magnitude may trigger sediment pulses in one area, but not in other regions with the same distance from the epicenter.

An increasing number of paleoseismic studies in the past decade (Lavé et al., 2005; Yule et al., 2006; Kumar et al., 2010; Mugnier et al., 2013; Bollinger et al., 2014, 2016; Sapkota et al., 2013; Rajendran et al., 2015) have documented precisely many of Nepal's historic earthquakes. However, information remains limited and partial as many key aspects of the paleoseimic history of Nepal are still heavily debated (Fig. 5.6 and 5.3); different studies (Le Roux-Mallouf et al., 2016; Mishra et al., 2016; Bollinger et al., 2016; Rajendran et al., 2015; Lavé et al., 2005) show various and often conflicting interpretations of epicenter locations, magnitudes (Table 5.2), rupture zones, and even the exact year of historic Himalayan earthquakes are heavily discussed. Several large medieval earthquakes are mentioned in written records as the king of Nepal died during the shaking; those are also known to the exact day (1255 and 1344 AD), while the exception is the ∼1100 AD earthquake, for which researchers have geological field evidence trench investigations (Lavé et al., 2005). In this regard, "paleoseismology is the study of prehistoric earthquakes, especially their location timing and size" (McCalpin, 2009). Paleoseismology is concerned with landforms, tectonics, sediment and geologic structures, geomorphic and stratigraphic evidence, as well as historical surface deformation (Keller et al., 1997; Yeats et al., 1997; Burbank and Anderson, 2001; McCalpin, 2009) and relies on rupture histories derived from fault trenches, written records, liquefaction features, and some from lake sediments. The sequence of sedimentological units of the Pokhara fan are among the few proxies (besides the radiocarbon ages) that independently corroborate these dates. Based on our findings, we argue that valley fills in the Himalayas can offer substantial and independent evidence for past earthquakes and thus augment the current portfolio of paleoseismological records. This is exemplified by evidence produced by earthquake shaking, or erosional and depositional response to shaking, but it is hardly recorded or yet found, in any Himalayan valley fills.

Using valley fills as palaeoseismological proxies can contribute useful and dearly needed data, given that the growing body of paleoseismological work on large Himalayan earthquakes features a number of contradicting reports about the rupture locations and inferred spatial patterns of ground acceleration during earthquakes. Whilst the rupture lengths of some of those earthquakes are more or less well constrained, almost nothing is known about the epicenter locations, let alone the resulting pattern of local ground acceleration

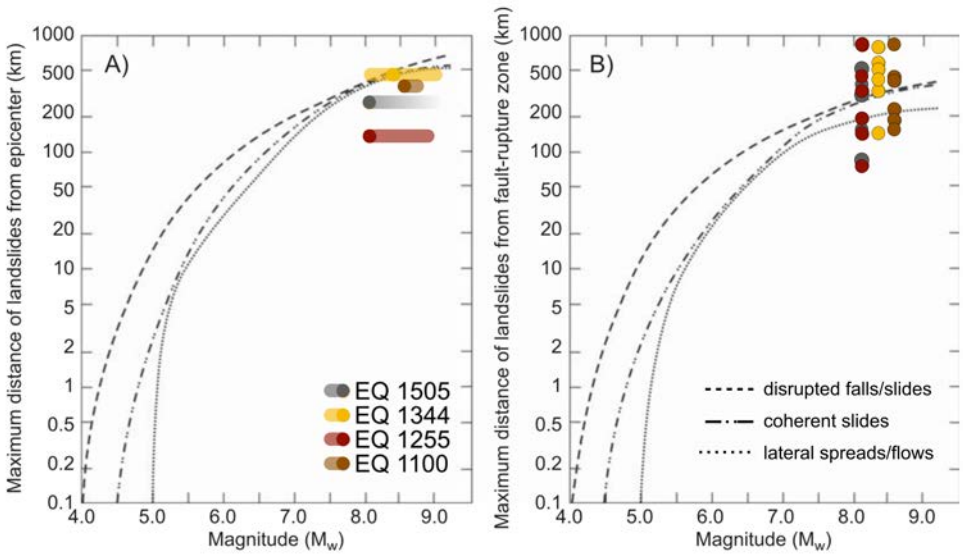

Figure 5.5.: Maximum distance to landslides from earthquake epicenter (A) and fault rupture (B) zone is dependent on different magnitudes. The dashed line is the upper bound for disrupted slides and falls, where the dash-double-dotted line is for coherent slides. The dotted line shows the upper bound for lateral spreads and flows. The colored dots are drawn based on Table 5.2, including the 1505 AD earthquake (Malik et al., 2017), although, we do not find any evidence for it in the Pokhara Formation. Modified after Keefer (1984) and McCalpin (2009).

and topographic amplification, which largely govern slope stability and thus potential sources of landslides and debris flows. Based on Figure 5.5 we follow the approaches by Keefer (1984) and McCalpin (2009) that are consistent with our conclusion that medieval earthquakes have triggered at least three sediment pulses originating from the Annapurna Massif. Based on fault rupture extents, it clearly shows that all three earthquakes we document in this study might have sufficient potential, at least judging from their epicenter and fault rupture to the Sabche Cirque, to trigger debris flows in the Annapurna area (Table 5.2). Even though the 1344 AD earthquake hardly touches the upper curve of slides and flows (Fig. 5.5). Yet, the event is still within the frame of generating sufficient ground shakng to trigger massive sediment volumes in the Sabche Cirque, from its epicentral distance alone. The third pulse was less voluminous than the previous two, with the shortest extent, and the lowest thickness (see section 3.5).

In general, information about historic earthquakes in Nepal are hard to come by. Researchers have been working in various trenches (Fig. 5.6, Table 5.3) along the Main Frontal Thrust, but whether an earthquake triggers landslides or sediment pulses also depends on its focal depth. For example, earthquakes with greater focal depth than 30 km trigger landslides at greater distances than shallower earthquakes of similar magnitude (McCalpin,

Table 5.3.: Trench locations along the Himalayan range. This table is the base of Figure 5.6

Location	Lat (°N)	Long (°E)	EQ 1100	EQ 1255	EQ 1344	EQ 1505
Hajipur	34.608	73.514			Jayangondaperumal et al. (2016)	
Chandigarh	30.774	76.822			Mugnier et al. (2013)	
Kala Amb	30.509	77.109			Mugnier et al. (2013)	
Rampur Ganda	30.478	77.289			Mugnier et al. (2013)	
Dehra Dun	30.376	77.485			Mugnier et al. (2013)	
Lal Dhang	29.858	78.270			Mugnier et al. (2013)	
Ramnagar (Belparo)	29.489	78.989		Sapkota et al. (2013)	Mugnier et al. (2013)	Mugnier et al. (2013)
					Mishra et al. (2016)	Mishra et al. (2016)
						Malik et al. (2017)
Chor Ghalia	29.163	79.649				Bollinger et al. (2014)
						Malik et al. (2017)
Mohana	28.918	80.508		Mugnier et al. (2013)	Mugnier et al. (2013)	Mugnier et al. (2013)
						Bollinger et al. (2014)
						Malik et al. (2017)
Koilabas	27.717	82.512	Lavé et al. (2005)	Mugnier et al. (2013)	Mugnier et al. (2013)	Mugnier et al. (2013)
					Bollinger et al. (2014)	Malik et al. (2017)
Bandel Pokhari	27.693	83.370		Mugnier et al. (2013)		Mugnier et al. (2013)
						Malik et al. (2017)
Pokhara	28.238	83.996	Stolle et al. (2017)	Stolle et al. (2017)	Stolle et al. (2017)	
Katmandu	27.717	85.324	Mugnier et al. (2013)	Mugnier et al. (2013)	Mugnier et al. (2013)	
			Lavé et al. (2005)			
Marha	27.122	85.547	Mugnier et al. (2013)	Mugnier et al. (2013)		
			Lavé et al. (2005)	Mishra et al. (2016)		
Sir Khola	27.008	85.872	Mugnier et al. (2013)	Mugnier et al. (2013)		
				Bollinger et al. (2014)		
				Mishra et al. (2016)		
				Sapkota et al. (2013)		
Tokla	26.623	88.050	Mugnier et al. (2013)			
Hokse	26.891	88.166	Mugnier et al. (2013)	Mugnier et al. (2013)		
				Bollinger et al. (2014)		
				Mishra et al. (2016)		
Singimuni (Panjihora)	26.925	88.533	Mugnier et al. (2013)	Mishra et al. (2016)		
				Kumar et al. (2010)		
Chalsa	26.856	88.594	Mugnier et al. (2013)	Mishra et al. (2016)		
			Kumar et al. (2010)			
Narmeri	26.914	92.764	Kumar et al. (2010)	Mugnier et al. (2013)		
				Mishra et al. (2016)		
Harmutti	27.097	93.757		Mugnier et al. (2013)		
				Mishra et al. (2016)		

2009). Figure 5.6 underlines the ongoing debate about these historic earthquakes. Yet, the 1255 AD earthquake would have affected an area spanned over 1000 km, while the 1344 or 1505 AD earthquake had a smaller rupture length. When summarizing dated trenches, we follow among others, the historic earthquake model of Arora and Malik (2017) and clearly show with Figure 5.6 that massive sedimentation triggered by those earthquakes was definitely possible in the Pokhara area (see Fig. C.4 of Arora and Malik (2017) for comparison).

In the Pokhara Formation (F1, F2) we hardly find any cross bedding and soft sediment structures, nor do we find current structures in lithofacies F2 that would indicate any paleoseismic structural evidence. The finer the material and the more upstream in tributary catchments (F3), the more soft-sediment deformation structures such as loading or dewatering structures we found, at least at a few places (Fig. 3.5). Such deformation features in unlithified sediments are called seismites if caused by earthquakes, such as those inferred for deposits of the Kathmandu basin (Fig. 5.7, Sakai et al. (2015)); hence detailed

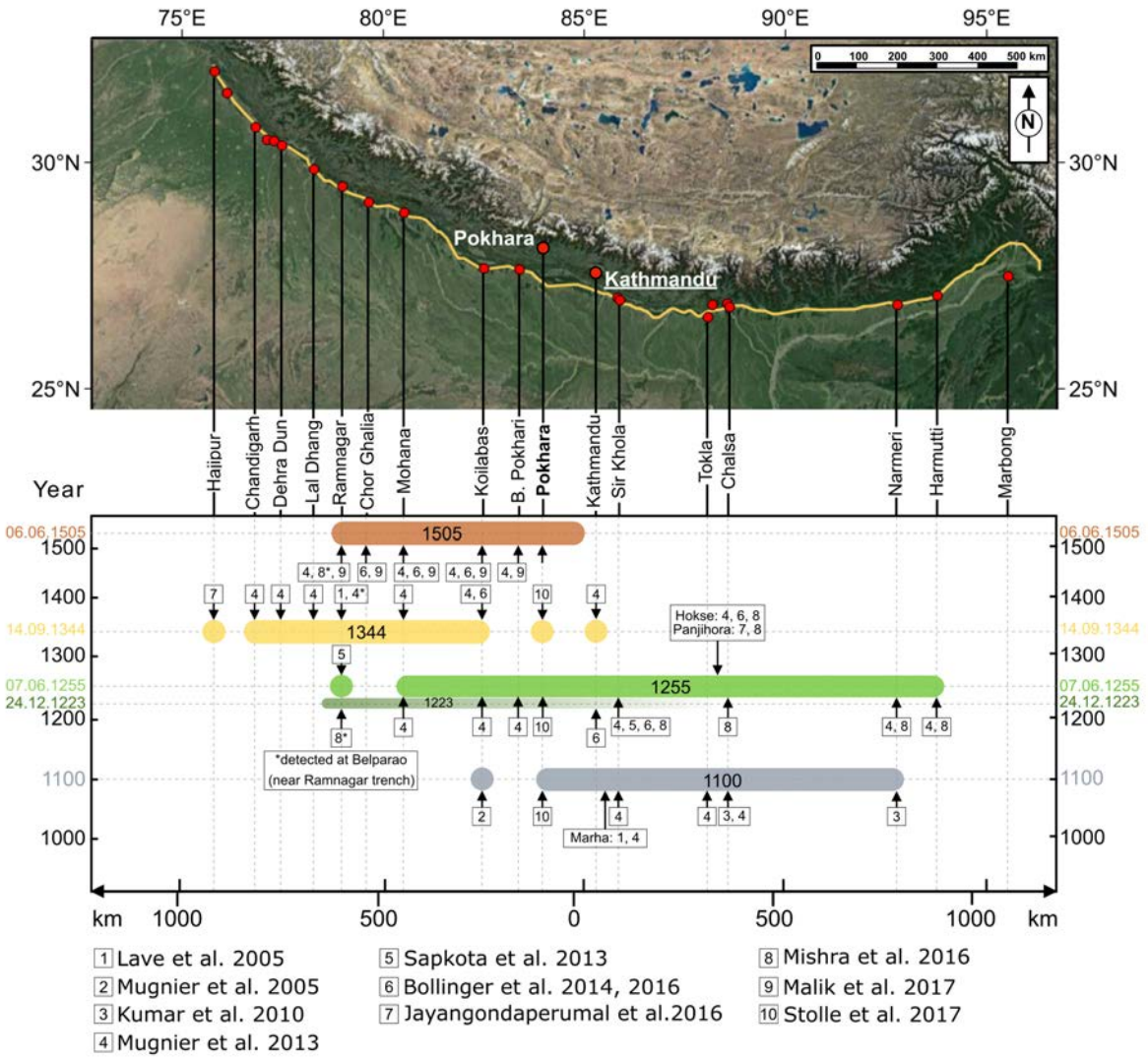

Figure 5.6.: Review of the surface displacement along the Himalayan front. These five historic earthquakes are inferred from fault trenches along the Himalayan front in Nepal. Trench locations and extent of individual earthquakes are collected from different studies (Lavé et al., 2005; Mugnier et al., 2005; Kumar et al., 2010; Mugnier et al., 2013; Sapkota et al., 2013; Bollinger et al., 2014, 2016; Jayangondaperumal et al., 2016; Mishra et al., 2016; Malik et al., 2017; Stolle et al., 2017) and summarized in this overview map. The 1223 AD earthquake is besides the 1255 AD earthquake possible to have triggered massive aggradation and sediment pulses in the Pokhara Valley. However, there is not much data available to better distinguish and analyze the two events. The horizontal scale along the trenches is the distance along the Himalayan arc. Red dots are rupture trench locations and the yellow line marks the HFT. Horizontal bars are rupture length as in Fig. 3.11. Numbers indicating references. Background image is taken from google earth.

sedimentological studies may offer clues about Himalayan mega-earthquakes (Mugnier et al., 2011). How do our soft-sediment structures differ from seismites? The few outcrops of candidate structures we found are ambiguous, especially as such structures can also form in non-seismic conditions through sediment deposition rather than cyclic shaking

(Fig. 5.7). However, some soft-sediment structures we found (e.g. flames) are distinct and characteristic for non-seismic processes. Yet, some sediment structures in the older sediment pulse layers may represent seismites by the 1255, 1344 AD or even younger earthquakes, though more detailed research is required here. We did not find any traces or any faulting in the area even though the MCT is adjacent to our study area in the north. However, recent faults are being recovered in the past years in the Himalayas (Mridula et al., 2016). The MCT is not visible as a lineament, but rather marks a major topographic break in the area; seismically active in segments (Mukhopadhyay, 2011). Outcrops of the MCT extend over several hundred meters at least and likely mark a broad shear zone (Dhital, 2015); Pokhara area is close to the ramp of the Main Himalayan Thrust where fault ruptures occur, hence earthquake epicenters are usually deeper (Avouac, 2015; Searle et al., 2017).

How does the sedimentology of the Pokhara Formation fit to the interpretation of earthquake triggered pulses? Our sedimentological results point to rapidly settled slackwater deposits that plugged the mouths of tributaries with HH material. We find catastrophic sediment pulses with layers of cohesive debris flows rather than gradual sedimentation. The key for rapid aggradation and settling of massive slackwater deposits is described as lithofacies F3. They resemble lake sediments due to their fine texture. However, they lack the organic carbon content microscopically , characteristic for gradual lacustrine deposition as observed in lakes in the Pokhara Valley (Ross and Gilbert, 1999).

Megaflood sedimentation reflects high-energy, large-scale, and freshwater floods (Carling, 2013). All four lithofacies show such diagnostics of megaflood deposits, as the capping debris-flow facies (F4) thickening downstream, or fine sediment characteristics of lithofacies F2 and F3 upon entering tributary mouths (Carling, 2013; Baker, 1987). In any case, these sediment layers indicate some of the processes likely responsible for the infill. Together with our ^{14}C chronology, we independently test and augment the paleoseismologic data from trenches and offset landforms. The still debated epicenter location, rupture length, and affected shaking areas of the earthquakes remain obscure but our radiocarbon dates might help to refine the affected areas of significant ground motion in complementing the different published data in Figure 5.6. Radiocarbon ages, sediment pulses and catastrophic deposits indicate that the Pokhara valley was filled following at least three medieval earthquakes. Anyhow, there are a few other possibilities such as climatic drivers or outburst flows that are discussed in the following section.

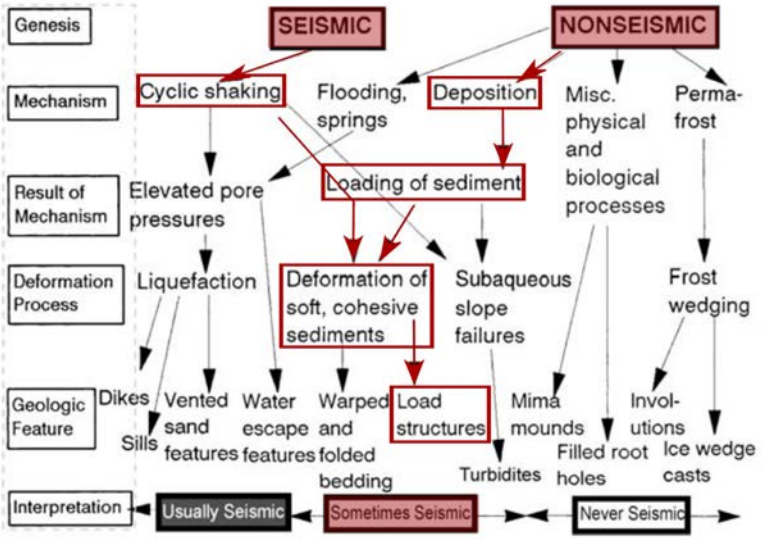

Figure 5.7.: Geological features of sediment deformation. They can either be caused by seismic or nonseismic causes. Features on the left side are usually caused by earthqukes, while those on the right side are never caused by earthquakes. The features found in the Pokhara Formation can be caused (excluding the triggering mechanism) by nonseismic through deposition of sediments pulses on top of older sediments. However, sediment features in the older sediment pulse layers might be caused by the shaking of the second or third medieval earthquake. Modified after Obermeier (2009).

5.3. Process and triggering mechanism

Another key question is which processes we might see as plausible for generating the catastrophic sediment pulses that characterize most of the Pokhara Formation? Candidate processes to mobilize, deliver, and deposits such large volumes of debris-flow material include: 1) numerous smaller, but widespread landslides and debris flows from many sources, 2) one or several giant rock/ice-avalanches or sudden outburst flows from large lakes to produce such debris flows (Chapter 2), and 3) catastrophic outburst floods from naturally dammed lakes.

1) Individual paleoseismological studies and historical documented earthquakes records have shown that large earthquakes can generate massive sediment pulses (Keefer, 2002; Schuster and Highland, 2007) or thousands of landslides (Keefer, 1984; Kargel et al., 2016; Hovius et al., 2011; Marc et al., 2016) mostly commensurate with earthquake magnitude or distance from the rupturing fault in a large area. We exclude this scenario of numerous local landslides as triggering mechanism as our sediment provenance shows evidence for a HH origin of the Pokhara Formation (Fig. 3.6) rather than LHS material that could have come from nearby local hills. However, local coseismic landslide deposits could lie below the Pokhara Formation, while those gravels were

deposited month or years after the earthquake shaking. Examples for local landsliding are numerous earthquakes in Nepal; the most recent ones including their aftershocks in 2015 produced at least 25,000 landslides (Roback et al., 2018).

2) Rock/ice-avalanches may comprise several debris-flow phases in their final runout stage (Korup and Tweed, 2007; Evans et al., 2009a; Shang et al., 2003), but would have had to travel for tens of kilometers to deliver large volumes of debris from the HH to the LHS areas. The storage in the Sabche Cirque is mostly derived from rock/ice avalanches that form a specific type of very coarse subglacial till. According to Kargel et al. (2013) the entire cirque basin was most likely occupied by ice in the Pleistocene, whereas today glaciers have retreated to position along the steep mountain slopes of the Annapurna peaks. Snow avalanches and rock debris from bedrock walls feed the cirque with loose material of about 500-600 m thick waiting to get mobilized, but covered by glaciers and lakes in the upper part (Kargel et al., 2013). One example of such an event is the 1962 Nevado Huascarán mass movements that originated as rock/ice fall but transformed into a sediment-laden flood incorporating with snow and melting water from the glacier (Fig. 5.8A, Evans et al. (2009a)), while entering a major river some 15 km away from the detachment zone (Korup and Tweed, 2007). The event was triggered by an offshore subduction zone earthquake (M_w ~8.7) (Abe, 1972) with an epicentral distance of 150 km, releasing 0.05 km^3 of material (Keefer, 2002).
3) We note (Appendix A) that our radiocarbon dates do not correlate conclusively with the temperature and monsoon proxies for the region (Fig. A.9), nor with available paleoclimatic proxies that we also exclude climatic variability as trigger. The medieval warm (~900-1300 AD) climatic conditions (Rühland et al., 2006; Zhou et al., 2011; Nawaz and Juyal, 2013) may have led to glacial melting that have created moraine dams in the Annapurna Sabche Cirque. Not only moraine, but also landslide or rockslide dams may have blocked the Seti Gorge, creating lakes that are able to release sufficient amounts of melt water catastrophically during a sudden dam collapse. Triggers might have been groundwater erosion, heavy precipitation, landslides or avalanches into the lake, or strong earthquake shaking. The bowl shaped Annapurna Cirque is exceptional as it can hold masses of material for longer times and we do not find something similar anywhere in the Himalayas. Judging from aerial imagery, it seems easy to block the upper Seti Gorge creating a lake with huge amounts of water (Fig. A.6). Catastrophic outburst flows may explain the rapid sedimentation limited to the Pokhara area.

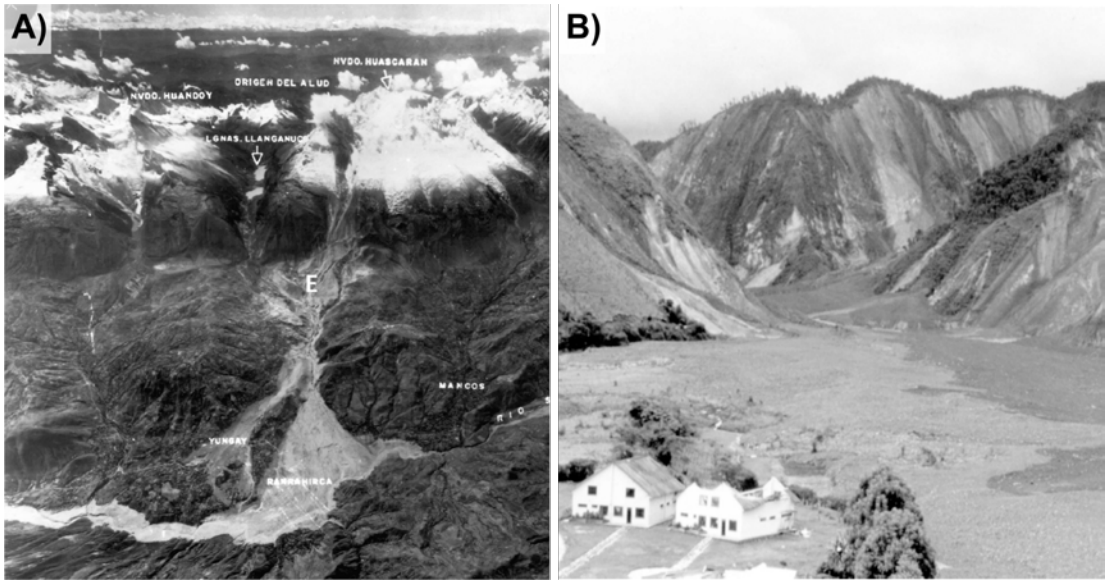

Figure 5.8.: Earthquake-triggered sedimentation events. A) The catastrophic mass flow event at Nevado Huascarán. with its source, path, and deposition devastating the city of Yungay in 1970 (Evans et al., 2009a). **B)** Massive debris flows and slides triggered by the 1994 Paez earthquake in Columbia (Schuster and Highland, 2007).

Consequently, the triggering mechanism of the three sediment pulses might have been a cascade of natural hazards releasing such amounts of sediments. Prolonged rainfall hardly seems an option in the upper Annapurna Massif as the location of rainfall maxima is controlled by the topography near the barrier of the Lesser and Greater Himalaya; here, rainfall peaks at ∼3 km below the highest mean elevation and about 5-6 km below the highest Himalyan peaks (Bookhagen and Burbank, 2006). The few paleoclimatic records for the study region reveal few clues (e.g. snow melting) about potential aseismic triggers. A still unresolved question is how the material traveled across the deep gorge of the upper Seti River between the Sabche Cirque and the apex of the Pokhara Formation fan. One possibility would have been a giant 'jump' or overflow from the cirque on the rocky bar, as observed at the Huascarán event, and because the Seti Gorge is only a few meters wide in most of its length.

In the Himalayas and elsewhere alluvial fans occupying large intramontane basins (Blöthe and Korup, 2013) but none of them are illustrated in such detail as the Pokhara Valley. Though, our radiocarbon chronology of fan sedimentation around Pokhara shares the same distinct clusters of large medieval earthquakes in the Himalayas by judging from the compelling coincidence of valley-fill ages and the timing of earthquakes. We do not think that excluding a seismic origin of the Pokhara Formation is advisable. Several case studies illustrate the complex and multi-phased nature of long-runout debris flows. In

this regard, massive sedimentation in response to earthquakes in the Pokhara area may follow the notion of Jibson (2009): *"Thus, earthquakes can deposit large pulses of sediment into alluvial systems, which can (1) lead to creation of new fans, (2) cause widespread aggradation of channels, (3) provide material for subsequent deposition on fan surfaces by debris flows and hyperconcentrated flows, and (4) affect the overall development of the fan surface on the long term"*. However, sediment pulses released by earthquakes can leave evidence in the depositional record of alluvial systems (Jibson, 2009). Sediment pulses in combination with earthquakes are a gap in literature. Davies and Korup (2007) point out that "the reconstruction of former earthquake-induced sediment pulses requires further detailed research", and large events such as the Pokhara Valley are rather rare. However, earthquake-triggered massive sedimentation events can be found at a few places around the world. Schuster et al. (1996) refer to a mass wasting event in Ecuador in 1987. After a month of heavy rain, the earthquake-triggered soil failures that transformed into fluid debris avalanches and debris flows mobilizing 0.07-0.1 km^3 of material. A similar event in Columbia (Fig. 5.8B) affected an area of 250 km^2 (Schuster and Highland, 2007) by numerous debris flows. In comparison, the three medieval earthquakes in Nepal released roughly >5 km^3 of debris forming the Pokhara Formation. We could picture a similar scenario for the Pokhara Valley; debris-flow and sediment-laden flood deposits as well as a possible equal trigger mechanism, yet, longer run-out distances (70 km) and a fan surface of about 150 km^2.

5.4. Fluvial Response

The uncertainty about the triggering mechanism and transport processes responsible for the Pokhara Formation flank the uncertainty regarding its residual hazard. Little is known about how rivers respond over centuries to the sudden supply of excess sediment. While earthquake-induced mass movements are in many cases the main regional sediment-supply mechanism, much of the material may be stored for years to decades, if not centuries, in the drainage network, before being transported out of the rivers and valleys (Pearce and Watson, 1986; Hewitt, 1998; Hewitt et al., 2008). How long and how much of the material will be stored in a given river system is highly variable and subject to debate (Pain and Bowler, 1973; Dadson et al., 2004; Koi et al., 2008; Matsuoka et al., 2008; Hovius et al.,

2011; Li et al., 2016). Here, we raise the question of how recovery is defined and how much volume remains in the valley while the system is adjusted to a new environment?

Geomorphologists studied the response of sediment budgets (Huang and Montgomery, 2012), river morphology, pre- and post-event denudation rates, and the propagation of knickpoints (Olen et al., 2015), while river sensitivity is a measure of recurrence interval and recovery times (Downs and Gregory, 2004; Fryirs, 2017). We follow this debate and test the consistency of river response and recovery metrics with various proxies (Chapter 4). We investigate upstream infilled tributary rivers of the Seti Khola (Fig. 4.1, inset) with terraces 5 to 50 m thick (upstream at fan margins to the center of the fan) that exist as remnants of the catastrophic formed valley fill. These rivers incised into the valley infill over the last 800 years and are still eroding lateral terrace debris, while vertically incising into the Formation. These terraces formed when rivers switch between incising and aggrading of sediments which is dependent on the balance between river transport capacity and the supply of sediments from nearby hillslopes (Lane, 1955; Scherler et al., 2016). In a dynamic equilibrium input and output to given river reach balance over time by virtue of mass conservation. Ideally, the amount of sediment entering a river is roughly balanced by the river's sediment transport capacity. Rivers are constantly adjusting to approach the balance between incision and aggradation (Scherler et al., 2016). Fryirs (2017) document disturbed river systems with several such estimates but it hinges on how one measures fluvial response and recovery. Moreover, in several studies we find applied concepts on how landscape and rivers response to disturbances with parameters such as thresholds (Schumm, 1979), disturbance type and responses, recovery, and lag times (Allen, 1974; Chappell, 2007), or sediment flux and budget (Walling, 1983); others write about catastrophic disturbances that alter stream-energy and directly initiate channel changes and its response which can affect the entire fluvial system (Simon, 1992). Downs and Gregory (2004) summarize that the probability of change is dependent on disturbing and resistant forces, and adjustment occurs whenever perturbation exceeds the ability of the river to resist the disturbance (Fryirs, 2017). Channel adjustment tend to be rapid after such disorder and leads to spatial and temporal trends of river response towards a new "steady state" from disequilibrium (Simon, 1992). Is it fluvial recovery, response, relaxation, river sensitivity or adjustment? We argue that the combination of these terms leads to protracted recovery (Chapter 4, Fig. 1.5). Moreover, erosion associated with

earthquake induced catastrophic sedimentation is one of the important influences on the topographical evolution (Reading, 1996; Ouimet et al., 2009).

The challenge by using ^{10}Be erosion rates as background denudation for our proxies, are the different apparent integration times that range from 500 to 1,700 years. Therefore, a comparison with our volumetric erosion rates which are calculated over a time range over 660-800 years (Table C.2) is not possible. In this regard, we cannot use ^{10}Be erosion rates as proxy for fluvial recovery in this area as we do not have any measurements to compare before the events happened. Erosion and incision are most relevant to answer the question about recovery times of the Seti Khola river system. The centennial importance of erosion rates is prevalent in comparison with regional slope erosion and erosion inferred from fluvial sediment discharge (Keefer, 1994) over just a few years. We estimate the overall volume of deposited material for the valley infill to 5-7 km^3 (Chapter 3) from which some 1.9±0.2 km^3 (Chapter 4) were eroded by rivers since the early 13^{th} century. According to that, we believe that ∼70% of material still remains in the valley. Although, we do not know the topography of the former valley, nor the volume and size of the older formation (Ghachok Formation) that is sitting below the Pokhara Formation at some places. We find rare information of detailed reviews about different proxies used to define river recovery.

Our estimated erosion rates from volumetric calculations tend to decrease downstream in tributary valleys, but increase with distance in the main river (Fig. 4.5). Numerous knickpoints along the Seti River and upward convex longitudinal profiles reflect ongoing adjustment of the drainage network (Bishop et al., 2005; Wobus et al., 2006); while upstream tributaries highly differ in channel-bed elevations reflecting the ongoing adjustment to trunk-stream aggradation, other tributary mouths have hanging longitudinal profiles (Fig. 5.9). The Seti Khola cuts through older consolidated valley fill deposits (Ghachock Formation) around Pokhara city as it suddenly disappears in a very narrow (10-25 m wide) and steep (up to 70 m) gorge (for example in Ramghat, Pokhara city, Fig. 3.1). However, we could not find any knickpoint clustering in Figure 4.6 related to knickpoint retreat as a function of upslope area (Bishop et al., 2005). We rather find that knickpoints appear randomly distributed with no obvious signs of base-level changes. Nevertheless, using knickpoints in the longitudinal profile as function to the adjustment to a concave channel bed, we argue that we can measure the percentage that is missing for the river to reach this stage of equilibrium. However, Figure 5.9 illustrates that tributaries are unable to keep pace with the faster incising Seti Khola (Goode and Burbank, 2009), developing

Figure 5.9.: Protracted fluvial response revealed through knickpoints at tributary junctions. A) Recently developed knickpoint at the Mardi Khola confluence. **B)** knickpoint at one of the northernmost tributaries within the Pokhara Formation (Sardi Khola). **C)** Saraudi Khola confluence, shortly before one of the bigger knickpoints of the Seti Khola into bedrock. Just upstream of this point, Saraudi Khola gently flows into the Seti Khola but with speed. **D)** Ghatte Khola confluence is almost a waterfall into the Seti Khola, while **E)** Phusre Khola flows parallel for a while but on different elevation levels before joining the Seti Khola downstream (see Fig. 3.1 for tributary locations).

knickpoints at river junctions. Thus, tributaries might have stalled where laterally shifted rivers incise into bedrock (Phillips and Lutz, 2008) or the older Ghachock Formation that lies below the Pokhara Formation in the southern part of the valley (Fort, 1987). In this case, knickpoints can be proxies to measure fluvial recovery times, not as stand-alone proxies but rather in a combination of many, as we do have the exact timing of infill and the possibility to measure fluvial recovery over this specific time frame. Clast counts are another promising measurement for recovery times, when calculating the percentage of local LHS material to HH terrace gravels on active river beds; results range from about 30-70 % of HH abundance in tributary valleys, still waiting to get transported. With

these measurements we try to find a point or better the range on a declining curve since aggradation took place until the full recovery of the river network.

Our calculated volumetric erosion rates range from 1.6-2.1 mm yr^{-1} as amongst the highest values calculated for the Lesser Himalaya (0.2-2.0 mm yr^{-1}) (Andermann et al., 2012). Our discussion of fluvial response is not only linked to river erosion or incision, but is related with the dynamics of subsurface flows within the Pokhara Formation. These high volumetric erosion rates might also be influenced by human activities as extensive gravel mining for construction purposes are conducted along the Seti River (see Chapter 1 for some detailed information). Will it increase incision and erosion by lowering the channel gradient, or will it simply help the river system to faster adjust to its new environment? Gravel pits (Fig. 1.4) are a main issue along Nepal's rivers. Nepalese government officials say about these sites that gravel miners are damaging the rivers, and they should be stopped (Dave, 2013), but if they close them, people are mining illegal at the rivers, which would not improve the mining situation. All the material taken out from the Seti is part of our volumetric estimations, so we may overestimate our incision rates calculated over the past 800 years. We do not have any numbers of how much cubic meters are mined along the Seti river per year, but from other studies (Sayami and Tamrakar, 2007; Manariotis and Yannopoulos, 2014), we do know that channel lowering, bank collapses and the undercutting of bridges and roads are main issues and results of river mining. River mining started some 20 to 30 years ago in the Pokhara area that the proportion to the volume that is being removed since medieval times may not be as large as considered in our measurements.

The Pokhara gravels have a high calcareous content as their sedimentary origin are HH gravels with a high amount of Nilgiri limestone (Waltham, 1972), making the area highly prone to karst weathering and sinkholes. In the Pokhara area we have to distinguish two types of subsurface outwash: 1) karst features that occur in hard conglomerates of the Ghachok Formation in the west and southern parts of Pokhara city and 2) sinkholes that appear and are related to piping within the slackwater deposits (Armala, north or Pokhara city) in relation to fluctuation of groundwater level. New sinkholes of different size develop every year during monsoon season (Kaphle et al., 2007). There have been around 100 sinkholes in 10 years (2004-2014) of which >10 have appeared after 2013 along the Kali Khola (Fig. 3.1) (Rimal et al., 2015). The risk for local people increases, as it does for tourists; many famous places like the Powerhouse, Gupteshwar and Mahendra

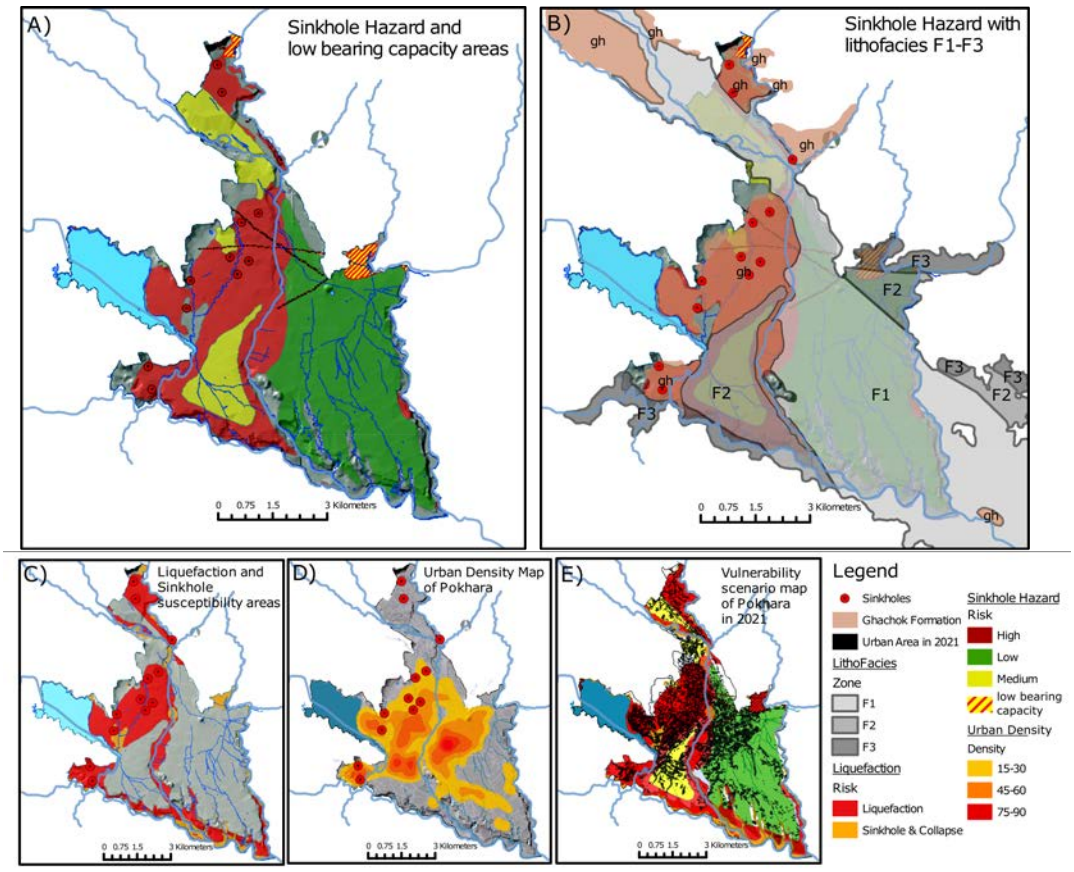

Figure 5.10.: Sinkhole hazard, susceptibility, and vulnerability maps of and around Pokhara city. A) This hazard map shows pronounced sinkholes (red dots) and their hazard including from low (green) to high (red) respectively. **B)** the same map as shown in A) together with our grouped lithofacies (F1-F3, gray) and the Ghachock Formation (brown). Sinkholes clearly occur along the boundary of Pokhara and Ghachock Formation. **C)** Liquefaction and susceptibility areas around Pokhara city. **D)** Urban density map of Pokhara with observed sinkholes. This map underlines how many people live on hazardous ground in and around Pokhara city. **E)** Vulnerability scenario map of Pokhara in 2021. The city is still growing and expanding, not only in low and medium sinkhole prone areas, but also in high risky areas. Figures are combined and (modified after United Nations Develop Program et al., 2009).

cave areas, which are regularly visited by tourists, have a high likelihood of sinkhole development (see geological map with potential sinkhole hazard areas in Fig. C.5 and 5.10, Rimal et al. (2015); Koirala et al. (1998)). Many of the sinkholes close to settlements are filled by river gravels and sands collected from the nearby rivers (Rijal, 2017). Re-filling sinkholes is partly successful, although many of them re-activate due to mining, and heavy rainfalls (Pokhrel et al., 2015b). In the Pokhara area the government agency prompt the re-filling, but during monsoon season, they got washed out from below. Thus, rapid groundwater flows seem the main issue of sinkhole development in the Pokhara and Ghachock Formations (Pokhrel et al., 2015b).

Are these modern hazards part of fluvial response from massive sediment pulses during medieval times? They might as the Pokhara gravels are very calcareous, and the monsoon rain is very strong in this region. With the following outlook, I underline the present issues of vulnerability to natural hazards, population growth in the Pokhara area, and the sinkhole appearance on the fan surface; I combine hazards maps with sedimentological results of this thesis to show further steps and future research possibilities for the Pokhara Valley.

5.5. Outlook and Perspective - The Pokhara Formation as link to contemporary hazards

Recent projections about climate change due to global warming attribute 'extreme' vulnerability to Nepal, making it the 4^{th} most climate vulnerable country in the world, the 11^{th} for earthquakes, and the 30^{th} for flooding (MoHa, 2015) (Fig. 5.11). This mountain region of Nepal is by their rugged topography, high relief, active tectonic process, and intense climatic conditions affected by natural hazards such as earthquakes and landslides, where the southern Terai region has to deal with huge flooding. Thus, these hazards threat the life of its inhabitants (MoHa, 2015). Natural hazard events that occurred recently show the problematic issues as expressed by Gurung et al. (2015): "the event however complex it may seem, is a natural process, which went on to become a disaster due to lack of preparedness". This will be the real challenge for authorities in charge in the Pokhara Valley (Fort et al., in press), but we can help with the geological and geomorphic background, and the response of a river network after such disturbances.

Population growth in mountain regions is often concomitant with poverty and an increase of land use where people have to expand into more hazardous areas exposed to natural hazards (Lennartz, 2015). The combination of natural hazards and an increasing exposition of vulnerable populations raises natural risk and compromises the sustainable development in the long-term (Björnsen Gurung et al., 2012). This situation is seen in the Pokhara Valley (Fig. 1.2). Its population has been growing rapidly (United Nations Develop Program et al., 2009) to ∼250,000 people; the whole valley already is home to more than 400,000 inhabitants in 2010 (Central Bureau of Statistics, 2011). Accordingly, the history of Pokhara city is very short, while the rate of urban development is increasing and high (Adhikari and Seddon, 2002). In the Pokhara area, not only hazards like earth-

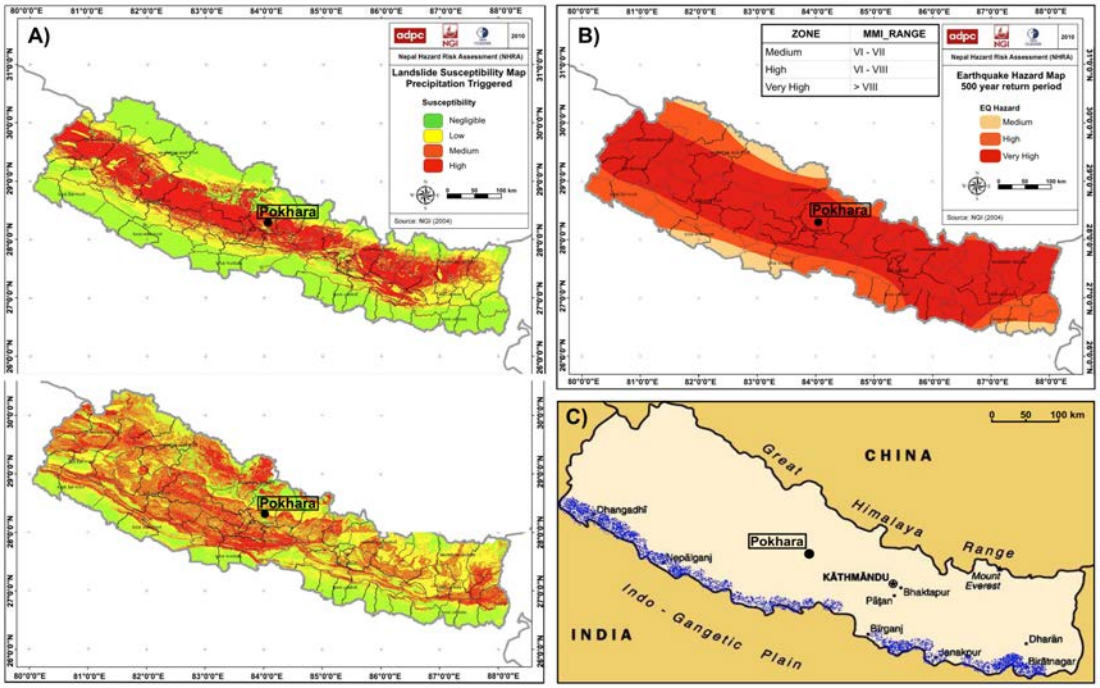

Figure 5.11.: Vulnerability of Nepal to **A)** earthquake and precipitation triggered landslides, **B)** earthquakes and **C)** floods. The maps A) and B) are from ADPC et al. (2010), map C) is part of a Nepal hazard vulnerability map from DG ECHO and Directorate General for Humanitarian Aid and Civil Protection (2012)

quakes, floods, terrace collapses, or undercutting (Dhital and Giri, 1993) are very serious issues, land subsidence and sinkhole collapses threaten the local residents in Pokhara city (Pokhrel et al., 2015b) more frequently than a few years ago.

The deposited calcareous material of the Pokhara Formation is highly prone to karst structures such as sinkholes, subsurface flows, caves, slot gorges, and solution cavities. These are widely developed in the area (Fig. 5.12 and 5.10) not only at the surface, but also the subsurface (Gautam et al., 2000), and are rather hard to judge. Either they are slow and lead to gradual ground subsidence or to catastrophic collapses (sinkholes) (Zhou et al., 2011). Several investigations by Pokhrel et al. (2015a) and Chiaro et al. (2015) during and after the monsoon in 2014 show that not only new sinkholes developed within five months but also several re-activated. Most hazardous seems a shallow weak soil layer which they believe to be the location for future sinkholes.

In Chapter 3, the sedimentological descriptions (Fig. 3.4) of lithofacies F3 (Table 3.2) fit to the whitish clay rich silt layer, very homogeneous and at many locations massive and thick, that are descried by Pokhrel et al. (2015a) as weak layer that is most prone for sinkholes. They observed a 2.5 m high cavity at a depth of 7.5 to 10 m surrounded by such clay and

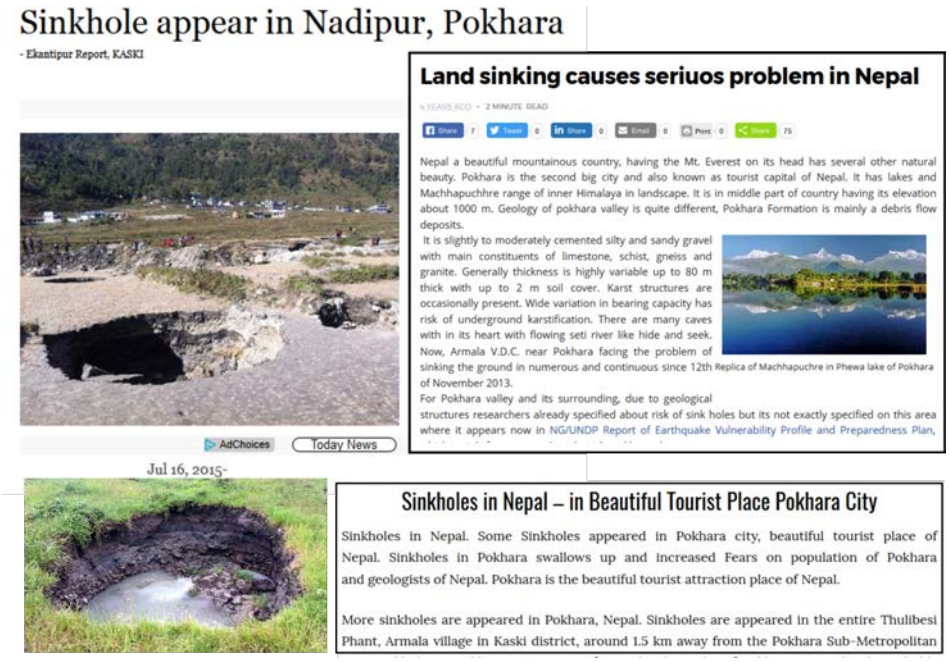

Figure 5.12.: Newspaper articles about recent sinkholes in the Pokhara Area are a main issue for the local people since a few years. Articles are taken from "The Himalayan Times" and "The Kathmandu Post - Ekantipur".

silt layers that may be the layer where sinkholes appear. Additionally, the most recent sinkholes (Pokhrel et al., 2015a) in the Armala region, along Kali Khola, are located within the F3 lithofacies with high clay to silty layers. Sinkholes and sinkhole susceptible areas are going along with our lithofacies (Fig. 5.10B); karst features are recorded within the older Ghachock Formation and along the contact of its terraces to the Pokhara Formation (Fig. 5.10). This contact seems, beside the F2 and F3 silt layers, a main issue where water penetrates into the Formation transferring into subsurface flows. The exact locations of sinkholes and occurrence would need some more detailed research. Nevertheless, most people in Pokhara city live in the high risk zone for sinkholes and liquefaction (Fig. 5.10E), while rapid urbanization will expand on the most hazardous areas. The United Nations Develop Program et al. (2009) Report noted that the status of land use change to urban areas reveals 322% of increase from 1979 to 1996. Since then, urban areas increased to another 116% within the next nine years. Simulations until 2021 show that suitable land for urban areas will reach ∼50% of change, but will expand on high sinkhole hazard susceptible land if the current trend of growing population for Pokhara city continues (Fig. 5.10).

Although, there was not much damage after the Gorkha Earthquake in 2015 in Pokhara, since then, risk of new sinkholes still exists as white turbid water continuously springs

at various locations (Pokhrel et al., 2015b) indicating that subsurface had altered the subsoil conditions and erosion of clayey silt layer is still progressing and disturbed (Chiaro et al., 2015). Besides sinkholes as one serious modern hazard, terrace collapses during monsoon season and liquefaction are two hazardous processes to keep in mind in the future. Summarizing these "modern" hazards, it is alarming that many local residents do not know about them. The flash flood event along the Seti Khola in Mai 2012, was a "small" (0.022 km^3) event showing that the Annapurna cirque clearly is prone to catastrophic rock avalanches, and still contains masses of material awaiting to get transported (Bhandary et al., 2012). The event is a warning of what can happen again in the near future and a reminder of the past medieval events illustrated in this thesis. This rock-wall collapse was not triggered by rainfall nor an earthquake, but large enough to destroy the villages north of Pokhara at the Pokhara fan apex.

Future research should focus on the protection, from future hazards, of the Pokhara Valley residents. We show that modern hazards as further step following the results of Chapter 4 can reduce the vulnerability by informing the population which would raise people's awareness. Investigations can be geophysical methods such as the implementation of detailed hazard and risk maps, geotechnical surveys prior constructions, and subsurface imaging to research subsurface structures and in the best case, to find cavities in the area. More observations on the sedimentology (lithofacies F1-F4, Fig. 5.10) and the combination or connection to sinkholes would help to understand the mechanism but also to find out those sediment layers that are water soluble. However, despite the promising results from this thesis, frequent earthquakes, floods and landslides in Nepal may require future study and in this situation worth looking into more closely. Specifically the details behind the process and event that was able to release such amount of material in very short time. We argue that the Pokhara valley is unique or outstanding in its geology, climate condition, and geomorphic features and we were not able to find something similar in its size, deposits and geomorphic setting anywhere in mountain areas to compare our results. But we show the one example of a very young but massive valley fill that is the perfect place to research more on sediment archives, valley fill geomorphology, fluvial adjustment, and (in future) on resulting "modern" hazards with the issue of population growth into more hazardous areas.

6 Conclusion

The Pokhara Valley and its geomorphic legacy of at least three earthquake-driven sedimentation pulses are unique in the Himalayas. Long-runout debris flows from a single HH source in the Annapurna Massif with widespread sedimentation up to 70 km downstream characterizes the fan morphology rather than aggradation in response to local coseismic landsliding. Our detailed sedimentary and provenance analyses reveal tributary plugging by rapid fluvial aggradation shown in extensive sediment beds dipping upstream into these catchments. Our sedimentological catalog is the first systematic inquiry of the Pokhara Formation. The entire fan sedimentology is grouped to four lithofacies that offer key diagnostics of catastrophic sedimentation, fining from big boulders and gravels in the fan center to tributary mouths and slackwater deposits that fill tributary catchments upstream to the fan margin. Samples of radiocarbon dates are taken on the entire fan and conspicuously cluster to medieval times, establishing that these pulses are largely coincident with three documented dates of great Himalayan earthquakes. Not only the sedimentology and ^{14}C ages but also XRF spectrometry support the hypothesis of these three earthquake connected to fast aggraded sediment pulses. The spatial and temporal relationship of 37 ^{14}C ages in combination with sedimentological findings corroborate the previous assumption of rapid sedimentation giving clues to the individual volumes of each pulse and the entire valley infill. We follow the logical way thinking about the response after strong perturbation and come up with a number of independent proxies testing adjustment and recovery times. We use dated re-exhumed tree trunks that record a fast and continuous aggradation in the early 13^{th} century. Their location and exposure reveal that the river-bed may have almost reached its former elevation, whereas only the upper 12% of the active channel stores local LHS deposits yet. Clast count measures to the percentage of HH verses LHS deposits range from 30-70% for different tributary catchments, while the longitudinal profile of the entire river network shows that there are 30% missing to reach equilibrium and to recover from perturbation. Contemporary rates of river incision and sediment yields

remain very high, triggering bank erosion, terrace collapses and local ground subsidence. The Pokhara Valley needs centuries to recover from earthquake perturbation in medieval times, as ∼70% of the catastrophic deposits still remain untouched in the valley today. Such geomorphic legacy is important to acknowledge in post-seismic hazard appraisals. With this study, we offer the first evidence that earthquake-induced catastrophic sedimentation in mountain rivers may protract fluvial, and hence also, landscape response much more than previously documented. The geological past of the Pokhara valley gives insight to the long-term geomorphic impact of Himalayan earthquakes on major drainage basins and helps to investigate the consequences on 'modern' hazards. Our results motivate some rethinking of post-seismic hazard appraisals and infrastructural planning in mountainous regions and shows that natural hazards and anthropogenic factors influence the environment. The rapid growing population has induced arbitrary urbanization, diffusing to high vulnerable parts of the city, and increasing the vulnerability and potential risk for those people that are living in the Pokhara Valley. This study results in the largest, youngest and most extensively dated sediment records of valley infill today, combining the geologic and geomorphic past with the present dramatic landscape involving modern hazards and population growth.

A

Appendix

Supplementary Content: Study I

Repeated catastrophic valley infill following medieval earthquakes in the Nepal Himalaya

Wolfgang Schwanghart[1], Anne Bernhardt[1], Amelie Stolle[1], Philipp Hoelzmann[2], Basanta R. Adhikari[3], Christoff Andermann[4], Stefanie Tofelde[1], Silke Merchel[5], Georg Rugel[5], Monique Fort[6], Oliver Korup[1]

[1]Institute of Earth and Environmental Science, University of Potsdam, Potsdam, Germany.

[2]Institute of Geographical Sciences, Freie UniversitÃđt Berlin, Berlin, Germany.

[3]Institute of Engineering, Tribhuvan University, Kathmandu, Nepal.

[4]Helmholtz-Zentrum Potsdam, German Centre for Geosciences GFZ, Germany.

[5]Helmholtz-Zentrum Dresden-Rossendorf, Helmholtz Institute Freiberg for Resource Technology, Dresden, Germany.

[6]CNRS UMR 8586 Prodig, DÃľpartement de GÃľographie, UniversitÃľ Paris-Diderot-SPC, Paris, France.

This supplementary content has been published within the following publication: *Schwanghart, W., Bernhardt, A., Stolle, A., Hoelzmann, P., Adhikari, B.R., Andermann, C., Tofelde, S., Merchel, S., Rugel, G., Fort, M., Korup, O., Repeated catastrophic valley infill following medieval earthquakes in the Nepal Himalaya. Science (New York, N.Y.), v. 351, no. 6269, p. 147-150, doi: 10.1126/science.aac9865*

Materials and Methods

Radiocarbon sampling and modeling

The Pokhara Formation has so far eluded any direct dating, mainly because it lacks organic material. Eight previously reported ^{14}C dates (Fort, 1987; Yamanaka et al., 1982) come from samples of peat layers, humic silt or wood remnants found in fine-grained sediments exposed in the ponded tributaries of the Seti Khola (Figs. A.1 und A.2). We add 18 new samples that we collected in September 2012, March 2013, and October 2014 (Table A.1). We recovered two samples from fine-grained slackwater deposits in the Saraudi Khola and Magdi Khola ~2 and ~5 km upstream of their confluence with the Seti Khola, respectively. We also sampled these deposits in the lower Phusre, Anpu, Saraudi, Magdi, and Gondang Khola, which are all major tributaries of the Seti Khola (Fig.2.2).

We used OxCal4.2 (`https://c14.arch.ox.ac.uk/`) and the IntCal13 curve to specify several Bayesian models for calibrating our ^{14}C ages to calendar years (Bronk Ramsey, 2009b). The advantage of Bayesian calibration of ^{14}C ages is that it allows incorporating explicitly our prior beliefs about the relative stratigraphy of the ages that we derived from the field context (Bronk Ramsey, 2009b). Apart from generating calibrated calendric ages, we were also interested in learning whether these were linked to documented medieval earthquakes or simply spread throughout time without any clear pattern. To this end, we investigated several possible models: The simplest approach for calibration is a uniform prior for a single phase delimited by the oldest and youngest ^{14}C ages. The model input consists of the sorted uncalibrated ^{14}C dates, assuming that all of the dates are equally likely to occur anytime during the phase.

We also calibrated our ^{14}C ages using a prior informed by field stratigraphy and the assumption that our samples captured three sedimentation phases that we tied to earthquake dates at ~1100, 1255, and 1505 C.E. These $M > 8$ earthquakes have well established ages with rupture zones large enough such that strong seismic shaking would have affected the Pokhara region (Rajendran et al., 2015). The motivation for assuming three sedimentation phases comes from the calibration using the uniform phase model, which returns a pooled posterior distribution with three distinct peaks close to those dates. We ran both uniform and exponential phase models (Bronk Ramsey, 2009b), but found no significant differences in the resulting posterior distributions that largely emphasize the peaks of the uniform phase model. The informed prior assuming sedimentation phases tied to medieval earthquakes further emphasizes the three peaks in our uniform phase model (Fig. A.4, Table S2). Similarly, adding the 1344 C.E. earthquake as another distinct phase hardly changes

our results. Hence, even without including the timing of large medieval earthquakes in our prior assumptions, the calibration returns distinct peaks in the pooled posterior distributions very similar to those that we would obtain if including knowledge about these earthquakes beforehand. We excluded a potential earthquake in 1408 C.E., as this is likely the same event as the one in 1344 C.E. due to calendric revisions (Rajendran et al., 2015). We used a clustering-based Gaussian mixture model (Fraley and Raftery, 2003) with a Bayesian Information Criterion to objectively extract the major contributing peaks in the posterior distributions assuming that mapping of Gaussian distributed ^{14}C data onto the calibration curve return mixed Gaussians in calendric ages. Regardless of whether we choose a uniform-phase model or one that includes three or four distinct sedimentation phases tied to medieval earthquakes, the Gaussian mixture model consistently reproduces three major peaks at 1045-1075, 1204-1233, and 1337-1361 C.E. We relate these peaks to the 1100, 1255, and 1344 C.E. earthquakes, respectively (Fig. A.4). We calibrated our ^{14}C ages using additional stratigraphic constraints from field observations. At Phusre Khola (Fig. 2.1), we obtained four ^{14}C samples from an outcrop in their stratigraphic context such that we modeled this as a single phase.

We further tested whether the calibrated dates were randomly distributed through time. We searched for a potential Poisson process in the data by checking whether the intervals between successive dates approximated an exponential distribution. We generated N = 10,000 sets containing 26 dates each by randomly sampling from the posterior distributions of the calendric ages obtained from the uniform-phase calibration, assigning weights scaled to the posterior probability densities. We then computed the empirical and theoretical exceedance probabilities for the time spans between successive dates for each of the 10,000 simulated sets. We expressed our confidence of detecting a Poisson process in the data by the percentage of all sets that had a root mean squared (RMS) deviation <0.05 between the measured and the theoretical exceedance probabilities. Based on this approach we exclude with 95% confidence that the 26 dates are randomly distributed in time (Fig. A.3).

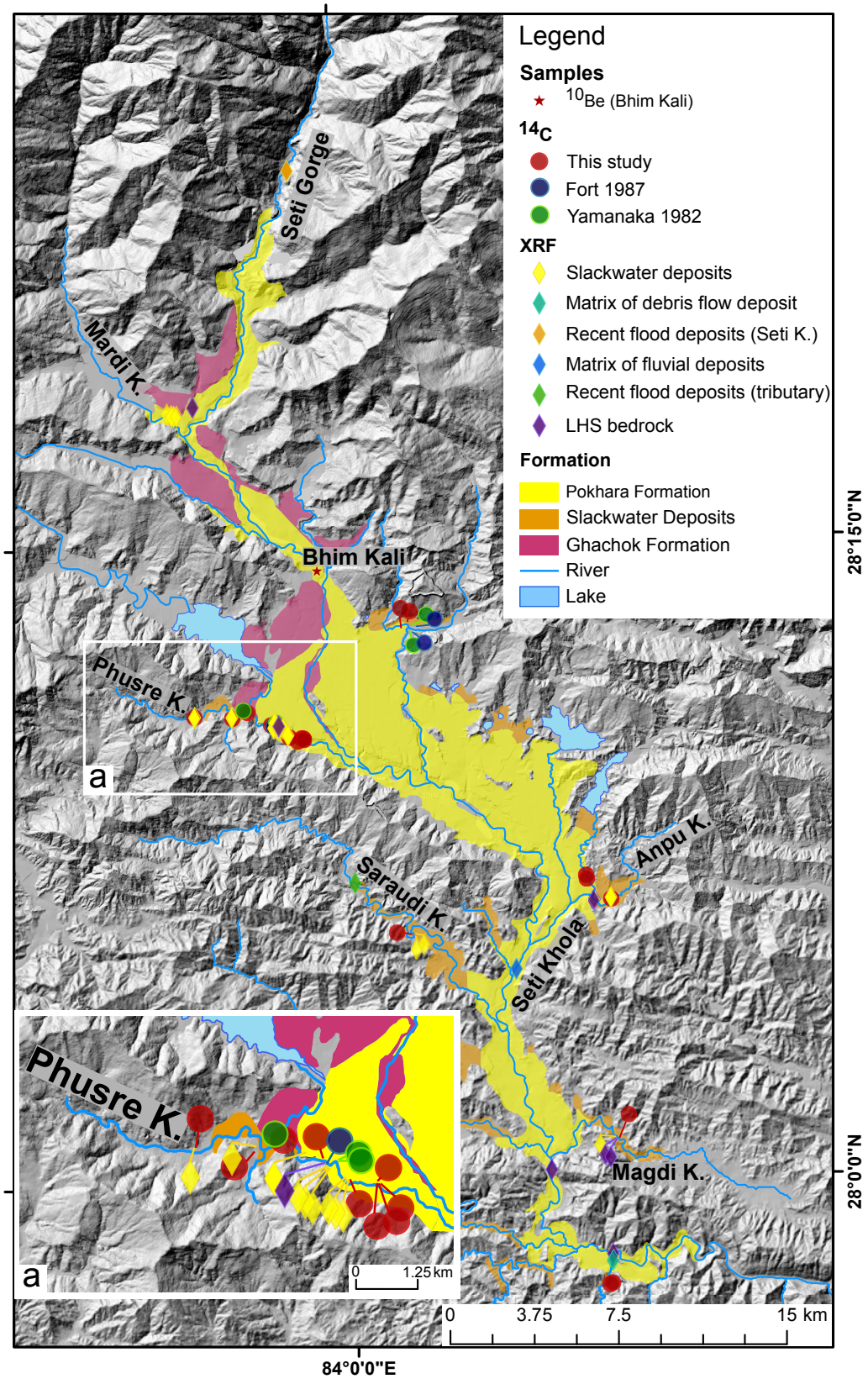

Figure A.1.: Locations of samples for radiocarbon dating and x-ray fluorescence analysis (see Fig. 2.1 for general orientation).

Figure A.2.: Field photos of slackwater deposits of the Pokhara Formation containing organic debris, and crystalline Bhim Kali boulder. Organic debris includes (A) intact leaves, (B) partly intact logs, (C) ripped-up soil pocket incorporated into debris-flow deposits, (D) and organic layers between silt and sand beds. (E) Sampling the top surface of the 11-m long Bhim Kali boulder for ^{10}Be exposure dating.

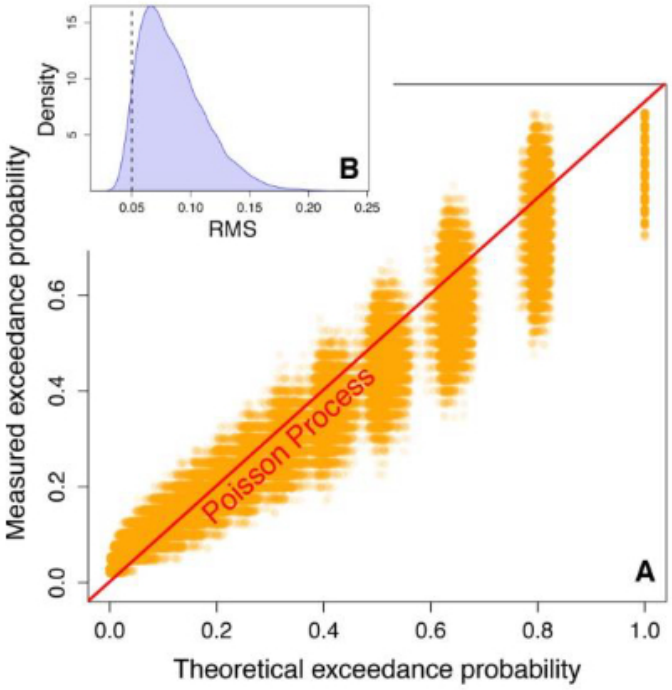

Figure A.3.: Test results for temporal clustering of 26 ^{14}C dates from tributaries of the Seti Khola, Pokhara region. (A)Set of N = 10,000 measured versus theoretical exceedance probabilities (orange dots) of intervals between 26 successive calibrated ^{14}C dates in tributaries around Pokhara, sampled from the modeled posterior distributions in Fig. A.4. Red 1:1 line shows theoretical point pattern for a Poisson process. (B) Probability density estimate of root mean squared deviation of measured from theoretical exceedance probabilities. Vertical dashed line indicates that ~5% of all differences in probabilities have a RMS <0.05, which we set as the maximum tolerance for finding a Poisson process in the data. Hence we infer that the calendric ages are not randomly distributed in time.

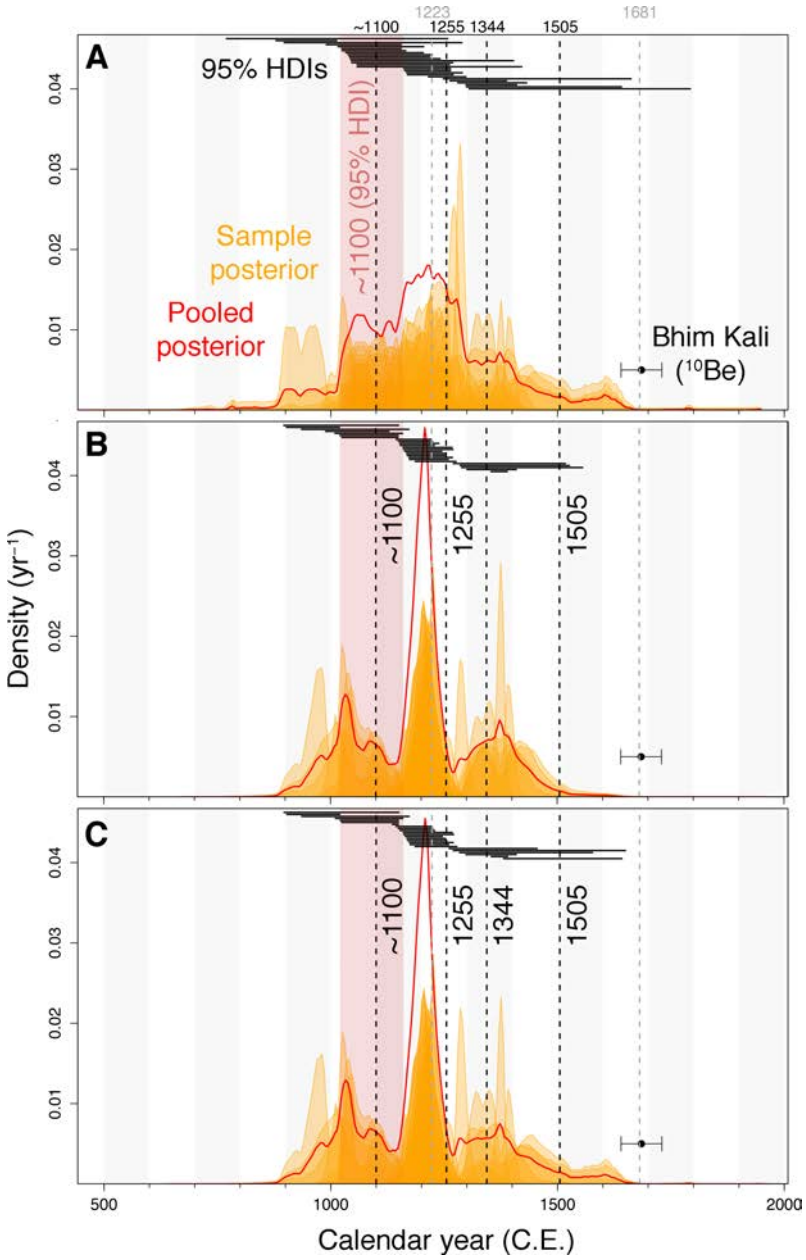

Figure A.4.: Posterior probability density functions (orange) of 26 ^{14}C ages from Bayesian calibration using OxCal4.2 and the IntCal13 curve, and cosmogenic ^{10}Be in situ exposure age of the Bhim Kali boulder. (A) Uniform-phase model with pooled posterior (red) have three distinct peaks coinciding with major historic and inferred earthquakes at ~1100, 1255, and 1344 C.E. (black dashed lines; gray dashed lines are other historic earthquake dates with little information on rupture extent). Horizontal lines are 95% highest density intervals (HDIs) of the 26 dates. Red box is 95% HDI (1020-1160 C.E.) for the ~1100 C.E. earthquake from seven published ^{14}C ages (Galetzka et al., 2015) that we re-calibrated for consistency. (B) Three-phase model assuming uniform spread of ages related to three earthquakes in ~1100, 1255, and 1505 C.E. (C) Four-phase model assuming uniform spread of ages related to four earthquakes in ~1100, 1255, 1344, and 1505 C.E. Note how all models return three major and consistent peak locations in the pooled posteriors. Whiskers are $\pm 1\sigma$ uncertainties around the ^{10}Be exposure age.

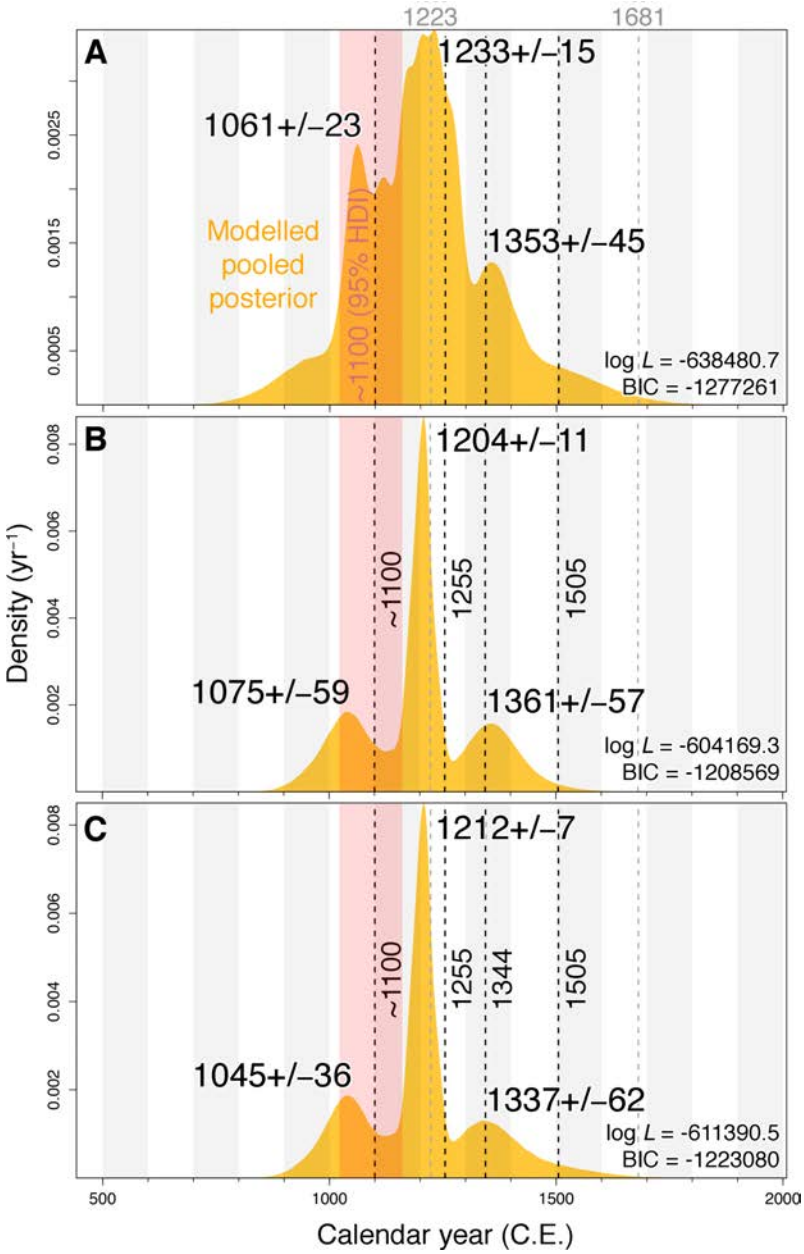

Figure A.5.: Modeled pooled posterior distribution of calibrated ^{14}C ages using a clustering-based Gaussian mixture model. Shown here are only the three most distinct peaks for (A) uniform phase model (mix of nine Gaussian components), (B) three-phase model assuming uniform spread of ages tied to three earthquakes (mix of nine Gaussian components), and (C) four-phase model assuming uniform spread of ages tied to four earthquakes (mix of seven Gaussian components); log L is log likelihood, and BIC is the Bayesian Information Criterion for full model cases that include minor peaks in the modeled distributions. Dashed lines are dates of large medieval earthquakes. Gray dates refer to other historic earthquake dates with little information on rupture extent.

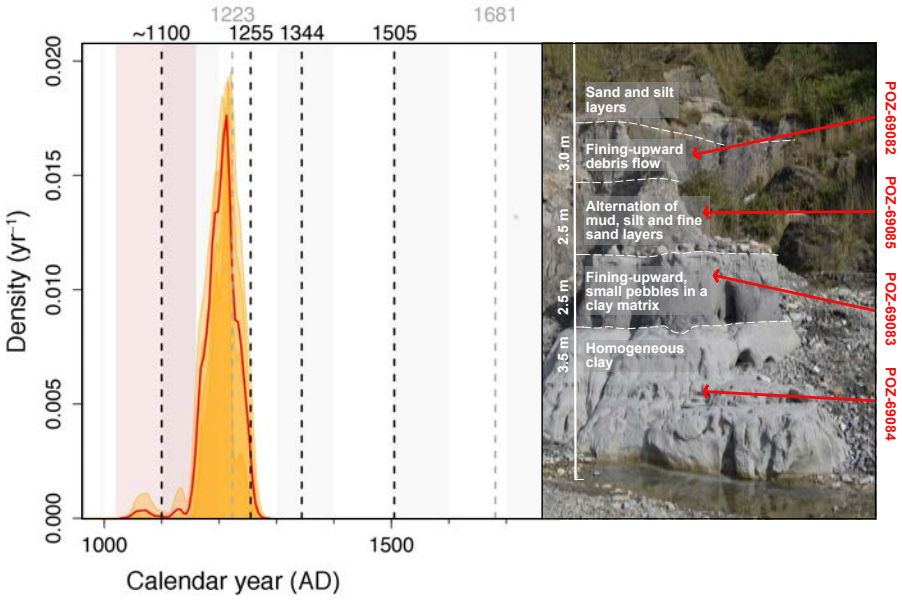

Figure A.6.: Posterior probabilty density function (orange) of four [14]C ages at Phusre Khola using OxCal 4.2 and the IntCal13 curve. Inset shows photo of field setting and major sedimentary units. The calibrated ^{14}C dates are indistinguishable, so that we cannot establish whether aggradation occurred in several successive pulses or during a single event.

Cosmogenic ^{10}Be exposure dating

We sampled Bhim Kali (28.24°N, 83.99°E, 920 m a.s.l., Fig. A.2), a fluvially sculpted HHC gneiss boulder with a diameter of 11 m lodged on top of the Pokhara Formation for cosmogenic ^{10}Be exposure dating. The prominent 3000-ton metamorphic boulder is located in the premises of the Prithivi Narayan Campus, ~200 m from the right bank, and 50 m above the active channel bed, of the Seti Khola. We chiseled rock chips (~2 cm) from a bare and flat rock surface on top of the boulder that showed no evidence of erosion or weathering. We extracted pure quartz minerals with standard mineral separation techniques (Wittmann et al., 2007). The cleaned sample was spiked with ~300 μg of a ^{9}Be carrier (made from phenakite at the University of Hannover, Germany). The total Be inventory (^{10}Be and ^{9}Be) was extracted with standard chemistry methods (Wittmann et al., 2007), ignited to BeO and mixed with Nb for accelerator mass spectrometry (AMS). The sample was analyzed at the AMS facility in Dresden/Rossendorf DREAMS, Germany, against the secondary standard SMD-Be-12 (ref. (Akhmadaliev et al., 2013)). The ^{10}Be/^{9}Be analyses are traceable via cross-calibration to the primary standard NIST-SRM 4325 with a ^{10}Be/^{9}Be ratio of (2.79 ± 0.03) x 10^{11} (Nishiizumi et al., 2007).

We calculated the production rate P(0) and shielding factor S_{topo} using a ~90m digital elevation model (Jarvis et al., 2008). The elevation scaling scheme of P(0) was calculated after Stone (2000) for the constant reference latitude of 30°N and a ^{10}Be sea-level corrected (1.387 x 10^{6} yr, Korschinek et al. (2010)) weighted mean of the published SLHL production rates (Balco et al., 2009; Briner et al., 2012; Fenton et al., 2011; Goehring et al., 2012). $\lambda_{neut.}$, λ_{μ} stopped and λ_{μ} fast parameters are 160, 1,500, and 4,320, respectively (Braucher et al., 2011). For the exposure calculation we used CosmoCalc 2.2 (Vermeesch, 2007).

The cosmogenic exposure age that we obtained from the top of the boulder is in excellent agreement with the timing of a major earthquake in 1681 AD. While we cannot rule out a simple coincidence based on this single date, the low concentration of cosmogenic ^{10}Be in this boulder does not cater for any significant inheritance from a previous exposure history. Instead, the boulder must have been moved or unearthed some 330 years ago, either by highly competent water-sediment flows or by toppling. Paleohydraulic flow competence estimates (O'Connor, 1993) based on the boulder's size require a minimum flow velocity of ~20 m s^{-1} and a basal shear stress of $>10^{3}$ N m^{-2} for onset of motion. Even a scenario in which the boulder was etched from the surrounding Pokhara Formation requires that large floods or debris flows impacted the Pokhara fan surface as recently as 330 years ago,

in addition to those events that we capture by our radiocarbon chronology. Subsequent downcutting of the Seti Khola into the post-seismic debris would have been extremely rapid at an average rate of 150 mm yr^{-1} to satisfy the current channel-bed elevation. Alternatively, and in the absence of any local undermining, a toppling of the boulder in dry conditions is difficult to explain unless aided by strong seismic ground motion. In either case, the strikingly low ^{10}Be concentration of Bhim Kali's top independently supports the geologically very recent and active history of the Pokhara Formation and its link to large earthquakes and coeval sedimentation pulses, while providing a minimum age for the Pokhara Formation. Historic photos (Fort, 1987) show that the Pokhara fan surface featured many braided channels before it was transformed by the rapidly growing city. We suspect that several other smaller boulders, which are visible today on Pokhara's streets, are remnants of a coarse surface deposit that had been quarried for building houses and roads, as in common practice in Nepal (Fort, 1987).

X-ray fluorescence spectrometry (XRF)

We used a portable Analyticon NITON XL3t energy-dispersive x-ray fluorescence spectrometer (P-EDXRF) equipped with a CCD-camera and a semi-conductor detector for analyzing the elemental composition of 29 samples that we took from bedrock, flood-, debris-flow, and slackwater deposits in the Seti Khola and its tributaries. We crushed bedrock samples placed into plastic bags, homogenized all samples using an agate swing mill, and kept them dry at 55°C. We placed ~4 g of the powdery samples into plastic cups and sealed them with a mylar foil (0.4 μm). The cups were mounted on the P-EDXRF and measured for 120 s with different filters to detect specific elements (Table S4). We calibrated the P-EDXRF using the certified reference material (CRM) GBW07312 (stream sediment) Lot. Nr. 200560 and re-checked the calibration with the CRM every ten measurements. Table S5 shows the recovery values for CRM GBW0731. We took into account only those elements that had minimum values two times larger than their 1σ measurement uncertainty (Al, Ca, Cl, Fe, K, Rb, Si, Sr, Ti) (Database S1). We analyzed the elemental compositions in a hierarchical cluster analysis using Ward linkage and a Euclidean distance metric to identify classes of sediments with similar geochemical signatures. Prior to clustering we transformed the data using centered log ratios to account for the requirements for measuring differences in a compositional dataset (Pincus, 1988). To quantify the effects of measurement uncertainty on the classification results, we carried out 10,000 numerical experiments, each time deriving three classes. In each of these runs we added

offsets to each data value randomly drawn from a normal distribution with zero mean and standard deviation informed by the analytical measurement error of the XRF analysis. None of these simulations changed the class membership of any of the samples.

X-ray diffraction analysis

We examined qualitative and semi-quantitative mineralogical compounds by x-ray powder diffraction. An air-dried powdered sample (~1-10 μm particle diameter) was pressed without regulation into the sample holder and analyzed with a RIGAKU Miniflex600 diffractometer at 15 mA/40 kV (Cu kα) from 3°to 80°(2θ) with a goniometer step velocity of 0.02°steps and 0.5°min^1. We used the software X-Pert HighScore Version 1.0b by PHILIPS Analytical B.V. for semi-quantitatively identifying the mineral composition. Within this program outliers were corrected, the kα_2-Peaks were eliminated, calibrated to the quartz100 main peak (d = 3.34). Powder Diffraction Files (PDF) of the ICDD (International Centre for Diffraction Data) were used to identify the peaks.

Outburst flood modeling

We used a 15 m-digital elevation model derived from topographic contours (Department of Survey, 1996) to estimate the maximum sediment and water volume that hypothetical landslide dams of four arbitrarily defined heights could accommodate at each channel pixel along the Seti gorge. We derived volumetric estimates for dam heights of 300, 500, 1000 and 1500 m above the present river, and corrected for the upstream facing landslide-dam volume. We calculated peak discharges from a dam-break model (Walder and O'Connor, 1997; O'Connor and Beebee, 2009) assuming a full breach, complete emtying, and the highest reported dam-breach rate of 1000 m h^{-1} (Walder and O'Connor, 1997) to constrain the plausible maximum flow peaks.

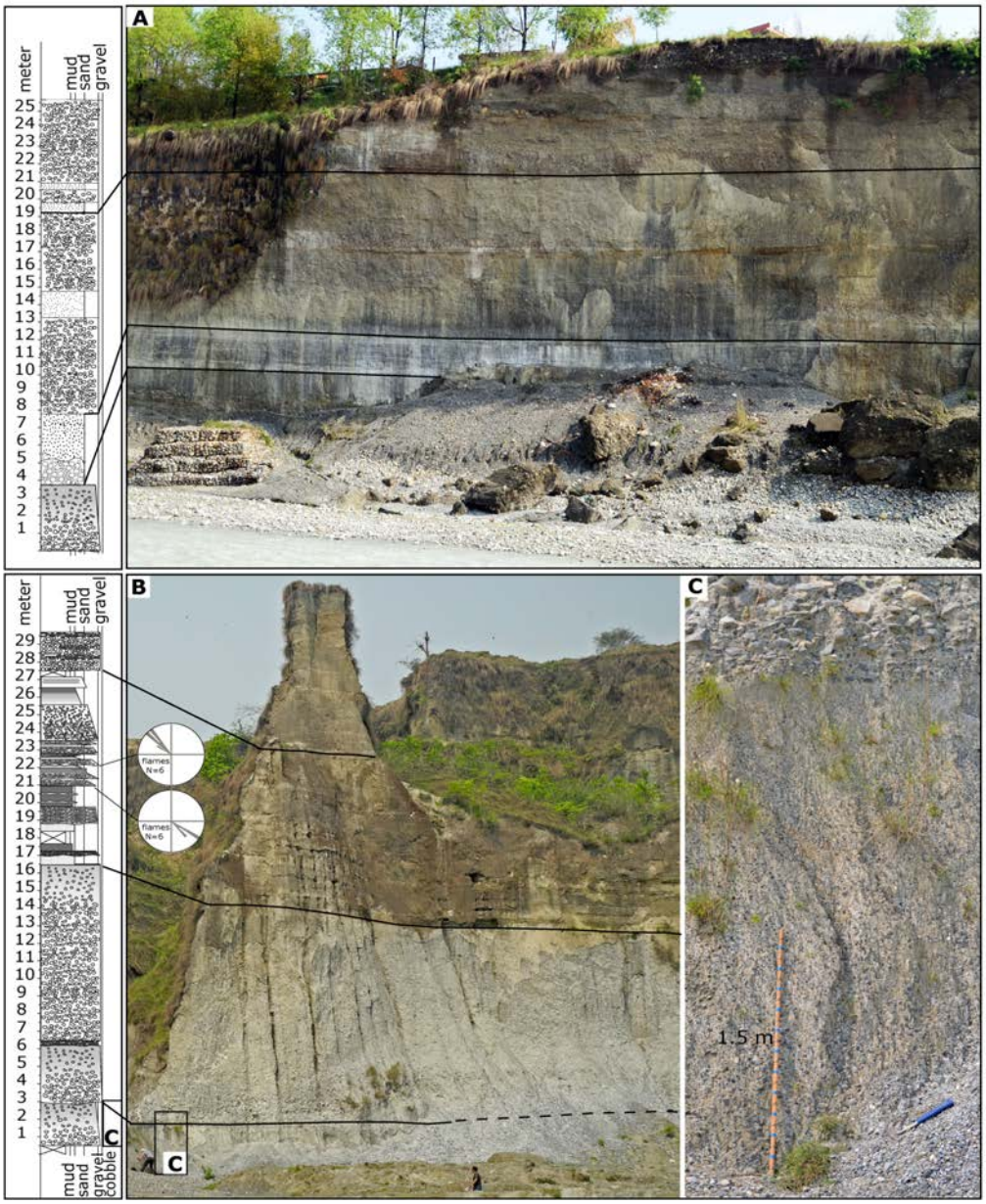

Figure A.7.: Stratigraphic logs of the Pokhara Formation. (A) Type location of the Pokhara Formation within the main Seti Khola valley at Ramghat. The section exposes laterally continuous and several meter-thick poorly sorted, clast-supported conglomerates devoid of current structures, interpreted as deposits that rapidly settled during fully turbulent, sediment-laden flow. (B) Type location of the valley-marginal deposits of the Pokhara Formation at Magdi Khola. The lower 16 m of the section feature three units of mud-matrix supported, fining-upward conglomerate that we interpret as debris-flow deposits. The upper section between 19 m and 27 m has intercalated pebble conglomerate, sand, silt, and clay layers with opposing paleocurrent indicators (flame structures) topped by clast-supported fluvial conglomerate. (C) Detail of the basal debris-flow unit.

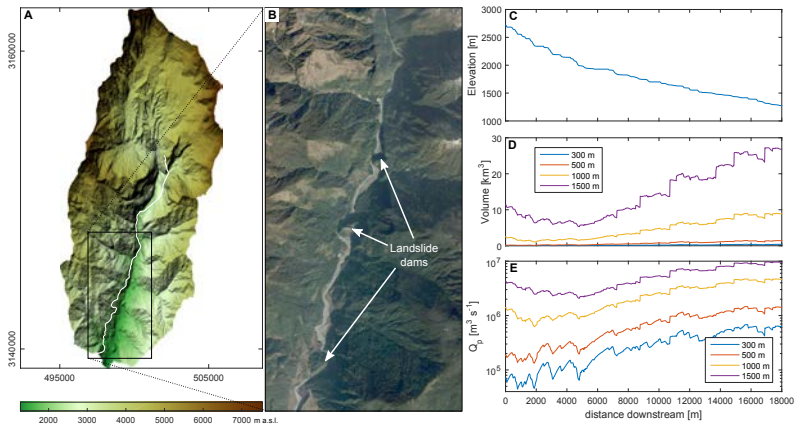

Figure A.8.: Numerical simulation of potential lake volumes and peak discharge from catastrophic lake outbursts, upper Seti Khola. (A) Shaded relief of 15-m digital elevation model of the upper Seti Khola. (B) High-resolution satellite imagery (Source: Digital Globe, Google Earth) showng three former 100-300 m high landslide dams in the gorge. (C) River longitudinal profile; (D) Maximum lake volumes that could be impounded in the Seti Khola for four hypothetical landslide-dam heights; (E) Estimated peak discharge Q_p following the catastrophic release of the water volumes computed in D.

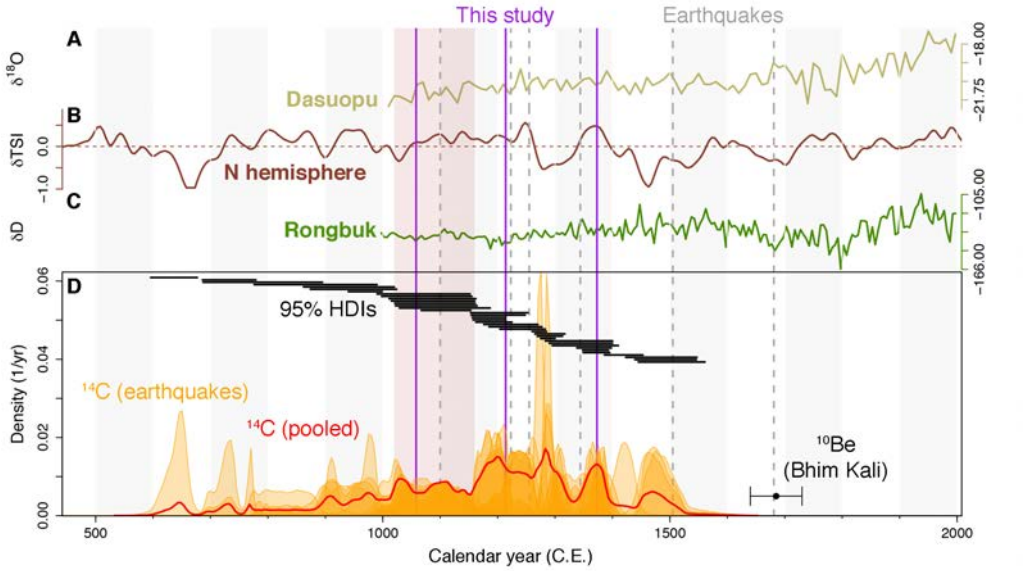

Figure A.9.: Time series of paleoclimatic proxies and calibrated ^{14}C dates (orange) used to establish the timing of medieval earthquakes (gray dashed lines). Paleoclimatic proxies include (A) δ^{18}O from ice-core record of Dasuopu glacier in eastern Nepal as a proxy of summer temperature (Thompson et al., 2000); (B) anomaly of total solar irradiance (δTSI, measured in [W m^{-2}]) derived from cosmogenic nuclide production for the northern hemisphere (Steinhilber et al., 2009); and (C) δD from ice-core record of Rongbuk glacier in eastern Nepal as a proxy of summer monsoon precipitation (Kaspari et al., 2007). None of the three sedimentation phases in D show any consistent timing with peaks of lows in these paleoclimatic time series. (D) Calibrated ^{14}C of large medieval earthquakes in the Himalayas. Black horizontal lines are 95% HDIs. Purple lines show locations of maximum posterior densities for the 26 ^{14}C dates of slackwater sediments in the Pokhara region.

Interpretation: Climate oscillations such as the Medieval Warm Period or the Little Ice Age could have propted glacier advances and the subsequent formation of one or several moraine dams in Sabche Cirque. If long-lived, such moraine dams can retain sufficient amounts of meltwater to be released catastrophically during sudden dam collapse induced by groundwater erosion, heavy rainfall, landslides, or avalanches into the lake, or strong earthquake shaking. Alternatively, degrading mountain permafrost during warmer periods could have contributed to gradually lowering rock-mass shear strength. Higher air temperatures could thus have favored lower triggering thresholds for large rock or rock-ice avalanches from the high-altitude rock sloes in the Annapurna Massif. However, our ^{14}C ages show no obvious correlation with extremes or trends in the available temperature and rainfall paleoclimatic proxies, and thus offer little support for climatic triggers of catastrophic medieval aggradation in the Pokhara valley.

Table A.1.: Radiocarbon ages. The table also contains recalibrated ^{14}C ages reported in previous studies (Yamanaka et al., 1982; Fort, 1987).

Lab.No	Sample ID	Location	Lat [°N]	Long [°E]	Elevation [m asl]	Material	Radiocarbon age [Y BP]	Calibrated age [cal. Y BP]	Reference
BS-464	83-PQ523	Bijaypur Khola	28.21	84.029	-	Charcoal	390 ± 110	420 ± 100	Fort (1987)
BS-465	83-PQ525	Bijaypur Khola	28.21	84.023	-	Wood	510 ± 140	510 ± 130	Fort (1987)
Gif-6220	83-PQ641	Phusre Khola	28.18	83.971	-	Wood	450 ± 100	470 ± 100	Fort (1987)
-	TH-719	Power station, Phusre Khola	28.18	83.971	-	Wood	750+100/-90	710 ± 90	Yamanaka et al. (1982)
-	TH-720	Power station, Phusre Khola	28.18	83.971	-	Wood	970+100/-110	900 ± 110	Yamanaka et al. (1982)
-	TH-721	Shharepatan	28.186	83.956	-	Humic Silt	1070 ± 100	1010 ± 120	Yamanaka et al. (1982)
-	TH-722	Bijaypur Khola	28.215	84.03	-	Peat	590 ± 110	600 ± 70	Yamanaka et al. (1982)
-	TH-723	Bijaypur Khola	28.218	84.031	-	Peat	770+100/-110	750 ± 90	Yamanaka et al. (1982)
COL1915.1.1	BIJ02	Bijaypur Khola	28.219	84.029	820	Humic Silt	772 ± 46	720 ± 30	Yamanaka et al. (1982)
COL1916.1.1	PH02C	Power station, Phusre Khola	28.18	83.968	730	Leaves	846 ± 42	790 ± 60	This study
COL1917.1.1	PHUSRE03	Phusre Khola	28.183	83.951	740	Charcoal	944 ± 46	870 ± 60	This study
COL2150.1.1	SARA1-1	Saraudi Khola	28.096	84.029	541	Wood	746 ± 37	700 ± 30	This study
COL2151.1.2	MADHI2	Magdi Khola	28.015	84.117	495	Charcoal	985 ± 36	890 ± 60	This study
COL2152.1.1	PH6	Phusre Khola	28.175	83.976	703	Wood	880 ± 36	830 ± 70	This study
Poz-69082	Phusre010	Phusre Khola	28.175	83.982	705.59	Wood	875 ± 30	820 ± 60	This study
Poz-69083	Phusre012	Phusre Khola	28.175	83.982	697.81	Leaves	810 ± 30	730 ± 30	This study
Poz-69084	Phusre013	Phusre Khola	28.175	83.982	696.06	Wood	845 ± 30	760 ± 40	This study
Poz-69085	Phusre14	Phusre Khola	28.175	83.982	700.5	Charcoal	825 ± 30	740 ± 40	This study
Poz-69086	PhusreFa	Phusre Khola	28.185	83.958	728	Charcoal	910 ± 30	850 ± 50	This study
Poz-69088	PRE 14C 1	Phusre Khola	28.184	83.934	747.9	Charcoal	595 ± 30	610 ± 40	This study
Poz-69089	GD03	Gondang Khola	27.958	84.112	479.02	Charcoal	890 ± 30	830 ± 60	This study
Poz-69090	GD06	Gondang Khola	27.958	84.112	481.12	Humic Silt	1110 ± 30	1020 ± 40	This study
Poz-69092	KBP03	Kalti Khola	28.218	84.027	824.99	Wood	695 ± 30	640 ± 50	This study
Poz-69093	TAL02	Tal Khola	28.117	84.105	583.42	Wood	830 ± 30	750 ± 40	This study
Poz-69094	TAL05	Tal Khola	28.117	84.105	614	Wood	930 ± 30	860 ± 50	This study
Poz-69260	Anpu02	Anpu Khola	28.109	84.116	590.56	Humic Silt	950 ± 30	870 ± 50	This study

Table A.2.: Highest density intervals (HDIs) from Bayesian radiocarbon calibration models using OxCal4.2 and the IntCal13 calibration.

Model	Number (and %) of 95% HDIs overlapping with historic earthquake dates*	95% HDI of dated leaves (Sample #)**
Single-phase uniform	25 (96%)	**1169-1270 AD** (Poz-69083) **1046-1269 AD** (Col-1916.1.1)
Four-phase uniform (1100, 1255, 1344, and 1505 AD)	24 (92%)	**1175-1260 AD** (Poz-69083) **1161-1254 AD** (Col-1916.1.1)
Four-phase exponential (1100, 1255, 1344, and 1505 AD)	24 (92%)	**1181-1261 AD** (Poz-69083) **1160-1257 AD** (Col-1916.1.1)
Three-phase uniform (1100, 1255, and 1505 AD)	24 (92%)	**1174-1260 AD** (Poz-69083) **1161-1253 AD** (Col-1916.1.1)
Three-phase exponential (1100, 1255, and 1505 AD)	24 (92%)	**1181-1261 AD** (Poz-69083) **1160-1257 AD** (Col-1916.1.1)

*For the timing of the ∼1100 AD earthquake we used a 95% HDI of 1020-1160 AD, based on a recent review of large Himalayan earthquakes (Mugnier et al., 2013), and recalibration of published ^{14}C dates for that earthquake (Lavé et al., 2005).
** **Bold font** indicates overlap with the 1255 AD earthquake. Note that we,excluded the historic 1223 AD earthquake (Bollinger et al., 2014); adding this event would, further increase the number of samples with HDIs containing earthquake dates in the middle column.

Table A.3.: Mineral composition of bedrock and fine grain-size deposits of the Pokhara Formation.

Lab-Nr.	Sample Name	Material	Mineral	Quartz	Calcite	Dolomite	Gypsum	Pyrite	Kaolinite-Mont-morillonite	Chlorite	Muskovite	Ortho-clas	Amphibole	Epidote
			PDF-Number	79-1906	72-1651	71-1662	74-1433	71-1680	29-1940	83-1380	74-0345	71-1540	73-1135	78-2440
WS1	Anpu Ku	Bedrock		+++++					++		+++			
WS2	BPh	Bedrock		+++++					+++	++(+)	+++			
WS3	Kancha 01	Bedrock		+++++				(?)	+++	+++	++++			
WS4a	Seti 3_03	Pebble NL (light)		+++(+)	+++++						+++	++		
WS4b	Seti 3_03	Pebble NL (dark)		+++	+++++	+++		+			++(+)	++		
WS5	Ramghat 01	Clay		++++	+++++	++				++	+++	++		
WS6	SARAE SW 01	Slackwater		++++	+++++	+(+)		(?)		+(+)	++++	+	+	
WS7	EBG-Fan SW	Slackwater		+++(+)	+++++	+++	+(+)			+(+)	+++	+		
WS8	PRE SW	Slackwater		++	+++++	+(+)			(?)	++	++++		(+)	
WS9	PRF 02	Clay		+++	+++++	+				++	+++		(+)	
WS10	PRA 01	Sand		++++	+++++	++				+(+)	+++	++		
WS11	PRB 02	Slackwater		+++(+)	+++++	++				+(+)	+++	++		
WS12	AnpuC 02	Clay		++	+++++	(+)	+(+)	(+)		+(+)	+++	+		+?

+++++ highest intensity (counts per second); main component (at least peaks I1-5 identified)
++++ high intensity; at least peaks $I_{1\text{-}4}$ identified
+++ medium intensity; at least peaks $I_{1\text{-}3}$ identified
++ lower intensity; at least peaks $I_{1\text{-}2}$ identified
+ low intensity; at least peak I_1 identified
(+) low intensity peak I_1 just above background

Table A.4.: P-EDXRF specifications.

X-Ray source:	Ag-anode	
$U_{max} \bullet I_{max}$	2 W	
U_{max}		40 kV
I_{max}		100 μA
Used filters	Main	30 sec at 50 kV with 40 μA
	Low	30 sec at 20 kV with 100 μA
	Light	30 sec at 8 kV with 250 μA
	High	30 sec at 50 kV with 40 μA

Table A.5.: Mineral concentrations and recovery values of the certified reference material.

Mineral	Certified concentrations	Recovery values (%)
Al_2O_3	9.30%	101.6-112.1
SiO_2	77.29%	100.2-103.5
CaO	1.16%	99.6-102.7
K_2O	2.91%	99.4-102.6
Fe_2O_3	4.88%	100-101.6
Cl	163 μg/g dw*	93.8-104.2
Pb	285 μg/g dw	100-102.3
Rb	270 μg/g dw	98.4-100.3
S	940 μg/g dw	88.6-106.6
Sr	24.4 μg/g dw	101.5-110.4
Ti	1510 μg/g dw	97.9-104.9
V	46.6 μg/g dw	90.8-116.7
Zn	498 μg/g dw	98.4-102.9

*(non-certified concentration)

Table A.6.: Elemental concentrations derived from XRF analysis.

Nr	SAMPLE_NEW	Type	Location	Reading No	Time	Units	Sigma Value	NOTE	Al	Al Error	Ca	Ca Error	Cl	Cl Error	Fe	Fe Error	K	K Error	Rb	Rb Error	Si	Si Error	Sr	Sr Error	Ti	Ti Error
1	PHUSRE05	Slackwater deposits	Phusre	2709	6/10/2015 11:20	ppm	2	kalib. mit RF3	209281.05	4663.84	394747.19	2491.39	45.04	5.15	21772.23	348.51	27150.23	414.02	87.89	7.41	223225.7	1790.9	427.83	10.74	3553.14	88.44
2	PHUSRE06	Slackwater deposits	Phusre	2719	6/10/2015 11:49	ppm	2	kalib. mit RF3	166088.81	3375.72	330622.03	1694.03	30.77	3.93	17182.49	234.45	21954.27	334.55	103.67	5.47	168108.67	1454.05	454.53	8.65	2371.21	59.94
3	SARAUDIFD01	Flood deposits (Saraudi)	Saraudi	2693	6/10/2015 10:33	ppm	2	kalib. mit RF3	152994.98	1670.79	308.47	106.31	10.32	2.3	27743.4	262.91	29756.8	342.54	130.76	5.2	443009.59	1877.75	20.26	1.75	2793.83	43.22
4	PHUSREBR01	Bedrock	Phusre	2688	6/10/2015 10:18	ppm	2	kalib. mit RF3	252000.86	2418.13	2958.69	180.71	10.29	2.5	64040.02	466.99	40810.75	496.12	240.67	6.79	398087.16	1777.15	38.8	2.37	4359.98	70.5
5	GONDANGBR01	Bedrock	Gondang	2689	6/10/2015 10:21	ppm	2	kalib. mit RF3	250190.5	2380.23	237.75	169.98	6.14	2.47	48611.84	385.78	54169.62	549.91	261.72	6.94	383604.97	1737.82	22.81	1.93	3877.99	62.02
6	SETIMAGDIBR01	Bedrock	Seti/Magdi	2686	6/10/2015 10:12	ppm	2	kalib. mit RF3	9241.89	978.36	99087.34	560.97	16.23	2.59	2312.14	72.81	425	64.45	13.31	3.15	398819.5	1798.92	14.21	1.49	21.38	6.9
7	ANPUBR01	Bedrock	Anpu	2696	6/10/2015 10:42	ppm	2	kalib. mit RF3	207652.45	2112.32	527.4	137.33	12.74	2.53	41126.42	339.22	36494.34	425.64	163.77	5.7	440345.31	1874.52	42.7	2.35	3439.88	55.18
8	MARDIBR01	Bedrock	Mardi	2687	6/10/2015 10:15	ppm	2	kalib. mit RF3	205597.28	1967.11	2826.2	139.95	12.57	2.35	30364.32	277.02	36811.66	403.57	202.58	5.93	415642.06	1793.6	59.45	2.63	2899.11	46.86
9	GONDANGDF01	Debris flow matrix	Gondang	2694	6/10/2015 10:36	ppm	2	kalib. mit RF3	107372.89	2364.12	274500.03	1441.7	30.59	3.46	19865.54	251.15	16391.14	278.65	95.61	5.34	171520.84	1414.56	392.07	7.8	1911.19	48.5
10	SETIFD01	Flood deposits (Seti)	Seti	2698	6/10/2015 10:48	ppm	2	kalib. mit RF3	120456.81	2445.01	268061.53	1418.18	25.66	3.36	16276.39	222.63	17775.03	286.94	93.17	5.3	186850.09	1427.38	382.6	7.63	1875.75	47.52
11	ANPU01	Slackwater deposits	Anpu	2762	6/10/2015 14:13	ppm	2	kalib. mit RF3	152484.27	3064.65	323137.22	1634.86	41.03	3.86	12973.29	195.94	17601.36	293.22	84.48	5.11	189079.75	1482.87	443.73	8.32	1981.96	52.1
12	MARDI01	Slackwater deposits	Mardi	2743	6/10/2015 13:05	ppm	2	kalib. mit RF3	129181.65	2785.42	314208.31	1604.79	29.42	3.65	11178.93	180.51	13498.71	262.1	70.09	4.93	208017.58	1539.68	437.64	8.24	1564.93	45.76
13	MARDI02	Slackwater deposits	Mardi	2747	6/10/2015 13:17	ppm	2	kalib. mit RF3	143628.02	3101.58	351106.78	1752.84	32.72	3.81	11084.27	181.09	15297.17	280.71	73.25	4.91	172372.16	1459.76	494.55	8.96	1719.43	50.12
14	MARDI03	Slackwater deposits	Mardi	2745	6/10/2015 13:11	ppm	2	kalib. mit RF3	154658.8	3028.27	307274.91	1556.34	26.53	3.63	11929.22	184.21	18786.89	295.05	85.09	5.07	210338.14	1544.86	409.62	7.81	2070.02	51.52
15	MARDI04	Slackwater deposits	Mardi	2744	6/10/2015 13:08	ppm	2	kalib. mit RF3	134558.77	2841.48	318696.28	1615.34	30.74	3.6	15142.73	213.84	12554.61	256.65	62.98	4.85	216855.09	1546.89	427.64	8.16	1664.93	47.8
16	MARDI05	Slackwater deposits	Mardi	2746	6/10/2015 13:14	ppm	2	kalib. mit RF3	115370.17	2641.15	321767.25	1621.31	34.2	3.67	12735.44	192.56	11181.84	243.74	54.85	4.7	195145.44	1501.11	426.21	8.07	1436.99	44.22
17	MAGDI01	Slackwater deposits	Magdi	2750	6/10/2015 13:27	ppm	2	kalib. mit RF3	149935.86	2967.65	299740.34	1532.63	30.89	3.69	13617.52	198.52	19165.65	305.39	86.77	5.13	208082.69	1534.31	407.83	7.81	2158.01	53.78
18	MAGDIBR01	Bedrock	Magdi	2749	6/10/2015 13:23	ppm	2	kalib. mit RF3	39839.5	1381.76	183600.95	921.87	27.72	2.94	1848.61	66.91	1561.48	102.58	14.78	3.24	212280.61	1421.77	55.98	2.43	164.77	12.46
19	MAGDIBR02	Bedrock	Magdi	2751	6/10/2015 13:30	ppm	2	kalib. mit RF3	36888.77	1341.3	179982.7	920.59	24.04	2.86	2176.6	72.9	1605.89	99.66	14.89	3.37	226134.53	1457.9	50.98	2.38	210.2	13.06
20	PHUSRE04	Slackwater deposits	Phusre	2757	6/10/2015 13:56	ppm	2	kalib. mit RF3	137659.5	3030.13	340398.97	1696.75	36.26	3.75	27428.87	309.92	11694.63	263.15	73.27	5	179920.77	1490.8	441.82	8.51	1767.16	52.84
21	PHUSRE01	Slackwater deposits	Phusre	2759	6/10/2015 14:02	ppm	2	kalib. mit RF3	155255.19	3274.02	327178.06	1678.05	37.95	4.09	12103.58	191.52	20066.01	304.55	94.29	5.36	170959.86	1511.09	457.71	8.61	1951.91	51.02
22	PHUSRE02	Slackwater deposits	Phusre	2760	6/10/2015 14:06	ppm	2	kalib. mit RF3	167299.41	3218.03	282769.06	1463.17	42.72	4.02	13720.11	199.8	24283.75	328.24	116.56	5.5	220169.45	1608.52	384.85	7.55	2559.8	56.19
23	PH01	Slackwater deposits	Phusre	2761	6/10/2015 14:10	ppm	2	kalib. mit RF3	152301.78	2878.99	284302.38	1474.93	40.21	3.75	13445.23	197.24	20842.81	312.68	91.52	5.21	214384.45	1532.54	388.9	7.59	2210.65	53.18
24	PH02	Slackwater deposits	Phusre	2758	6/10/2015 13:59	ppm	2	kalib. mit RF3	158734.03	3130.54	285220.81	1481.67	32.9	3.91	14553.81	207.93	24349.63	331.54	116.02	5.5	201087.44	1571.58	387.75	7.64	2436.38	55.41
25	PH03	Slackwater deposits	Phusre	2756	6/10/2015 13:52	ppm	2	kalib. mit RF3	144952.33	3210.98	376312.44	1870.99	32.42	3.8	13737.38	207.21	11098.21	249.55	55.65	4.87	154041.31	1408.34	514.23	9.35	1506.37	48.17
26	PHUSRE03	Slackwater deposits	Phusre	2753	6/10/2015 13:42	ppm	2	kalib. mit RF3	175807.47	3410.17	335301.75	1705.57	27.84	3.8	12836.41	196.8	21706.15	323.92	95.84	5.37	168433.38	1455.13	466.97	8.68	2137.88	55.38
27	SETI01	Conglomerate	Seti Gorge	2755	6/10/2015 13:49	ppm	2	kalib. mit RF3	139923.75	2589.71	221147.97	1196.36	31.15	3.6	13814.25	196.13	27008.51	339.18	119.83	5.47	266030.94	1649.89	209.3	5.24	2708.09	54.09
28	SARAUDI1	Slackwater deposits	Saraudi	2752	6/10/2015 13:37	ppm	2	kalib. mit RF3	170997.75	3077.58	277777.66	1440.41	28.53	3.63	17615.48	230.51	21750.25	315.07	113.51	5.48	210236.33	1524.93	383.66	7.57	2137.67	51.53
29	SARAUDI2	Slackwater deposits	Saraudi	2754	6/10/2015 13:45	ppm	2	kalib. mit RF3	181797.47	3142.4	239295.64	1289.55	30.4	3.74	23888.98	275.9	29905.6	373.6	154.73	6.13	234081.06	1613.04	323.85	6.87	2900.15	60.23

B

Appendix

Supplementary Content: Study III

Protracted river recovery from medieval earthquakes

Amelie Stolle[1], Wolfgang Schwanghart[1], Christoff Andermann[2], Anne Bernhardt[3], Monique Fort[4], John D. Jansen[5], Hella Wittmann[2], Silke Merchel[6], Georg Rugel[6], Basanta Raj Adhikari[7], Oliver Korup[1]

[1]Institute of Earth and Environmental Sciences, University of Potsdam, Germany

[2]GFZ German Research Centre for Geosciences, Potsdam, Germany

[3]Institute of Geological Sciences, Freie Universität Berlin, Berlin, Germany

[4]Département de Géographie, Université Paris-Diderot-SPC, Paris, France

[5]Department of Geoscience, Aarhus University, Aarhus, Denmark

[6]Helmholtz-Zentrum Dresden-Rossendorf, Helmholtz Institute Freiberg for Resource Technology, Dresden, Germany

[7]Department of Civil Engineering, Tribhuvan University, Kathmandu, Nepal

This supplementary content has been submitted with the following manuscript: *Stolle, A., Schwanghart, W., Andermann, C., Bernhardt, A., Fort, M., Jansen, J., Wittmann, H., Merchel, S., Rugel, S., Adhikari, B., Korup, O., Protracted fluvial recovery from medieval earthquakes. Earth Surface Landforms and Processes, submitted in February 2018*

Table B.1.: Estimated removed volume of valley infill with corresponding erosion rates and sediment yields.

Location	DEMs	Lat	Long	Catchment Area	Volume removed	Volumetric sediment yield			Volumetric erosion rate
						mean[c]	min[c]	max[c]	mean[c]
		[°N]	[°E]	[km^2]	[km^3]	[m^3 km^{-2} yr^{-1}]a	[t km^{-2} yr^{-1}][a,b]		[mm yr^{-1}]
Seti	ALOS	27.969	84.154	1400	1.90±0.076	2089.79±83.07	3343.67±132.91	4179.58±166.13	2.09±0.08
Seti_upstream	ALOS	28.293	83.933	343	0.32±0.006	1434.19±28.59	2294.71±45.74	2868.39±57.18	1.43±0.03
Mardi	ALOS	28.294	83.932	143	0.03±0.003	361.59 ±29.75	578.55±47.59	723.18±59.49	0.36±0.03
Mardi_upstream	ALOS	28.300	83.927	486	0.36±0.003	114653±8.51	1834.46±13.62	2293.07±17.02	1.15±0.01
Yangdi	ALOS	28.251	83.969	30	0.01±0.001	729.97±69.24	1167.96±110.78	1459.95±138.48	0.73±0.07
Yangdi_upstream	ALOS	28.251	83.971	532	0.53±0.010	1544.27±29.26	2470.84±46.82	3088.55±58.52	1.54±0.03
Phusre	ALOS	28.163	84.008	166	0.08±0.004	765.36±36.63	1224.31±58.61	1530.38±73.26	0.77±0.04
Phusre_upstream	ALOS	28.161	84.011	752	0.08±0.000	1628.51±35.94	2605.62±57.51	3257.02±71.89	1.63±0.04
Bijaypur	ALOS	28.157	84.037	68	0.05±0.001	1160.81±23.80	1857.29±38.07	2321.62±47.59	1.16±0.02
Bijaypur_upstream	ALOS	28.155	84.039	830	0.98±0.023	1824.69±43.34	2919.51±69.34	3649.39±86.67	1.82±0.04
Anpu	ALOS	28.092	84.081	108	0.06±0.008	894.35±110.83	1430.96±177.32	1788.70±221.65	0.89±0.11
Anpu_upstream	ALOS	28.091	84.079	980	1.44±0.050	2069.18±77.95	3630.68±124.72	4538.35±155.90	2.27±0.08
Saraudi	ALOS	28.059	84.068	94	0.04±0.002	643.52±35.75	1029.63±57.2	1287.04±71.50	0.64±0.04
Saraudi_upstream	ALOS	28.058	84.069	1094	1.59±0.056	2238.49±78.64	3581.58±125.83	4476.97±157.28	2.24±0.08
Kyandi	ALOS	28.011	84.084	97	0.02±0.002	243.31±34.43	389.30±55.08	486.62±68.85	0.24±0.03
Kyandi_upstream	ALOS	28.010	84.085	1221	1.79±0.056	2251.88±70.80	3603.01±113.29	4503.77±141.61	2.25±0.07
Magdi	ALOS	28.008	84.087	69	0.01±0.002	226.47±36.39	362.36±58.22	452.95±72.77	0.23±0.04
Magdi_upstream	ALOS	28.008	84.087	1290	1.8±0.063	2144.97±74.95	3431.94±119.93	4289.93±149.91	2.14±0.07

a The time range used for this calculations are over 650 years.

b min and max values refer to bulk densities of 1.6 and 2.9 t m-3, respectively.

c mean, min, and max values derived from different DEMs: ALOS-3D (AW3D; provided by JAXA andthe Japanese Aerospace Exploration Agency)
Tandem-X (provided by the German Aerospace Center DLR)
Nepal DEM (provided by the Alpine Consultancy Pvt. Ltd Nepal)

Materials and Methods

Cosmogenic ^{10}Be exposure dating

To obtain independent erosion estimates, we collected samples of quartz-rich fluvial sands from five tributary catchments along the Seti River. We sampled fresh deposits (Fig. 4.1) upstream of the Pokhara Valley fan margins to exclude inheritance effects of actively eroding valley fill, and to minimize human disturbances. The samples were dried and sieved to the 250-1000 μm grain size fraction, and the pure quartz fraction was extracted using weak HF leaching methods. Cleaned samples were spiked with ~300 μg of a ^{9}Be carrier (made from phenakite at University of Hannover, Germany) with a concentration of 369.5 ± 2.0 μg/g. Cosmogenic ^{10}Be and stable ^{9}Be were extracted by using standard chemistry methods (Wittmann et al., 2016), oxidized to BeO, mixed with Nb, and measured at the accelerator mass spectrometry (AMS) facility in Dresden/Rossendorf DREAMS, Germany, against the secondary standard SMD-Be-12 (Akhmadaliev et al., 2013). The ^{10}Be/^{9}Be analyses are traceable via cross-calibration to the primary standard NIST-SRM 4325 with a ^{10}Be/^{9}Be ratio of (2.79 ± 0.03) x 10-11 (Nishiizumi et al., 2007) recalibrated to a half-life of ^{10}Be (1.387 ± 0.012) Myr (Chmeleff et al., 2010; Korschinek et al., 2010). Measured ^{10}Be/^{9}Be ratios were corrected for blank influence using a processing blank ratio of (7.6 ± 2.4) x 10-16. For the basin-wide denudation analysis the total production rate of ^{10}Be, P(0) in at g-1 yr^{-1}, and the topographic shielding Stopo were calculated using the R skyview factor package svf (Van doninck, 2016) routines from a 90-m SRTM-4 digital elevation model (Jarvis et al., 2008). The elevation scaling scheme of P(0) was calculated after Stone (2000) by linearly interpolating the scaling factors to the mean catchment latitude. We used 3.94 ± 0.2 at g^{-1} yr^{-1} (Heyman, 2014) as the regional representative ^{10}Be sea-level high-latitude (SLHL) production rate. We used neutron- (Lneut, in g/cm^2) and stopped and fast muon-induced (LÎij stopped and LÎij fast, in g/cm^2) attenuation lengths of 160, 1500 and 4320, respectively (Braucher et al., 2011). Topographic shielding was corrected on a pixel scale using a horizontal radius of 15 km, which is larger than the average ridge-to-ridge valley width (~10 km). From the production rate map, we extracted the respective mean P(0) of each catchment to calculate mean catchment-wide denudation rates (Blanckenburg, 2005) assuming a spatially uniform rock density ρ of 2.65 g/cm^3 with a decay constant of the nuclide of (4.997 ± 0.043) x 10-7 λ yr^{-1}. We further assumed homogeneous quartz distribution and rock erodibility. We did not correct for recent sediment contribution from landslides, nor did we correct for partial shielding by

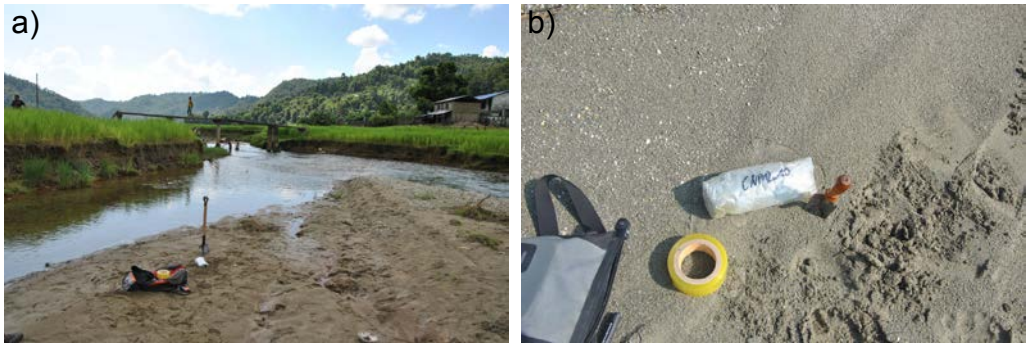

Figure B.1.: Field images of a) sampling location and b) sampling equipment (Photos by Christoff Andermann)

seasonal snow cover at high elevations. Permanent ice cover is not present in the sampled catchments, hence a correction is not needed.

C

Appendix

Supplementary Content: This thesis

This supplementary content has not been submitted or published within one of the three studies (Chapters 2- 4). This additional information is part of the entire thesis, completing all chapters with supplementary tables and figures.

Complete table of XRF-Analysis used for Fig 3.6 in Chapter 3

Table C.1.: Elemental concentrations (all samples) derived from XRF analysis.

Sample	Sample_Id	Location	Lat [°N]	Lon [°E]	Material	Al	Al Error	Ca	Ca Error	Cl	Cl Error	Fe	Fe Error	K	K Error	Rb	Rb Error	Si	Si Error	Sr	Sr Error	Ti	Ti Error
A1_clay	AnSWD 01	Anpu	28.110	84.116	Slackwater Deposits	152484.27	3064.65	323137.22	1634.86	41.03	3.86	12973.29	195.94	17601.36	293.22	84.48	5.11	189079.75	1482.87	443.73	8.32	1981.96	52.10
Anpu FD01	AnFD 01	Anpu	28.107	84.111	Tributary flood deposit	115832.42	2580.44	304087.97	1541.14	28.11	3.55	13039.89	194.21	11625.4	238.96	62.82	4.76	205826.70	1512.58	407.2	7.82	1760.99	46.71
Anpu KN	AnBdr 01	Anpu	28.111	84.120	LH Bedrock	322343	2867.14	1.42	188.05	7.03	2.76	65113.78	482.58	58438.05	615.80	342.82	8.19	410056.31	1811.65	40.64	2.44	3653.98	65.35
AnpuC01	AnSWD 02	Anpu	28.111	84.106	Slackwater Deposits	113339.58	2394.22	280194.69	1485.49	29.09	3.43	13509.86	202.03	16314.79	277.60	82.04	5.24	183053.88	1424.15	414.92	8.07	1749.47	46.26
AnpuC02	AnSWD 03	Anpu	28.109	84.116	Slackwater Deposits	132606.94	2705.99	288345.53	1533.94	36.44	3.71	14895.75	216.48	22713.6	326.59	111.89	5.63	162352.91	1390.24	428.18	8.34	2184.14	53.29
AnpuC03	AnSWD 04	Anpu	28.109	84.116	Slackwater Deposits	106344.55	2367.28	279011.41	1436.65	26.79	3.41	13187.56	194.47	12863.62	248.11	71.63	4.78	221776.45	1531.95	381.36	7.48	1754.52	45.60
BG	GonBdr 01	Gondang	27.970	84.113	LH Bedrock	252569.31	2380.23	521.43	169.98	6.14	2.47	47726.99	385.78	53711.31	549.91	262.85	6.94	390429.34	1737.82	22.65	1.93	3786.26	62.02
BPFD01	BijFD 01	Bijaypur	28.230	84.055	Tributary flood deposit	175807.47	1895.38	5232.31	147.41	16.67	2.32	32414.33	284.52	30496.06	361.83	128.11	5.02	168433.38	1792.56	53.79	2.47	2957.55	47.30
BPh	PhBdr 01	Phusre	28.179	83.969	LH Bedrock	258165.89	2418.13	3513.58	180.71	10.29	2.50	64998.37	466.99	41627.7	496.12	244.35	6.79	405527.72	1777.15	41.51	2.37	4293.93	70.50
CAVE 1	SetiMVD 07	Seti	28.189	83.957	Main Valley Deposits	127815.54	2521.78	246089.17	1314.62	29.72	3.58	14321.65	203.07	21455.88	309.57	87.52	5.12	256846.73	1642.47	65.85	3.01	2502.14	53.79
Cave 2	SetiMVD 08	Seti	28.189	83.957	Main Valley Deposits	134938.8	3197.77	291409.25	1661.99	43.91	4.43	47800.46	501.30	18259.38	330.28	80.18	6.05	208521.77	1682.08	80.4	3.90	2790.87	68.53
DOLOMITE	SetiBdr 01	Seti	28.004	84.087	LH Bedrock	13322.27	978.36	100719.16	560.97	16.23	2.59	2248.67	72.81	453.29	64.45	9	3.15	417321.00	1798.92	13.35	1.44	25.57	6.90
EBG 02	AnBdr 02	Anpu	28.109	84.109	LH Bedrock	207652.45	2112.32	527.40	137.33	12.74	2.53	41126.42	339.22	36494.34	425.64	163.77	5.70	440345.31	1874.52	42.7	2.35	3439.88	55.18
EBG_Fan sw	AnSWD 05	Anpu	28.110	84.121	Slackwater Deposits	121368.02	2570.93	295220.06	1560.04	29.22	3.53	12821.62	199.63	17434.32	284.67	95.44	5.34	161334.36	1379.66	455.34	8.67	1708.46	46.09
GD05	GonDF 01	Gondang	27.958	84.112	Debris flow deposits	137853.8	2802.65	292987.09	1506.16	28.75	3.61	17178.2	228.13	18569.98	301.70	93.14	5.20	195402.03	1493.72	370.35	7.44	2262.82	55.04
GD07	GonSWD 01	Gondang	27.958	84.112	Slackwater Deposits	163426.08	3122.53	273672.41	1437.37	22.76	3.71	15687.14	216.10	26400.98	349.76	125.46	5.68	199816.44	1554.31	376.28	7.49	2795.44	60.10
GD08	GonSWD 02	Gondang	27.958	84.112	Slackwater Deposits	152442.27	2930.75	283836.47	1462.48	29.95	3.63	15540.97	213.12	21379.88	317.73	97.53	5.24	224511.05	1564.28	376.55	7.42	2393.31	55.66
KD01	KyFD 01	Kyandi	28.018	84.064	Tributary flood deposit	104695.15	1867.20	140772.88	821.04	18.92	2.88	28865.81	293.04	20031.45	298.01	96.01	5.05	313374.63	1644.70	182.16	4.78	2776.84	52.39
KUNCHA 01	SetiBdr 02	Seti	28.305	83.937	LH Bedrock	210082.64	1967.11	2979.09	139.95	12.57	2.35	29920.95	277.02	36114.89	403.57	201.32	5.93	442103.84	1793.60	60.78	2.63	2844.37	46.86
ldf 01	GonDF 02	Gondang	27.968	84.113	Debris flow deposits	107372.89	2364.12	274500.03	1441.70	30.59	3.46	19865.54	251.15	16391.14	278.65	95.61	5.34	171520.84	1414.56	392.07	7.80	1911.19	48.50
Mardi 01	MarSWD 01	Mardi	28.301	83.927	Slackwater Deposits	129181.65	2785.42	314208.31	1604.79	29.42	3.65	11178.93	180.51	13498.71	262.10	70.09	4.93	208017.58	1539.68	437.64	8.24	1564.93	45.76
Mardi 02	MarSWD 02	Mardi	28.301	83.927	Slackwater Deposits	143628.02	3101.58	351106.78	1752.84	32.72	3.81	11084.27	181.09	15297.17	280.71	73.25	4.91	172372.16	1459.76	494.55	8.96	1719.43	50.12
Mardi 03	MarSWD 03	Mardi	28.301	83.927	Slackwater Deposits	154658.8	3028.27	307274.91	1556.34	26.53	3.63	11929.22	184.21	18786.89	295.05	85.09	5.07	210338.14	1544.86	409.62	7.81	2070.02	51.52
Mardi 04	MarSWD 04	Mardi	28.301	83.927	Slackwater Deposits	134558.77	2841.48	318696.28	1615.34	30.74	3.60	15142.73	213.84	12554.61	256.65	62.98	4.85	216855.09	1546.89	427.64	8.16	1664.93	47.80
Mardi 05	MarSWD 05	Mardi	28.301	83.927	Slackwater Deposits	115370.17	2641.15	321767.25	1621.31	34.2	3.67	12735.44	192.56	11181.84	243.74	54.85	4.70	195145.44	1501.11	426.21	8.07	1436.99	44.22
P1_Silt	PhSWD 01	Phusre	28.175	83.976	Slackwater Deposits	137659.5	3030.13	340398.97	1696.75	36.26	3.75	27428.87	309.92	11694.63	263.15	73.27	5.00	179920.77	1490.80	441.82	8.51	1767.16	52.84
P2_clay	PhSWD 02	Phusre	28.175	83.976	Slackwater Deposits	155255.19	3274.02	327178.06	1678.05	37.95	4.09	12103.58	191.52	20066.01	304.55	94.29	5.36	170959.86	1511.09	457.71	8.61	1951.91	51.02
P2_Silt2	PhSWD 03	Phusre	28.175	83.976	Slackwater Deposits	167299.41	3218.03	282769.06	1463.17	42.72	4.02	13720.11	199.80	24283.75	328.24	116.56	5.50	220169.45	1608.52	384.85	7.55	2559.8	56.19
PH_01	PhSWD 04	Phusre	28.179	83.969	Slackwater Deposits	152301.78	2878.99	284302.38	1474.93	40.21	3.75	13445.23	197.24	20842.81	312.68	91.52	5.21	214384.45	1532.54	388.9	7.59	2210.65	53.18
Ph1_mud	PhSWD 05	Phusre	28.179	83.969	Slackwater Deposits	158734.03	3130.54	285220.81	1481.67	32.9	3.91	14553.81	207.93	24349.63	331.54	116.02	5.50	201087.44	1571.58	387.75	7.64	2436.38	55.41
Ph1_sand	PhSWD 06	Phusre	28.179	83.969	Slackwater Deposits	144952.33	3210.98	376312.44	1870.99	32.42	3.80	13737.38	207.21	11098.21	249.55	55.65	4.87	154041.31	1408.34	514.23	9.35	1506.37	48.17
Phusre 03	PhSWD 07	Phusre	28.183	83.951	Slackwater Deposits	175807.47	3410.17	335301.75	1705.57	27.84	3.80	12836.41	196.80	21706.15	323.92	95.84	5.37	168433.38	1455.13	466.97	8.68	2137.88	55.38
Phusre G	PhSWD 08	Phusre	28.181	83.970	Slackwater Deposits	209281.05	4663.84	394747.19	2491.39	45.04	5.15	21772.23	348.51	27150.23	414.02	87.89	7.41	223225.70	1790.90	427.83	10.74	3553.14	88.44
PR Bedrock	PhBdr 02	Phusre	28.174	83.980	LH Bedrock	322577.78	3053.55	2300.19	215.31	10.93	2.92	83526.51	626.29	52934.7	624.57	242.37	7.80	410867.13	1861.81	48.4	2.92	4664.92	81.37
PRA01	PhSWD 09	Phusre	28.174	83.982	Slackwater Deposits	136054.2	2741.00	292868.41	1512.12	30.4	3.57	19231.56	245.50	17189.04	291.79	87.64	5.19	177571.88	1420.09	386.82	7.70	2070.84	52.60
PRB01	PhSWD 10	Phusre	28.183	83.953	Slackwater Deposits	155542.78	3081.61	312910.50	1613.36	27.98	3.73	16308.46	225.80	18458.65	299.51	87.67	5.27	191722.48	1503.18	421.33	8.19	2259.63	55.49
PRB02	PhSWD 11	Phusre	28.172	83.983	Slackwater Deposits	150217.08	2974.28	311809.53	1584.18	31.15	3.66	15988.9	219.95	16927.67	289.62	81.71	5.03	200550.09	1509.10	409.68	7.93	1966.22	51.69
PRB03	PhDF 01	Phusre	28.183	83.953	Debris flow deposits	145522.63	2973.86	308315.97	1598.64	31.63	3.75	15104.67	215.72	18893.52	303.99	87.6	5.29	189693.41	1491.02	415.28	8.10	2120.98	53.85

Sample	Sample_Id	Location	Lat [°N]	Lon [°E]	Material	Al	Al Error	Ca	Ca Error	Cl	Cl Error	Fe	Fe Error	K	K Error	Rb	Rb Error	Si	Si Error	Sr	Sr Error	Ti	Ti Error
PRB04	PhDF 02	Phusre	28.183	83.953	Debris flow deposits	165817.8	2494.63	157977.36	905.17	24.81	3.20	32743.08	320.26	25220.2	342.67	103.91	5.24	305072.03	1666.02	231.71	5.50	2938.47	56.60
PRC01	PhSWD 12	Phusre	28.185	83.918	Slackwater Deposits	164327.3	3262.50	328700.00	1697.13	32.48	3.90	13451.88	204.47	21955.07	324.88	107.41	5.59	158952.17	1427.31	463.91	8.75	2222.06	56.06
PRC02	PhSWD 13	Phusre	28.185	83.918	Slackwater Deposits	132715.17	3025.17	358984.31	1789.63	32.56	3.79	15486	219.90	11949.8	260.97	60.94	4.82	154279.83	1402.57	480.69	8.90	1536.12	48.91
PRC03	PhSWD 14	Phusre	28.185	83.918	Slackwater Deposits	145459.59	2793.02	275638.84	1439.51	26.45	3.57	15050.77	210.37	21232.53	318.02	86.99	5.08	235501.42	1579.68	46.71	2.63	2524.57	57.08
PRE SW	PhSWD 15	Phusre	28.184	83.934	Slackwater Deposits	166088.81	3375.72	330622.03	1694.03	30.77	3.93	17182.49	234.45	21954.27	334.55	103.67	5.47	168108.67	1454.05	454.53	8.65	2371.21	59.94
PRE SW02	PhSWD 16	Phusre	28.184	83.934	Slackwater Deposits	201482.63	3200.30	194351.81	1100.39	25.44	3.71	31921.92	328.01	33697.03	407.81	172.7	6.45	261754.23	1669.98	280.55	6.33	3840.37	69.92
PRF 01	PhSWD 17	Phusre	28.186	83.955	Slackwater Deposits	124192.92	2684.16	308361.13	1563.75	26.4	3.53	12037.67	185.87	13833.83	263.52	71.15	4.85	209965.11	1535.29	412.69	7.87	1697.73	47.29
PRF 02	PhSWD 18	Phusre	28.186	83.955	Slackwater Deposits	138775.48	3151.18	366409.13	1855.56	30.33	3.89	10753.59	181.87	16449.74	292.90	72.96	5.09	135320.23	1356.62	465.17	8.82	1837.72	53.18
PRFD 01	PhFD 01	Phusre	28.174	83.980	Tributary flood deposit	157616.53	2530.77	155890.42	906.09	28.92	3.44	27552.47	290.29	25404.58	340.28	113.72	5.50	355563.94	1799.77	218.25	5.35	3637.17	62.67
Ramghat 01	SetiMVD 01	Seti	28.216	83.992	Main Valley Deposits	117203.28	2514.11	285414.47	1522.24	32.78	3.57	14080.11	210.64	18982.92	290.53	103.66	5.56	159156.59	1367.20	440.68	8.52	1961.97	48.40
Ramghat 02	SetiMVD 02	Seti	28.216	83.992	Main Valley Deposits	127458.27	2904.96	356691.63	1779.52	32.28	3.72	15985.43	224.09	11351.22	254.87	61.91	4.82	158320.00	1405.63	475.82	8.85	1470.19	47.66
S_cgl 3	SetiMVD 03	Seti Gorge	28.396	83.981	Main Valley Deposits	139923.75	2589.71	221147.97	1196.36	31.15	3.60	13814.25	196.13	27008.51	339.18	119.83	5.47	266030.94	1649.89	209.3	5.24	2708.09	54.09
S1-2_14C	SaSWD 01	Saraudi	28.096	84.030	Slackwater Deposits	170997.75	3077.58	277777.66	1440.41	28.53	3.63	17615.48	230.51	21750.25	315.07	113.51	5.48	210236.33	1524.93	383.66	7.57	2137.67	51.53
S1-3_14C	SaSWD 02	Saraudi	28.096	84.030	Slackwater Deposits	181797.47	3142.40	239295.64	1289.55	30.4	3.74	23888.98	275.90	29905.6	373.60	154.73	6.13	234081.06	1613.04	323.85	6.87	2900.15	60.23
SARA1_01	SaSWD 03	Saraudi	28.096	84.029	Slackwater Deposits	142081.56	1498.12	310.71	96.38	14.07	2.18	20860.96	216.71	26204.69	306.22	104.47	4.70	458251.31	1854.21	14.38	1.53	3349.27	45.84
SARA1_02	SaSWD 04	Saraudi	28.096	84.029	Slackwater Deposits	237607.53	2268.37	852.73	150.64	9.96	2.48	46029.78	368.40	42606.59	467.71	227.74	6.50	405423.53	1788.33	31.03	2.11	3829	59.38
SARA1_03	SaSWD 05	Saraudi	28.096	84.029	Slackwater Deposits	158175.91	3145.23	294574.63	1516.04	26.83	3.81	13146.98	194.95	22401.46	321.70	99.98	5.33	202734.39	1573.37	401.29	7.74	2486.81	56.78
SARA1_04	SaSWD 06	Saraudi	28.096	84.029	Slackwater Deposits	127220.01	2842.16	315619.53	1589.09	25.55	3.66	15814.21	217.61	13507.25	260.12	62.53	4.77	203563.88	1557.31	392.36	7.69	1800.12	48.76
SaraE SW01	SaSWD 07	Saraudi	28.089	84.044	Slackwater Deposits	149204.67	3129.87	339641.28	1742.94	29.25	3.78	12305.51	194.69	16202.97	288.83	75.44	5.16	164263.88	1435.13	477.86	8.92	1787.23	51.09
SaraE02	SaDF 01	Saraudi	28.089	84.044	Debris flow deposits	154172.56	3053.71	314111.78	1613.80	28.54	3.70	14523.41	209.93	19037.93	306.31	82.08	5.15	190815.47	1495.44	436.66	8.30	2212.38	55.44
SaraG FD	SaFD 01	Saraudi	28.085	84.047	Tributary flood deposit	138802.61	2221.92	154219.72	866.83	22.45	3.04	22006.99	245.44	19010.63	279.96	110.52	5.12	357478.44	1754.52	203.78	4.98	2502.23	48.09
Seti_1	SetiMRS 01	Seti	28.314	83.954	Seti flood deposits	114911.16	2172.12	213257.16	1143.08	27.94	3.19	24548.24	272.46	16764.19	278.00	95.47	5.14	259289.91	1560.36	318.05	6.62	2662.21	54.58
Seti001 LS	SetiLS 01	Seti	28.396	83.981	LandslideSample	140149.45	2432.82	169871.91	970.35	24.42	3.40	19631.16	237.56	28599.75	351.39	133.52	5.63	298827.13	1710.05	219.8	5.36	2965.46	54.96
Seti3_01	SetiDF 01	Seti	28.082	84.074	Debris flow deposits	120456.81	2445.01	268061.53	1418.18	25.66	3.36	16276.39	222.63	17775.03	286.94	93.17	5.30	186850.09	1427.38	382.6	7.63	1875.75	47.52
Seti3_02	SetiMVD 04	Seti	28.082	84.074	Main Valley Deposits	112431.28	2337.69	281244.97	1454.15	31.16	3.31	20455.22	253.61	14152.28	261.18	91.15	5.20	173677.31	1378.77	384.79	7.65	1718.92	46.01
Seti3_03	SetiDF 02	Seti	28.082	84.074	Debris flow deposits	129748.47	2734.20	320980.16	1662.78	29.73	3.57	14025.76	210.42	14922.9	273.08	5.08	5.08	155724.80	1367.35	474.76	8.92	1597.08	46.55
SRFD01	SaFD 02	Saraudi	28.117	84.003	Tributary flood deposit	152994.98	1670.79	308.47	106.31	10.32	2.30	27743.4	262.91	29756.8	342.54	130.76	5.20	443009.59	1877.75	20.26	1.75	2793.83	43.22
SRG1	SaFD 03	Saraudi	28.072	84.056	Tributary flood deposit	122537.13	1985.26	130201.06	745.01	17.7	2.89	22090.95	237.02	19027.88	279.10	105.45	4.88	350710.03	1715.08	147.36	4.06	2288.03	44.84
SW 001	SetiMVD 05	Seti	28.387	83.975	Main Valley Deposits	117607.94	2514.28	264408.69	1360.99	29.02	3.55	15688.03	211.29	12284.26	241.24	78.19	4.96	243669.63	1618.45	350.26	7.02	2133.05	49.54
SW 002	SetiMVD 06	Seti	28.387	83.975	Main Valley Deposits	105217.96	2385.03	289379.81	1489.49	33.92	3.57	17668.88	232.21	11737.45	244.82	77.8	5.05	175152.61	1418.72	375.55	7.52	2344.23	54.70
TribAP01	AnDF 01	Anpu	28.116	84.131	Debris flow deposits	148936.03	2910.53	291775.94	1490.56	29.63	3.66	15656.15	213.53	20176.03	313.59	92.89	5.13	209316.33	1531.58	395.1	7.63	2369.92	56.47

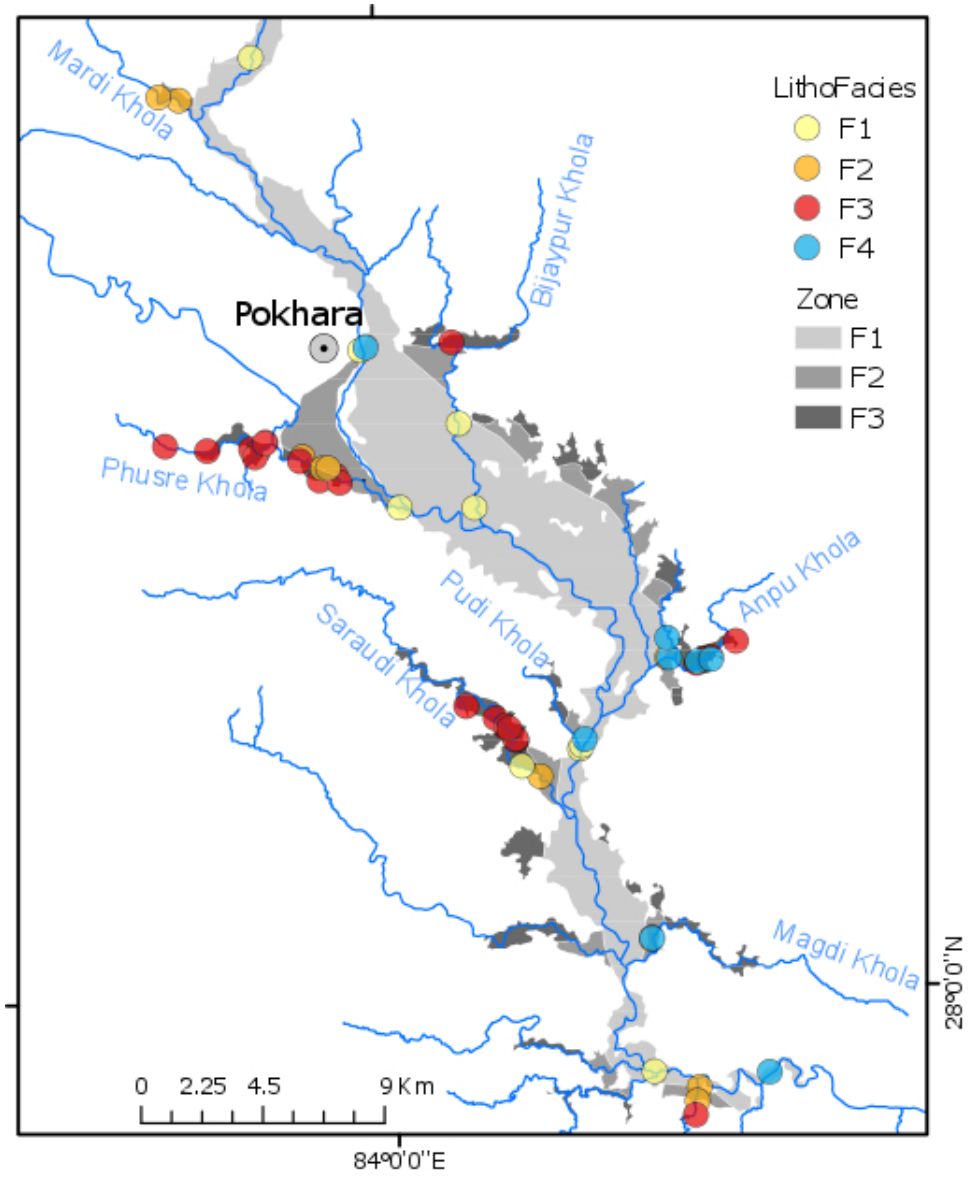

Figure C.1.: Map of lithofacies including field locations. Additional map showing the four lithofacies, their locations and estimated extend.

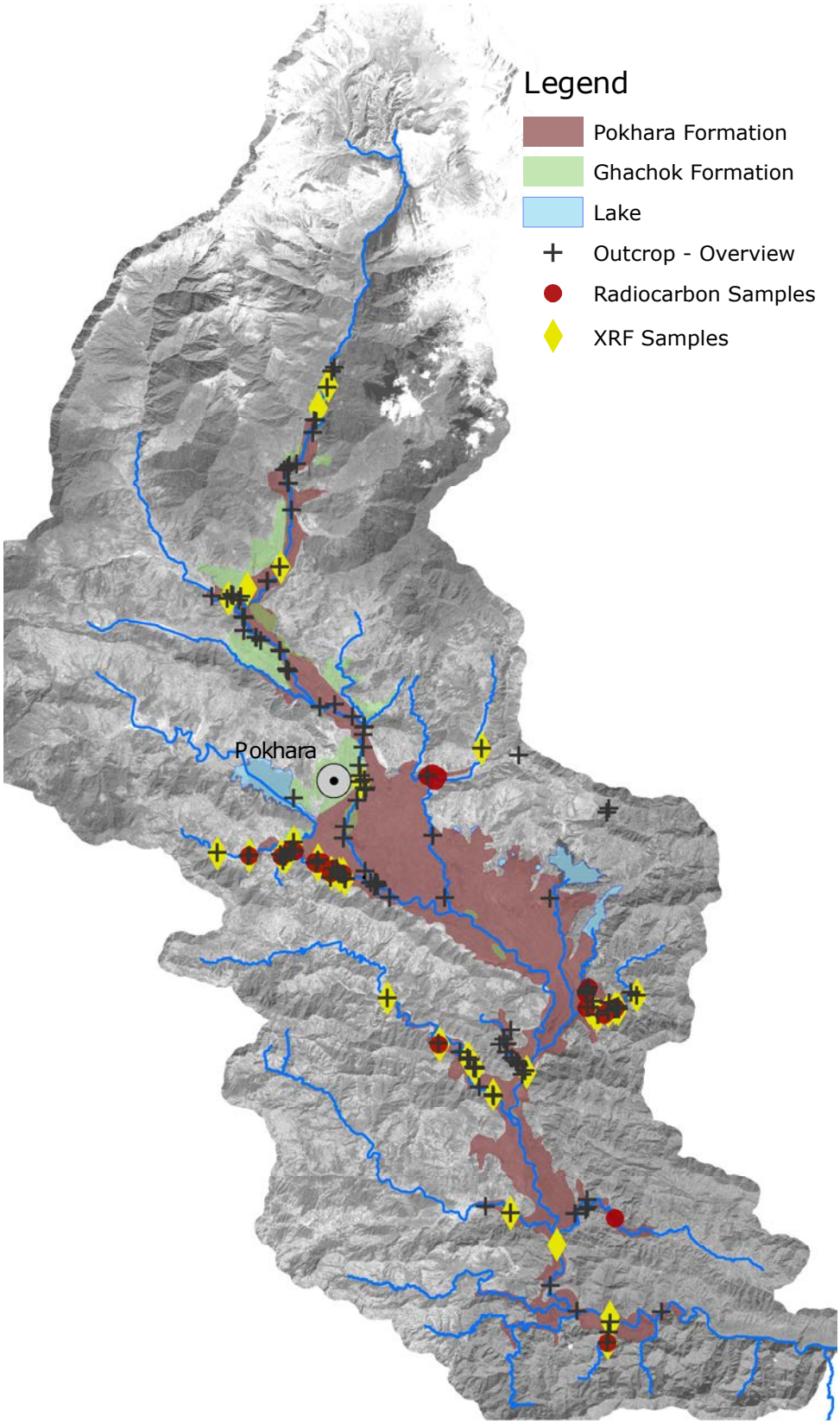

Figure C.2.: Map with outcrops visited in the field and sample locations in the Pokhara Valley. Additional map showing the study area with all field locations from four field campaigns.

Volumetric calculations (all measurements); Supplementary material - Chapter 4

Table C.2.: Volumetric calculations for the entire fluvial network of the Pokhara Valley. Names are river names with *pkFm* (calculated for the area covered by the Pokhara Formation only) or *upstream* calculated from the confluence with the Seti Khola for the area upstream.

Name	Images	Distance	Cat. Area	Volume removed	Volume			Erosion		
		[km][a]	[km^2]	[km^3]	[m^3 yr^{-1}][b]	[m^3 yr^{-1}][c]	[m^3 yr^{-1}][d]	[mm yr^{-1}][b]	[mm yr^{-1}][c]	[mm yr^{-1}][d]
Upper_seti	ALOS_5m	81.66	343.36	0.324	497852.16	431471.87	404504.88	1.45	1.26	1.18
Upper_seti	ALOS_5m_3px	81.66	343.36	0.324	497924.33	431534.42	404563.52	1.45	1.26	1.18
Upper_seti	TanDEMX_12m	81.66	343.36	0.323	496249.60	430082.99	403202.80	1.45	1.25	1.17
Upper_seti	DEM_15m	81.66	343.36	0.311	477770.73	414067.97	388188.72	1.39	1.21	1.13
Mardi	ALOS_5m	81.55	142.54	0.031	48063.94	41655.41	39051.95	0.34	0.29	0.27
Mardi	ALOS_5m_3px	81.55	142.54	0.031	48136.46	41718.26	39110.87	0.34	0.29	0.27
Mardi	TanDEMX_12m	81.55	142.54	0.035	53170.69	46081.26	43201.19	0.37	0.32	0.30
Mardi	DEM_15m	81.55	142.54	0.037	56793.90	49221.38	46145.04	0.40	0.35	0.32
Mardi_pkFm	ALOS_5m	81.55	3.41	0.031	48063.94	41655.41	39051.95	14.09	12.21	11.45
Mardi_pkFm	ALOS_5m_3px	81.55	3.41	0.031	48136.46	41718.26	39110.87	14.11	12.23	11.47
Mardi_pkFm	TanDEMX_12m	81.55	3.41	0.035	53170.69	46081.26	43201.19	15.59	13.51	12.67
Mardi_pkFm	DEM_15m	81.55	3.41	0.037	56793.90	49221.38	46145.04	16.65	14.43	13.53
Mardi_upstream	ALOS_5m	81.55	485.90	0.362	556282.98	482111.91	451979.92	1.14	0.99	0.93
Mardi_upstream	ALOS_5m_3px	81.55	485.90	0.362	556423.88	482234.03	452094.40	1.15	0.99	0.93
Mardi_upstream	TanDEMX_12m	81.55	485.90	0.366	562809.70	487768.41	457282.88	1.16	1.00	0.94
Mardi_upstream	DEM_15m	81.55	485.90	0.359	552906.73	479185.83	449236.72	1.14	0.99	0.92
Yangdi	ALOS_5m	74.30	29.81	0.013	20402.72	17682.36	16577.21	0.68	0.59	0.56
Yangdi	ALOS_5m_3px	74.30	29.81	0.014	21276.10	18439.29	17286.83	0.71	0.62	0.58
Yangdi	TanDEMX_12m	74.30	29.81	0.013	20559.61	17818.33	16704.69	0.69	0.60	0.56
Yangdi	DEM_15m	74.30	29.81	0.016	24803.54	21496.40	20152.87	0.83	0.72	0.68
Yangdi_pkFm	ALOS_5m	74.30	2.92	0.013	20402.72	17682.36	16577.21	6.98	6.05	5.67
Yangdi_pkFm	ALOS_5m_3px	74.30	2.92	0.014	21276.10	18439.29	17286.83	7.27	6.30	5.91
Yangdi_pkFm	TanDEMX_12m	74.30	2.92	0.013	20559.61	17818.33	16704.69	7.03	6.09	5.71
Yangdi_pkFm	DEM_15m	74.30	2.92	0.016	24803.54	21496.40	20152.87	8.48	7.35	6.89
Yangdi_upstream	ALOS_5m	74.30	532.44	0.531	816201.01	707374.21	663163.32	1.53	1.33	1.25
Yangdi_upstream	ALOS_5m_3px	74.30	532.44	0.531	816541.78	707669.55	663440.20	1.53	1.33	1.25

Name	Images	Distance	Cat. Area	Volume removed	Volume			Erosion		
		[km][a]	[km^2]	[km^3]	[m^3 yr^{-1}][b]	[m^3 yr^{-1}][c]	[m^3 yr^{-1}][d]	[mm yr^{-1}][b]	[mm yr^{-1}][c]	[mm yr^{-1}][d]
Yangdi_upstream	TanDEMX_12m	74.30	532.44	0.549	845272.02	732569.09	686783.52	1.59	1.38	1.29
Yangdi_upstream	DEM_15m	74.30	532.44	0.527	810894.47	702775.21	658851.76	1.52	1.32	1.24
Kali	ALOS_5m	70.53	29.34	0.027	41449.45	35922.86	33677.68	1.41	1.22	1.15
Kali	ALOS_5m_3px	70.53	29.34	0.027	41483.92	35952.73	33705.69	1.41	1.23	1.15
Kali	TanDEMX_12m	70.53	29.34	0.028	42721.99	37025.72	34711.62	1.46	1.26	1.18
Kali	DEM_15m	70.53	29.34	0.028	42514.05	36845.51	34542.66	1.45	1.26	1.18
Kali_pkFm	ALOS_5m	70.53	3.36	0.027	41449.45	35922.86	33677.68	12.35	10.70	10.03
Kali_pkFm	ALOS_5m_3px	70.53	3.36	0.027	41483.92	35952.73	33705.69	12.36	10.71	10.04
Kali_pkFm	TanDEMX_12m	70.53	3.36	0.028	42721.99	37025.72	34711.62	12.73	11.03	10.34
Kali_pkFm	DEM_15m	70.53	3.36	0.028	42514.05	36845.51	34542.66	12.67	10.98	10.29
Kali_upstream	ALOS_5m	70.53	571.29	0.581	893198.57	774105.43	725723.84	1.56	1.36	1.27
Kali_upstream	ALOS_5m_3px	70.53	571.29	0.581	894130.22	774912.85	726480.80	1.57	1.36	1.27
Kali_upstream	TanDEMX_12m	70.53	571.29	0.600	923433.26	800308.82	750289.52	1.62	1.40	1.31
Kali_upstream	DEM_15m	70.53	571.29	0.574	883655.09	765834.41	717969.76	1.55	1.34	1.26
Phusre	ALOS_5m	58.93	165.86	0.084	129790.49	112485.09	105454.77	0.78	0.68	0.64
Phusre	ALOS_5m_3px	58.93	165.86	0.084	129920.31	112597.60	105560.25	0.78	0.68	0.64
Phusre	TanDEMX_12m	58.93	165.86	0.085	130144.42	112791.83	105742.34	0.78	0.68	0.64
Phusre	DEM_15m	58.93	165.86	0.077	117804.00	102096.80	95715.75	0.71	0.62	0.58
Phusre_wo_H_phusre	ALOS_5m	58.93	41.11	0.084	129194.79	111968.82	104970.77	3.14	2.72	2.55
Phusre_wo_H_phusre	ALOS_5m_3px	58.93	41.11	0.084	129323.86	112080.68	105075.64	3.15	2.73	2.56
Phusre_wo_H_phusre	TanDEMX_12m	58.93	41.11	0.084	129548.73	112275.56	105258.34	3.15	2.73	2.56
Phusre_wo_H_phusre	DEM_15m	58.93	41.11	0.076	117387.00	101735.40	95376.94	2.86	2.47	2.32
Phusre_pkFm	ALOS_5m	58.93	18.60	0.084	129790.49	112485.09	105454.77	6.98	6.05	5.67
Phusre_pkFm	ALOS_5m_3px	58.93	18.60	0.084	129920.31	112597.60	105560.25	6.99	6.05	5.68
Phusre_pkFm	TanDEMX_12m	58.93	18.60	0.085	130144.42	112791.83	105742.34	7.00	6.06	5.69
Phusre_pkFm	DEM_15m	58.93	18.60	0.077	117804.00	102096.80	95715.75	6.33	5.49	5.15
Phusre_upstream	ALOS_5m	58.93	751.89	0.797	1226379.52	1062862.25	996433.36	1.63	1.41	1.33
Phusre_upstream	ALOS_5m_3px	58.93	751.89	0.800	1230053.12	1066046.04	999418.16	1.64	1.42	1.33
Phusre_upstream	TanDEMX_12m	58.93	751.89	0.815	1253342.62	1086230.27	1018340.88	1.67	1.44	1.35
Phusre_upstream	DEM_15m	58.93	751.89	0.772	1188098.36	1029685.25	965329.92	1.58	1.37	1.28

Name	Images	Distance	Cat. Area	Volume removed	Volume			Erosion		
		[km][a]	[km^2]	[km^3]	[m^3 yr^{-1}][b]	[m^3 yr^{-1}][c]	[m^3 yr^{-1}][d]	[mm yr^{-1}][b]	[mm yr^{-1}][c]	[mm yr^{-1}][d]
Bijaypur	ALOS_5m	54.07	67.64	0.052	79592.06	68979.78	64668.55	1.18	1.02	0.96
Bijaypur	ALOS_5m_3px	54.07	67.64	0.052	79642.39	69023.41	64709.45	1.18	1.02	0.96
Bijaypur	TanDEMX_12m	54.07	67.64	0.051	78627.39	68143.74	63884.76	1.16	1.01	0.94
Bijaypur	DEM_15m	54.07	67.64	0.050	76206.66	66045.78	61917.92	1.13	0.98	0.92
Bijaypur_pkFm	ALOS_5m	54.07	11.62	0.052	79592.06	68979.78	64668.55	6.85	5.94	5.56
Bijaypur_pkFm	ALOS_5m_3px	54.07	11.62	0.052	79642.39	69023.41	64709.45	6.85	5.94	5.57
Bijaypur_pkFm	TanDEMX_12m	54.07	11.62	0.051	78627.39	68143.74	63884.76	6.77	5.86	5.50
Bijaypur_pkFm	DEM_15m	54.07	11.62	0.050	76206.66	66045.78	61917.92	6.56	5.68	5.33
Bijaypur_upstream	ALOS_5m	54.07	830.18	0.988	1519712.30	1317083.99	1234766.24	1.83	1.59	1.49
Bijaypur_upstream	ALOS_5m_3px	54.07	830.18	0.990	1523599.36	1320452.78	1237924.48	1.84	1.59	1.49
Bijaypur_upstream	TanDEMX_12m	54.07	830.18	1.008	1550923.08	1344133.33	1260125.00	1.87	1.62	1.52
Bijaypur_upstream	DEM_15m	54.07	830.18	0.952	1465033.45	1269695.66	1190339.68	1.76	1.53	1.43
Anpu	ALOS_5m	40.61	107.81	0.065	99841.40	86529.22	81121.14	0.93	0.80	0.75
Anpu	ALOS_5m_3px	40.61	107.81	0.065	100226.71	86863.15	81434.21	0.93	0.81	0.76
Anpu	TanDEMX_12m	40.61	107.81	0.069	106515.56	92313.48	86543.89	0.99	0.86	0.80
Anpu	DEM_15m	40.61	107.81	0.051	79094.97	68548.98	64264.67	0.73	0.64	0.60
Anpu_pkFm	ALOS_5m	40.61	22.44	0.065	99841.40	86529.22	81121.14	4.45	3.86	3.61
Anpu_pkFm	ALOS_5m_3px	40.61	22.44	0.065	100226.71	86863.15	81434.21	4.47	3.87	3.63
Anpu_pkFm	TanDEMX_12m	40.61	22.44	0.069	106515.56	92313.48	86543.89	4.75	4.11	3.86
Anpu_pkFm	DEM_15m	40.61	22.44	0.051	79094.97	68548.98	64264.67	3.52	3.05	2.86
Anpu_wo_RT	ALOS_5m	40.61	34.73	0.034	51684.50	44793.23	41993.65	1.49	1.29	1.21
Anpu_wo_RT	ALOS_5m_3px	40.61	34.73	0.034	51960.73	45032.63	42218.09	1.50	1.30	1.22
Anpu_wo_RT	TanDEMX_12m	40.61	34.73	0.037	57496.69	49830.46	46716.06	1.66	1.43	1.35
Anpu_wo_RT	DEM_15m	40.61	34.73	0.028	42868.50	37152.70	34830.66	1.23	1.07	1.00
Anpu_pkFm_wo_RT	ALOS_5m	40.61	3.97	0.034	51684.50	44793.23	41993.65	13.01	11.28	10.57
Anpu_pkFm_wo_RT	ALOS_5m_3px	40.61	3.97	0.034	51960.73	45032.63	42218.09	13.08	11.34	10.63
Anpu_pkFm_wo_RT	TanDEMX_12m	40.61	3.97	0.037	57496.69	49830.46	46716.06	14.48	12.55	11.76
Anpu_pkFm_wo_RT	DEM_15m	40.61	3.97	0.028	42868.50	37152.70	34830.66	10.79	9.35	8.77
Anpu_upstream	ALOS_5m	40.61	979.57	1.456	2239538.46	1940933.33	1819625.00	2.29	1.98	1.86
Anpu_upstream	ALOS_5m_3px	40.61	979.57	1.459	2244461.54	1945200.00	1823625.00	2.29	1.99	1.86

Name	Images	Distance	Cat. Area	Volume removed	Volume			Erosion		
		[km][a]	[km^2]	[km^3]	[m^3 yr^{-1}][b]	[m^3 yr^{-1}][c]	[m^3 yr^{-1}][d]	[mm yr^{-1}][b]	[mm yr^{-1}][c]	[mm yr^{-1}][d]
Anpu_upstream	TanDEMX_12m	40.61	979.57	1.491	2293076.92	1987333.33	1863125.00	2.34	2.03	1.90
Anpu_upstream	DEM_15m	40.61	979.57	1.374	2114153.85	1832266.67	1717750.00	2.16	1.87	1.75
Tal	ALOS_5m	40.61	31.97	0.006	9043.08	7837.33	7347.50	0.28	0.25	0.23
Tal	ALOS_5m_3px	40.61	31.97	0.006	9098.83	7885.65	7392.80	0.28	0.25	0.23
Tal	TanDEMX_12m	40.61	31.97	0.006	9380.10	8129.42	7621.33	0.29	0.25	0.24
Tal	DEM_15m	40.61	31.97	0.003	4866.62	4217.73	3954.13	0.15	0.13	0.12
Tal_pkFm	ALOS_5m	40.61	3.44	0.006	9043.08	7837.33	7347.50	2.63	2.28	2.14
Tal_pkFm	ALOS_5m_3px	40.61	3.44	0.006	9098.83	7885.65	7392.80	2.64	2.29	2.15
Tal_pkFm	TanDEMX_12m	40.61	3.44	0.006	9380.10	8129.42	7621.33	2.73	2.36	2.21
Tal_pkFm	DEM_15m	40.61	3.44	0.003	4866.62	4217.73	3954.13	1.41	1.23	1.15
Rupa	ALOS_5m	40.61	41.11	0.025	39113.83	33898.65	31779.99	0.95	0.82	0.77
Rupa	ALOS_5m_3px	40.61	41.11	0.025	39167.15	33944.87	31823.31	0.95	0.83	0.77
Rupa	TanDEMX_12m	40.61	41.11	0.026	39638.77	34353.60	32206.50	0.96	0.84	0.78
Rupa	DEM_15m	40.61	41.11	0.020	31359.86	27178.54	25479.89	0.76	0.66	0.62
Rupa_pkFm	ALOS_5m	40.61	15.03	0.025	39113.83	33898.65	31779.99	2.60	2.26	2.11
Rupa_pkFm	ALOS_5m_3px	40.61	15.03	0.025	39167.15	33944.87	31823.31	2.61	2.26	2.12
Rupa_pkFm	TanDEMX_12m	40.61	15.03	0.026	39638.77	34353.60	32206.50	2.64	2.29	2.14
Rupa_pkFm	DEM_15m	40.61	15.03	0.020	31359.86	27178.54	25479.89	2.09	1.81	1.70
Pudi	ALOS_5m	38.88	10.40	0.007	10484.46	9086.53	8518.63	1.01	0.87	0.82
Pudi	ALOS_5m_3px	39.88	10.40	0.007	10506.00	9105.20	8536.13	1.01	0.88	0.82
Pudi	TanDEMX_12m	38.88	10.40	0.009	13569.73	11760.43	11025.40	1.30	1.13	1.06
Pudi	DEM_15m	39.88	10.40	0.009	13121.75	11372.19	10661.42	1.26	1.09	1.03
Pudi_pkFm	ALOS_5m	40.88	1.51	0.007	10484.46	9086.53	8518.63	6.95	6.02	5.65
Pudi_pkFm	ALOS_5m_3px	41.88	1.51	0.007	10506.00	9105.20	8536.13	6.96	6.03	5.66
Pudi_pkFm	TanDEMX_12m	42.88	1.51	0.009	13569.73	11760.43	11025.40	8.99	7.79	7.31
Pudi_pkFm	DEM_15m	43.88	1.51	0.009	13121.75	11372.19	10661.42	8.70	7.54	7.07
Saraudi	ALOS_5m	35.32	93.79	0.038	58997.59	51131.25	47935.55	0.63	0.55	0.51
Saraudi	ALOS_5m_3px	35.32	93.79	0.039	60215.13	52186.45	48924.80	0.64	0.56	0.52

Name	Images	Distance	Cat. Area	Volume removed	Volume			Erosion		
		[km][a]	[km^2]	[km^3]	[m^3 yr^{-1}][b]	[m^3 yr^{-1}][c]	[m^3 yr^{-1}][d]	[mm yr^{-1}][b]	[mm yr^{-1}][c]	[mm yr^{-1}][d]
Saraudi	TanDEMX_12m	35.32	93.79	0.042	65025.42	56355.37	52833.16	0.69	0.60	0.56
Saraudi	DEM_15m	35.32	93.79	0.037	57184.65	49560.03	46462.53	0.61	0.53	0.50
Saraudi_pkFm	ALOS_5m	35.32	6.50	0.038	58997.59	51131.25	47935.55	9.08	7.87	7.38
Saraudi_pkFm	ALOS_5m_3px	35.32	6.50	0.039	60215.13	52186.45	48924.80	9.27	8.03	7.53
Saraudi_pkFm	TanDEMX_12m	35.32	6.50	0.042	65025.42	56355.37	52833.16	10.01	8.67	8.13
Saraudi_pkFm	DEM_15m	35.32	6.50	0.037	57184.65	49560.03	46462.53	8.80	7.63	7.15
Saraudi_upstream	ALOS_5m	35.32	1094.49	1.601	2463538.46	2135066.67	2001625.00	2.25	1.95	1.83
Saraudi_upstream	ALOS_5m_3px	35.32	1094.49	1.605	2469846.15	2140533.33	2006750.00	2.26	1.96	1.83
Saraudi_upstream	TanDEMX_12m	35.32	1094.49	1.648	2536000.00	2197866.67	2060500.00	2.32	2.01	1.88
Saraudi_upstream	DEM_15m	35.32	1094.49	1.515	2330615.39	2019866.67	1893625.00	2.13	1.85	1.73
Kyandi	ALOS_5m	27.69	97.37	0.016	24221.19	20991.70	19679.72	0.25	0.22	0.20
Kyandi	ALOS_5m_3px	27.69	97.37	0.016	24259.21	21024.65	19710.61	0.25	0.22	0.20
Kyandi	TanDEMX_12m	27.69	97.37	0.018	27173.66	23550.51	22078.60	0.28	0.24	0.23
Kyandi	DEM_15m	27.69	97.37	0.012	19110.74	16562.64	15527.48	0.20	0.17	0.16
Kyandi_pkFm	ALOS_5m	27.69	3.50	0.016	24221.19	20991.70	19679.72	6.92	6.00	5.62
Kyandi_pkFm	ALOS_5m_3px	27.69	3.50	0.016	24259.21	21024.65	19710.61	6.93	6.01	5.63
Kyandi_pkFm	TanDEMX_12m	27.69	3.50	0.018	27173.66	23550.51	22078.60	7.76	6.73	6.31
Kyandi_pkFm	DEM_15m	27.69	3.50	0.012	19110.74	16562.64	15527.48	5.46	4.73	4.44
Kyandi_upstream	ALOS_5m	27.69	1221.08	1.791	2755538.46	2388133.33	2238875.00	2.26	1.96	1.83
Kyandi_upstream	ALOS_5m_3px	27.69	1221.08	1.796	2762615.39	2394266.67	2244625.00	2.26	1.96	1.84
Kyandi_upstream	TanDEMX_12m	27.69	1221.08	1.850	2845384.62	2466000.00	2311875.00	2.33	2.02	1.89
Kyandi_upstream	DEM_15m	27.69	1221.08	1.713	2635384.62	2284000.00	2141250.00	2.16	1.87	1.75
Magdi	ALOS_5m	27.28	68.71	0.011	16715.66	14486.91	13581.48	0.24	0.21	0.20
Magdi	ALOS_5m_3px	27.28	68.71	0.011	16752.30	14518.66	13611.25	0.24	0.21	0.20
Magdi	TanDEMX_12m	27.28	68.71	0.011	16961.43	14699.90	13781.16	0.25	0.21	0.20
Magdi	DEM_15m	27.28	68.71	0.008	11814.46	10239.20	9599.25	0.17	0.15	0.14
Magdi_pkFm	ALOS_5m	27.28	4.46	0.011	16715.66	14486.91	13581.48	3.75	3.25	3.04
Magdi_pkFm	ALOS_5m_3px	27.28	4.46	0.011	16752.30	14518.66	13611.25	3.76	3.25	3.05

Name	Images	Distance	Cat. Area	Volume removed	Volume			Erosion		
		[km][a]	[km^2]	[km^3]	[m^3 yr^{-1}][b]	[m^3 yr^{-1}][c]	[m^3 yr^{-1}][d]	[mm yr^{-1}][b]	[mm yr^{-1}][c]	[mm yr^{-1}][d]
Magdi_pkFm	TanDEMX_12m	27.28	4.46	0.011	16961.43	14699.90	13781.16	3.80	3.30	3.09
Magdi_pkFm	DEM_15m	27.28	4.46	0.008	11814.46	10239.20	9599.25	2.65	2.30	2.15
Magdi_upstream	ALOS_5m	27.28	1289.89	1.806	2778153.85	2407733.33	2257250.00	2.15	1.87	1.75
Magdi_upstream	ALOS_5m_3px	27.28	1289.89	1.810	2785230.77	2413866.67	2263000.00	2.16	1.87	1.75
Magdi_upstream	TanDEMX_12m	27.28	1289.89	1.864	2868307.69	2485866.67	2330500.00	2.22	1.93	1.81
Magdi_upstream	DEM_15m	27.28	1289.89	1.713	2635384.62	2284000.00	2141250.00	2.04	1.77	1.66
Siddi	ALOS_5m	21.15	26.25	0.006	9597.08	8317.47	7797.63	0.37	0.32	0.30
Siddi	ALOS_5m_3px	21.15	26.25	0.006	9645.85	8359.73	7837.25	0.37	0.32	0.30
Siddi	TanDEMX_12m	21.15	26.25	0.007	10686.85	9261.94	8683.07	0.41	0.35	0.33
Siddi	DEM_15m	21.15	26.25	0.006	8752.31	7585.33	7111.25	0.33	0.29	0.27
Siddi_pkFm	ALOS_5m	21.15	1.88	0.006	9597.08	8317.47	7797.63	5.10	4.42	4.15
Siddi_pkFm	ALOS_5m_3px	21.15	1.88	0.006	9645.85	8359.73	7837.25	5.13	4.44	4.17
Siddi_pkFm	TanDEMX_12m	21.15	1.88	0.007	10686.85	9261.94	8683.07	5.68	4.92	4.62
Siddi_pkFm	DEM_15m	21.15	1.88	0.006	8752.31	7585.33	7111.25	4.65	4.03	3.78
Siddi_upstream	ALOS_5m	21.15	1326.79	1.907	2933846.15	2542666.67	2383750.00	2.21	1.92	1.80
Siddi_upstream	ALOS_5m_3px	21.15	1326.79	1.856	2855692.31	2474933.33	2320250.00	2.15	1.87	1.75
Siddi_upstream	TanDEMX_12m	21.15	1326.79	1.916	2946923.08	2554000.00	2394375.00	2.22	1.92	1.80
Siddi_upstream	DEM_15m	21.15	1326.79	1.753	2696923.08	2337333.33	2191250.00	2.03	1.76	1.65
Sigdi	ALOS_5m	20.43		0.000	385.98	334.52	313.61	0.01	0.01	0.01
Sigdi	ALOS_5m_3px	20.43	33.74	0.000	384.03	332.83	312.03	0.01	0.01	0.01
Sigdi	TanDEMX_12m	20.43	33.74	0.000	467.57	405.23	379.90	0.01	0.01	0.01
Sigdi	DEM_15m	20.43	33.74	0.000	375.60	325.52	305.18	0.01	0.01	0.01
Sigdi_pkFm	ALOS_5m	20.43	1.52	0.000	385.98	334.52	313.61	0.25	0.22	0.21
Sigdi_pkFm	ALOS_5m_3px	20.43	1.52	0.000	384.03	332.83	312.03	0.25	0.22	0.21
Sigdi_pkFm	TanDEMX_12m	20.43	1.52	0.000	467.57	405.23	379.90	0.31	0.27	0.25
Sigdi_pkFm	DEM_15m	20.43	1.52	0.000	375.60	325.52	305.18	0.25	0.21	0.20
Sigdi_upstream	ALOS_5m	20.43	1360.67	1.851	2848153.85	2468400.00	2314125.00	2.09	1.81	1.70
Sigdi_upstream	ALOS_5m_3px	20.43	1360.67	1.861	2863538.46	2481733.33	2326625.00	2.10	1.82	1.71

Name	Images	Distance	Cat. Area	Volume removed	Volume			Erosion		
		[km][a]	[km^2]	[km^3]	[m^3 yr^{-1}][b]	[m^3 yr^{-1}][c]	[m^3 yr^{-1}][d]	[mm yr^{-1}][b]	[mm yr^{-1}][c]	[mm yr^{-1}][d]
Sigdi_upstream	TanDEMX_12m	20.43	1360.67	1.929	2967076.92	2571466.67	2410750.00	2.18	1.89	1.77
Sigdi_upstream	DEM_15m	20.43	1360.67	1.757	2703692.31	2343200.00	2196750.00	1.99	1.72	1.61
Gondang	ALOS_5m	18.56	11.41	0.004	5972.92	5176.53	4853.00	0.52	0.45	0.43
Gondang	ALOS_5m_3px	18.56	11.41	0.004	5988.55	5190.08	4865.70	0.53	0.46	0.43
Gondang	TanDEMX_12m	18.56	11.41	0.004	6874.51	5957.91	5585.54	0.60	0.52	0.49
Gondang	DEM_15m	18.56	11.41	0.003	4647.10	4027.49	3775.77	0.41	0.35	0.33
Gondang_pkFm	ALOS_5m	18.56	0.79	0.004	5972.92	5176.53	4853.00	7.56	6.55	6.14
Gondang_pkFm	ALOS_5m_3px	18.56	0.79	0.004	5988.55	5190.08	4865.70	7.58	6.57	6.16
Gondang_pkFm	TanDEMX_12m	18.56	0.79	0.004	6874.51	5957.91	5585.54	8.70	7.54	7.07
Gondang_pkFm	DEM_15m	18.56	0.79	0.003	4647.10	4027.49	3775.77	5.88	5.10	4.78
Seti	ALOS_5m	10.87	1400.25	1.907	2933846.15	2542666.67	2383750.00	2.10	1.82	1.70
Seti	ALOS_5m_3px	10.87	1400.25	1.912	2941692.31	2549466.67	2390125.00	2.10	1.82	1.71
Seti	TanDEMX_12m	10.87	1400.25	1.987	3056153.85	2648666.67	2483125.00	2.18	1.89	1.77
Seti	DEM_15m	10.87	1400.25	1.803	2773230.77	2403466.67	2253250.00	1.98	1.72	1.61
Seti_wo_trip_pkFm	ALOS_5m	10.87	175.99	1.552	2388331.20	2069887.04	1940519.10	13.57	11.76	11.03
Seti_wo_trip_pkFm	ALOS_5m_3px	10.87	175.99	1.556	2393255.34	2074154.63	1944519.96	13.60	11.79	11.05
Seti_wo_trip_pkFm	TanDEMX_12m	10.87	175.99	1.614	2483655.02	2152501.02	2017969.71	14.11	12.23	11.47
Seti_wo_trip_pkFm	DEM_15m	10.87	175.99	1.470	2261007.04	1959539.44	1837068.22	12.85	11.13	10.44

a Distance along Seti Khola from down- to upstream
b Values calculated over 660 years
c Values calculated over 750 years
d Values calculated over 800 years
e Values calculated with a bulk density of 1.6 [g cm^{-3}]
f Values calculated with a bulk density of 1.8 [g cm^{-3}]
g Values calculated with a bulk density of 2.0 [g cm^{-3}]

Table C.3.: Voumetric calculations for the fluvial network of the Pokhara Formation. Sediment Yield rates measured with different bulk densities and over different times scales. Names are river names with *pkFm* - calculated for the area covered by the Pokhara Formation only - or *upstream* - calculated from the confluence with the Seti Khola for the area upstream.

Name	Images	Sediment Yield [m^3 km^2 yr^{-1}]			Sediment Yield [t km^2 yr^{-1}]								
		b	c	d	b,e	b,f	b,g	c,e	c,f	c,g	d,e	d,f	d,g
Upper_seti	ALOS_5m	1449.93	1256.61	1178.07	2319.89	2609.87	2899.86	2010.57	2261.89	2513.21	1884.91	2120.52	2356.14
Upper_seti	ALOS_5m_3px	1450.14	1256.79	1178.24	2320.22	2610.25	2900.28	2010.86	2262.22	2513.58	1885.18	2120.83	2356.48
Upper_seti	TanDEMX_12m	1445.26	1252.56	1174.28	2312.42	2601.47	2890.52	2004.10	2254.61	2505.12	1878.84	2113.70	2348.55
Upper_seti	DEM_15m	1391.45	1205.92	1130.55	2226.31	2504.60	2782.89	1929.47	2170.65	2411.84	1808.88	2034.99	2261.10
Mardi	ALOS_5m	337.19	292.23	273.97	539.51	606.95	674.39	467.58	526.02	584.47	438.35	493.15	547.94
Mardi	ALOS_5m_3px	337.70	292.68	274.38	540.32	607.86	675.41	468.28	526.82	585.35	439.01	493.89	548.77
Mardi	TanDEMX_12m	373.02	323.28	303.08	596.83	671.44	746.04	517.25	581.91	646.57	484.93	545.54	606.16
Mardi	DEM_15m	398.44	345.31	323.73	637.50	717.19	796.88	552.50	621.56	690.63	517.97	582.72	647.46
Mardi_pkFm	ALOS_5m	14093.51	12214.37	11450.98	22549.61	25368.32	28187.02	19543.00	21985.87	24428.75	18321.56	20611.76	22901.95
Mardi_pkFm	ALOS_5m_3px	14114.77	12232.80	11468.25	22583.64	25406.59	28229.54	19572.48	22019.05	24465.61	18349.20	20642.85	22936.51
Mardi_pkFm	TanDEMX_12m	15590.93	13512.14	12667.63	24945.49	28063.68	31181.86	21619.43	24321.85	27024.28	20268.21	22801.74	25335.26
Mardi_pkFm	DEM_15m	16653.34	14432.90	13530.84	26645.35	29976.02	33306.69	23092.64	25979.22	28865.79	21649.35	24355.51	27061.68
Mardi_upstream	ALOS_5m	1144.84	992.20	930.18	1831.75	2060.71	2289.68	1587.51	1785.95	1984.39	1488.29	1674.33	1860.37
Mardi_upstream	ALOS_5m_3px	1145.13	992.45	930.42	1832.21	2061.24	2290.26	1587.92	1786.40	1984.89	1488.67	1674.75	1860.84
Mardi_upstream	TanDEMX_12m	1158.27	1003.84	941.10	1853.24	2084.89	2316.55	1606.14	1806.91	2007.67	1505.76	1693.97	1882.19
Mardi_upstream	DEM_15m	1137.89	986.17	924.54	1820.63	2048.21	2275.79	1577.88	1775.11	1972.35	1479.26	1664.17	1849.08
Yangdi	ALOS_5m	684.42	593.16	556.09	1095.07	1231.95	1368.83	949.06	1067.69	1186.32	889.74	1000.96	1112.18
Yangdi	ALOS_5m_3px	713.71	618.55	579.89	1141.94	1284.69	1427.43	989.68	1113.39	1237.10	927.83	1043.81	1159.79
Yangdi	TanDEMX_12m	689.68	597.72	560.36	1103.49	1241.42	1379.36	956.36	1075.90	1195.44	896.58	1008.66	1120.73
Yangdi	DEM_15m	832.04	721.10	676.03	1331.27	1497.68	1664.09	1153.77	1297.99	1442.21	1081.66	1216.86	1352.07
Yangdi_pkFm	ALOS_5m	6975.39	6045.33	5667.50	11160.62	12555.69	13950.77	9672.53	10881.60	12090.67	9068.00	10201.50	11335.00
Yangdi_pkFm	ALOS_5m_3px	7273.98	6304.12	5910.11	11638.37	13093.16	14547.96	10086.59	11347.41	12608.23	9456.17	10638.20	11820.22
Yangdi_pkFm	TanDEMX_12m	7029.02	6091.82	5711.08	11246.44	12652.24	14058.05	9746.91	10965.28	12183.64	9137.73	10279.95	11422.16
Yangdi_pkFm	DEM_15m	8479.96	7349.30	6889.97	13567.93	15263.92	16959.91	11758.87	13228.73	14698.59	11023.94	12401.94	13779.93
Yangdi_upstream	ALOS_5m	1532.96	1328.56	1245.53	2452.73	2759.32	3065.91	2125.70	2391.41	2657.12	1992.84	2241.95	2491.05
Yangdi_upstream	ALOS_5m_3px	1533.60	1329.12	1246.05	2453.75	2760.47	3067.19	2126.59	2392.41	2658.23	1993.67	2242.88	2492.09
Yangdi_upstream	TanDEMX_12m	1587.56	1375.88	1289.89	2540.09	2857.60	3175.11	2201.41	2476.59	2751.76	2063.82	2321.80	2579.78
Yangdi_upstream	DEM_15m	1522.99	1319.92	1237.43	2436.78	2741.38	3045.98	2111.88	2375.86	2639.85	1979.89	2227.37	2474.86

Name	Images	Sediment Yield [m^3 km^2 yr^{-1}]						Sediment Yield [t km^2 yr^{-1}]					
		b	c	d	b,e	b,f	b,g	c,e	c,f	c,g	d,e	d,f	d,g
Kali	ALOS_5m	1412.69	1224.34	1147.81	2260.31	2542.85	2825.39	1958.94	2203.80	2448.67	1836.50	2066.07	2295.63
Kali	ALOS_5m_3px	1413.87	1225.35	1148.77	2262.19	2544.97	2827.74	1960.57	2205.64	2450.71	1838.03	2067.78	2297.54
Kali	TanDEMX_12m	1456.07	1261.92	1183.05	2329.71	2620.92	2912.13	2019.08	2271.46	2523.85	1892.89	2129.50	2366.11
Kali	DEM_15m	1448.98	1255.78	1177.30	2318.37	2608.16	2897.96	2009.25	2260.41	2511.56	1883.67	2119.13	2354.59
Kali_pkFm	ALOS_5m	12348.24	10701.81	10032.94	19757.18	22226.83	24696.48	17122.89	19263.25	21403.61	16052.71	18059.30	20065.89
Kali_pkFm	ALOS_5m_3px	12358.51	10710.71	10041.29	19773.61	22245.31	24717.01	17137.13	19279.27	21421.41	16066.06	18074.32	20082.57
Kali_pkFm	TanDEMX_12m	12727.34	11030.36	10340.96	20363.74	22909.21	25454.68	17648.58	19854.65	22060.72	16545.54	18613.73	20681.93
Kali_pkFm	DEM_15m	12665.39	10976.67	10290.63	20264.63	22797.70	25330.78	17562.68	19758.01	21953.35	16465.01	18523.14	20581.26
Kali_upstream	ALOS_5m	1563.48	1355.02	1270.33	2501.57	2814.27	3126.96	2168.03	2439.03	2710.04	2032.53	2286.59	2540.66
Kali_upstream	ALOS_5m_3px	1565.11	1356.43	1271.65	2504.18	2817.20	3130.23	2170.29	2441.58	2712.86	2034.65	2288.98	2543.31
Kali_upstream	TanDEMX_12m	1616.41	1400.89	1313.33	2586.25	2909.53	3232.81	2241.42	2521.59	2801.77	2101.33	2363.99	2626.66
Kali_upstream	DEM_15m	1546.78	1340.54	1256.76	2474.84	2784.20	3093.55	2144.86	2412.97	2681.08	2010.81	2262.16	2513.51
Phusre	ALOS_5m	782.53	678.19	635.81	1252.05	1408.55	1565.06	1085.11	1220.75	1356.39	1017.29	1144.45	1271.61
Phusre	ALOS_5m_3px	783.31	678.87	636.44	1253.30	1409.96	1566.63	1086.19	1221.97	1357.74	1018.31	1145.60	1272.88
Phusre	TanDEMX_12m	784.66	680.04	637.54	1255.46	1412.40	1569.33	1088.07	1224.08	1360.08	1020.06	1147.57	1275.08
Phusre	DEM_15m	710.26	615.56	577.09	1136.42	1278.47	1420.52	984.90	1108.01	1231.12	923.34	1038.76	1154.18
Phusre_wo_H_phusre	ALOS_5m	3142.42	2723.43	2553.22	5027.88	5656.36	6284.85	4357.49	4902.18	5446.87	4085.15	4595.80	5106.44
Phusre_wo_H_phusre	ALOS_5m_3px	3145.56	2726.15	2555.77	5032.90	5662.01	6291.13	4361.85	4907.08	5452.31	4089.23	4600.39	5111.54
Phusre_wo_H_phusre	TanDEMX_12m	3151.03	2730.90	2560.21	5041.65	5671.86	6302.07	4369.43	4915.61	5461.79	4096.34	4608.39	5120.43
Phusre_wo_H_phusre	DEM_15m	2855.22	2474.53	2319.87	4568.35	5139.40	5710.44	3959.24	4454.15	4949.05	3711.79	4175.76	4639.73
Phusre_pkFm	ALOS_5m	6978.70	6048.20	5670.19	11165.91	12561.65	13957.39	9677.13	10886.77	12096.41	9072.30	10206.34	11340.38
Phusre_pkFm	ALOS_5m_3px	6985.68	6054.25	5675.86	11177.08	12574.22	13971.35	9686.80	10897.66	12108.51	9081.38	10216.55	11351.72
Phusre_pkFm	TanDEMX_12m	6997.73	6064.70	5685.65	11196.36	12595.91	13995.45	9703.51	10916.45	12129.39	9097.04	10234.18	11371.31
Phusre_pkFm	DEM_15m	6334.20	5489.64	5146.53	10134.71	11401.55	12668.39	8783.42	9881.34	10979.27	8234.45	9263.76	10293.07
Phusre_upstream	ALOS_5m	1631.05	1413.58	1325.23	2609.69	2935.90	3262.11	2261.73	2544.44	2827.16	2120.37	2385.42	2650.46
Phusre_upstream	ALOS_5m_3px	1635.94	1417.81	1329.20	2617.50	2944.69	3271.88	2268.50	2552.07	2835.63	2126.72	2392.56	2658.40
Phusre_upstream	TanDEMX_12m	1666.91	1444.66	1354.37	2667.06	3000.45	3333.83	2311.45	2600.39	2889.32	2166.99	2437.86	2708.74
Phusre_upstream	DEM_15m	1580.14	1369.46	1283.86	2528.23	2844.25	3160.28	2191.13	2465.02	2738.91	2054.18	2310.96	2567.73
Bijaypur	ALOS_5m	1176.75	1019.85	956.11	1882.81	2118.16	2353.51	1631.76	1835.73	2039.71	1529.78	1721.00	1912.22
Bijaypur	ALOS_5m_3px	1177.50	1020.50	956.72	1884.00	2119.50	2354.99	1632.80	1836.90	2041.00	1530.75	1722.09	1913.43

Name	Images	Sediment Yield [m^3 km^2 yr^{-1}]						Sediment Yield [t km^2 yr^{-1}]					
		b	c	d	b,e	b,f	b,g	c,e	c,f	c,g	d,e	d,f	d,g
Bijaypur	TanDEMX_12m	1162.49	1007.49	944.52	1859.99	2092.48	2324.98	1611.99	1813.49	2014.98	1511.24	1700.14	1889.05
Bijaypur	DEM_15m	1126.70	976.47	915.44	1802.72	2028.06	2253.40	1562.36	1757.65	1952.95	1464.71	1647.80	1830.89
Bijaypur_pkFm	ALOS_5m	6848.99	5935.79	5564.80	10958.38	12328.17	13697.97	9497.26	10684.42	11871.57	8903.68	10016.64	11129.60
Bijaypur_pkFm	ALOS_5m_3px	6853.32	5939.54	5568.32	10965.31	12335.97	13706.63	9503.27	10691.17	11879.08	8909.31	10022.98	11136.64
Bijaypur_pkFm	TanDEMX_12m	6765.97	5863.84	5497.35	10825.56	12178.75	13531.95	9382.15	10554.92	11727.69	8795.77	9895.24	10994.71
Bijaypur_pkFm	DEM_15m	6557.67	5683.31	5328.11	10492.27	11803.80	13115.34	9093.30	10229.96	11366.63	8524.97	9590.59	10656.21
Bijaypur_upstream	ALOS_5m	1830.59	1586.51	1487.35	2928.94	3295.06	3661.18	2538.42	2855.72	3173.02	2379.77	2677.24	2974.71
Bijaypur_upstream	ALOS_5m_3px	1835.27	1590.57	1491.16	2936.44	3303.49	3670.55	2544.91	2863.03	3181.14	2385.85	2684.09	2982.32
Bijaypur_upstream	TanDEMX_12m	1868.19	1619.09	1517.90	2989.10	3362.73	3736.37	2590.55	2914.37	3238.19	2428.64	2732.22	3035.80
Bijaypur_upstream	DEM_15m	1764.73	1529.43	1433.84	2823.56	3176.51	3529.45	2447.09	2752.97	3058.86	2294.14	2580.91	2867.68
Anpu	ALOS_5m	926.11	802.63	752.47	1481.78	1667.00	1852.22	1284.21	1444.74	1605.26	1203.95	1354.44	1504.93
Anpu	ALOS_5m_3px	929.69	805.73	755.37	1487.50	1673.44	1859.37	1289.17	1450.31	1611.46	1208.59	1359.67	1510.74
Anpu	TanDEMX_12m	988.02	856.28	802.77	1580.83	1778.44	1976.04	1370.06	1541.31	1712.57	1284.43	1444.98	1605.53
Anpu	DEM_15m	733.67	635.85	596.11	1173.88	1320.61	1467.34	1017.36	1144.53	1271.70	953.77	1073.00	1192.22
Anpu_pkFm	ALOS_5m	4448.73	3855.56	3614.59	7117.96	8007.71	8897.45	6168.90	6940.01	7711.12	5783.34	6506.26	7229.18
Anpu_pkFm	ALOS_5m_3px	4465.89	3870.44	3628.54	7145.43	8038.61	8931.79	6192.71	6966.79	7740.88	5805.66	6531.37	7257.08
Anpu_pkFm	TanDEMX_12m	4746.11	4113.30	3856.22	7593.78	8543.00	9492.22	6581.27	7403.93	8226.59	6169.94	6941.19	7712.43
Anpu_pkFm	DEM_15m	3524.31	3054.40	2863.50	5638.89	6343.75	7048.61	4887.04	5497.92	6108.80	4581.60	5154.30	5727.00
Anpu_wo_RT	ALOS_5m	1488.12	1289.70	1209.10	2380.99	2678.62	2976.24	2063.53	2321.47	2579.41	1934.56	2176.38	2418.20
Anpu_wo_RT	ALOS_5m_3px	1496.07	1296.60	1215.56	2393.72	2692.93	2992.15	2074.56	2333.87	2593.19	1944.90	2188.01	2431.12
Anpu_wo_RT	TanDEMX_12m	1655.47	1434.74	1345.07	2648.75	2979.84	3310.93	2295.58	2582.53	2869.48	2152.11	2421.12	2690.13
Anpu_wo_RT	DEM_15m	1234.29	1069.71	1002.86	1974.86	2221.72	2468.57	1711.54	1925.49	2139.43	1604.57	1805.14	2005.72
Anpu_pkFm_wo_RT	ALOS_5m	13012.67	11277.65	10572.79	20820.27	23422.80	26025.34	18044.23	20299.76	22555.29	16916.47	19031.03	21145.59
Anpu_pkFm_wo_RT	ALOS_5m_3px	13082.22	11337.92	10629.30	20931.55	23547.99	26164.43	18140.67	20408.26	22675.84	17006.88	19132.74	21258.60
Anpu_pkFm_wo_RT	TanDEMX_12m	14476.01	12545.88	11761.76	23161.62	26056.82	28952.02	20073.40	22582.58	25091.75	18818.81	21171.17	23523.52
Anpu_pkFm_wo_RT	DEM_15m	10793.05	9353.98	8769.36	17268.89	19427.50	21586.11	14966.37	16837.16	18707.96	14030.97	15784.84	17538.71
Anpu_upstream	ALOS_5m	2286.26	1981.42	1857.58	3658.01	4115.26	4572.51	3170.27	3566.56	3962.84	2972.13	3343.65	3715.17
Anpu_upstream	ALOS_5m_3px	2291.28	1985.78	1861.67	3666.05	4124.31	4582.56	3177.24	3574.40	3971.55	2978.67	3351.00	3723.33
Anpu_upstream	TanDEMX_12m	2340.91	2028.79	1901.99	3745.46	4213.64	4681.82	3246.06	3651.82	4057.58	3043.18	3423.58	3803.98
Anpu_upstream	DEM_15m	2158.26	1870.49	1753.58	3453.21	3884.86	4316.51	2992.78	3366.88	3740.98	2805.73	3156.45	3507.17

Name	Images	Sediment Yield [m^3 km^2 yr^{-1}]						Sediment Yield [t km^2 yr^{-1}]					
		b	c	d	b,e	b,f	b,g	c,e	c,f	c,g	d,e	d,f	d,g
Tal	ALOS_5m	282.87	245.16	229.83	452.60	509.17	565.75	392.25	441.28	490.31	367.73	413.70	459.67
Tal	ALOS_5m_3px	284.62	246.67	231.25	455.39	512.31	569.23	394.67	444.00	493.34	370.00	416.25	462.50
Tal	TanDEMX_12m	293.42	254.29	238.40	469.46	528.15	586.83	406.87	457.73	508.59	381.44	429.12	476.80
Tal	DEM_15m	152.23	131.93	123.69	243.57	274.02	304.46	211.09	237.48	263.87	197.90	222.64	247.37
Tal_pkFm	ALOS_5m	2627.70	2277.34	2135.01	4204.32	4729.86	5255.40	3643.75	4099.21	4554.68	3416.01	3843.01	4270.01
Tal_pkFm	ALOS_5m_3px	2643.90	2291.38	2148.17	4230.24	4759.02	5287.80	3666.21	4124.49	4582.76	3437.07	3866.71	4296.34
Tal_pkFm	TanDEMX_12m	2725.63	2362.22	2214.58	4361.01	4906.14	5451.27	3779.54	4251.99	4724.43	3543.32	3986.24	4429.15
Tal_pkFm	DEM_15m	1414.12	1225.57	1148.97	2262.59	2545.42	2828.24	1960.92	2206.03	2451.14	1838.36	2068.15	2297.95
Rupa	ALOS_5m	951.51	824.65	773.11	1522.42	1712.73	1903.03	1319.43	1484.36	1649.29	1236.97	1391.59	1546.21
Rupa	ALOS_5m_3px	952.81	825.77	774.16	1524.50	1715.06	1905.62	1321.23	1486.39	1651.54	1238.66	1393.49	1548.32
Rupa	TanDEMX_12m	964.28	835.71	783.48	1542.86	1735.71	1928.57	1337.14	1504.28	1671.43	1253.57	1410.27	1566.96
Rupa	DEM_15m	762.89	661.17	619.84	1220.62	1373.19	1525.77	1057.87	1190.10	1322.33	991.75	1115.72	1239.69
Rupa_pkFm	ALOS_5m	2602.49	2255.49	2114.52	4163.98	4684.48	5204.98	3608.78	4059.88	4510.98	3383.23	3806.14	4229.04
Rupa_pkFm	ALOS_5m_3px	2606.04	2258.56	2117.40	4169.66	4690.86	5212.07	3613.70	4065.42	4517.13	3387.85	3811.33	4234.81
Rupa_pkFm	TanDEMX_12m	2637.42	2285.76	2142.90	4219.86	4747.35	5274.83	3657.22	4114.37	4571.52	3428.64	3857.22	4285.80
Rupa_pkFm	DEM_15m	2086.57	1808.36	1695.34	3338.51	3755.82	4173.14	2893.37	3255.05	3616.72	2712.54	3051.61	3390.67
Pudi	ALOS_5m	1008.11	873.70	819.09	1612.98	1814.60	2016.22	1397.91	1572.65	1747.39	1310.55	1474.36	1638.18
Pudi	ALOS_5m_3px	1010.18	875.49	820.77	1616.29	1818.33	2020.37	1400.79	1575.88	1750.98	1313.24	1477.39	1641.55
Pudi	TanDEMX_12m	1304.77	1130.80	1060.12	2087.63	2348.58	2609.54	1809.28	2035.44	2261.60	1696.20	1908.22	2120.25
Pudi	DEM_15m	1261.69	1093.47	1025.13	2018.71	2271.05	2523.39	1749.55	1968.24	2186.94	1640.20	1845.23	2050.25
Pudi_pkFm	ALOS_5m	6947.82	6021.44	5645.10	11116.50	12506.07	13895.63	9634.30	10838.59	12042.88	9032.16	10161.18	11290.20
Pudi_pkFm	ALOS_5m_3px	6962.09	6033.81	5656.70	11139.34	12531.76	13924.18	9654.10	10860.86	12067.62	9050.71	10182.05	11313.39
Pudi_pkFm	TanDEMX_12m	8992.35	7793.37	7306.28	14387.76	16186.23	17984.70	12469.39	14028.07	15586.74	11690.06	13151.31	14612.57
Pudi_pkFm	DEM_15m	8695.49	7536.09	7065.08	13912.78	15651.88	17390.98	12057.74	13564.96	15072.18	11304.13	12717.15	14130.17
Saraudi	ALOS_5m	629.02	545.15	511.08	1006.44	1132.24	1258.05	872.25	981.28	1090.31	817.73	919.95	1022.16
Saraudi	ALOS_5m_3px	642.01	556.40	521.63	1027.21	1155.61	1284.01	890.25	1001.53	1112.81	834.61	938.93	1043.26
Saraudi	TanDEMX_12m	693.29	600.85	563.30	1109.27	1247.93	1386.58	961.37	1081.54	1201.71	901.28	1013.94	1126.60
Saraudi	DEM_15m	609.70	528.40	495.38	975.51	1097.45	1219.39	845.44	951.12	1056.80	792.60	891.68	990.75

Name	Images	Sediment Yield [m^3 km^2 yr^{-1}]						Sediment Yield [t km^2 yr^{-1}]					
		b	c	d	b,e	b,f	b,g	c,e	c,f	c,g	d,e	d,f	d,g
Saraudi_pkFm	ALOS_5m	9081.69	7870.80	7378.88	14530.71	16347.05	18163.39	12593.28	14167.44	15741.60	11806.20	13281.98	14757.75
Saraudi_pkFm	ALOS_5m_3px	9269.11	8033.23	7531.16	14830.58	16684.41	18538.23	12853.17	14459.82	16066.46	12049.85	13556.08	15062.31
Saraudi_pkFm	TanDEMX_12m	10009.58	8674.97	8132.78	16015.32	18017.24	20019.16	13879.95	15614.94	17349.94	13012.45	14639.01	16265.56
Saraudi_pkFm	DEM_15m	8802.62	7628.94	7152.13	14084.20	15844.72	17605.24	12206.30	13732.09	15257.88	11443.41	12873.84	14304.26
Saraudi_upstream	ALOS_5m	2250.86	1950.74	1828.82	3601.37	4051.54	4501.71	3121.19	3511.33	3901.48	2926.11	3291.88	3657.64
Saraudi_upstream	ALOS_5m_3px	2256.62	1955.74	1833.50	3610.59	4061.91	4513.24	3129.18	3520.32	3911.47	2933.60	3300.30	3667.00
Saraudi_upstream	TanDEMX_12m	2317.06	2008.12	1882.61	3707.30	4170.71	4634.12	3212.99	3614.62	4016.24	3012.18	3388.70	3765.22
Saraudi_upstream	DEM_15m	2129.41	1845.49	1730.14	3407.05	3832.93	4258.82	2952.78	3321.88	3690.97	2768.23	3114.26	3460.29
Kyandi	ALOS_5m	248.76	215.59	202.11	398.01	447.76	497.51	344.94	388.06	431.18	323.38	363.81	404.23
Kyandi	ALOS_5m_3px	249.15	215.93	202.43	398.63	448.46	498.29	345.48	388.67	431.85	323.89	364.38	404.86
Kyandi	TanDEMX_12m	279.08	241.87	226.75	446.53	502.34	558.16	386.99	435.36	483.74	362.80	408.15	453.50
Kyandi	DEM_15m	196.27	170.10	159.47	314.03	353.29	392.54	272.16	306.18	340.20	255.15	287.05	318.94
Kyandi_pkFm	ALOS_5m	6920.34	5997.63	5622.78	11072.54	12456.61	13840.68	9596.20	10795.73	11995.26	8996.44	10121.00	11245.55
Kyandi_pkFm	ALOS_5m_3px	6931.20	6007.04	5631.60	11089.93	12476.17	13862.41	9611.27	10812.68	12014.09	9010.56	10136.89	11263.21
Kyandi_pkFm	TanDEMX_12m	7763.90	6728.72	6308.17	12422.25	13975.03	15527.81	10765.95	12111.69	13457.43	10093.07	11354.71	12616.34
Kyandi_pkFm	DEM_15m	5460.21	4732.18	4436.42	8736.34	9828.38	10920.42	7571.49	8517.93	9464.37	7098.28	7985.56	8872.85
Kyandi_upstream	ALOS_5m	2256.64	1955.76	1833.52	3610.62	4061.95	4513.28	3129.21	3520.36	3911.51	2933.63	3300.34	3667.04
Kyandi_upstream	ALOS_5m_3px	2262.44	1960.78	1838.23	3619.90	4072.38	4524.87	3137.24	3529.40	3921.56	2941.17	3308.81	3676.46
Kyandi_upstream	TanDEMX_12m	2330.22	2019.52	1893.30	3728.35	4194.40	4660.44	3231.24	3635.14	4039.05	3029.29	3407.95	3786.61
Kyandi_upstream	DEM_15m	2158.24	1870.48	1753.57	3453.19	3884.83	4316.48	2992.76	3366.86	3740.95	2805.71	3156.43	3507.14
Magdi	ALOS_5m	243.29	210.86	197.68	389.27	437.93	486.59	337.37	379.54	421.71	316.28	355.82	395.35
Magdi	ALOS_5m_3px	243.83	211.32	198.11	390.12	438.89	487.66	338.11	380.37	422.64	316.98	356.60	396.22
Magdi	TanDEMX_12m	246.87	213.96	200.58	394.99	444.37	493.74	342.33	385.12	427.91	320.93	361.05	401.17
Magdi	DEM_15m	171.96	149.03	139.72	275.13	309.52	343.92	238.45	268.25	298.06	223.55	251.49	279.43
Magdi_pkFm	ALOS_5m	3747.37	3247.72	3044.74	5995.79	6745.26	7494.74	5196.35	5845.90	6495.44	4871.58	5480.53	6089.47
Magdi_pkFm	ALOS_5m_3px	3755.58	3254.84	3051.41	6008.93	6760.05	7511.17	5207.74	5858.71	6509.68	4882.26	5492.54	6102.82
Magdi_pkFm	TanDEMX_12m	3802.47	3295.47	3089.50	6083.94	6844.44	7604.93	5272.75	5931.85	6590.94	4943.20	5561.11	6179.01
Magdi_pkFm	DEM_15m	2648.60	2295.46	2151.99	4237.76	4767.48	5297.20	3672.73	4131.82	4590.91	3443.18	3873.58	4303.98

Name	Images	Sediment Yield [m^3 km^2 yr^{-1}]						Sediment Yield [t km^2 yr^{-1}]					
		b	c	d	b,e	b,f	b,g	c,e	c,f	c,g	d,e	d,f	d,g
Magdi_upstream	ALOS_5m	2153.79	1866.62	1749.96	3446.07	3876.82	4307.58	2986.59	3359.91	3733.24	2799.93	3149.92	3499.91
Magdi_upstream	ALOS_5m_3px	2159.28	1871.37	1754.41	3454.84	3886.70	4318.56	2994.20	3368.47	3742.75	2807.06	3157.94	3508.83
Magdi_upstream	TanDEMX_12m	2223.68	1927.19	1806.74	3557.89	4002.63	4447.37	3083.51	3468.95	3854.39	2890.79	3252.14	3613.49
Magdi_upstream	DEM_15m	2043.11	1770.69	1660.03	3268.97	3677.59	4086.22	2833.11	3187.25	3541.39	2656.04	2988.05	3320.05
Siddi	ALOS_5m	365.57	316.82	297.02	584.91	658.02	731.13	506.92	570.28	633.65	475.24	534.64	594.05
Siddi	ALOS_5m_3px	367.42	318.43	298.53	587.88	661.36	734.85	509.50	573.18	636.87	477.65	537.36	597.06
Siddi	TanDEMX_12m	407.08	352.80	330.75	651.32	732.74	814.16	564.48	635.04	705.60	529.20	595.35	661.50
Siddi	DEM_15m	333.39	288.94	270.88	533.42	600.10	666.78	462.30	520.09	577.87	433.40	487.58	541.76
Siddi_pkFm	ALOS_5m	5102.85	4422.47	4146.06	8164.55	9185.12	10205.69	7075.95	7960.44	8844.93	6633.70	7462.91	8292.13
Siddi_pkFm	ALOS_5m_3px	5128.78	4444.94	4167.13	8206.04	9231.80	10257.56	7111.91	8000.89	8889.88	6667.41	7500.84	8334.26
Siddi_pkFm	TanDEMX_12m	5682.29	4924.65	4616.86	9091.66	10228.12	11364.58	7879.44	8864.37	9849.30	7386.98	8310.35	9233.72
Siddi_pkFm	DEM_15m	4653.68	4033.19	3781.11	7445.88	8376.62	9307.35	6453.10	7259.73	8066.37	6049.78	6806.00	7562.22
Siddi_upstream	ALOS_5m	2211.24	1916.40	1796.63	3537.98	3980.23	4422.47	3066.25	3449.53	3832.81	2874.61	3233.93	3593.26
Siddi_upstream	ALOS_5m_3px	2152.33	1865.35	1748.77	3443.73	3874.20	4304.66	2984.57	3357.64	3730.71	2798.03	3147.79	3497.54
Siddi_upstream	TanDEMX_12m	2221.09	1924.95	1804.64	3553.75	3997.97	4442.18	3079.91	3464.90	3849.89	2887.42	3248.35	3609.28
Siddi_upstream	DEM_15m	2032.67	1761.65	1651.54	3252.27	3658.80	4065.34	2818.63	3170.96	3523.29	2642.47	2972.78	3303.08
Sigdi	ALOS_5m	11.44	9.92	9.30	18.31	20.59	22.88	15.87	17.85	19.83	14.87	16.73	18.59
Sigdi	ALOS_5m_3px	11.38	9.87	9.25	18.21	20.49	22.77	15.79	17.76	19.73	14.80	16.65	18.50
Sigdi	TanDEMX_12m	13.86	12.01	11.26	22.18	24.95	27.72	19.22	21.62	24.02	18.02	20.27	22.52
Sigdi	DEM_15m	11.13	9.65	9.05	17.81	20.04	22.27	15.44	17.37	19.30	14.47	16.28	18.09
Sigdi_pkFm	ALOS_5m	254.57	220.63	206.84	407.32	458.23	509.14	353.01	397.13	441.26	330.94	372.31	413.68
Sigdi_pkFm	ALOS_5m_3px	253.28	219.51	205.79	405.25	455.91	506.57	351.22	395.12	439.02	329.27	370.43	411.59
Sigdi_pkFm	TanDEMX_12m	308.38	267.26	250.56	493.41	555.08	616.76	427.62	481.07	534.53	400.89	451.01	501.12
Sigdi_pkFm	DEM_15m	247.72	214.69	201.27	396.36	445.90	495.45	343.51	386.45	429.39	322.04	362.29	402.55
Sigdi_upstream	ALOS_5m	2093.20	1814.11	1700.72	3349.12	3767.76	4186.40	2902.57	3265.39	3628.21	2721.16	3061.30	3401.45
Sigdi_upstream	ALOS_5m_3px	2104.51	1823.91	1709.91	3367.21	3788.11	4209.01	2918.25	3283.03	3647.81	2735.86	3077.84	3419.82

Name	Images	Sediment Yield [m^3 km^2 yr^{-1}]						Sediment Yield [t km^2 yr^{-1}]					
		b	c	d	b,e	b,f	b,g	c,e	c,f	c,g	d,e	d,f	d,g
Sigdi_upstream	TanDEMX_12m	2180.60	1889.85	1771.74	3488.96	3925.08	4361.20	3023.77	3401.74	3779.71	2834.78	3189.13	3543.47
Sigdi_upstream	DEM_15m	1987.03	1722.09	1614.46	3179.25	3576.65	3974.06	2755.35	3099.77	3444.19	2583.14	2906.03	3228.92
Gondang	ALOS_5m	523.69	453.86	425.50	837.90	942.64	1047.38	726.18	816.95	907.73	680.79	765.89	850.99
Gondang	ALOS_5m_3px	525.06	455.05	426.61	840.09	945.10	1050.12	728.08	819.09	910.10	682.58	767.90	853.22
Gondang	TanDEMX_12m	602.74	522.37	489.72	964.38	1084.93	1205.47	835.79	940.27	1044.74	783.56	881.50	979.45
Gondang	DEM_15m	407.44	353.12	331.05	651.91	733.40	814.89	564.99	635.61	706.24	529.68	595.89	662.10
Gondang_pkFm	ALOS_5m	7560.50	6552.43	6142.91	12096.80	13608.90	15121.00	10483.89	11794.38	13104.87	9828.65	11057.23	12285.81
Gondang_pkFm	ALOS_5m_3px	7580.28	6569.58	6158.98	12128.45	13644.50	15160.56	10511.32	11825.24	13139.15	9854.36	11086.16	12317.95
Gondang_pkFm	TanDEMX_12m	8701.72	7541.49	7070.15	13922.75	15663.10	17403.44	12066.39	13574.69	15082.98	11312.24	12726.27	14140.30
Gondang_pkFm	DEM_15m	5882.28	5097.97	4779.35	9411.64	10588.10	11764.55	8156.76	9176.35	10195.95	7646.96	8602.83	9558.70
Seti	ALOS_5m	2095.23	1815.87	1702.37	3352.37	3771.41	4190.46	2905.39	3268.56	3631.73	2723.80	3064.27	3404.75
Seti	ALOS_5m_3px	2100.83	1820.72	1706.93	3361.33	3781.50	4201.67	2913.16	3277.30	3641.44	2731.08	3072.47	3413.85
Seti	TanDEMX_12m	2182.58	1891.57	1773.34	3492.12	3928.64	4365.15	3026.51	3404.82	3783.13	2837.35	3192.02	3546.69
Seti	DEM_15m	1980.53	1716.46	1609.18	3168.84	3564.95	3961.05	2746.33	3089.62	3432.91	2574.68	2896.52	3218.35
Seti_wo_trip_pkFm	ALOS_5m	13570.60	11761.19	11026.12	21712.97	24427.09	27141.21	18817.90	21170.14	23522.38	17641.78	19847.01	22052.23
Seti_wo_trip_pkFm	ALOS_5m_3px	13598.58	11785.44	11048.85	21757.73	24477.45	27197.17	18856.70	21213.79	23570.88	17678.16	19887.93	22097.70
Seti_wo_trip_pkFm	TanDEMX_12m	14112.24	12230.61	11466.19	22579.58	25402.03	28224.48	19568.97	22015.09	24461.21	18345.91	20639.15	22932.39
Seti_wo_trip_pkFm	DEM_15m	12847.14	11134.19	10438.30	20555.43	23124.86	25694.28	17814.70	20041.54	22268.38	16701.28	18788.94	20876.61

a Distance along Seti Khola river course from down- to upstream
b Values calculated over 660 years
c Values calculated over 750 years
d Values calculated over 800 years
e Values calculated with 1.6 for bulk density [g cm-3]
f Values calculated with 1.8 for bulk density [g cm-3]
g Values calculated with 2.0 for bulk density [g cm-3]

Figure C.3.: Field images of re-exhumed tree trunks. A) Tree trunks in growth position in and along Anpu Khola. **B)** Close-up of one of the two trees in the Phusre Khola. **C)** Nicely washed-out tree trunk close to the water level in Anpu Khola. The terraces behind are ∼30 m high. **D)** Dated tree with in the Pokhara Formation some 12.5 m above water level. **E)** The biggest tree we dated; it stands out of the Pokhara Formation within lithofacies F3; see Figure 4.1 for locations.

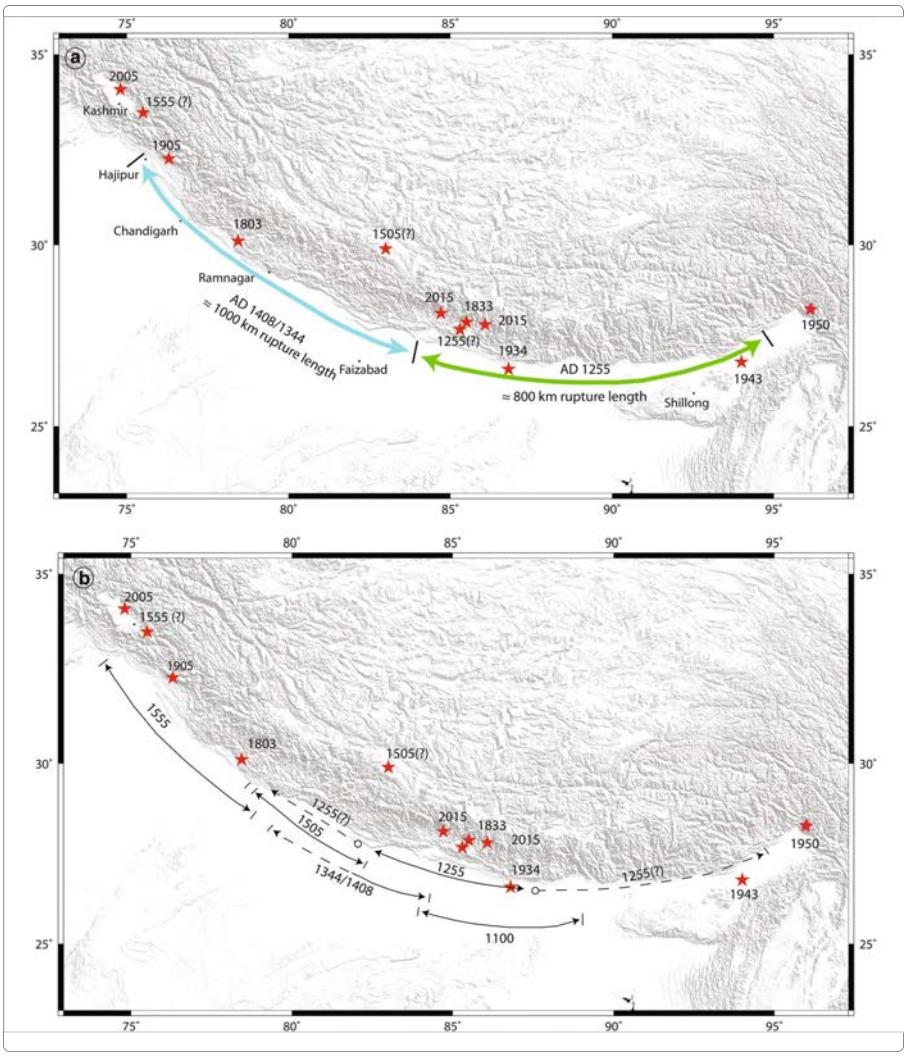

Figure C.4.: Paleo-earthquake model and review. a) This map shows the extent of the surface rupture of the 1255 and 1344/1408 AD events reviewed by Arora and Malik (2017). Limitations and error bars in ages may misleads the extent and overestimates the seismic hazard in the Himalaya. **b)** This map shows the overlap in estimated surface rupture of the medieval earthquakes and the uncertainty associated with extending the surface rupture of each event. It clearly shows, that all three medieval earthquakes (~1100, 1255, and 1344 AD are possible earthquake that may have triggered the sediment pulses forming the Pokhara Valley. This figure is copied from Arora and Malik (2017).

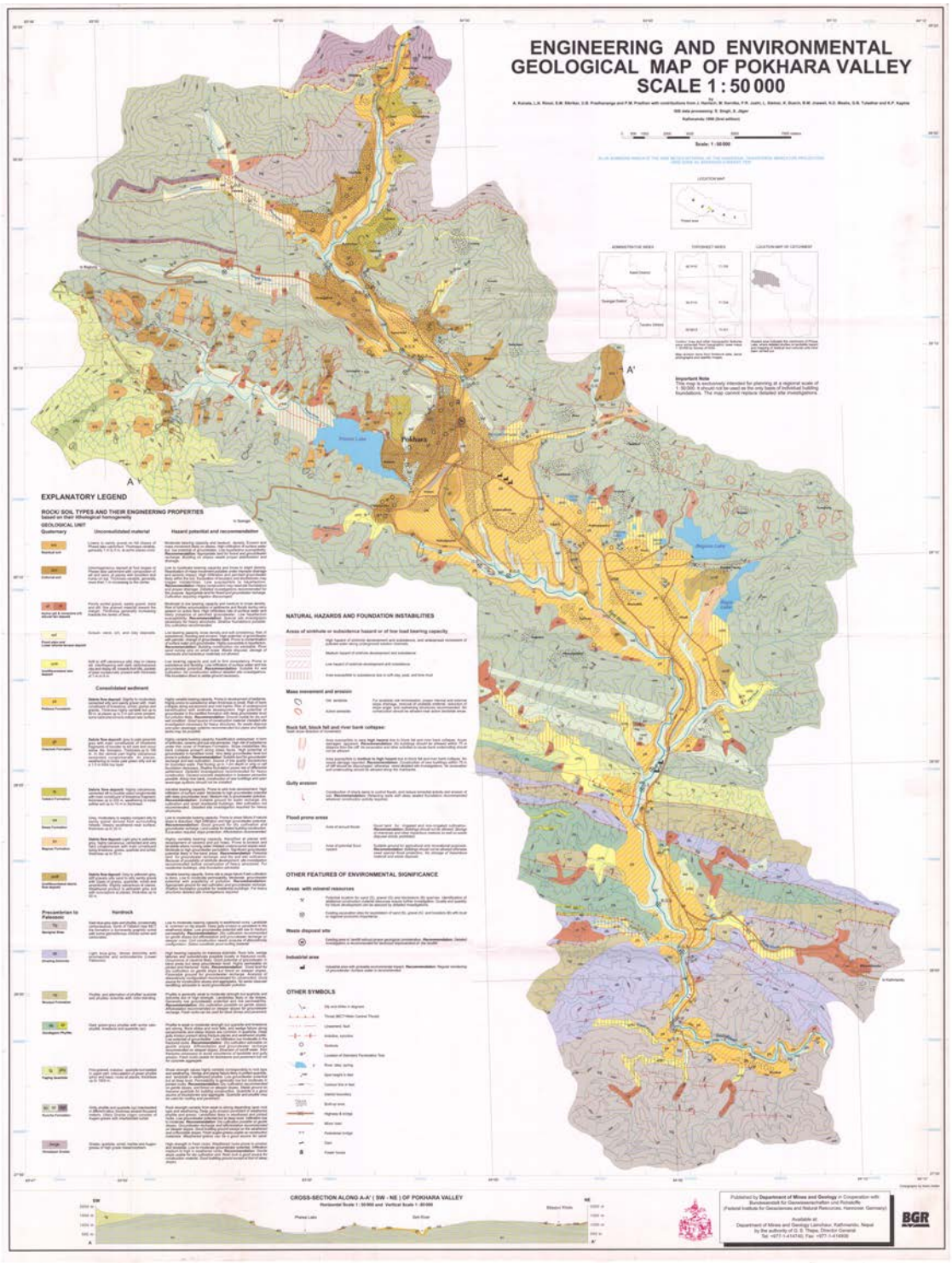

Figure C.5.: Geological map of the Pokhara Valley. Around Pokhara city, areas of high hazards of sinkhole development and subsidence are drawn on the map. These areas are all urban areas (Fig. 5.10, Koirala et al. (1998)).

Bibliography

Abe, K., 1972. Mechanisms and tectonic implications of the 1966 and 1970 Peru earthquake. Physics of the Earth and Planetary Interiors 5, 367–379.

Adhikari, B. R., Tamrakar, N. K., 2005. Bank instability and erosion problems of Bishnumati River, Kathmandu, Nepal. Journal of Nepal Geological Society 32 (Special Issue).

Adhikari, J., Seddon, D., 2002. POKHARA: Biography of a Town. Mandala Book Point, Kathmandu.

ADPC, Asian Disaster Preparedness Center, Norwegian Geotechnical Institure, Centre for International Studies and Cooperation, International Institute of Applied System Analysis, Austria, The World Bank, 2010. Nepal Hazard Risk assessment.

Akhmadaliev, S., Heller, R., Hanf, D., Rugel, G., Merchel, S., 2013. The new 6mv AMS-facility DREAMS at Dresden. Nucl. Instruments Methods Phys. Res. Sect. B Beam Interact. with Mater. Atoms 294, 5–10.

Allen, J., 1974. Reaction, relaxation and lag in natural sedimentary systems: general principles, examples and lessons. Earth-Science Reviews 10, 263–342.

Ambraseys, N. N., Douglas, J., 2004. Magnitude calibration of north Indian earthquakes. Geophysical journal international 159 (1), 165–206.

Andermann, C., Crave, A., Gloaguen, R., Davy, P., Bonnet, S., 2012. Connecting source and transport: Suspended sediments in the Nepal Himalayas. Earth and Planetary Science Letters 351-352, 158–170.

Arora, S., Malik, J. N., 2017. Overestimation of the earthquake hazard along the Himalaya: constraints in bracketing of medieval earthquakes from paleoseismic studies. Geoscience Letters 4 (1), 1–15.

Avouac, J.-P., 2015. Mountain Building: From Earthquakes to Geologic Deformation. In: Treatise on Geophysics. Elsevier, pp. 381–432.

Baker, V. R., 1987. Paleoflood hydrology and extraordinary flood events. Journal of Hydrology 96 (1-4), 79–99.

Baker, V. R., Kochel, R. C., Patton, P. C., Pickup, G., 1983. Palaeohydrologic Analysis of Holocene Flood Slack-Water Sediments. In: Collinson, J., Lewin, J. (Eds.), Modern and ancient fluvial systems. Vol. number 6 of the International Association of Sedimentologists of Special publication. Blackwell Scientific Publications, Boston, pp. 229–239.

Balco, G., Briner, J., Finkel, R. C., Rayburn, J. A., Ridge, J. C., Schaefer, J. M., 2009. Regional beryllium-10 production rate calibration for late-glacial northeastern North America. Quaternary Geochronology 4 (2), 93–107.

Balco, G., Purvance, M. D., Rood, D. H., 2011. Exposure dating of precariously balanced rocks. Quaternary Geochronology 6, 295–303.

Berryman, K. R., Cochran, U. A., Clark, K. J., Biasi, G. P., Langridge, R. M., Villamor, P., 2012. Major earthquakes occur regularly on an isolated plate boundary fault. Science 336 (6089), 1690–1693.

Bhandary, N. P., Dahal, R. K., Okamura, M., 2012. Preliminary understanding of the Seti River debris-flood in Pokhara, Nepal, on may 5th, 2012 -: A report based on a quick field visit program. ISSMGE Bulletin 6 (4), 8–18.

Bilham, R., 2015. Raising Kathmandu. Nature Geoscience 8 (8), 582–584.

Bilham, R., Gaur, V. K., Molnar, P., 2001. Himalayan seismic hazard. Science 293, 1442–1444.

Bishop, P., Hoey, T., Jansen, J., Artza, I. L., 2005. Knickpoint recession rate and catchment area: the case of uplifted rivers in Eastern Scotland. Earth Surface Processes and Landforms 30, 767–778.

Björnsen Gurung, A., Waymann von Dach, S., Price, M. F., Aspinall, R., Balsiger, J., Baron, J. S., Sharma, E., Greenwood, G., Kohler, T., 2012. Global Change and the World's Mountains — research needs and emerging themes for sustainable development. Mountain Research and Development 32 (S1), 47–54.

Blanckenburg, F. V., 2005. The control mechanisms of erosion and weathering at basin scale from cosmogenic nuclides in river sediment. Earth and Planetary Science Letters 237, 462–476.

Blöthe, J. H., Korup, O., 2013. Millennial lag times in the Himalayan sediment routing system. Earth and Planetary Science Letters 382, 38–46.

Bolla Pittaluga, M., Luchi, R., Seminara, G., 2014. On the equilibrium profile of river beds. Journal of Geophysical Research: Earth Surface 119 (2), 317–332.

Bollinger, L., Avouac, J. P., Beyssac, O., Catlos, E. J., Harrison, T. M., Grove, M., Goffé, B., Sapkota, S., 2004. Thermal structure and exhumation history of the Lesser Himalaya in central Nepal. Tectonics 23 (5), TC5015–TC5015.

Bollinger, L., Sapkota, S. N., Tapponnier, P., Klinger, Y., Rizza, M., van der Woerd, J., Tiwari, D. R., Pandey, R., Bitri, A., Bes de Berc, S., 2014. Estimating the return times of great Himalayan earthquakes in eastern Nepal: Evidence from the Patu and Bardibas strands of the Main Frontal Thrust. Journal of Geophysical Research: Solid Earth 119 (9), 7123–7163.

Bollinger, L., Tapponnier, P., Sapkota, S. N., Klinger, Y., 2016. Slip deficit in central Nepal: Omen for a repeat of the 1344 AD earthquake? Earth, Planets and Space 68 (1), 2119.

Bookhagen, B., Burbank, D. W., 2006. Topography, relief and TRMM-derived rainfall variations along the Himalaya. Geophysical Research Letters 33 (L08405), 1–5.

Braucher, R., Merchel, S., Borgomano, J., Bourlès, D. L., 2011. Production of cosmogenic radionuclides at great depth: A multi element approach. Earth and Planetary Science Letters 309, 1–9.

Brierley, G. J., Hickin, E. J., 1985. The downstream gradation of particles sizes in the Squamisch river, British Columbia. Earth Surface Processes and Landforms 10, 597–606.

Briner, J. P., Young, N. E., Goehring, B. M., Schaefer, J. M., 2012. Constraining Holocene 10Be production rates in Greenland. Journal of Quaternary Science 27 (1), 2–6.

Bronk Ramsey, C., 2008. Deposition models for chronological records. Quaternary Science Reviews 27 (1), 42–60.

Bronk Ramsey, C., 2009a. Bayesian Analysis of Radiocarbon Dates. Radiocarbon 51 (1), 337–360.

Bronk Ramsey, C., 2009b. Dealing with outliers and offsets in Radiocarbon Dating. Radiocarbon 51 (3), 1023–1045.

Bronk Ramsey, C., van der Plicht, J., Weninger, B., 2001. 'wiggle matching' radiocarbon dates. Radiocarbon 43 (2A), 381–389.

Brundsen, D., Thornes, J. B., 1979. Landscape sensitivity and change. Transactions of the Intstitute of Britisch Geographers 4 (4), 463–484.

Buck, C. E., Kenworthy, J. B., Litton, C. D., Smith, A., 1991. Combining archaeological and radiocarbon information: a Bayesian approach to calibration. Antiquity 65, 808–821.

Burbank, D. W., Anderson, R. S., 2001. Tectonic geomorphology. Blackwell Science, Oxford.

Burbank, D. W., Blythe, A. E., Putkonen, J., Pratt-Sitaula, B., Gabet, E., Oskin, M., Barros, A., Ojha, T. P., 2003. Decoupling of erosion and precipitation in the Himalayas. Nature 426 (6967), 652–655.

Carling, P., Villanueva, I., Herget, J., Wright, N., Borodavko, P., Morvan, H., 2010. Unsteady 1d and 2d hydraulic models with ice dam break for Qaternary megaflood, altai mountains, southern siberia. Global and Planetary Change 70 (1), 24–34.

Carling, P. A., 2013. Freshwater megaflood sedimentation: What can we learn about generic processes? Earth-Science Reviews 125, 87–113.

Central Bureau of Statistics, 2011. Environment statistics of Nepal and Nepal Population Report.

Chappell, J., 2007. Thresholds and lags in geomorphologic changes. Australian Geographer 15 (6), 357–366.

Chaudhary, S., Shukla, U., Sundriyal, Y., Srivastava, P., Jalal, P., 2015. Formation of paleovalleys in the Central Himalaya during valley aggradation. Quaternary International 371, 254–267.

Chen, C. Y., 2009. Sedimentary impacts from landslides in the Tachia River basin, Taiwan. Geomorphology 105, 355–365.

Chiaro, G., Kiyota, T., Pokhrel, R. M., Goda, K., Katagiri, T., Sharma, K., 2015. Reconnaissance report on geotechnical and structural damage caused by the 2015 Gorkha Earthquake, Nepal. Soils and Foundations 55 (5), 1030–1043.

Chmeleff, J., Blanckenburg, F. V., Kossert, K., Jakob, D., 2010. Determination of the 10Be half-life by multicollector ICP-MS and liquid scintillation counting. Nuclear Instruments & Methods in Physics Research Section B- Beam Interactions with Materials and Atoms 268(2), 192–199.

Clague, J., 2000. A review of catastrophic drainage of moraine-dammed lakes in British Columbia. Quaternary Science Reviews 19 (17-18), 1763–1783.

Clarke, G., Leverington, D., Teller, J., Dyke, A., 2003. Superlakes, Megafloods, and Abrupt climage Change. Science 301 (5635), 922–923.

Colchen, M., Le Fort, P., Pêcher, A., 1981. Geological map of Annapurna-Manaslu-Ganesh Himalaya of Nepal.

Coxon, P., Owen, L. A., Mitchell, W. A., 1996. A late Qaternary catastrophic flood in the Lahul Himalayas. Journal of Quaternary Science 11 (6), 495–510.

Croissant, T., Lague, D., Steer, P., Davy, P., 2017. Rapid post-seismic landslide evacuation boosted by dynamic river width. Nature Geoscience 10, 680–684.

Crosby, B., Whipple, K. X., Gasparini, N. M., Wobus, C., 2007. Formation of fluvial hanging valleys: Theory and simulation. Geophys. Res. 112 (F03S10).

Dadson, S. J., Hovius, N., Chen, H., Dade, W. B., Lin, J. C., Hsu, M. L., Lin, C. H., Horng, M. J., Chen, T. C., 2004. Earthquake-triggered increase in sediment delivery from an active mountain belt. Geology 32 (8), 733.

Dave, 2013. Mining the river Seti in Pokhara.
URL https://www.thelongestwayhome.com/blog/nepal/river-mining-seti-river-pokhara/

Davies, T., Korup, O., 2007. Persistent alluvial fanhead trenching resulting from large, infrequent sediment inputs. Earth Surface Processes and Landforms 32 (5), 725–742.

de Vries, A., Ripley, B. D., 2016. Package 'ggdendro': Create Dendrograms and Tree Diagrams Tsing 'ggplot'.
URL https://github.com/andrie/ggdendro

Department of Survey, 1996. Topographical map of the Pokhara area.

DG ECHO, Directorate General for Humanitarian Aid and Civil Protection, 2012. Humanitarian Implementation Plan South Asia: DIPECHO 6th Action Plan, 2012.

Dhital, M. R., 2015. Geology of the Nepal Himalaya. Springer International Publishing, Cham.

Dhital, M. R., Giri, S., 1993. Engineering-Geological investigations at collapsed the Seti Bridge site, Pokhara. Bulletin of Geology, Tribhuvan University Kathmandu 3 (1), 119–141.

Downs, P. W., Gregory, K. J., 2004. River Channel Management: Towards Sustainable Catchment Hydrosystems. Arnold, London.

Dunne, T., Aalto, R. E., 2013. Large River Floodplains. In: Treatise on Geomorphology. Elsevier, pp. 645–678.

Ekström, G., Stark, C. P., 2013. Simple scaling of catastrophic landslide dynamics. Science (New York, N.Y.) 339 (6126), 1416–1419.

English, R., 1985. Himalayan state formation and the impact of british rule in the nineteenth century. Mountain Research and Development 5 (1), 61–78.

Evans, S. G., Bishop, N. F., Fidel Smoll, L., Valderrama Murillo, P., Delaney, K., Oliver-Smith, A., 2009a. A re-examination of the mechanism and human impact of catas-

trophic mass flows originating on nevado huascarán, Cordillera Blanca, Peru in 1962 and 1970. Engineering Geology 108 (1-2), 96–118.

Evans, S. G., Tutubalina, O. V., Drobyshev, V. N., Chernomorets, S. S., McDougall, S., Petrakov, D. A., Hungr, O., 2009b. Catastrophic detachment and high-velocity long-runout flow of Kolka Glacier, Caucasus Mountains, Russia in 2002. Geomorphology 105 (3-4), 314–321.

Fenton, C. R., Hermanns, R. L., Blikra, L. H., Kubik, P. W., Bryant, C., Niedermann, S., Meixner, A., Goethals, M. M., 2011. Regional 10Be production rate calibration for the past 12ka deduced from the radiocarbon-dated Grøtlandsura and Russenes rock avalanches at 69Âř n, Norway. Quaternary Geochronology 6 (5), 437–452.

Fort, M., 1984. Phases d'accumulations sédimentaires internes et phases orogéniques au sud du massif de l'Annapurna: l'example du basin de Pokhara (népal). Rev. Geograph. Pyrénées, special issue "Montagne et Piémonts" 1, 25–47.

Fort, M., 1986. Glacial extension and catastrophic dynamics along the Annapurna Front, Nepal Himalaya. Göttinger Geographische Abhandlungen 81, 105–125.

Fort, M., 1987. Sporadic morphogenesis in a continental subduction setting: An example from the Annapurna Range, Nepal Himalaya. Z. Geomorph N. F., 9–36.

Fort, M., 2000. Glaciers and mass wasting processes: their influence on the shaping of the Kali Gandaki Valley (higher Himalaya of Nepal). Quaternary International 65/66, 101–191.

Fort, M., 2010. The Pokhara Valley: A Product of a Natural Catastrophe. In: Migon, P. (Ed.), Geomorphological Landscapes of the World. Springer Netherlands, Dordrecht, pp. 265–274.

Fort, M., Adhikari, B. R., Rimal, B., in press. Pokhara (Central Nepal): A Dramatic yet Geomorphologically active Environment versus a Dynamic, Rapidly Developing City. In: Thornbush, M., Allen, C. (Eds.), Urban Geomorphology: Landforms and Processes in Cities. Elsevier, p. Ch. 12.

Fort, M., Cossart, É., Deline, R., Dzikowski, M., Nicoud, G., Ravanel, L., Schoeneich, P., Wassmer, P., 2009. Geomorphic impacts of large and rapid mass movements: A review. Geomorphology 1/2009, 47–64.

Fort, M., Freytet, P., 1982. The Qaternary sedimentary evolution of the intra-montane basin of Pokhara in relation to the Himalaya Midlands and their hinterland. In: Singh, A., Nautiyal, S. P. (Eds.), Contemporary Geoscientific Research in the Himalaya. Vol. 2. Bishen Singh Mahendra Pal Singh, Dehra Dun, India, pp. 91–96.

Fort, M., Peulvast, J. P., 1995. Catastrophic mass-movement and morphogenesis in the peri-tibetan ranges, examples from [W]est Kunlun, East Pamir and Ladakh. Wiley & Sons.

Fraley, C., Raftery, A. E., 2003. Enhanced Model-Based Clustering, Density Estimation, and Discriminant Analysis Software: MCLUST. Journal of Classification 20 (2), 263–286.

Fryirs, K. A., 2017. River sensitivity: A lost foundation concept in fluvial geomorphology. Earth Surface Processes and Landforms 42 (1), 55–70.

Fryirs, K. A., Brierley, G. J., Preston, N. J., Kasai, M., 2007. Buffers, barriers and blankets: The (dis)connectivity of catchment-scale sediment cascades. CATENA 70 (1), 49–67.

Gabet, E. J., Burbank, D. W., Putkonen, J. K., Pratt-Sitaula, B. A., Ojha, T., 2004. Rainfall thresholds for landsliding in the Himalayas of Nepal. Geomorphology 63, 131–143.

Galetzka, J., Melgar, D., Genrich, J. F., Geng, J., Owen, S., Lindsey, E. O., Xu, X., Bock, Y., Avouac, J.-P., Adhikari, L. B., Upreti, B. N., Pratt-Sitaula, B., Bhattarai, T. N., Sitaula, B. P., Moore, A., Hudnut, K. W., Szeliga, W., Normandeau, J., Fend, M., Flouzat, M., Bollinger, L., Shrestha, P., Koirala, B., Gautam, U., Bhatterai, M., Gupta, R., Kandel, T., Timsina, C., Sapkota, S. N., Rajaure, S., Maharjan, N., 2015. Slip pulse and resonance of the Kathmandu basin during the 2015 gorkha earthquake, Nepal. Science (New York, N.Y.) 349 (6252), 1091–1095.

Gautam, P., Raj Pant, S., Ando, H., 2000. Mapping of subsurface karst structure with gamma ray and electrical resistivity profiles: a case study from Pokhara valley, central Nepal. Journal of Applied Geophysics 45 (2), 97–110.

Godard, V., Bourles, D. L., Spinabella, F., Burbank, D. W., Bookhagen, B., Fisher, G. B., Moulin, A., Leanni, L., 2014. Dominance of tectonics over climate in Himalayan denudation. Geology 42 (3), 243–246.

Godard, V., Burbank, D. W., Bourlès, D. L., Bookhagen, B., Braucher, R., Fisher, G. B., 2012. Impact of glacial erosion on 10Be concentrations in fluvial sediments of the Marsyandi catchment, central Nepal. Journal of Geophysical Research: Earth Surface 117 (F3), 1–17.

Goehring, B. M., Lohne, Ø., Mangerud, J., Svendsen, J. I., Gyllencreutz, R., Schaefer, J., Finkel, R., 2012. Late glacial and holocene 10Be production rates for western Norway. Journal of Quaternary Science 27 (1), 89–96.

Goode, J. K., Burbank, D. W., 2009. Numerical study of degradation of fluvial hanging valleys due to climate change. Journal of Geophysical Research 114 (F1), 1–13.

Gran, K. B., Czuba, J. A., 2017. Sediment pulse evolution and the role of network structure. Geomorphology 277, 17–30.

Grandin, R., Doin, M.-P., Bollinger, L., Pinel-Puyssegur, B., Ducret, G., Jolivet, R., Sapkota, S. N., 2012. Long-term growth of the Himalaya inferred from interseismic InSAR measurement. Geology 40 (12), 1059–1062.

Guilderson, T. P., Reimer, P. J., Brown, T. A., 2005. The Boon and B]ane of Radiocarbon Dating. Science 307, 362–364.

Gurung, D. R., Maharjan, S. B., Khanal, N. R., Hoshi, G., Murthy, M., 2015. Seti Flash Flood: Technical Analysis and DDR Interventions. In: Rameshwor Dangal (Ed.), Nepal Disaster Report 2015. Vol. 4.4. Kathmandu, pp. 101–110.

Gurung, H. B., 1970. Geomorphology of the Pokhara Valley. Vol. 2-3. Himalayan Review, Kathmandu.

Hagen, T., 1969. Report on the Geological Survey of Nepal. Denkschr. d. Schweiz. Naturf. Ges. 1, 1–185.

Hanisch, J., Koirala, B., 2010. Pokhara Valley: a place under permanent threat. Journal of the Nepal Geological Society 41, 119.

Hasegawa, S., Dahal, R. K., Yamanaka, M., Bhandary, N. P., Yatabe, R., Inagaki, H., 2009. Causes of large-scale landslides in the Lesser Himalaya of central Nepal. Environmental geology 57 (6), 1423–1434.

Hayes, S. K., Montgomery, D. R., Newhall, C. G., 2002. Fluvial sediment transport and deposition following the 1991 eruption of Mount Pinatubo. Geomorphology 45 (3), 211–224.

Herman, F., Copeland, P., Avouac, J.-P., Bollinger, L., Mahéo, G., Le Fort, P., Rai, S., Foster, D., Pêcher, A., Stüwe, K., Henry, P., 2010. Exhumation, crustal deformation, and thermal structure of the Nepal Himalaya derived from the inversion of thermochronological and thermobarometric data and modeling of the topography. Journal of Geophysical Research 115 (B6), 1–38.

Hewitt, K., 1998. Himalayan Indus Streams in the Holocene: Glacier-, and Landslide-"interrupted" fluvial systems. In: Stellrecht, I. (Ed.), Karakorum-Hindu Kush-Himalaya: dynamics of change part I. Vol. 87. Rudiger Koppe, Köln, pp. 1–38.

Hewitt, K., Clague, J., Orwin, J. F., 2008. Legacies of catastrophic rock slope failures in mountain landscapes. Earth Science Reviews 87 (1), 1–38.

Heyman, J., 2014. Paleoglaciation of the Tibetan Plateau and surrounding mountains based on exposure ages and ELA depression estimates. Quaternary Science Reviews 91, 30–41.

Hinderer, M., 2012. From gullies to mountain belts: A review of sediment budgets at various scales. Sedimentary Geology 280, 21–59.

Hodges, K. V., Parrish, R. R., Searle, M. P., 1996. Tectonic evolution of the central Annapurna Range, Nepalese Himalayas. Tectonics 15 (6), 1264–1291.

Hodges, K. V., Wobus, C., Ruhl, K., Schildgen, T., Whipple, K., 2004. Qaternary deformation, river steepening, and heavy precipitation at the front of the Higher Himalayan ranges. Earth and Planetary Science Letters 220 (3-4), 379–389.

Hoeltgen, L., Setzer, S., Weickert, J., 2013. An Optimal Control Approach to find sparse data for Laplace Interpolation. In: Heyden, A., Kahl, F., Olsson, C., Oskarsson, M., Tai, X.-C. (Eds.), Energy Minimization Methods in Computer Vision and Pattern Recognition. Vol. 8081 of Lecture Notes in Computer Science. Springer Berlin Heidelberg, Berlin, Heidelberg, pp. 151–164.

Hormann, K., 1974. Die Terrassen an der Seti Khola: Ein beitrag zur Quartären Morphogenese in Zentralnepal. Erdkunde 28 (3), 161–176.

Hovius, N., Meunier, P., Lin, C.-W., Chen, H., Chen, Y.-G., Dadson, S., Horng, M.-J., Lines, M., 2011. Prolonged seismically induced erosion and the mass balance of a large earthquake. Earth and Planetary Science Letters 304 (3-4), 347–355.

Howarth, J. D., Fitzsimons, S. J., Norris, R. J., Jacobsen, G. E., 2012. Lake sediments record cycles of sediment flux driven by large earthquakes on the Alpine fault, New Zealand. Geology : a venture in earth science reporting 40 (12), 1091–1095.

Huang, M.-F., Montgomery, D. R., 2012. Fluvial response to rapid episodic erosion by earthquake and typhoons, Tachia River, central Taiwan. Geomorphology 175-176, 126–138.

Hungr, O., Evans, S. G., Bovis, M. J., Hutchinson, J. N., 2001. A Review of the Classification of Landslides of the Flow Type. Environmental & Engineering Geoscience 7 (3), 221–238.

Ives, J. D., Messerli, B., 1989. The Himalayan dilemma: Reconciling development and conservation. United Nations University and Routledge, London and New York.

Jakob, M., Hungr, O., 2005. Debris flow hazards and related phenomena. Springer and Praxis Publ.

Jarvis, A., 1973. On the identification of the convex hull of a finite set of points in the plane. Information Processing Letters 2, 18–21.

Jarvis, A., Reuter, H. I., Nelson, A., Guevara, E., 2008. Hole-filled srtm for the glove version 4.
URL http://www.cgiar-csi.org/data/srtm-90m-digital-elevation-database-v4-1

Jayangondaperumal, R., Kumahara, Y., Thakur, V., Kumar, A., Srivastava, P., Dubey, S., Joevivek, V., Dubey, A. K., 2016. Great earthquake surface ruptures along backthrust of the janauri anticline, NW Himalaya. Journal of Asian Earth Sciences 133, 89–101.

Jayangondaperumal, R., Mugnier, J. L., Dubey, A. K., 2013. Earthquake slip estimation from the scarp geometry of Himalayan Frontal Thrust, western Himalaya: implications for seismic hazard assessment. International Journal of Earth Sciences 102 (7), 1937–1955.

Jibson, R., 2009. Using Landslides for Paleoseismic Analysis. In: McCalpin, J. P. (Ed.), Paleoseismology. Vol. 95 of International Geophysics. Academic Press, pp. 565–601.

Kaphle, K. P., Rimal, L. N., Duvadi, A. K., Nepali, D., 2007. Geohazards and environmental degradation insome of the urban areas of Nepal. Journal of Nepal Geological Society 36 (Sp. issue), 23.

Kargel, J. S., Leonard, G. J., Shugar, D. H., Haritashya, U. K., Bevington, A., Fielding, E. J., Fujita, K., Geertsema, M., Miles, E. S., Steiner, J., Anderson, E., Bajracharya, S., Bawden, G. W., Breashears, D. F., Byers, A., Collins, B., Dhital, M. R., Donnellan, A., Evans, T. L., Geai, M. L., Glasscoe, M. T., Green, D., Gurung, D. R., Heijenk, R., Hilborn, A., Hudnut, K., Huyck, C., Immerzeel, W. W., Liming, J., Jibson, R., Kaab, A., Khanal, N. R., Kirschbaum, D., Kraaijenbrink, P. D. A., Lamsal, D., Shiyin, L., Mingyang, L., McKinney, D., Nahirnick, N. K., Zhuotong, N., Ojha, S., Olsenholler, J., Painter, T. H., Pleasants, M., Pratima, K. C., Yuan, Q. I., Raup, B. H., Regmi, D., Rounce, D. R., Sakai, A., Donghui, S., Shea, J. M., Shrestha, A. B., Shukla, A., Stumm, D., van der Kooij, M., Voss, K., Xin, W., Weihs, B., Wolfe, D., Lizong, W., Xiaojun, Y., Yoder, M. R., Young, N., 2016. Geomorphic and geologic controls of geohazards induced by Nepal's 2015 gorkha earthquake. Science (New York, N.Y.) 351 (6269), aac8353.

Kargel, J. S., Paudel, L., Leonard, G. J., Regmi, D., Josh, S., Poudel, K., Thapa, B., Watanabe, T., Fort, M., 2013. Causes and Human Impacts of the Seti River (Nepal) Disaster of 2012.

Kaspari, S., Mayewski, P., Kang, S., Sneed, S., Hou, S., Hooke, R., Kreutz, K., Introne, D., Handley, M., Maasch, K., Qin, D., Ren, J., 2007. Reduction in northward incursions of the south asian monsoon since $\sim$ 1400 AD inferred from a Mt. Everest ice core. Geophys. Res. Lett. 34 (L16701).

Keefer, D. K., 1984. Landslides caused by earthquakes. Geological Society of America Bulletin 95 (4), 406.

Keefer, D. K., 1994. The importance of earthquake-induced landslides to long-term slope erosion and slope-failure hazards in seismically active regions. In: Geomorphology and Natural Hazards. Elsevier, pp. 265–284.

Keefer, D. K., 2002. Investigating Landslides Caused by Earthquakes – a Historical Review. Surveys in Geophysics 23 (6), 473–510.

Keller, E. A., Pinter, N., Green, D. J., 1997. Active Tectonics, Earthquakes, Uplift, and Landscape. Environmental & engineering geoscience : serving professionals in engineering, environmental and ground-water geology 3 (3), 463.

Kharel, B., Koirala, A., Neupane, D., Chaudhari, S. N., 1992. Preliminary evaluation of the problem concerning sand extraction in the Kathmandu Valley. Department Mines and Geology.

Kim, D. E., Seong, Y. B., Choi, K. H., Yu, B. Y., 2017. Role of debris flow on the change of 10Be concentration in rapidly eroding watersheds: A case study on the Seti River, central Nepal. Journal of Mountain Science 14 (4), 716–730.

Knighton, A. D., 1989. River adjustment to changes in sediment load: The effects of tin mining on the Ringarooma River, tasmania, 1875-1984. Earth Surface Processes and Landforms 14, 333–359.

Koi, T., Hotta, N., Ishigaki, I., Matuzaki, N., Uchiyama, Y., Suzuki, M., 2008. Prolonged impact of earthquake-induced landslides on sediment yield in a mountain watershed: The Tanzawa region, Japan. Geomorphology 101 (4), 692–702.

Koirala, A., Rimal, L. N., Sikrikar, S. M., Pradhananga, U. B., Pradhan, P. M., 1998. Engineering and environmental geological map of Pokhara Valley scale, 1:50000.

Korschinek, G., Bergmaier, A., Faestermann, T., Gerstmann, U., Knie, K., Rugel, G., Wallner, A., Dillmann, I., Dollinger, G., von Gostomski, C. L., Kossert, K., Maiti, M., Poutivtsev, M., Remmert, A., 2010. A new value for the half-life of 10Be by Heavy-ion Elastic Recoil Detection and liquid scintillation counting. Nuclear Instruments and Methods in Physics Research Section B: Beam Interactions with Materials and Atoms 268 (2), 187–191.

Korup, O., 2012. Earth's portfolio of extreme sediment transport events. Earth-Science Reviews 112 (3-4), 115–125.

Korup, O., Tweed, F., 2007. Ice, moraine, and landslide dams in mountainous terrain. Quaternary Science Reviews 26 (25-28), 3406–3422.

Kumahara, Y., Jayangondaperumal, R., 2013. Paleoseismic evidence of a surface rupture along the northwestern Himalayan Frontal Thrust (hft). Geomorphology 180–181, 47–56.

Kumar, S., Wesnousky, S. G., Jayangondaperumal, R., Nakata, T., Kumahara, Y., Singh, V., 2010. Paleoseismological evidence of surface faulting along the northeastern Himalayan front, India: Timing, size, and spatial extent of great earthquakes. J. Geophys. Res. 115 (B12422).

Kumar, S., Wesnousky, S. G., Rockwell, T. K., Briggs, R. W., Thakur, V. C., Jayangondaperumal, R., 2006. Paleoseismic evidence of great surface rupture earthquakes along the Indian Himalaya. Journal of Geophysical Research: Solid Earth 111 (B3), n/a–n/a.

Lane, E. W., 1955. The importance of fluvial morphology in hydraulic engineering. American Society of Civil Engineers Proceedings Separate 81 (745), 1–17.

Lavé, J., Avouac, J. P., 2000. Active folding of fluvial terraces across the Siwaliks Hills, Himalayas of central Nepal. Journal of Geophysical Research: Solid Earth 105 (B3), 5735–5770.

Lavé, J., Avouac, J. P., 2001. Fluvial incision and tectonic uplift across the himalays of central Nepal. Journal of Geophysical Research 106 (B11), 561–591.

Lavé, J., Yule, D., Sapkota, S., Basant, K., Madden, C., Attal, M., Pandey, R., 2005. Evidence for a Great Medieval Earthquake (˜1100 A.D.) in the Central himalyas, Nepal. Science 307, 1302–1305.

Le Fort, P., Cuney, M., Deniel, C., France-Lanord, C., Sheppard, S., Upreti, B. N., Vidal, P., 1987. Crustal generation of the Himalayan leucogranites. Tectonophysics 134 (1-3), 39–57.

Le Roux-Mallouf, R., Ferry, M., Ritz, J.-F., Berthet, T., Cattin, R., Drukpa, D., 2016. First paleoseismic evidence for great surface-rupturing earthquakes in the Bhutan Himalayas. Journal of Geophysical Research: Solid Earth 121 (10), 7271–7283.

Leibundgut, G., Sudmeier-Rieux, K., Devkota, S., Jaboyedoff, M., Derron, M., Penna, I., Nguyen, L., 2016. Rural earthen roads impact assessment in Phewa watershed, Western region, Nepal. Geoenvironmental Disasters 3 (13), 1–21.

Lennartz, T., 2015. Naturgefahren und alltaÌĺgliche Risiken der Lebenssicherung: Verwundbarkeit gegenuÌĺber gravitativen Massenbewegungen in Nepal. Ph.D. thesis, UniversitaÌĺt Heidelberg, Heidelberg.

Li, G., West, A. J., Densmore, A. L., Hammond, D. E., Jin, Z., Zhang, F., Wang, J., Hilton, R. G., 2016. Connectivity of earthquake-triggered landslides with the fluvial network: Implications for landslide sediment transport after the 2008 Wenchuan earthquake. Journal of Geophysical Research: Earth Surface 121 (4), 703–724.

Li, G., West, A. J., Densmore, A. L., Jin, Z., Parker, R. N., Hilton, R. G., 2014. Seismic mountain building: Landslides associated with the 2008 Wenchuan earthquake in the context of a generalized model for earthquake volume balance. Geochemistry, Geophysics, Geosystems 15 (4), 833–844.

Lin, G. W., Chen, H., Chen, C. Y., Horng, M. J., 2008a. Influence of typhoons and earthquakes on rainfall-induced landslides and suspended sediment discharge. Engeneering Geology 97, 32–41.

Lin, G. W., Chen, H., Hovius, N., Horng, M. J., Dadson, S., Meunier, P., Lines, M., 2008b. Effects of earthquake and cyclone sequencing on landsliding and fluvial sediment transfer in a mountain catchment. Earth Surface Processes and Landforms 33 (9), 1354–1373.

Liu, F., Yang, S., 2015. The effect of the Wenchuan earthquake on the fluvial morphology in the Longmen Shan, eastern Tibetan Plateau: Discussion and speculation. Quaternary International 371, 280–289.

Lupker, M., Blard, P. H., Lavé, J., France-Lanord, C., Leanni, L., Puchol, N., Charreau, J., Bourlès, D., 2012. 10Be-derived Himalayan denudation rates and sediment budgets in the Ganga basin. Earth and Planetary Science Letters 333-334, 146–156.

Malik, J. N., Naik, S. P., Sahoo, S., Okumura, K., Mohanty, A., 2017. Paleoseismic evidence of the CE 1505 (?) and CE 1803 earthquakes from the foothill zone of the K]umaon Himalaya along the Himalayan Frontal Thrust (hft), India. Tectonophysics 714-715, 133–145.

Manariotis, I. D., Yannopoulos, P. C., 2014. Impact of human activities in infrastrucutre works on hydro morphological characteristics of alfeios River, Greece. Global NEST Journal 16 (1), 136–145.

Marc, O., Hovius, N., Meunier, P., Gorum, T., Uchida, T., 2016. A seismologically consistent expression for the total area and volume of earthquake-triggered landsliding. Journal of Geophysical Research: Earth Surface 121 (4), 640–663.

Marc, O., Hovius, N., Meunier, P., Uchida, T., Hayashi, S., 2015. Transient changes of landslide rates after earthquakes. Geology 43 (10), 883–886.

Martin, A. J., DeCelles, P. G., Gehrels, G. E., Patchett, P. J., Isachsen, C., 2005. Isotopic and structural constraints on the location of the Main Central thrust in the Annapurna Range, central Nepal Himalaya. Geological Society of America Bulletin 117 (7), 926.

Mascle, G., Pêcher, A., Guillot, S., Rai, S. M., Gajurel, A. P., 2012. The Himalaya–Tibet collision. Nepal Geological Society and Société Géologique de France, Paris.

Mathworks, 2017. Image processing toolbox. user's guide r2017a.
URL `www.mathworks.com/help`

Matsuoka, A., Yamakoshi, T., Tamura, K., Maruyama, J., Ogawa, K., 2008. Sediment yield from seismically-disturbed mountainous watersheds revealed by multi-temporal aerial liDAR surveys. Association Internationale des Sciences Hydrologiques 325, 208–216.

Matthes, F. E., 1930. Geologic history of the Yosemite Valley, U.S. Geol. Surv. Prof. Pap. 160, 137.

McCalpin, J. P. (Ed.), 2009. Paleoseismology, 2nd Edition. Vol. 95 of International Geophysics. Academic Press.

MCTCA, Ministry of Culture, Tourism & Civil Aviation, 2014. Nepal Tourism Statistics 2013. Kathmandu.

Mishra, R. L., Singh, I., Pandey, A., Rao, P. S., Sahoo, H. K., Jayangondaperumal, R., 2016. Paleoseismic evidence of a giant medieval earthquake in the eastern Himalaya. Geophysical Research Letters 43 (11), 5707–5715.

MoHa, 2015. Nepal Disaster report 2015. Kathmandu.

Montgomery, D. R., Hallet, B., Yuping, L., Finnegan, N., Anders, A., Gillespie, A., Greenberg, H. M., 2004. Evidence for Holocene megafloods down the tsangpo River gorge, southeastern Tibet. Quaternary Research 62 (02), 201–207.

Mridula, S., Sinvhal, A., Wason, H. R., Rajput, S. S., 2016. Segmentation of Main boundary Thrust and Main Central Thrust in Western Himalaya for assessment of seismic hazard. Natural Hazards 84 (1), 383–403.

Mugnier, J.-L., Gajurel, A., Huyghe, P., Jayangondaperumal, R., Jouanne, F., Upreti, B., 2013. Structural interpretation of the great earthquakes of the last millennium in the central Himalaya. Earth-Science Reviews 127, 30–47.

Mugnier, J.-L., Huyghe, P., Gajurel, A., Becel, D., 2005. Frontal and piggy-back seismic ruptures in the external thrust belt of Western Nepal. Journal of Asian Earth Sciences 25 (5), 707–717.

Mugnier, J. L., Huyghe, P., Gajurel, A. P., Upreti, B. N., Jouanne, F., 2011. Seismites in the Kathmandu basin and seismic hazard in central Himalaya. Tectonophysics 509 (1-2), 33–49.

Mukhopadhyay, B., 2011. Clusters of Moderate Size Earthquakes along Main Central Thrust (MCT) in Himalaya. International Journal of Geosciences (2), 318–325.

Nawaz, A. S., Juyal, N., 2013. Chronology of late quaternary glaciations in Indian Himalaya: A critical review. Journal of the Geological Society of India 82 (6), 628–638.

Nishiizumi, K., Imamura, M., Caffee, M., Southon, J., Finkel, R., McAninch, J., 2007. Absolute calibration of 10Be AMS standards. Nucl. Instruments Methods Phys. Res. Sect. B Beam Interact. with Mater. Atoms 258 (2), 403–413.
URL doi:10.1016/j.nimb.2007.01.297

Obermeier, S. F., 2009. Using Liquefaction-Induced and Other Soft-Sediment Features for Paleoseismic Analysis. In: McCalpin, J. P. (Ed.), Paleoseismology. Vol. 95 of International Geophysics. Academic Press, pp. 479–564.

O'Connor, J. E. (Ed.), 1993. Hydrology, hydraulics, and geomorphology of the Bonneville flood. Vol. 274 of Special paper. Geological Society of America, Boulder, Colo.

O'Connor, J. E., Baker, V. R., 1992. Magnitudes and implications of peak discharges from glacial Lake Missoula. Geological Society of America Bulletin 104 (3), 267–279.

O'Connor, J. E., Beebee, R. A., 2009. Floods for natural rock-material dams. In: Burr, D., Baker, V. R., Carling, P. (Eds.), Megaflooding on Earth and Mars. Cambridge University Press, Cambridge UK and New York, pp. 128–171.

Olen, S. M., Bookhagen, B., Hoffmann, B., Sachse, D., Adhikari, D. P., Strecker, M. R., 2015. Understanding erosion rates in the Himalayan orogen: A case study from the Arun Valley. Journal of Geophysical Research: Earth Surface 120 (10), 2080–2102.

Ouimet, W. B., Whipple, K. X., Granger, D. E., 2009. Beyond threshold hillslopes Channel adjustment to base-level fall in tectonically active mountain ranges. Geology 37 (7), 579–582.

Pain, C. F., Bowler, J. M., 1973. Denudation following the November 1970 earthquake at Madang, Papua New Guinea. Zeitschrift für Geomorphologie Supplementband NF 18, 92–104.

Pandey, R. N., 1987. Palaeo-environment and Prehistory of Nepal. Contribution to Nepal Studies, CNAS-TU Kathmandu 14 (2), 111–124.

Parsons, A. J., Law, R. D., Searle, M. P., Phillips, R. J., Lloyd, G. E., 2015. Geology of the Dhaulagiri-Annapurna-Manaslu Himalaya, Western Region, Nepal. 1: 200,000. Journal of Maps 12 (1), 100–110.

Paudel, M. R., Sakai, H., 2008. Stratigraphy and depositional environments of basin-fill sediments in southern Kathmandu Valley, Central Nepal. Bulletin of the Department of Geology 11 (0).

Pearce, A. J., Watson, A. J., 1986. Effects of earthquake-induced landslides on sediment budget and transport over a 50-yr period. Geology 14 (1), 52–55.

Pêcher, A., 1991. The contact between the Higher Himalaya Crystalline and the Tibetan Sedimentary Series: Miocene large-scale dextral shearing. Tectonics 10 (3), 587–598.

Perron, J. T., Royden, L. H., 2013. An integral approach to bedrock river profile analysis. Earth Surface Processes and Landforms 38, 570–576.

Phillips, J. D., Lutz, J. D., 2008. Profile convexities in bedrock and alluvial streams. Geomorphology 102 (3), 554–566.

Pincus, R., 1988. Aitchison, j: The Statistical Analysis of Compositional Data. chapman and hall, london - new york 1986, xii, 416 pp., £ 25,00. Biometrical Journal 30 (7), 794.

Pokhrel, D., 2016. Inaguration of Pokhara international airport. Aviation Nepal.
URL https://www.aviationnepal.com/inaguration-of-pokhara-international-airport/

Pokhrel, R. M., Kiyota, T., Kuwano, R., Chiaro, G., Katagiri, T. (Eds.), 2015a. Site investigation of Sinkhole Damage in the Armala Area, Pokhara, Nepal. ICGE.

Pokhrel, R. M., Kiyota, T., Kuwano, R., Chiaro, G., Katagiri, T., Arai, I., 2015b. Preliminary Field Assessment of Sinkhole Damage in Pokhara, Nepal. International Journal of Geoengineering case histories 3 (2), 113–125.

Pratt, B., Burbank, D. W., Heimsath, A., Ojha, T., 2002. Impulsive alluviation during early Holocene strengthened monsoons, central Nepal Himalaya. Geology : a venture in earth science reporting 30 (10), 911–914.

Pratt-Sitaula, B., Burbank, D. W., Heimsath, A., Ojha, T., 2004. Landscape disequilibrium on 1000–10,000 year scales Marsyandi River, Nepal, central Himalaya. Geomorphology 58 (1-4), 223–241.

Pratt-Sitaula, B., Garde, M., Burbank, D. W., Oskin, M., Heimsath, A., Gabet, E., 2007. Bedload-to-suspended load ratio and rapid bedrock incision from Himalayan landslide-dam lake record. Quaternary Research 68 (1), 111–120.

Press, W. H., 2010. Cs395t Computaional Statistics with Application to Bioinformatics.

Rai, A. K., 2000. Limnological characteristics of subtropical Lakes Phewa, Begnas, and Rupa in Pokhara Valley, Nepal. Limnology 1 (1), 33–46.

Rajendran, C. P., John, B., Rajendran, K., 2015. Medieval pulse of great earthquakes in the central Himalaya: Viewing past activities on the frontal thrust. Journal of Geophysical Research: Solid Earth 120 (3), 1623–1641.

Reading, H. G. (Ed.), 1996. Sedimentary Environments: Processes, Facies and Stratigraphy, 3rd Edition. Blackwell Publishing Ltd.

Reimer, P., 2013. Intcal13 and Marine13 Radiocarbon Age Calibration Curves 0–50,000 Years cal BP. Radiocarbon 55 (4), 1869–1887.

Reimer, P. J., Bard, E., Bayliss, A., Beck, J. W., Blackwell, P. G., Bronk Ramsey, C., Buck, C. E., Cheng, H., Edwards, R. L., Friedrich, M., Grootes, P. M., Guilderson, T. P., Haflidason, H., Hajdas, I., Hatté, C., Heaton, T. J., Hoffmann, D. L., Hogg, A. G., Hughen, K. A., Kaiser, K. F., Kromer, B., Manning, S. W., Niu, M., Reimer, R. W., Richards, D. A., Scott, E. M., Southon, J. R., Staff, R. A., Turney, C., van der Plicht, J., 2013. Intcal13 and Marine13 radiocarbon age calibration curves 0-50,000 years cal BP. Radiocarbon 55 (4), 1869–1887.

Ren, Z., Zhang, Z., Yin, J., 2017. Erosion Associated with Seismically-Induced Landslides in the Middle Longmen Shan Region, Eastern Tibetan Plateau, China. Remote Sensing 9 (8), 864.

Richard, B., Waitt, J. R., 1985. Case for periodic colossal jökulhlaups from Pleistocene glacial Lake Missoula. Geological Society of America Bulletin 96, 1271–1286.

Rijal, M. L., 2017. Characterization of Sinkholes affected area of Thulibeshi Phat, Armala, Kaski, Nepal. Journal of Institute of Science and Technology 22 (1), 17.

Rimal, B., 2013. Urbanization and the decline of Agricultural Land in Pokhara Submetropolitan City, Nepal. Journal of Agricultural Science 5 (1).

Rimal, B., Baral, H., Stork, N., Paudyal, K., Rijal, S., 2015. Growing city and rapid land use transition: Assessing multiple hazards and Risks in the Pokhara Valley, Nepal. Land 4 (4), 957–978.

Roback, K., Clark, M. K., West, A. J., Zekkos, D., Li, G., Gallen, S. F., Chamlagain, D., Godt, J. W., 2018. The size, distribution, and mobility of landslides caused by the 2015 Mw 7.8 Gorkha earthquake, Nepal. Geomorphology 301, 121–138.

Robert, X., van der Beek, P., Braun, J., Perry, C., Dubille, M., Mugnier, J.-L., 2009. Assessing Qaternary reactivation of the Main Central thrust zone (central Nepal Himalaya) New thermochronologic data and numerical modeling. Geology 37 (8), 731–734.

Robinson, D. M., Martin, A. J., 2014. Reconstructing the Greater Indian margin: A balanced cross section in central Nepal focusing on the Lesser Himalayan duplex. Tectonics 33 (11), 2143–2168.

Ross, J., Gilbert, R., 1999. Lacustrine sedimentation in a monsoon environment: the record from Phewa Tal, middle mountain region of Nepal. Geomorphology 27, 307–323.

Rudoy, A. N., Baker, V. R., 1993. Sedimentary effects of cataclysmic late pleistocene glacial outburst flooding, aAtay Mountains, Siberia. Sedimentary Geology 85 (1-4), 53–62.

Rühland, K., Phadtare, N. R., Pant, R. K., Sangode, S. J., Smol, J. P., 2006. Accelerated melting of Himalayan snow and ice triggers pronounced changes in a valley peatland from northern India. Geophysical research letters : GRL 33 (15).

Russell, A. J., 2005. Sedimentary processes: Catastrophic floods. In: Selley, R. C., Cooks, L.R.M. Plimer, I.R. (Eds.), Encyclopedia of Geology. Academic Press, pp. 628–641.

Sakai, H., Fujii, R., Sugimoto, M., Setoguchi, R., Paudel, M. R., 2016. Two times lowering of lake water at around 48 and 38 ka, caused by possible earthquakes, recorded in the paleo-Kathmandu lake, central Nepal Himalaya. Earth, Planets and Space 68 (1), 1–10.

Sakai, T., Gajurel, A. P., Tabata, H., 2015. Seismites in the pleistocene succession and recurrence period of large earthquakes in the Kathmandu Valley, Nepal. Geoenvironmental Disasters 2 (1), 1–17.

Sapkota, S. N., Bollinger, L., Klinger, Y., Tapponnier, P., Gaudemer, Y., Tiwari, D., 2013. Primary surface ruptures of the great Himalayan earthquakes in 1934 and 1255. Nature Geoscience.

Sayami, M., Tamrakar, N. K., 2007. Status of sand mining and quality in northern Kathmandu, Central, Nepal. Bulletin of Geology, Tribhuvan University Kathmandu 10, 89–98.

Scherler, D., Lamb, M. P., Rhodes, E. J., Avouac, J. P., 2016. Climate-change versus landslide origin of fill terraces in a rapidly eroding bedrock landscape: San Gabriel River, california. GSA Bulletin 128 (7/8), 1228–1248.

Schiffer, M. B., 1986. Radiocarbon dating and the "old wood" problem: The case of the hohokam chronology. Journal of Archaeological Science 13, 13–30.

Schumm, S. A., 1979. Geomorphic Thresholds: The concept and its applications. Transactions of the Institute of British Geographers 54, 485–515.

Schuster, R. L., Highland, L. M., 2007. Overview of the effect of mass wasting on the natural environment. Environmental & Engineering Geoscience XIII (1), 25–44.

Schuster, R. L., Nieto, A. S., O'Rourke, T. D., Crespo, E., Plaza-Nieteo, G., 1996. Mass wasting triggered by the 5 March 1987 Ecuador earthquakes. Engineering Geology 42, 1–23.

Schwanghart, W., Bernhardt, A., Stolle, A., Hoelzmann, P., Adhikari, B. R., Andermann, C., Tofelde, S., Merchel, S., Rugel, G., Fort, M., Korup, O., 2016. Repeated catastrophic valley infill following medieval earthquakes in the Nepal Himalaya. Science (New York, N.Y.) 351 (6269), 147–150.

Schwanghart, W., Scherler, D., 2014. Short communication: TopoToolbox 2 – matlab-based software for topographic analysis and modeling in earth surface sciences. Earth Surface Dynamics 2 (1), 1–7.

Searle, M., Avouac, J.-P., Elliott, J., Dyck, B., 2017. Ductile shearing to brittle thrusting along the Nepal Himalaya: Linking miocene channel flow and critical wedge tectonics to 25th April 2015 Gorkha earthquake. Tectonophysics 714–715, 117–124.

Shang, Y., Yang, Z., Li, L., Liu, D., Liao, Q., Wang, Y., 2003. A super-large landslide in Tibet in 2000: Background, occurrence, disaster, and origin. Geomorphology 54 (3-4), 225–243.

Shrestha, O., Shakya, U., Hanisch, J., 1992. Engineering geological repost on the collapse of the bridge over the Seti River Gorge at Pokhara (Nepal). DMG Report Kathmandu.

Simon, A., 1992. Energy, time, and channel evolution in catastrophically disturbed fluvial systems. Geomorphology 5 (3-5), 345–372.

Simpson, G., Castelltort, S., 2012. Model shows that rivers transmit high-frequency climate cycles to the sedimentary record. Geology : a venture in earth science reporting 40 (12), 1131–1135.

Steinhilber, F., Beer, J., Fröhlich, C., 2009. Total solar irradiance during the Holocene. Geophys. Res. Lett. 36 (L19704).

Stolle, A., Bernhardt, A., Schwanghart, W., Hoelzmann, P., Adhikari, B. R., Fort, M., Korup, O., 2017. Catastrophic valley fills as archives of large Himalayan earthquakes, Pokhara, Nepal. Quaternary Science Reviews 177, 88–103.

Stone, J. O., 2000. Air pressure and cosmogenic isotope production. J. Geophys. Res. 105 (B10), 23753–23759.

Straumann, R. K., Korup, O., 2009. Quantifying postglacial sediment storage at the mountain-belt scale. Geology : a venture in earth science reporting 37 (12), 1079–1083.

Strom, A. L., 2009. Catastrophic Slides and Avalanches. In: Sassa, K., Canuti, P. (Eds.), Landslides. Springer, pp. 379–399.

Tamrakar, N. K., 2004. Disturbances and instabilities in the Bishnumati river corridor, Kathmandu basin. JUSAN 9 (16), 7–18.

Thompson, L. G., Yao, T., Mosley-Thompson, E., Davis, M. E., Henderson, K. A., Lin, P., 2000. A high -resolution millennial record o f the south Asian monsoon from h imalayan ice cores. Science 289, 1916–1920.

Tuladhar, D., Shrestha, S. (Eds.), 2010. Nepalese Folklore: Legends from Pokhara. Ratna Pustak Bhandar, Kathmandu, Nepal.

Uchida, T., Niwa, S., Horie, K., Hida, Y., Okamura, S., Hayashi, S., Kanbara, J., 2014. Prolonged Effects of Large Sediment Yield Events on Sediment Dynamics in Mountainous Catchments. Civil Engineering Journal 56 (10), 43–51.

Ulloa, H., Iloume, A., Picco, L., Mohr, C. H., Mazzorana, B., Lenzi, M. A., Mao, L., 2016. Spatial analysis of the impacts of the chaitén volcano eruption (chile) in three fluvial systems. Journal of South American Earth Sciences 69, 213–225.

United Nations Develop Program, Earthquake Risk Resuction, Recovery Preparedness Programm for Nepal, 2009. Report on Impact of Settlement Pattern, Land-Use Practice and Options in High Risk Areas: - Pokhara Sub-Metropolitan City. Kathmandu.

United Nations Develop Program, Earthquake Risk Resuction, Recovery Preparedness Programm for Nepal, 2010. Earthquake Vulnerability Pofile and Preparedness Plan: - Pokhara Sub-MetropolitanCity. Kathmandu.
URL `http://errrp.org.np/document/study_report/`

Van doninck, 2016. R: Package: Horizon search algorithm.
URL `https://CRAN.R-project.org/package=horizon`

Vance, D., Bickle, M., Ivy-Ochs, S., Kubik, P. W., 2003. Erosion and exhumation in the Himalaya from cosmogenic isotope inventories of river sediments. Earth and Planetary Science Letters 206 (3-4), 273–288.

Venditti, J. G., Dietrich, W. E., Nelson, P. A., Wydzga, M. A., Fadde, J., Sklar, L., 2010. Effect of sediment pulse grain size on sediment transport rates and bed mobility in gravel bed rivers. Journal of Geophysical Research 115 (F03039), 1–19.

Vermeesch, P., 2007. Cosmocalc: An Excel add-in for cosmogenic nuclide calculations. Geochem. Geophys. Geosyst. 8 (Q 08003).

Walder, J. S., O'Connor, J. E., 1997. Methods for prediciting peak discharge of floods caused by failure of natural and constructed earthen dams. Water Resour. Res. 33, 2447–2348.

Walker, M. J. C., 2005. Qaternary dating methods. J. Wiley, Chichester West Sussex England.

Walling, D. E., 1983. The sediment delivery problem. Journal of Hydrology 65 (1-3), 209–237.

Waltham, A. C., 1972. A contribution to the geology of the Annapurna and Nilgiri Himals, Nepal. Geol. Magazine 109, 205–214.

Waltham, T., 1996. Very large landslides in the Himalayas. Geology today 12 (5), 181–185.

Wang, W., Godard, V., Liu-Zeng, J., Scherler, D., Xu, C., Zhang, J., Xie, K., Bellier, O., Ansberque, C., Sigoyer, J., 2017. Perturbation of fluvial sediment fluxes following the 2008 Wenchuan earthquake. Earth surface processes and landforms : the journal of the British Geomorphological Research Group 42 (15), 2611–2622.

West, A. J., Hetzel, R., Li, G., Jin, Z., Zhang, F., Hilton, R. G., Densmore, A. L., 2014. Dilution of 10Be in detrital quartz by earthquake-induced landslides: Implications for determining denudation rates and potential to provide insights into landslide sediment dynamics. Earth and Planetary Science Letters 396, 143–153.

Westoby, M. J., Glasser, N. F., Hambrey, M. J., Brasington, J., Reynolds, J. M., Hassan, M. A., 2014. Reconstructing historic Glacial Lake Outburst Floods through numerical modelling and geomorphological assessment: Extreme events in the Himalaya. Earth Surface Processes and Landforms 38 (D09106), n/a–n/a.

Willet, P., 1987. Similarity and Clustering in Chemical Information Systems. Research Studies Press Wiley, N.Y.

Willet, S. D., McCoy, S. W., Perron, J. T., Goren, L., Chen, C. Y., 2014. Dynamic Reorganization of River Basins. Science 343.

Wittmann, H., Blanckenburg, F. V., Kruesmann, T., Norton, K. P., Kubik, P. W., 2007. Relation between rock uplift and denudation from cosmogenic nuclides in river sediment in the Central alps of Switzerland. Journal of Geophysical Research 112 (F4), L14307.

Wittmann, H., Malusà, M. G., Resentini, A., Garzanti, E., Niedermann, S., 2016. The cosmogenic record of mountain erosion transmitted across a foreland basin: Source-to-sink analysis of in situ 10 be, 26 al and 21 ne in sediment of the Po river catchment. Earth and Planetary Science Letters 452, 258–271.

Wobus, C., Whipple, K., Kirby, E., Snyder, N., Johnson, J., Spyropolou, K., Crosby, B., Sheehan, D., 2006. Tectonics from topography: procedures, promise, and pitfalls. GSA Special Papers 398, 55–74.

Wobus, C. W., Hodges, K. V., Whipple, K. X., 2003. Has focused denudation sustained active thrusting at the Himalayan topographic front? Geology 31 (10), 861.

Wolman, M. G., 1954. A method of sampling coarse river bed material. Trans. Am. Geophys. Union 35, 951–956.

Wolman, M. G., 1979. A cycle of sedimentation and erosion in urban river channels. Geogr. Ann. 49, 385–395.

Yamanaka, H., 1982. Radiocarbon ages of upper Qaternary Deposit in Central Nepal and their Geomorphological Significance. The Science Reports of Tohoku 32 (1), 46–60.

Yamanaka, H., Yoshida, M., Arita, K., 1982. Terrace Landform and Qaternary deposit around Pokhara Valley, Central Nepal. J. of Nepal Geol. Soc. 4 (special issue), 101–120.

Yanites, B. J., Tucker, G. E., Mueller, K. J., Chen, Y.-G., 2010. How rivers react to large earthquakes: Evidence from central Taiwan. Geology 38 (7), 639–642.

Yeats, R. S., Sieh, K., Allen, C. R., Geist, E. L., 1997. The Geology of Earthquakes. Pure and applied geophysics : PAGEOPH 150 (2), 353–354.

Yule, D., Dawson, S., Lavé, J., Sapkota, S., Tiwari, D., 2006. Possible evidence for surface rupture of the Main Frontal Thrust during the great 1505 Himalayan earthquake, Far-Western Nepal. EOS Trans. AGU (Fall Meet. Suppl. Abstract S33C-05) 52.

Zhou, T. J., Li, B., Man, W. M., Zhang, L. X., Zhang, J., 2011. A comparison of the Medieval Warm Period, Little Ice Age and 20th century warming simulated by the FGOALS climate system model. Chinese Science Bulletin 56 (28-29), 3028–3041.